Nanoscience and Technology

Hilmi Ünlü
Norman J. M. Horing *Editors*

Low Dimensional Semiconductor Structures

Characterization, Modeling and Applications

NanoScience and Technology

NanoScience and Technology

Series Editors:
P. Avouris B. Bhushan D. Bimberg K. von Klitzing H. Sakaki R. Wiesendanger

The series NanoScience and Technology is focused on the fascinating nano-world, mesoscopic physics, analysis with atomic resolution, nano and quantum-effect devices, nanomechanics and atomic-scale processes. All the basic aspects and technology-oriented developments in this emerging discipline are covered by comprehensive and timely books. The series constitutes a survey of the relevant special topics, which are presented by leading experts in the field. These books will appeal to researchers, engineers, and advanced students.

Please view available titles in *NanoScience and Technology* on series homepage
http://www.springer.com/series/3705/

Hilmi Ünlü
Norman J.M. Horing
(Editors)

Low Dimensional Semiconductor Structures

Characterization, Modeling and Applications

With 87 Figures

Editors:

Hilmi Ünlü
Istanbul Technical University
Department of Physics Engineering
Maslak, 34469 Istanbul, Turkey
hunlu@itu.edu.tr

Norman J.M. Horing
Stevens Institute of Technology
Department of Physics and Engineering Physics
Hoboken, USA
nhoring@stevens.edu

Series Editors:

Professor Dr. Phaedon Avouris
IBM Research Division
Nanometer Scale Science & Technology
Thomas J. Watson Research Center
P.O. Box 218
Yorktown Heights, NY 10598, USA

Professor Dr. Bharat Bhushan
Ohio State University
Nanotribology Laboratory
for Information Storage
and MEMS/NEMS (NLIM)
Suite 255, Ackerman Road 650
Columbus, Ohio 43210, USA

Professor Dr. Dieter Bimberg
TU Berlin, Fakutät Mathematik/
Naturwissenschaften
Institut für Festkörperphyisk
Hardenbergstr. 36
10623 Berlin, Germany

Professor Dr., Dres. h.c. Klaus von Klitzing
Max-Planck-Institut
für Festkörperforschung
Heisenbergstr. 1
70569 Stuttgart, Germany

Professor Hiroyuki Sakaki
University of Tokyo
Institute of Industrial Science
4-6-1 Komaba, Meguro-ku
Tokyo 153-8505, Japan

Professor Dr. Roland Wiesendanger
Institut für Angewandte Physik
Universität Hamburg
Jungiusstr. 11
20355 Hamburg, Germany

NanoScience and Technology ISSN 1434-4904
ISBN 978-3-642-28423-6 ISBN 978-3-642-28424-3 (eBook)
DOI 10.1007/978-3-642-28424-3
Springer Heidelberg New York Dordrecht London

Library of Congress Control Number: 2012947652

© Springer-Verlag Berlin Heidelberg 2013
This work is subject to copyright. All rights are reserved by the Publisher, whether the whole or part of the material is concerned, specifically the rights of translation, reprinting, reuse of illustrations, recitation, broadcasting, reproduction on microfilms or in any other physical way, and transmission or information storage and retrieval, electronic adaptation, computer software, or by similar or dissimilar methodology now known or hereafter developed. Exempted from this legal reservation are brief excerpts in connection with reviews or scholarly analysis or material supplied specifically for the purpose of being entered and executed on a computer system, for exclusive use by the purchaser of the work. Duplication of this publication or parts thereof is permitted only under the provisions of the Copyright Law of the Publisher's location, in its current version, and permission for use must always be obtained from Springer. Permissions for use may be obtained through RightsLink at the Copyright Clearance Center. Violations are liable to prosecution under the respective Copyright Law.
The use of general descriptive names, registered names, trademarks, service marks, etc. in this publication does not imply, even in the absence of a specific statement, that such names are exempt from the relevant protective laws and regulations and therefore free for general use.
While the advice and information in this book are believed to be true and accurate at the date of publication, neither the authors nor the editors nor the publisher can accept any legal responsibility for any errors or omissions that may be made. The publisher makes no warranty, express or implied, with respect to the material contained herein.

Printed on acid-free paper

Springer is part of Springer Science+Business Media (www.springer.com)

Preface

The modern world has witnessed the exceptionally rapid development of both our theoretical understanding and the technological advancement of semiconductor devices, following the invention of the first transistor in 1949. Improved techniques for growing semiconductor thin films of differing structural and electronic properties, even with layer thickness approaching atomic dimensions, have provided new opportunities for basic scientific studies and device applications. Such new fabrication technologies have made it possible to reduce device dimensions to the point where quantum size effects play a significant role in any realistic description of device operation and are required to reliably predict their performance in electronic and optical applications. Contemporary transistors operate much faster than conventional ones and have led to a many-thousand-fold increase in speed, which is crucial to the electronic and optical communication and computer industries.

Today's electronic and optical communications and information technology is still silicon- semiconductor-based and can, thus far, meet the current needs by either increasing the production rate or by developing new production technologies. As a result of intensive research and development activities, the size of the existing silicon semiconductor devices is expected to be about 10–20 nm in the year 2020. Accordingly, a new technology is needed for the production of electronic and optoelectronic devices that are smaller in size and volume and faster in speed. This will involve many new scientific and technological problems requiring solution before such a new technology is actually put into use to meet consumers' needs for better and faster electronics- and computer-based communications. In order to overcome these problems, the world's leading scientists and engineers have been carrying out intensive research on low dimensional/nanoscience and nanotechnology to create future information and communication technologies. Nanoscience and nanotechnology refer to the comprehensive interdisciplinary body of knowledge on the nanometer size scale involving the science (physics, chemistry, biology, and materials science) and engineering (electronics, computer, mechanical, chemical, construction, textiles, environment, etc.) fields.

Low dimensional/nanoscience and nanotechnology was put forward as a concept by Richard Feynman in a seminar called "There is plenty of room at the bottom",

which he gave at an American Physical Society meeting at the California Institute of Technology (Caltech) on December 29, 1959. The meaning of the word "nano" is small, and 1 nm is equal to one billionth of a meter (1 nm = 1/1,000,000,000 m). The physical and chemical properties of materials on that scale depend upon size and may be controlled using it. Indeed, the production of new low-dimensional materials is possible at the nanoscale. Feynman described a process to manipulate atoms and molecules to organize and operate devices and/or systems at lower dimensions, as needed. He also noted that scaling issues can arise due to possible changing of the magnitudes of physical phenomena, such as surface tension, van der Waals attraction, etc.

Since that first proposal of nanotechnology by Feynman in 1959, intensive research and development activities have gained momentum in the last 30 years. Nanotechnology and nanoscience had two major developments in the early 1980s: (1) cluster science and the discovery of the scanning tunneling microscope (STM), which led to the discovery of fullerenes in 1985 and carbon nanotubes just a few years later, and (2) further major developments in the area of the synthesis and properties of semiconductor nanocrystals, such as metal-oxide nanoparticles and quantum dots. Rapid development continued in the area of structural characterization of materials. The discovery of atomic force microscopy (AFM) took place just 6 years after the STM was invented.

In recent years, a truly extraordinary volume of research has been carried out all over the world on low-dimensional semiconductors, metals, ceramics, polymers, and composites containing nanostructured materials for applications in health/disease, pharmacology, energy, agriculture/food, electronics and communication, information processing and storage using the multiple functionality of the recently developed nanomaterials. This has spurred new industry in various fields, including defense technology. Newly created and improved technologies, including electronic communications, have intensified scientific research and technological development involving structures composed of atoms and molecules, as well as biological structures. Indeed, some recent scientific studies have been carried out on colloidal quantum dots. Since quantum dots have carriers confined in all directions (zero dimensions), they have a sharper density of states than that of higher dimensional (two- and three-dimensional) structures. Correspondingly, quantum dots have superior charge transport and optical properties and, consequently, much intensive research has been done to use them in making diode lasers, transistors, and biological sensors.

It was a great pleasure to host the International Conference on Nanomaterials and Nanosystems (NanoMats2009; http://www.nanomats.itu.edu.tr) and the Fourth National Conference on Nanoscience and Nanotechnology (NanoTr4; http://www.nanotr4.itu.edu.tr) at İstanbul Technical University, İstanbul, Turkey. In these conferences, all aspects of low dimensional/nanoscience and nanotechnology were addressed. The NanoMats2009 conference was endorsed by the European Materials Research Society (E-MRS; http://www.emrs-strasbourg.com/) and was organized in collaboration with scientists from İstanbul Technical University, İstanbul University, Stevens Institute of Technology, and the University of Essex. Both

NanoMats2009 and NanoTr4 have successfully brought together researchers from over a dozen countries in the areas of physics, chemistry, biology, materials science, and engineering to review the current status of the field. The participants of both NanoMats2009 and NanoTr4 had the opportunity to learn about the latest results and cutting-edge advances in all major areas of nanomaterials and nanosystems from leading international academic and industrial experts in the field. In NanoMats2009, 2 Plenary Lectures, 26 Invited Oral Presentations, 60 Oral Presentations, and 126 Poster presentations took place at the conference. Similar remarks pertain to NanoTr4. Participants addressed fundamental issues and solutions in nanomaterials and nanosystems involving a wide range of problems, sharing new ideas and results to delineate outstanding problems and guiding future research.

The focus of the conference presentations was concentrated on fundamental phenomena at the nanoscale, including in its scope the synthesis, properties, characterization and modeling of nanomaterials, nanotechnologies involving nanodevices and nanosystems, imaging, measuring, modeling, and manipulating low-dimensional matter at the nanoscale. The topics covered at the NanoMats2009 and NanoTr4 conferences are of vital importance in a wide range of modern technologies employed in most industries, communication, healthcare, energy conservation, biology, food, environment, and education, and thus will have a broad impact on our society. NanoMats2009 and NanoTr4 also had a strong educational and student outreach component that provided opportunities for young investigators to present their research findings and to learn about the most recent developments in this rapidly moving field. On the one hand, this was intended to facilitate fruitful and constructive discussions among the participants, leading to future collaborations between them. On the other hand, the strength of the educational component has led us to feel that its tutorial benefit to the larger body of students and uninitiated is best enhanced by publication in book form, rather than as a superficial conference proceedings of very short research reports. Nevertheless, the cutting-edge conference research papers selected for inclusion here are certainly of interest to all workers in the field.

This book covers a broad range of selected papers presented at NanoMats2009 and NanoTr4. On behalf of the Organizing Committee, we would like to thank all of the participants for their contributions to both NanoMats2009 and NanoTr4 with oral and/or poster presentations, as well as all other attending participants.

Istanbul — Hilmi Ünlü
Hoboken, NJ — Norman J. Horing

Contents

1 Advances in Low-Dimensional Semiconductor Structures 1
Hilmi Ünlü, Mohamed Rezaul Karim, H. Hakan Gürel, and Özden Akıncı
1.1 Introduction 1
1.2 Superlattices and Quantum Wells 2
1.3 Strained Superlattices and Quantum Wells 6
1.4 Modulation-Doped Field Effect Transistors 8
1.5 Heterostructure Bipolar Transistors 9
1.6 Developments at Nanoscale 10
1.7 Conclusion 16
References 17

2 Modeling of Low-Dimensional Semiconductors 19
Hilmi Ünlü, H. Hakan Gürel, Özden Akıncı, and Mohamed Rezaul Karim
2.1 Introduction 19
2.2 TB View of Semiconductor Structures 22
2.3 Semiempirical sp^3s^* TB Model 25
2.4 Band Structure of Ternary Semiconductors 28
2.5 Band Offsets in Ternary/Binary Structures 32
2.6 Semiempirical $sp^3d^5s^*$ TB Model 34
2.7 Conclusion 35
References 37

3 Graphene: Properties and Theory 39
Norman J. Morgenstern Horing
3.1 Graphene 40
3.1.1 Device-Friendly Material Properties 40
3.1.2 Applications 40
3.1.3 Introduction: Sample Preparation Techniques: Original Experiments 40

3.1.4 Introduction: Structure ... 41
3.1.5 Introduction: Structure, Massless Dirac Spectrum ... 41
3.2 Graphene Hamiltonian I ... 41
3.3 Graphene Hamiltonian II ... 42
3.4 Graphene Hamiltonian III ... 42
3.4.1 Graphene: Green's Functions for Null Field and Finite Magnetic Field ... 43
3.4.2 Graphene Quantum Dot in Magnetic Field ... 45
3.4.3 More about Graphene Quantum Dots ... 47
3.5 Dielectric Screening Function, K, (on the 2D Graphene Sheet) ... 47
3.5.1 Graphene Polarizability: Degenerate Limit ($T = 0°K$, No Magnetic Field) ... 48
3.5.2 Graphene Plasmon ... 49
3.5.3 New Graphene Transverse Electric Mode in Terahertz Range ... 50
3.5.4 Coupling of Graphene and Surface Plasmons ... 50
3.6 Graphene Energy Loss Spectroscopy and van der Waals Interaction ... 51
3.6.1 Atom/Graphene van der Waals Interaction I ... 52
3.6.2 Atom/Graphene van der Waals Interaction II ... 52
3.6.3 Graphene Double Layer van der Waals Interaction ... 53
3.6.4 Graphene Quasiparticle Self-Energy, $\sum$ ... 54
3.6.5 Electronic Superlattices in Corrugated Graphene ... 55
3.7 Graphene Transport: Experimental Background ... 55
3.8 Graphene Transport: Theoretical Background-A ... 56
3.9 Graphene Transport: Theoretical Background-B ... 56
3.10 Kinetic Equation for Graphene ... 57
3.10.1 Kinetic Equation Formulation for Current and Distribution Function ... 57
3.10.2 Kinetic Equation: Solution I ... 57
3.10.3 Kinetic Equation: Solution II ... 58
3.10.4 Kinetic Equation: Conductivity I ... 58
3.10.5 Static Screening Dielectric Function ... 59
3.10.6 Conductivity Results and Discussion I ... 59
3.10.7 Conductivity Results and Discussion II ... 59
3.10.8 Conductivity Results and Discussion III ... 60
3.10.9 Conductivity Results and Discussion IV ... 60
3.10.10 Conductivity Results and Discussion V ... 61
3.10.11 Conductivity Results and Discussion VI ... 61
3.11 Dynamic AC Conductivity ... 61
3.11.1 AC Kinetic Equation Formulation for Current and Distribution Function $\rightarrow \hat{\rho}$ ... 62
3.11.2 Dynamic AC Conductivity ... 64
3.11.3 AC Conclusions ... 66
3.12 Device-Friendly Features of Graphene I ... 66
3.12.1 Device-Friendly Features of Graphene II ... 66

3.12.2 Device-Friendly Features of Graphene III ... 67
3.12.3 Device-Friendly Features of Graphene IV ... 67
3.12.4 Device-Friendly Features of Graphene V ... 68
3.12.5 Device-Friendly Features of Graphene VI ... 68

4 Functionalization of Graphene Nanoribbons ... 69
Haldun Sevinçli, Mehmet Topsakal, and Salim Ciraci
4.1 Introduction ... 69
4.2 Electronic and Magnetic Properties of 2D and 1D Graphene ... 71
4.2.1 Electrons in Honeycomb Lattice ... 71
4.2.2 Electronic and Magnetic Properties of GNRs ... 73
4.3 Functionalization Through Superlattice Formation ... 75
4.3.1 Superlattices of Armchair Graphene Nanoribbons ... 75
4.3.2 Superlattices of Zigzag Graphene Nanoribbons ... 82
4.4 Functionalization Through TM-Atom Doping ... 86
4.5 Conclusions ... 90
References ... 91

5 Atom/Molecule van der Waals Interaction with Graphene ... 93
Norman J. Morgenstern Horing, Vassilios Fessatidis, and Jay D. Mancini
5.1 Introduction: Atom–Graphene van der Waals Interaction and the Plasma Image ... 93
5.2 Nonlocal Dipolar van der Waals Interaction of an Atom/Molecule and Graphene ... 97
References ... 99

6 Optical Studies of Semiconductor Quantum Dots ... 101
H. Yükselici, Ç. Allahverdi, A. Aşıkoğlu, H. Ünlü, A. Baysal, M. Çulha, R. İnce, A. İnce, M. Feeney, and H. Athalin
6.1 Introduction ... 101
6.2 Solid-Phase Precipitation in Glass ... 102
6.3 Particle-in-a-Box Model to Determine the Average Nanocrystal Radius and Size Distribution ... 104
6.4 Raman and Photoluminescence Spectroscopies ... 108
6.5 Photoabsorption spectra ... 111
6.6 Quantum Dots in Solution Phase ... 113
6.7 Interferometric Analysis of QD Samples ... 114
References ... 116

7 Friedel Sum Rule in One- and Quasi-One-Dimensional Wires ... 119
Vassilios Vargiamidis, Vassilios Fessatidis, and Norman J. Morgenstern Horing
7.1 Introduction ... 119
7.2 Local Density of States and Friedel Sum Rule for the One-Dimensional Wire ... 120
7.2.1 Local Density of States ... 122
7.2.2 Friedel Sum Rule ... 125

7.3 Friedel Sum Rule in a Quasi-One-Dimensional Wire 127
7.4 Summary 129
References 130

8 Effects of Temperature on the Scattering Phases and Density of States in Quantum Wires 131
Vassilios Vargiamidis, Vassilios Fessatidis, and Norman J. Morgenstern Horing
8.1 Introduction 131
8.2 Formulation 133
8.2.1 Local Density of States 133
8.2.2 Scattering Phases 135
8.2.3 Simple Model Scatterer 136
8.3 Finite Temperature Effects 138
8.4 Summary 141
References 141

9 Fabrication of Low Dimensional Nanowire-Based Devices using Dieletrophoresis 143
Ramazan Kizil
9.1 Introduction 143
9.2 NanoGap Electrodes 145
9.3 Nanotechnology Applied to Bio/Molecular Detection and Nanogap Electrodes 146
9.4 Dielectrophoresis 147
9.5 Applications of DEP 148
9.6 Nanowire Synthesis and Characterization 148
9.7 Integration of Nanowires with a Microsystem 150
9.8 Microchip Design 150
9.9 Nanowire Alignment by DEP 151
References 158

Index 161

Contributors

Özden Akıncı Computational Science Division, Informatics Institute, Istanbul Technical University, Maslak Istanbul, Turkey

Ç. Allahverdi Department of Physics, Yıldız Technical University, Davutpaşa, Istanbul, Turkey

A. Aşıkoğlu Department of Physics, Yıldız Technical University, Davutpaşa, Istanbul, Turkey

H. Athalin Inst Mat Jean Rouxel, Univ Nantes, CNRS, 2 Rue Houssiniere, Nantes, France

A. Baysal Department of Chemistry, Istanbul Technical University, Maslak, Istanbul, Turkey

Salim Ciraci Department of Physics, Bilkent University, Ankara, Turkey, ciraci@fen.bilkent.edu.tr

UNAM, Institute of Materials Science and Nanotechnology, Bilkent University, Ankara, Turkey

M. Çulha Department of Genetics and Bioengineering, Yeditepe University, Kayışdağı, Istanbul, Turkey

M. Feeney Department of Physics, Yeditepe University, Kayışdağı, Istanbul, Turkey

Vassilios Fessatidis Department of Physics, Fordham University, Bronx, NY, USA

H. Hakan Gürel Department of Physics, Istanbul Technical University, Maslak Istanbul, Turkey

Computational Science Division, Informatics Institute, Istanbul Technical University, Maslak Istanbul, Turkey

N.J.M. Horing Department of Physics and Engineering Physics, Stevens Institute of Technology, Hoboken, NJ, USA, nhoring@stevens.edu

A. İnce Department of Physics, Yeditepe University, Kayışdağı, Istanbul, Turkey

R. İnce Department of Physics, Yeditepe University, Kayışdağı, Istanbul, Turkey

Mohamed Rezaul Karim Department of Physics, Faculty of Science and Letters, Istanbul Technical University, Maslak, Istanbul, Turkey

Ramazan Kizil Chemical Engineering Department, Istanbul Technical University, Maslak 34469, Istanbul, kizilr@itu.edu.tr

Jay D. Mancini Department of Physical Sciences, Kingsborough College of the City University of New York, Brooklyn, NY, USA

Haldun Sevindi Department of Physics, Bilkent University, Ankara, Turkey

UNAM, Institute of Materials Science and Nanotechnology, Bilkent University, Ankara, Turkey

Institute for Materials Science, TU Dresden, Dresden, Germany

Mehmet Topsakal UNAM, Institute of Materials Science and Nanotechnology, Bilkent University, Ankara, Turkey

H. Ünlü Department of Physics, Faculty of Science and Letters, Istanbul Technical University, Maslak, Istanbul, Turkey

Computational Science Division, Informatics Institute, Istanbul Technical University, Maslak Istanbul, Turkey, hunlu@itu.edu.tr; hilmi.unlu74@gmail.com

Vassilios Vargiamidis Department of Physics, Aristotle University, Thessaloniki, Greece

Department of Applied Sciences, Technological Educational Institute of Thessaloniki, Sindos, Greece

H. Yükselici Department of Physics, Yıldız Technical University, Davutpaça, Istanbul, Turkey, mhyukselici@gmail.com

Chapter 1
Advances in Low-Dimensional Semiconductor Structures

Hilmi Ünlü, Mohamed Rezaul Karim, H. Hakan Gürel, and Özden Akıncı

Abstract Improved technologies for growing semiconductor thin films of different structural and electronic properties, and even with layer thickness approaching atomic dimensions, have provided new opportunities for basic scientific studies and device applications. New fabrication technologies have also made it possible to reduce device dimensions to the point where quantum size effects must be considered in order to realistically describe the device operation and reliably predict their performance for electronic and optical applications. In this chapter, we shall present a partial summary of advances in low-dimensional semiconductor materials and their device applications.

1.1 Introduction

The theoretical understanding and technology of semiconductor devices have developed with great rapidity since the first transistor was invented in 1949 [1]. Improved technologies for growing semiconductor thin films of different structural and electronic properties, and even with layer thickness approaching atomic dimensions, have provided new opportunities for basic scientific studies and device applications [2]. In this matter, new fabrication technologies have also made it possible to reduce device dimensions to the point where quantum size effects must be considered in order to realistically describe the device operation and reliably predict their performance for electronic and optical applications. Contemporary transistors operate much faster than conventional ones and have led to a many

H. Ünlü (✉)
Computational Science Division, Informatics Institute, Istanbul Technical University, Maslak Istanbul 80626, Turkey

Department of Physics, Faculty of Science and Letters, Istanbul Technical University, Maslak Istanbul 80626, Turkey
e-mail: hunlu@itu.edu.tr; hilmi.unlu74@gmail.com

H. Ünlü and N.J.M. Horing (eds.), *Low Dimensional Semiconductor Structures*, NanoScience and Technology, DOI 10.1007/978-3-642-28424-3_1,
© Springer-Verlag Berlin Heidelberg 2013

thousand-fold increase in speed, which is very crucial to the electronic and optical communication and computer industries.

An unexpected increase in the speed of transistors has resulted, partially, from a reduction of charge transit time between terminals. Shorter charge transit time implies minimum time delay of input signals to the output. Charge transit time has been shortened very effectively by choosing semiconductor materials and device structures in which signals propagate faster by employing semiconductors having high electron mobility and velocity. Intense research on silicon (Si)-based semiconductor devices over the decades has resulted in a detailed theoretical understanding of the operation of these devices and introduction of the new ones. Modern semiconductor growth and device fabrication technologies have made it possible to integrate Si and gallium arsenide (GaAs) devices for high-speed electronic and optoelectronic applications. Groups III–V compounds such as GaAs are formed by specific mixtures of elements (e.g., Ga and As) and have electronic and optical properties much superior to those of Si. For example, the mobility of bulk GaAs is about six times larger than that of Si for a donor density of $1 \times 10^{17}\,\text{cm}^{-3}$. Furthermore, the maximum electron drift velocity in bulk GaAs is almost twice that in Si and occurs at much lower electric fields (see Ref. [2]) making GaAs devices operate faster and at lower voltages.

Advances in multilayer thin-film growth techniques, particularly molecular beam epitaxy (MBE) and metal organic chemical vapor deposition (MOCVD), have made it possible to produce semiconductor heterojunctions between IV–IV, III–V, and II–VI compounds, shown in Fig. 1.1, with tailored electronic and optical properties that do not occur in nature [1–3]. One can now control the alloy composition and doping in ternary and quaternary IV–IV, III–V, and II–VI semiconductor compounds over atomic distances.

Despite the fact that these artificial heterostructures do violate steady-state chemical thermodynamics principles, they are easily grown on GaAs and Si substrates [4, 5] by nonequilibrium crystal growth techniques such as MBE and MOCVD. When these advanced growth techniques are combined with advanced characterization techniques and analysis, it is possible to fabricate high-performance devices for fast signal processing, as well as some novel structures that are of interest to solid-state scientists and device engineers. The epitaxial layers are so thin that quantum mechanical effects, which are important in the operation of heterostructure devices, have been realized.

1.2 Superlattices and Quantum Wells

The impact of heterostructures on charge carriers can be summarized as follows. First of all, one can make bipolar transistors with high injection efficiency based on a heterostructure formed between semiconductors (with different physical

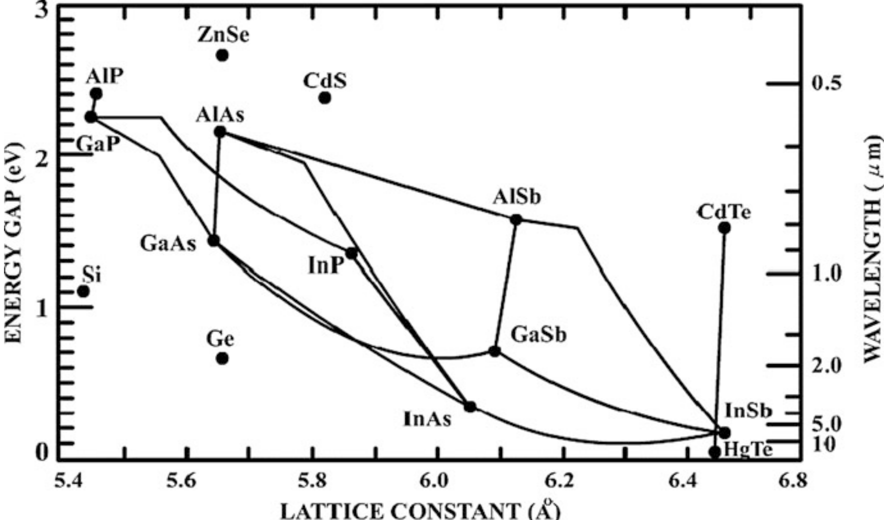

Fig. 1.1 Energy gap versus lattice constant for some semiconductors (often used as a reference in designing electronic and optoelectronic heterostructure devices)

properties) for carriers flowing from the wide-bandgap semiconductor emitter to the narrow-bandgap semiconductor base. Because this injection efficiency is related exponentially to the difference in the bandgap energies across the heterointerface, it can be made almost independent of doping levels [6]. To illustrate this, the equilibrium energy band diagram is shown in Fig. 1.2 for an N/p AlGaAs/GaAs heterostructure emitter of an npn AlGaAs/GaAs heterostructure bipolar transistors (HBT) in which the injection factor for electrons (holes) is related to the conduction (valence) band discontinuity but is often further enhanced by the electric field induced by charge transfer. There are other applications of heterostructures in making electronic and optical devices. In some cases, a particular compound can be grown on top of the original material as an ohmic (or Schottky) contact. For example, in GaAs/(Al,Ga)As laser diodes or modulation-doped field effect transistors (MODFETs), a GaAs layer is always used on top of the (Al,Ga)As layer in order to facilitate ohmic contacts since it is easier on smaller bandgap materials.

Advances in heteroepitaxial growth technologies have made it possible to realize potential wells for electrons and holes that have dimensions of the order of the mean free path of charged particles. Periodic extension of thin-layer pairs, so-called *superlattices*, causes an artificial perturbation of the crystal structure and modifies the bulk properties (1.3). Quantum wells and superlattices may have already stimulated much research in high-speed electronic devices and optical devices. In the case of modulation-doped heterostructure field effect transistors (MODFETs), the wide-gap semiconductor is doped, from which charge carriers diffuse to the nominally undoped narrow-gap semiconductor.

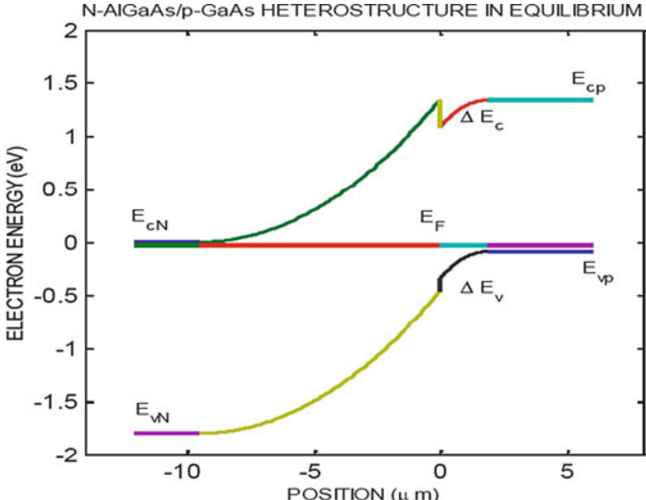

Fig. 1.2 The energy band diagram of an N-AlGaAs/p-GaAs heteroemitter in thermal equilibrium. When forward biased (wide-gap N-AlGaAs is connected to the negative terminal of the power supply), electrons injected by the N-AlGaAs emitter diffuse across the p-GaAs base. Some electrons recombine with holes at defect sites located at the heterointerface and some of the electrons diffusing in the base recombine with holes there

Semiconductor superlattices and multiple quantum wells (MQWs) are artificially grown structures formed by epitaxial deposition of alternating semiconductor layers or by introducing impurities into individual layers of a single semiconductor with layer thickness smaller than the carrier (electron or hole) mean free path. There are two kinds of superlattices: heterostructure superlattice, first proposed by Esaki and Tsu [10], and doped superlattices in which the dopant-type alternates between n- and p-type in close proximity, as proposed by Dohler [11]. The compositional superlattices can be grouped as: (1) Type I superlattices, where the bandgap of the barrier overlaps (straddles) that of the well (e.g., (Al,Ga)As/GaAs); and (2) Type II superlattices, where the bandgap of the barrier partially overlaps (straddles) that of the well (e.g., InGaAs/GaSbAs) or does not overlap at all (e.g., GaSb/InAs).

Superlattices are made of lattice-matched thin layers of two semiconductors with different electronic properties in alternation (Fig. 1.3). The thickness of alternate layers is less than approximately 10 nm so that the spatial variation of the electronic properties of the constituent materials leads to complex alignment of energy levels. Similar to the case of a periodic crystalline solid, there exist certain energy levels called “subbands” in a superlattice, as shown in Fig. 1.4 (see Ref. [1] for a detailed discussion of the structure and its applications). In superlattices, the energy levels of potential wells can be adjusted by the proper choice of the material and thickness. For example, by decreasing the barrier layer thickness, one can increase the subband energy levels. Therefore, the electronic structure of the artificially made superlattice

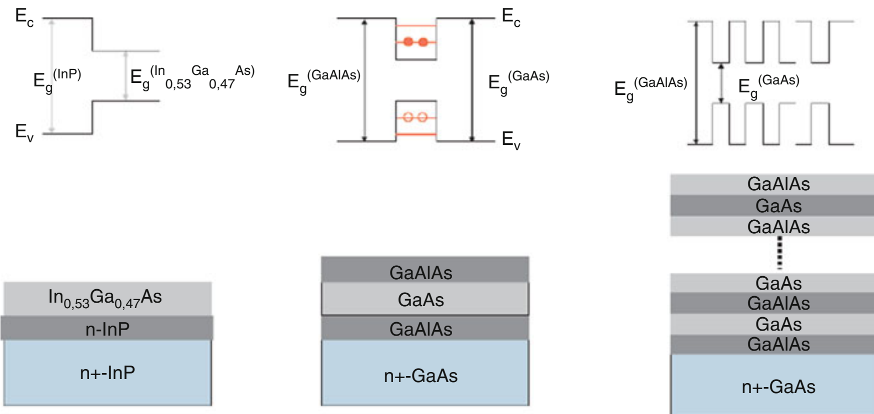

Fig. 1.3 Schematic energy band diagrams of single and multiple layer heterostructure (called superlattices on *far right*) samples

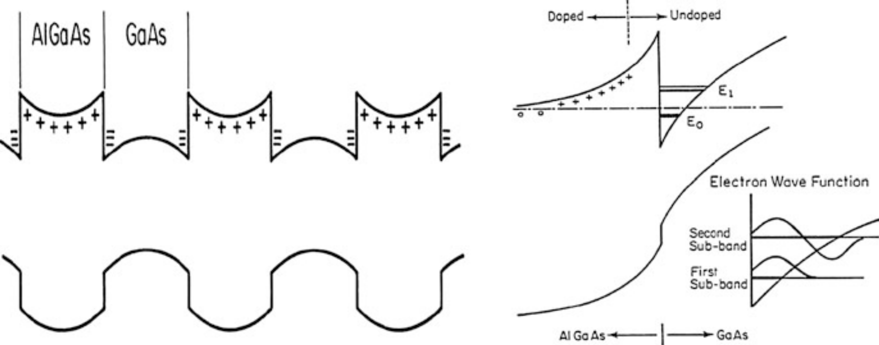

Fig. 1.4 Schematiciagram of an (Al,Ga)As/GaAs multiple quantum well (*left*). Carriers are confined to the GaAs well, leading to many interesting quantum phenomena. Details of the discrete energy levels (subbands) and wave functions are shown for a single interface structure (*right*). The triangular energy diagram also leads to quantization of the allowed energy levels near the interface. The first level E_0 (ground subband) and to some extent the second level E_1 (excited subband) are occupied. The wave function penetration into the larger bandgap material is apparent because the potential barrier is not infinite

crystal differs from that of the bulk crystal. The propagation of conducting electrons in the plane perpendicular to the layers is modified by the superlattice potential barriers. The total energy of electrons becomes quantized if their energy is below the continuum threshold. Such structures are called MQWs. The motion of carriers parallel to the layers is not affected much by the potential barrier of the superlattice. Assuming parabolic bands and infinite barriers, the conduction band subband energy levels, with respect to the bottom of the conduction band, can be described by:

$$E_n = \frac{\hbar^2}{2m_n^*}\left(\frac{n\pi}{L_z}\right)^2 \quad n = 1, 2, \ldots \tag{1.1}$$

where m_n^* is the effective mass of electrons in the conduction band and L_z is the quantum well thickness. The situation for holes is much more complex because of the presence of heavy and light holes.

With the present state of epitaxial technology, a large bandgap semiconductor and a narrow-bandgap semiconductor, such as AlGaAs and GaAs, respectively, can be easily grown alternately on one another. Favorable bandgap alignment gives a potential energy well in the conduction band is formed confining electrons in the GaAs. Quantum confinement of charge carriers (electrons or holes) in the well is analogous to that of a particle in a box where the confinement leads to quantized discrete energy states in the wells. Therefore, any electron and hole recombination yields radiation with larger energies than expected from the bulk material.

1.3 Strained Superlattices and Quantum Wells

It is well known that the performance of electronic and optical semiconductor devices depends on their specific electronic properties, such as energy gaps and refractive index discontinuities between the heterostructure constituents. In general, heterostructures are composed of semiconducting materials with identical lattice constants and thermal expansion coefficients. Many of the III–V compounds meet the former requirement, as illustrated in Fig. 1.1 where the variation of energy gap is shown as a function of lattice constant for several ternary and quaternary systems. Among them, the GaAs/AlGaAs ternary heterostructure system in particular has been extensively used in the fabrication of many electronic and optical devices due to the relative ease with which this high-quality lattice-matched structure can be grown and processed.

In heterostructures where lattice matching is achieved only over a limited range of alloy compositions, the quality of epitaxial layers depends critically on the degree of matching and on the compositional uniformity over the substrate area. The maximum mismatch percentage that can be accommodated by elastic strain in the layers lies below 1×10^{-2} depending on the application. For larger mismatches beyond this level, device degradation and extensive arrays of misfit dislocations take place. Figure 1.1 indicates the lattice-matching requirement for many III–V compounds. In nature, there are materials that cannot provide lattice matching and therefore do not have dislocation-free interfaces needed for device applications. This limitation on the choice of materials can be overcome by using thin layers made of mismatched materials, so-called *strained-layer heterostructures* (Fig. 1.3). The advent of such structures has greatly increased the number of materials suitable for electronic and optoelectronic device applications. Thus, with strained-layer

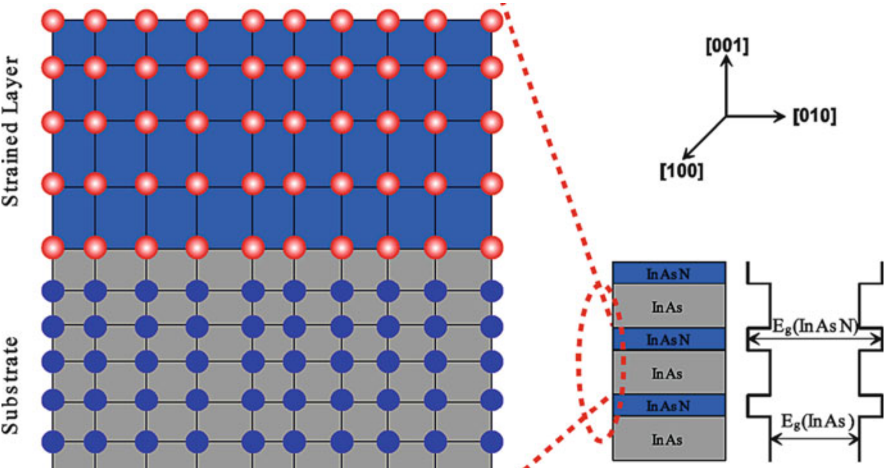

Fig. 1.5 Strained heterolayer epitaxy is a result of a stack of materials with dissimilar lattice constants. To accommodate the misfit strain, the individual layers contract or expand in the plane of the layers and in the plane of the growth, respectively

structures, an additional degree of freedom is obtained in the design of devices, leading to better tailoring of transport and optical properties [9].

The use of strained layers allows one to grow alternate layers with smaller or larger lattice constant than that of the substrate, such that the total stress on the substrate is 0. Depending on the needs of the device designer, the energy gaps of components and conduction and valence band offsets at heterointerfaces can be engineered using the strained layers. This is something that cannot be achieved with most of the lattice-matched materials in which the energy gaps and band offsets have fixed values. Furthermore, the anisotropy of the strain removes the degeneracy of the valence band. For example, biaxial compressive strain splits the heavy and light hole components of degenerate valence bands into two subbands: (1) a light hole band with a small mass in the plane of the layer and (2) a heavy hole band with large mass along the direction perpendicular to the plane of the layer, respectively.

Advances in experimental and theoretical work on superlattices have grown fast and in new directions. Using epitaxial techniques such as MBE, one can grow both heterostructures and doped superlattices from semiconductors with lattice mismatches of several percent as long as the constituent layer thicknesses are kept sufficiently small (Fig. 1.5). Since the lattice mismatch is accommodated by coherent elastic strain, there is no misfit dislocation generated at the heterointerfaces of a superlattice. The advantage of using a strained-layer superlattice (SLS) is that by adjusting the layer thickness, one can increase flexibility in the choice of layer materials. They lead to a wide range of adjustable electronic and optical properties, such as the change in energy gap and effective masses for light and heavy holes.

For example, under certain conditions, a direct-bandgap SLS can be produced from indirect-bandgap layer materials if the indirect-bandgap minimum is zone-folded to the zone center in the superlattice (1.6).

1.4 Modulation-Doped Field Effect Transistors

When the carriers are confined between two barriers in a thin semiconductor quantum well, as shown in Figs. 1.4 and 1.6, one observes a new "quantum phenomenon." Since the de Broglie wavelength of electrons needs to fit into the quantum well (or channel), there exist discrete energy levels, E_0, E_1, ..., called "quantum subband levels." When the separation of two subband energies (e.g., $E_0 - E_1$) is larger than thermal energy, $k_b T (k_b$ is the Boltzmann constant and T is the lattice temperature), the energy in the z-direction is a constant forcing the carriers to move in the xy-plane only. In this sense, the motion of the carriers is two dimensional, and the resultant system is called the *two-dimensional electron gas* (2DEG), which can easily be obtained in a semiconductor heterostructure made of two wide-bandgap semiconductors and one narrow-bandgap semiconductor, as shown in Fig. 1.6 for a 2DEG (Al,Ga)As/GaAs heterostructure.

The wide-gap (Al,Ga)As plays the role of a potential barrier, whereas the narrow-gap GaAs plays the role of a quantum well (confining the electrons to the heterointerface). Since both AlGaAs and GaAs have nearly the same lattice constants, and similar elastic properties, the interface quality is much better than in the conventional Si/SiO_2 system. The potential barrier in both conduction and valence bands at the (Al,Ga)As/GaAs heterointerface arises from the abrupt change in composition and leads to the depletion of electrons from the wide-bandgap barrier (Al,Ga)As and an accumulation of electrons in the narrow-bandgap channel GaAs.

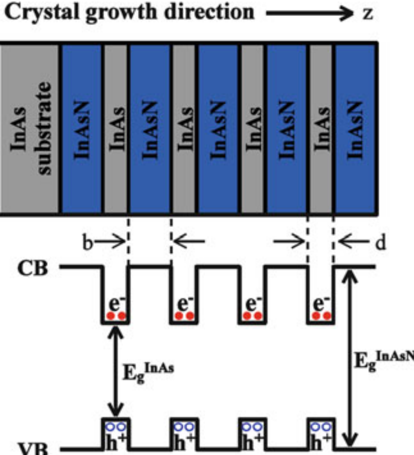

Fig. 1.6 Typical band profile for an SLS consisting of two semiconductors. The tensile and compressive elastic strains remove the degeneracy of the valence band and therefore modify the effective potential seen by carriers

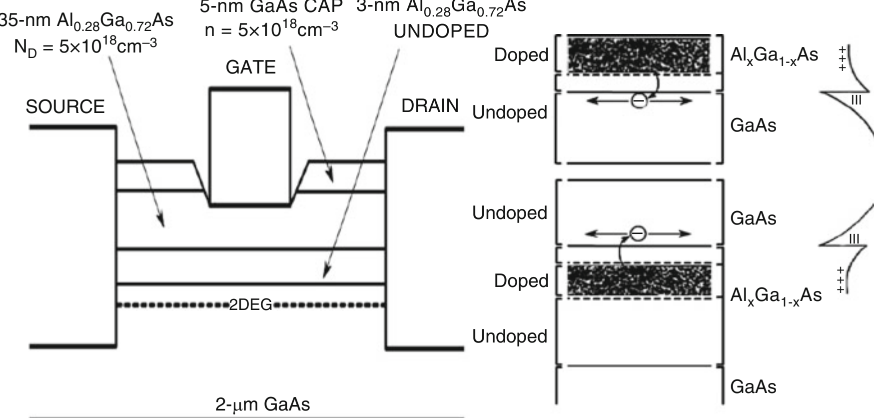

Fig. 1.7 Since interface heterostructures are used for heterojunction FETs, the structure with (Al,Ga). As grown on top of GaAs (a normal modulation-doped structure) is one that is commonly used for FETs. The diagram on the *right* shows the conduction electrons and valence holes

The potential "notch" at the interface confines the electrons to a quasi-triangular quantum well (or channel) about 5–10 nm thick (Fig. 1.7).

Quantized energy levels, or subbands, are formed in this channel, with the lowest generally filled by electrons and the second partially or fully filled, depending on the electron density. Thus, the Fermi level lies between the first and the second subbands. Free electrons confined in the channel conduct current parallel to the heterointerface between the source and drain of the field effect transistor (FET) when an electric field is applied parallel to the heterointerface. The current is proportional to the electron density, electron velocity (for submicron devices), or electron mobility. A negative bias applied to a metal gate on the surface of the (Al,Ga)As reduces the areal electron concentration and therefore channel current. When the gate voltage is sufficiently large, the entire channel region under the gate is depleted of electrons and the current is "pinched-off." When the gate is biased positively with respect to the channel, the current flow occurs.

1.5 Heterostructure Bipolar Transistors

The concept of a Heterostructure bipolar transistor (HBT) was theoretically proposed by Kroemer [7, 8] and experimentally explored and developed over the last three decades with the advancement of crystal growth techniques such as MBE. The HBT structure is different from FETs; a bipolar structure is a three-layer structure (either n/p/n or p/n/p) and consists of both n- and p-type semiconductor layers, whereas the unipolar structure consists of a doped barrier layer and undoped channel layer. In an n/p/n HBT structure, current is carried by minority electrons whereas

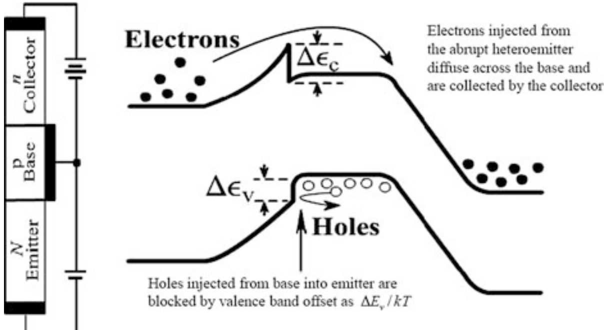

Fig. 1.8 Conduction and valence band edge profile of an n/p/n heterostructure bipolar transistors under normal bias conditions. The emitter–base junction is forward-biased (emitter connected to the negative terminal of the battery) and the base–collector junction is reverse-biased (collector is connected to the positive side of a different battery). Electrons injected from the emitter diffuse across the base and are collected by the collector. Along the way, some of them recombine with hole in the interior of the base and some recombine with holes at defect sites at the heterointerface

in p/n/p HBT structures current is carried by minority holes. Since the electron effective mass is smaller than that of the hole, minority electron transport is superior to minority hole transport, and npn HBTs are much superior over pnp HBTs. A schematic energy band diagram of a discrete HBT under normal biasing conditions is shown in Fig. 1.8.

In addition, the emitter doping can also be reduced, thereby decreasing the intrinsic base–emitter capacitance. Thus, it is possible to greatly increase current gain through the virtual elimination of the hole component of emitter current and to improve high-frequency performance at the same time by reducing the base resistance and base–emitter capacitance. Realization of the full potential of heterostructure bipolar devices (such as np (pn) diodes and npn (pnp) Heterostructure bipolar transistors (HBTs)) for electronic device technologies requires reliable and precise predictive process and performance simulation models that are consistent with the fundamental principles of solid-state physics and quantum mechanics.

1.6 Developments at Nanoscale

Today's electronic communications and information technology is Si semiconductor-based and can so far meet the current need by either increasing the production rate and/or developing new production technologies. As a result of intensive research and development activities, the size of existing Si semiconductor devices in 2020 is expected to be around 10–20 nm in size. This means that a new technology is needed for the production of electronic and optoelectronic devices that are smaller in size and volume and faster in speed. This will then create many new scientific and technological problems to be solved before the new technology is actually put in

force to meet the customer's needs for a better and faster electronics and computer-based communications. In order to overcome these problems, the world's leading scientists and engineers have been carrying out intensive work in nanoscience and nanotechnology to create future information and communication technologies.

Nanoscience and nanotechnology refer to the comprehensive interdisciplinary research involving science (physics, chemistry, biology, materials science) and engineering (electronics, computer, mechanical, chemical, construction, textiles and environment, etc.) fields. Nanoscience and nanotechnology was put forward as a concept by Richard Feynman in a seminar called *There is Plenty of Room at the Bottom*, which he gave at an American Physical Society meeting at California Institute of Technology (Caltech) on December 29, 1959. The meaning of the word "nano" is small and one nanometer is equal to one billionth meter ($1\,\text{nm} = 1/1000{,}000{,}000\,\text{m}$).

The physical and chemical properties of materials on that scale may change and may be controlled using size. Indeed, the production of new materials is possible at nanoscale. Feynman described a process to be able to manipulate atoms and molecules to organize and operate devices and/or systems at lower dimensions, as needed. He also noted that scaling issues can arise due to possible changing of the magnitudes of physical phenomena, such as surface tension and van der Waals attraction, etc.

Since the first proposal of nanotechnology by Feynman in 1959, intensive research and development activities have gained momentum in the last 30 years. Nanotechnology and nanoscience had two major developments in early 1980s: (1) cluster science and discovery of scanning tunneling microscope (STM) that led to the discovery of fullerenes in 1985 and carbon nanotubes just few years later and (2) further major developments in the area of the synthesis and properties of semiconductor nanocrystals, such as metal oxide nanoparticles and quantum dots. Rapid development continued in the area of structural characterization of materials. The discovery of atomic force microscopy (AFM) took place just 6 years after the STM was invented.

In recent years, a large amount of research has been carried out all over the world on metals, semiconductors, ceramics, polymers, and composites containing nanostructured materials for applications in health/disease, pharmacology, energy, agriculture, electronics and communication, and information processing and storage using the multifunctionality of the newly developed materials. This has spurred new industry in various fields, including defense technology. Rapidly changing technologies, including electronic communications, have intensified the scientific research and technological development involving structures composed of atoms and molecules—as well as biological structures. Indeed, some recent scientific studies have been carried out on colloidal quantum dots. Since quantum dots have zero dimensions, they have a sharper density of states than that of higher dimensional (two and three dimensional) structures. Correspondingly, quantum dots have superior charge transport and optical properties and, consequently, much intensive research has been carried out to use them in making diode lasers, transistors, and biological sensors.

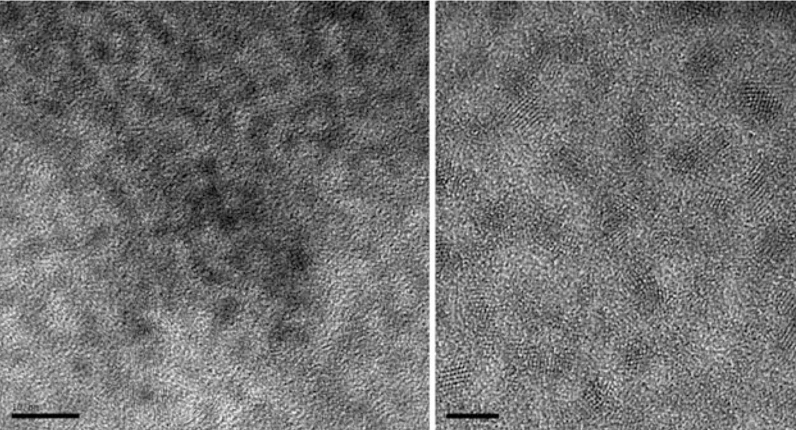

Fig. 1.9 TEM characterization of CdSe colloidal quantum dots prepared at 130°C and 160°C for 5 min of reaction time

Colloidal quantum dots are semiconductor nanocrystals that are synthesized from precursor compounds dissolved in chemical solutions that involves precursors, organic surfactants, and solvents. The precursors chemically transform into monomers when heating a reaction medium to a sufficiently high temperature. The nanocrystal starts to grow with a nucleation process when the monomers reach a high enough supersaturation level. The temperature during the growth process is one of the critical factors in determining optimal conditions for nanocrystal growth and determines the size and shape of the nanocrystal. Control of monomer concentration is another critical issue in nanocrystal growth. When the monomer concentration is high enough, the size distribution results in nearly mono-disperse particles. The colloidal quantum dots, with a diameter of 10–50 atoms, can contain as few as 100–100,000 atoms within the related volume, which corresponds to about 2–10 nm. Transmission electron microscopy (TEM) characterization of CdSe colloidal quantum dots is shown in Fig. 1.9.

Colorization of colloidal quantum dot is their immediate optical characteristics. While the bulk material that makes up a quantum dot defines its intrinsic energy property, the quantum confined size of a nanocrystal is more significant at energies near the fundamental bandgap of the material. Therefore, quantum dots formed from the same semiconducting material with different sizes can emit light of different colors, as shown in Fig. 1.10. This is due to the quantum confinement effect that occurs at nanoscale. The size of the quantum dot determines its color and fluorescence spectrum. When the dot size is large, the color of its fluorescence spectrum is red (lower energy). On the other hand, when the dot size is small, its color is bluer (higher photon energy). The color of quantum dots is directly related to its energy levels. The bandgap energy that determines the energy (or color) of the fluorescent light is inversely proportional to the size of the quantum dot.

Quantum dots with larger size have more closely spaced energy levels (in which electron–hole pairs can be trapped) that allows the quantum dot to absorb

Fig. 1.10 Colloidal CdSe nanoparticles prepared at 150°C during 1, 5, 10, 15, 20, 25, 30, and 35 min of reaction times

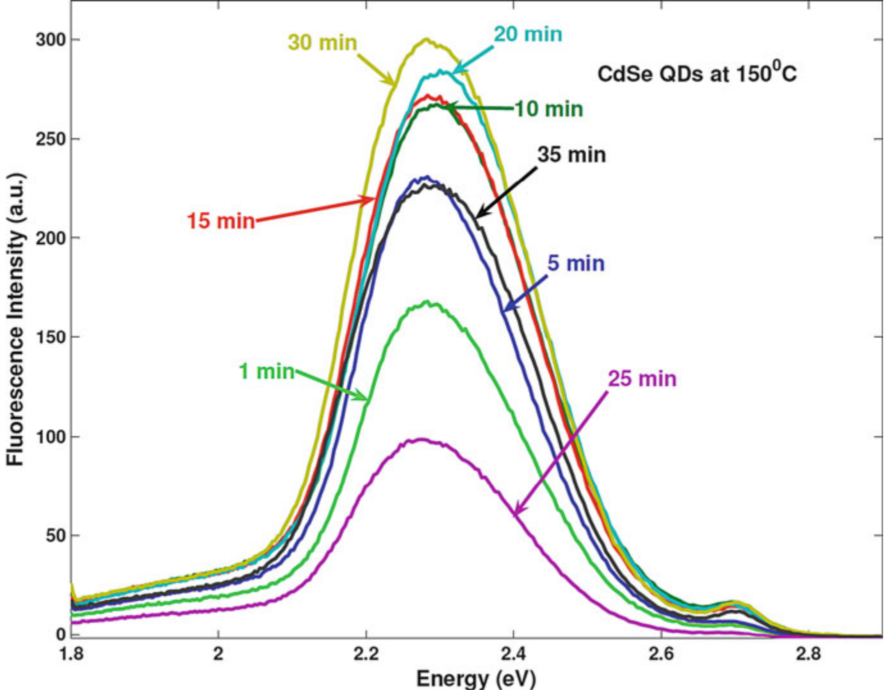

Fig. 1.11 Optical fluorescence spectrum of colloidal CdSe nanoparticles prepared at 150°C during 1, 5, 10, 15, 20, 25, 30, and 35 min of reaction times

photons with less energy (i.e., those closer to the red end of the spectrum). Since electron–hole pairs stay longer in quantum dots of larger size, these dots exhibit longer lifetime. The physical characteristics of quantum dots are related to the shape and size of the semiconductor crystal. The smaller the size of the crystal, the

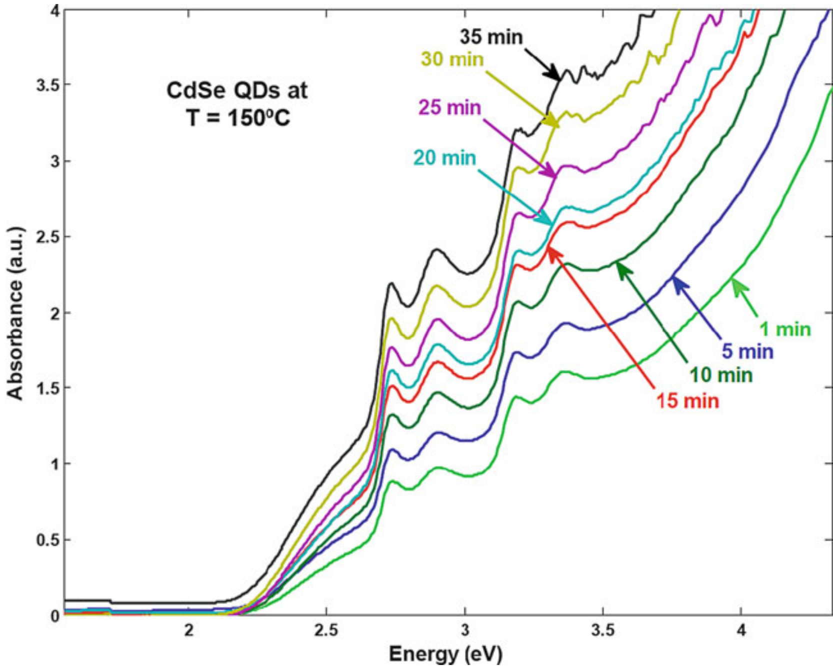

Fig. 1.12 Optical absorption spectrum of colloidal CdSe nanoparticles prepared at 150°C during 1, 5, 10, 15, 20, 25, 30, and 35 min of reaction times

larger the fundamental bandgap between the conduction and valence band energy levels. Therefore, more energy is necessary to excite the quantum dot and more energy is released when the crystal returns to its equilibrium state. Figures 1.11 and 1.12, respectively, show the fluorescence and absorption spectra of colloidal CdSe nanoparticles prepared in our laboratory at İstanbul Technical University. Absorption peaks in Fig. 1.12 show that the first, second, third, and fourth excited states obtained are temperature-dependent. Based on the first excitonic absorption peak, the average bandgap energy and size of CdSe nanoparticles at 150°C are 2.7 eV and 3.82 nm, respectively.

The quantum theory of charged particles whose motions are confined in all three space dimensions can be used to discuss the physics behind the measured peak values in Fig. 1.12. The Hamiltonian for charged particles in the nanocrystal is written as [12–15]

$$H = \frac{\hbar^2}{2m^*}\nabla^2 + \frac{\hbar^2}{2m^*}\nabla^2 + V_{\mathrm{e}}(\vec{r}_{\mathrm{e}}) + V_{\mathrm{h}}(\vec{r}_{\mathrm{h}}) - \frac{e^2}{\varepsilon\left|\vec{r} - \vec{r}\right|} \tag{1.2}$$

The first and second terms in (1.2) represent the kinetic energies of electrons and holes, the third and fourth terms are confinement potential energies, and the last term is the electron–hole Coulomb interaction energy. There are other terms such

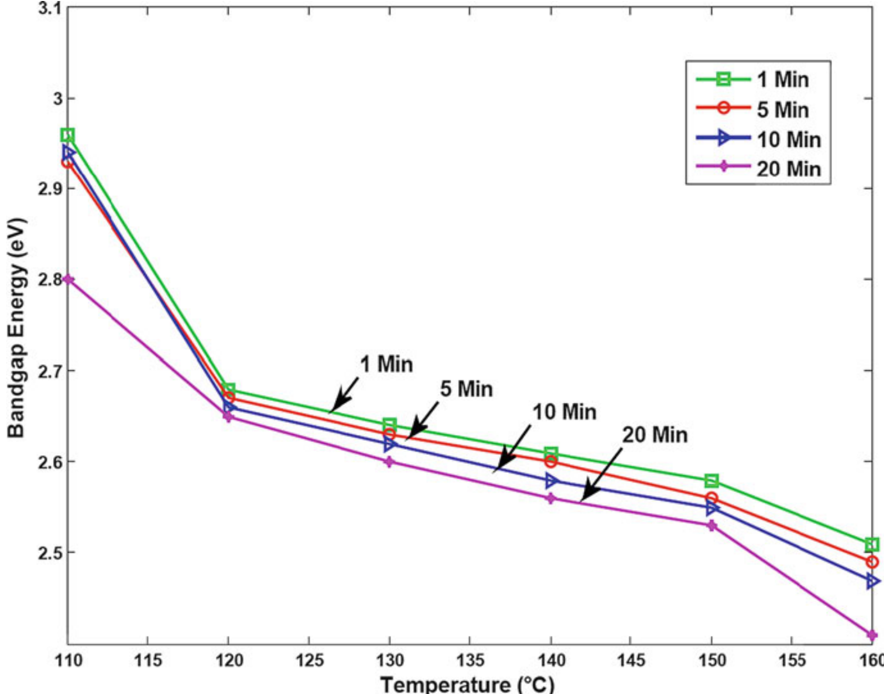

Fig. 1.13 Excitation energy (eV) of colloidal CdSe quantum dots as a function of growth temperature, obtained by using optical absorption spectrum for samples prepared at 110°C, 120°C, 130°C, 140°C, 150°C, and 160°C

as exchange interaction energy and interaction energy between the charges in the nanocrystal and their image charges in the dielectric host (polarization energy). The solution of the Schrödinger equation for a particle in a spherical box (representing a nanocrystal) yields the quantized energy levels as

$$E_{(n_e,l_e),(n_h,l_h)}(d) = E_g + \frac{2\hbar^2\pi^2}{d^2}\left[\frac{x^2_{n_e,l_e}}{m^*_e} + \frac{x^2_{n_h,l_h}}{m^*_h}\right] - \frac{3.572e^2}{\varepsilon d} - \frac{0.124e^4}{\hbar^2\varepsilon^2}\left[\frac{m^*_e m^*_h}{m^*_e + m^*_h}\right] \quad (1.3)$$

Here, $E_{\{(n_e,l_e),(n_h,l_h)\}}(d)$ is the excitation energy, E_g is the fundamental band gap of bulk CdSe, $m^*_e = 0.13m_0$ and $m^*_h = 0.43m_0$ are the electron and hole effective masses with free electron mass m_0 in vacuum, and $\varepsilon = 5.8\varepsilon_0$ is the optical dielectric constant. d is the radius of CdSe quantum dots and "2D" is the size of quantum dot, and $x_{n,l}$ is the root of first-order Bessel function $j_1(x_{n,l}) = 0$.

Normal and spin–orbit split valence band and conduction band transitions involves excitations between (1s, 1s) (1p, 1p), (1d, 1d), (1f, 1f), and (2s, 2s) energy levels. Thus, it is then possible to calculate the valence and conduction band transitions between the (1s, 1s) (1p, 1p), (1d, 1d), (1f, 1f), and (2s, 2s) transition energies. Shown in Fig. 1.13 is the effect of temperature on the first excitation

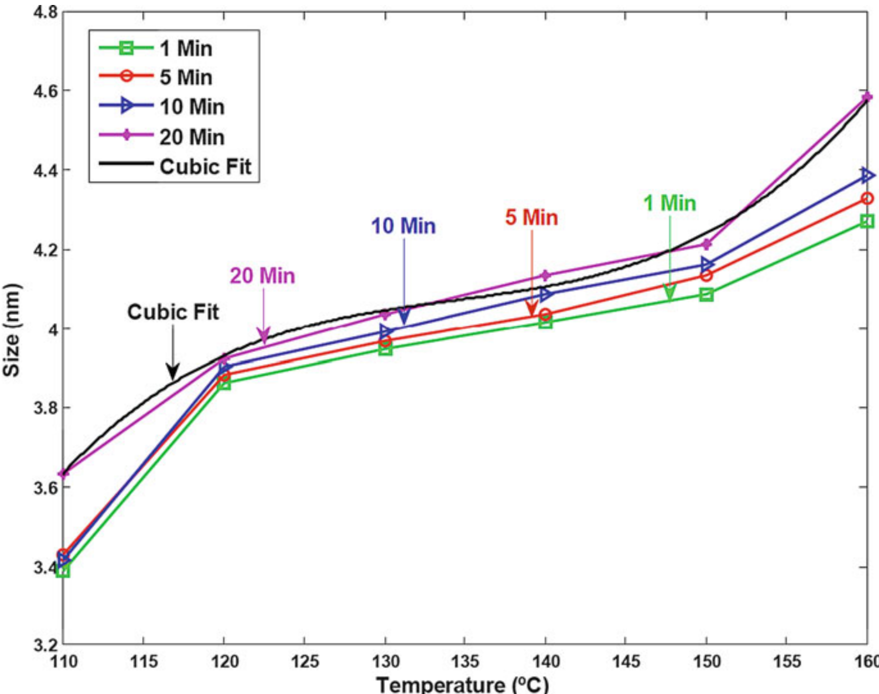

Fig. 1.14 Size (nm) of colloidal CdSe quantum dots as a function of growth temperature for samples prepared at 110°C, 120°C, 130°C, 140°C, 150°C, and 160°C

energy between the (2s, 2s) and (1s, 1s) transition, extracted from an optical absorption measurement by an ultraviolet visible spectrometer at room temperature. As Fig. 1.13 shows that the excitation energy decreases with increasing the growth temperature for colloidal CdSe nanoparticles. Solving the Schrödinger equation for d in terms of the first excitation energy level, one obtains the size (2d) of the CdSe quantum dot as a function of growth temperature. As shown in Fig. 1.14, the size of CdSe colloidal nanoparticles increases with growth temperature. Reaction time does not play a crucial role in the change of nanoparticle size.

1.7 Conclusion

Realization of the full potential of heterostructures for electronic and optoelectronic device technologies requires a reliable and precise predictive process and performance simulation models that are consistent with the fundamental principles of solid-state physics and quantum mechanics. In this chapter, we have presented a partial summary of advances in low-dimensional semiconductor materials and their device applications. Prediction of the performance of these low-dimensional

semiconductor devices requires a general methodology, atomistic materials theory-based modeling [16–25] that can proceed relatively independently of experiment. The features that must be incorporated within this general approach are extended tight-binding theory and density functional theories of band structure modeling, incorporated into the current transport theory of charge carriers to achieve accurate design and simulation of low-dimensional semiconductor devices.

Acknowledgements This work was partially supported by the Scientific and Technical Research Council of Turkey (TÜBİTAK) under Grant No: TBAG-105T463. Two of us, H. H. Gürel and Ö. Akıncı, greatly acknowledge the Ph.D. student fellowships by Turkish State Planning Agency (DPT). The authors would like to greatly acknowledge the computer usage of High Performance Computing Laboratory of Informatics Institute at istanbul Technical University.

References

1. H. Morkoç, H. Ünlü, G. Ji, *Principles and Technology of MODFETs*, vols. 1, 2 (Wiley, Chichester, 1991)
2. B. Gil (ed.), *Group III Nitride Semiconductors Compounds: Physics and Applications* (Oxford Science Publications, Oxford, 1998)
3. H. Ünlü, H. Morkoç, Solid State Technol. **31**, 83 (1988)
4. H. Morkoç, H.Ünlü, in *Semiconductors and Semimetals*, vol. 24, ed. by R. Dingle (1987), p. 135, (Academic Press, 1987)
5. H. Ünlü, H. Morkoç, S. Iyer, in *Gallium Arsenide Technology*, vol. 2, ed. by D.K. Ferry (1990), p. 231, (Howard & Sams, 1990)
6. H. Morkoç, H.Ünlü, H. Zabel, N. Otsuka, Solid State Technol. **31**, 71 (1988)
7. H. Kroemer, Proc. IRE **45**, 1535 (1957)
8. H. Kroemer, Proc. IEEE **70**, 13 (1982)
9. C.G. Osbourn, J. Appl. Phys. **53**, 1586 (1982)
10. L. Esaki, R. Tsu, IBM Res. Dev. **14**, 61 (1970)
11. G.H. Dohler, Phys. Status Solidi (B) **52**, 533 (1972)
12. L. Brus, Appl. Phys. **53**, 465 (1991)
13. V.L. Colvin, K.L. Cunningham, A.P. Alivisatos, J. Chem. Phys. **101**, 7122 (1994)
14. C. Flytzanis, D. Ricard, M.C. SchanneKlein, J. Lumin. **70**, 212 (1996)
15. A.L. Efros, M. Rosen, Annu. Rev. Mater. Sci. **30**, 475 (2000)
16. H. Ünlü, Phys. Status Solidi (B), **216**, 107 (1999)
17. Ö. Akıncı, H.H. Gürel, H. Ünlü, Thin Solid Films **517**, 2431 (2009)
18. H.H. Gürel, Ö. Akıncı, H. Ünlü, Thin Solid Films **516**, 7098 (2008)
19. Ö. Akıncı, H.H. Gürel, H. Ünlü, Phys. Status Solidi (C) **5**(2), 478 (2008)
20. Ö. Akıncı, H.H. Gürel, H. Ünlü, J. Nanosci. Nanotechnol. **8**, 540 (2008)
21. H.H. Gürel, Ö. Akıncı, H. Ünlü, Phys. Status Solidi (C) **4**(2), 316 (2007)
22. H.H. Gürel, Ö. Akıncı, H. Ünlü, Superlattices Microstruct. **40**(4–6), 588 (2006)
23. Ö. Akıncı, H.H. Gürel, H. Ünlü, Thin Solid Films **511–512**, 684 (2006)
24. H.H. Gürel, Ö. Akıncı, H. Ünlü, Comput. Mater. Sci. **33**, 269 (2005)
25. Ö. Akıncı, H.H. Gürel, H. Ünlü, Superlattices Microstruct. **36**, 685 (2004)

Chapter 2
Modeling of Low-Dimensional Semiconductors

Hilmi Ünlü, H. Hakan Gürel, Özden Akıncı, and Mohamed Rezaul Karim

Abstract In this chapter, we discuss the general methodology to carry out qualitatively reliable and quantitatively precise calculations of electronic band structure of heterostructures that are essential in the realistic modeling and prediction of device performance in technologically important semiconductor devices, which can proceed relatively independently of experiment.

2.1 Introduction

Realization of the full potential of low-dimensional semiconductor structures for making bipolar and unipolar electronic devices (such as heterostructure bipolar transistors (HBTs) and modulation-doped field effect transistors (MODFETs)) and optical devices (including heterostructure lasers and light-emitting diodes) requires a reliable, precise predictive process and performance simulation models based on the fundamental principles of solid-state physics and quantum mechanics. Among the key issues are the understanding of the formation and determination of the magnitude of conduction and valence band offsets at heterointerfaces, which dominate various device properties such as injection efficiency in HBTs and carrier confinement in MODFETs. These issues have received considerable attention among device scientists and engineers over the years [1, 2].

The use of low-dimensional semiconductor structures in device design enables device engineers to locally modify the energy band structure of the constituents

H. Ünlü (✉)
Computational Science Division, Informatics Institute, Istanbul Technical University, Maslak Istanbul 80626, Turkey

Department of Physics, Faculty of Science and Letters, Istanbul Technical University, Maslak Istanbul 80626, Turkey
e-mail: hunlu@itu.edu.tr; hilmi.unlu74@gmail.com

H. Ünlü and N.J.M. Horing (eds.), *Low Dimensional Semiconductor Structures*, NanoScience and Technology, DOI 10.1007/978-3-642-28424-3_2,
© Springer-Verlag Berlin Heidelberg 2013

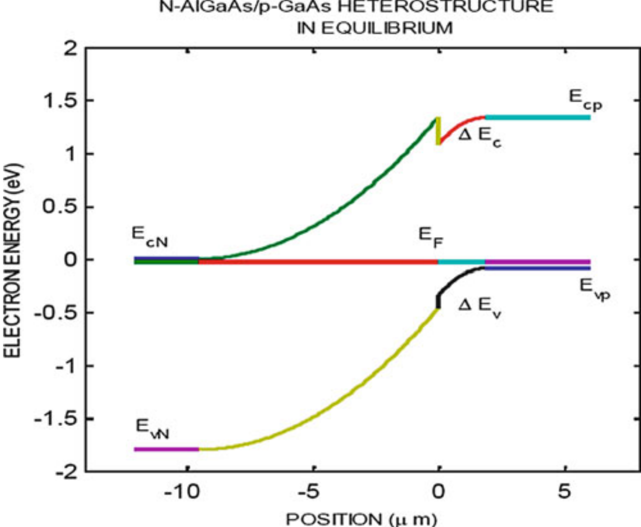

Fig. 2.1 Schematic energy band diagram of an n-AlGaAs/p-GaAs heterojunction in thermal equilibrium. When the semiconductor composition changes abruptly at the interface between constituents, the difference in their energy bands is accommodated by discontinuities in the conduction and valence bands

in order to control the motion of charge carriers [3, 4]. When two semiconductors having different physical and chemical properties and thicknesses are grown upon each other, the lattice mismatch and thermal expansion gradient at the growth temperature gives rise to interface strain that modifies the electronic properties of both materials near the interface, including the band offsets (as shown in Fig. 2.1 for an n-AlGaAs/p-GaAs heterojunction in thermal equilibrium) and consequently the energy profile experienced by moving charge carriers at the conduction and valence band edges. This facilitates the control of device performance [2–10].

In this chapter, we discuss the general methodology to carry out qualitatively reliable and quantitatively precise calculations of electronic band structure of heterostructures that are essential in the realistic modeling and prediction of device performance in technologically important semiconductor devices, which can proceed relatively independently of experiment. The models we shall discuss in this chapter are (1) the semiempirical sp^3 tight-binding (TB) theory in comparison with (2) density functional theory (DFT) of band structure modeling, which can be very easily implemented in extended current transport modeling in low-dimensional semiconductor structures.

When a wide-gap semiconductor is grown on a narrow-gap semiconductor base, the interface strain, caused by the lattice mismatch, modifies the structural and electronic properties of the constituent semiconductors in directions parallel and perpendicular to the interface [1]. The macroscopic observable consequences of lattice mismatch and thermal strains are the change in the bandgap, effective mass,

intrinsic carrier density, and dielectric constant as a function of temperature. The interface strain splits the heavy-hole, light-hole, and split-off valence band edges by its uniaxial component and shifts the position of the conduction and valence band edges, and the hydrostatic strain component alters the magnitude of the energy levels of the constituent semiconductors [11], as shown in Fig. 1.1. The positions of the heavy-hole, light-hole, and split-off valence band energies relative to the average valence band edge E_{v} are given by the following equations:

$$E_{\mathrm{vh}}(\varepsilon) = E_{\mathrm{v}}(\varepsilon) + \frac{1}{3}\Delta - \frac{1}{2}\delta E \tag{2.1}$$

$$E_{\mathrm{vl}}(\varepsilon) = E_{\mathrm{v}}(\varepsilon) - \frac{1}{6}\Delta + \frac{1}{4}\delta E + \frac{1}{2}\sqrt{\Delta^2 + \Delta\,\delta E + \frac{9}{4}\delta E^2} \tag{2.2}$$

$$E_{\mathrm{vs}}(\varepsilon) = E_{\mathrm{v}}(\varepsilon) - \frac{1}{6}\Delta + \frac{1}{4}\delta E - \frac{1}{2}\sqrt{\Delta^2 + \Delta\delta E + \frac{9}{4}\delta E^2} \tag{2.3}$$

where $\delta E = 2b(\varepsilon_{zz} - \varepsilon_{xx}) = 2b(\varepsilon_{\perp} - \varepsilon_{\parallel})$ and b is the shear deformation potential that describes the splitting in the valence band energy due to the [001] uniaxial strain. $E_{\mathrm{v}}(\varepsilon)$ is the average valence band maximum that is under the hydrostatic component of the biaxial strain. $E_{\mathrm{vh}}(\varepsilon)$ is the heavy-hole band, $E_{\mathrm{vl}}(\varepsilon)$ is the light-hole band, and $E_{\mathrm{vs}}(\varepsilon)$ is the split of band defined with respect to average valence band maximum.

Compressive or tensile strain (($\varepsilon_{xx} < 0$) or ($\varepsilon_{xx} > 0$)) on the epilayer results in an increase or decrease in its conduction and valence band energy levels (Fig. 2.2). Therefore, any interface strain will modify the band offsets that determine carrier transport across the interface of electronic or optical devices. Reliable and precise determination of the effects of strain on the electronic band structure is essential for the reliable design and precise performance predictions of HBTs as high speed, high power, and low noise bipolar transistors. In the following subsections, temperature, pressure, strain, and alloy composition effects on energy bandgaps and band offsets will be discussed by using the sp^3 TB theory of semiconductors [12–20].

Quantitatively reliable and numerically precise modeling and simulation of electronic properties of compound semiconductors and their ternary alloys permits better prediction of their material properties [12–20]. First-principles calculations are known to be computationally intensive and cannot be easily implemented for some optoelectronic devices [10]. In contrast, the semiempirical TB model is known to be not only simple but also reliable and easily implemented, and has great advantages over first-principles calculations in determining electronic properties such as band structure, density of states (DOS), and bandgaps of low-dimensional semiconductor structures. The semiempirical TB model is an atomistic approach and well suited to calculate the electronic band structure of low-dimensional semiconductor structures, including quantum wells and quantum dots [10]. In the following section, we discuss the use of second nearest neighbor (2NN) sp^3s^* [21] and nearest neighbor (NN) $sp^3d^5s^*$ [22, 23] TB models to calculate the composition, temperature, pressure, and strain effects on electronic properties (e.g.,

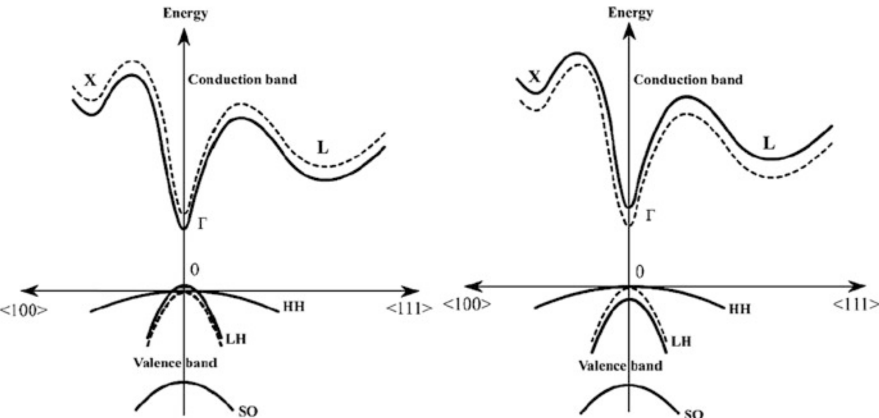

Fig. 2.2 The tensile strain ($\varepsilon_{xx} > 0$) (on *left*) results in the modification of the semiconductor energy band structure (e.g., bandgap decreases). On the other hand, compressive strain ($\varepsilon_{xx} < 0$) (on *right*) results in the modification of semiconductor energy band structure (e.g., bandgap increases). *HH*, *LH*, and *SO*, respectively, represent the heavy-hole, light-hole, and split-off band energies

band structure, DOS, bandgaps, and band widths) of semiconductor binaries and their ternaries.

2.2 TB View of Semiconductor Structures

Within the framework of Slater–Koster-type semiempirical sp^3 TB theory [24–26], one first writes the Schrodinger equation in matrix form as

$$\sum_{\beta}\left[H_{\alpha\beta}(k) - S_{\alpha\beta}(k)E\right]u_{\beta} = 0, \tag{2.4}$$

where E is the energy eigenvalue of the 10×10 Hamiltonian matrix $H_{\alpha\beta} = \langle\chi_{\alpha}(k)|H|\chi_{\beta}(k)\rangle$ and $S_{\alpha\beta} = \langle\chi_{\alpha}(k)|\chi_{\beta}(k)\rangle$ is the overlap integral between the atomic-like orbitals, with α and β that correspond to cation (c) and anion (a) s(p) atomic orbitals, respectively. $\chi(k)$ is the basis function formed by the linear combination of cation and anion s(p) atomic orbitals and u_{β} is the wave function coefficient. Considering a compound semiconductor having a zinc blende crystal structure, shown in Fig. 2.3, the interaction between s^a ile s^c orbits is written as

$$\langle s^c|H|s^a\rangle = E_{ss}\sum_{n=1}^{4} e^{ik,r_n} = E_{ss}\left(e^{ik,r_1} + e^{ik,r_2} + e^{ik,r_3} + e^{ik,r_4}\right) \tag{2.5}$$

where

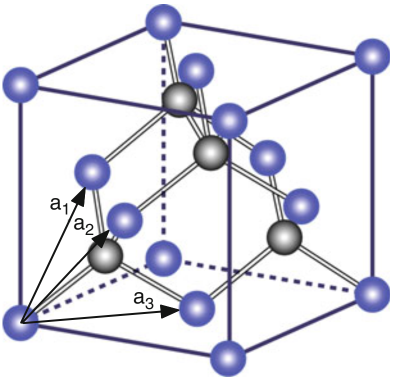

Fig. 2.3 Unit cell of zinc blende crystal structure

$$r_1 = (a/4)(+1, +1, +1),$$
$$r_2 = (a/4)(+1, -1, -1),$$
$$r_3 = (a/4)(-1, +1, -1),$$
$$r_4 = (a/4)(-1, -1, +1)$$

are the displacement vectors of NNs. The interaction between the s, p_x, p_y, p_z orbitals of the first cation atom and second NN anion atoms can be described by the following integral expressions:

$$\langle s^c|H|s^a\rangle = E_{ss}\left(e^{ik,r_1} + e^{ik,r_2} + e^{ik,r_3} + e^{ik,r_4}\right) = E_{ss}B_0(k), \quad (2.6)$$

$$\langle s^c|H|p_x^a\rangle = E_{sp}\left(e^{ik,r_1} + e^{ik,r_2} + e^{ik,r_3} + e^{ik,r_4}\right) = E_{sp}B_1(k), \quad (2.7)$$

$$\langle s^c|H|p_y^a\rangle = E_{sp}\left(e^{ik,r_1} + e^{ik,r_2} + e^{ik,r_3} + e^{ik,r_4}\right) = E_{sp}B_2(k), \quad (2.8)$$

$$\langle s^c|H|p_z^a\rangle = E_{sp}\left(e^{ik,r_1} + e^{ik,r_2} + e^{ik,r_3} + e^{ik,r_4}\right) = E_{sp}B_3(k). \quad (2.9)$$

The interactions between the same p-orbitals of cation and anion atoms are called diagonal matrix elements and are calculated by the following integral expressions:

$$\langle p_x^c|H|p_x^a\rangle = E_{xx}B_0(k), \quad (2.10)$$

$$\langle p_y^c|H|p_y^a\rangle = E_{xx}B_0(k), \quad (2.11)$$

$$\langle p_z^c|H|p_z^a\rangle = E_{xx}B_0(k). \quad (2.12)$$

The interactions between different p-orbitals of cation and anion atoms are called off-diagonal matrix elements and are calculated by the following integral expressions:

$$\langle p_x^c|H|p_y^a\rangle = \langle p_y^c|H|p_x^a\rangle = E_{xy}B_3(k), \quad (2.13)$$

$$\langle p_x^c|H|p_z^a\rangle = \langle p_z^c|H|p_x^a\rangle = E_{xy}B_2(k), \quad (2.14)$$

$$\langle p_y^c|H|p_z^a\rangle = \langle p_z^c|H|p_y^a\rangle = E_{xy}B_1(k). \quad (2.15)$$

The matrix of semiempirical SP^3 TB Hamiltonian that includes all interaction elements is given by

$$\mathbf{H} = \begin{bmatrix} E_s^c & 0 & 0 & 0 & B_0 E_{ss} & B_1 E_{sp} & B_2 E_{sp} & B_3 E_{sp} \\ 0 & E_p^c & 0 & 0 & -B_1 E_{sp} & B_0 E_{xx} & B_3 E_{xy} & B_2 E_{xy} \\ 0 & 0 & E_p^c & 0 & -B_2 E_{sp} & B_3 E_{xy} & B_0 E_{xx} & B_1 E_{xy} \\ 0 & 0 & 0 & E_p^c & -B_3 E_{sp} & B_2 E_{xy} & B_1 E_{xy} & B_0 E_{xx} \\ B_0^* E_{ss} & -B_1^* E_{sp} & B_2^* E_{sp} & B_3^* E_{sp} & E_s^a & 0 & 0 & 0 \\ B_1^* E_{sp} & B_0^* E_{xx} & B_3^* E_{xy} & B_2^* E_{xy} & 0 & E_p^a & 0 & 0 \\ B_2^* E_{sp} & B_3^* E_{xy} & B_0^* E_{xx} & B_1^* E_{xy} & 0 & 0 & E_p^a & 0 \\ B_3^* E_{sp} & B_2^* E_{xy} & B_1^* E_{xy} & B_0^* E_{xx} & 0 & 0 & 0 & E_p^a \end{bmatrix} \tag{2.16}$$

where E_{ss}, E_{xx}, $E_{s_a p_c}$, $E_{s_c p_a}$, E_{xy}, $E_{s^* p}$, and E_{ps^*} are known as hopping terms (transfer matrix elements). The values of $B_0(k)$, $B_1(k)$, $B_2(k)$, and $B_3(k)$ are:

$$\begin{aligned} B_0(k_x, k_y, k_z) &= +4\cos\left(\frac{k_x a}{2}\right)\cos\left(\frac{k_y a}{2}\right)\cos\left(\frac{k_z a}{2}\right) \\ &\quad -4i\sin\left(\frac{k_x a}{2}\right)\sin\left(\frac{k_y a}{2}\right)\sin\left(\frac{k_z a}{2}\right) \\ B_1(k_x, k_y, k_z) &= +4\cos\left(\frac{k_x a}{2}\right)\sin\left(\frac{k_y a}{2}\right)\sin\left(\frac{k_z a}{2}\right) \\ &\quad +4i\sin\left(\frac{k_x a}{2}\right)\cos\left(\frac{k_y a}{2}\right)\cos\left(\frac{k_z a}{2}\right) \\ B_2(k_x, k_y, k_z) &= -4\sin\left(\frac{k_x a}{2}\right)\cos\left(\frac{k_y a}{2}\right)\sin\left(\frac{k_z a}{2}\right) \\ &\quad +4i\sin\left(\frac{k_x a}{2}\right)\sin\left(\frac{k_y a}{2}\right)\cos\left(\frac{k_z a}{2}\right) \\ B_3(k_x, k_y, k_z) &= -4\sin\left(\frac{k_x a}{2}\right)\sin\left(\frac{k_y a}{2}\right)\cos\left(\frac{k_z a}{2}\right) \\ &\quad -4i\cos\left(\frac{k_x a}{2}\right)\cos\left(\frac{k_y a}{2}\right)\sin\left(\frac{k_z a}{2}\right) \end{aligned} \tag{2.17}$$

where B_i^* is the complex conjugate of B_i matrix element. It should be noted that although the Slater–Koster-type sp^3 TB approach [24–26] yields a good description of valence band dispersion curves, the conduction band dispersion curves are not accurately given, especially the indirect bandgap at the X symmetry point is not well reproduced. In order to overcome this obstacle, Vogl et al. [21] introduced an sp^{3}s* TB model in order to include the influence of excited d-states. In this model, each atom is described by not only its outer valence s orbital and three p orbitals but also the fictitious excited s* orbital to take into account the effect of

higher states. The inclusion of spin–orbit coupling of p-states to the sp^3s^* basis set reproduces the splitting between split-off band and the light- and heavy-hole bands. Accounting for 2NN interactions of cation and anion atoms improves the accuracy of the sp^3s^* ETB model in determining the conduction band structure features at X and L high symmetry points. It is possible to accurately calculate the conduction band dispersion curves at the X high symmetry point by adding the excited s* state with spin–orbit coupling to the sp^3s^* orbital basis. Moreover, inclusion of the 2NN interactions of cation and anion atoms in the basis set yields a better fit for the conduction band dispersion curve at the L symmetry point.

2.3 Semiempirical sp^3s^* TB Model

In the semiempirical sp^3s^* TB model Hamiltonian matrix, each cation atom and anion atom are described by their outer valence s orbital, the three outer p orbitals, and a fictitious excited s* orbital added to mimic the effects of higher lying d-states. The inclusion of second (2NN) interactions in the sp^3s^* TB model introduces two additional interaction parameters [10] and the Hamiltonian matrix $H_{\alpha\beta}$ is written as

$$H_{\alpha\beta} = \begin{bmatrix} E_s^c & -\varepsilon(s,p_x)B_6 & -\varepsilon(s,p_x)B_5 & -\varepsilon(s,p_x)B_4 & 0 & B_0E_{ss} & B_1E_{sp} & B_2E_{sp} & B_3E_{sp} & 0 \\ -\varepsilon(s,p_x)B_6 & E_p^c & \varepsilon(p_x,p_y)B_4 & \varepsilon(p_x,p_y)B_5 & 0 & -B_1E_{ps} & B_0E_{xx} & B_3E_{xy} & B_2E_{xy} & -B_1E_{ps^*} \\ -\varepsilon(s,p_x)B_5 & \varepsilon(p_x,p_y)B_4 & E_p^c & \varepsilon(p_x,p_y)B_6 & 0 & -B_2E_{ps} & B_3E_{xy} & B_0E_{xx} & B_1E_{xy} & -B_2E_{ps^*} \\ -\varepsilon(s,p_x)B_4 & \varepsilon(p_x,p_y)B_5 & \varepsilon(p_x,p_y)B_6 & E_p^c & 0 & -B_3E_{ps} & B_2E_{xy} & B_1E_{xy} & B_0E_{xx} & -B_3E_{ps^*} \\ 0 & 0 & 0 & 0 & E_{s^*}^c & 0 & B_1E_{s^*p} & B_2E_{s^*p} & B_3E_{s^*p} & 0 \\ B_0^*E_{ss} & -B_1^*E_{sp} & -B_2^*E_{sp} & -B_3^*E_{sp} & 0 & E_s^a & \varepsilon(s,p_x)B_6 & \varepsilon(s,p_x)B_5 & \varepsilon(s,p_x)B_4 & 0 \\ B_1^*E_{sp} & B_0^*E_{xx} & B_3^*E_{xy} & B_2^*E_{xy} & 0 & \varepsilon(s,p_x)B_6 & E_p^a & \varepsilon(p_x,p_y)B_4 & \varepsilon(p_x,p_y)B_5 & 0 \\ B_2^*E_{sp} & B_3^*E_{xy} & B_0^*E_{xx} & B_1^*E_{xy} & 0 & \varepsilon(s,p_x)B_5 & \varepsilon(p_x,p_y)B_4 & E_p^a & \varepsilon(p_x,p_y)B_6 & 0 \\ B_3^*E_{sp} & B_2^*E_{xy} & B_1^*E_{xy} & B_0^*E_{xx} & 0 & \varepsilon(s,p_x)B_4 & \varepsilon(p_x,p_y)B_5 & \varepsilon(p_x,p_y)B_6 & E_p^a & 0 \\ 0 & -B_1^*E_{ps^*} & -B_2^*E_{ps^*} & -B_3^*E_{ps^*} & 0 & 0 & 0 & 0 & 0 & E_{s^*}^a \end{bmatrix} \tag{2.18}$$

where E_s^a, E_s^c, E_p^a, E_p^c, $E_{s^*}^a$, and E_{s^*c} in $H_{\alpha\beta}$ are known as the on-site atomic energies of cation and anion atoms; E_{ss}, E_{xx}, $E_{s_a p_c}$, $E_{s_c p_a}$, E_{xy}, E_{s^*p}, and E_{ps^*} are known as hopping terms (transfer matrix elements); and $\varepsilon_{sx} = \varepsilon(sc(a), p_x c(a))$ and $\varepsilon_{xy} = \varepsilon(p_x c(a), p_y c(a))$ are the two 2NN transfer matrix elements for the cation and anion atoms. Here, s and p refer to the basis states, and a and c refer to anion (e.g., As, Sb, and N) and cation (e.g., Al, Ga, and In) atoms, respectively. Here, each cation and anion atoms are described by its outer valence orbitals for each spin: s, p_x, p_y, p_z and an additional s* orbital, which is an excited state of s orbital that accounts for higher lying states. B_0, B_1, B_2, and B_3 are given by (2.17) and others B_4, B_5, and B_6 are written as

$$B_4(k_x,k_y,k_z) = 4\sin(k_x a)\sin(k_y a),$$
$$B_5(k_x,k_y,k_z) = 4\sin(k_x a)\sin(k_z a),$$
$$B_6(k_x,k_y,k_z) = 4\sin(k_y a)\sin(k_z a).$$

Table 2.1 Bandgaps at high symmetry points of GaAs, InAs, GaP, GaN, and InN compounds [28–30] used as input parameters to produce 2NN sp^3s^* TB parameters in Table 2.2

(eV)	GaAs	InAs	GaP	GaN	InN
E_g^Γ	1.519	0.430	2.878	3.287	0.872
E_g^X	1.980	2.278	2.330	4.691	2.827
E_g^L	1.818	1.605	2.563	6.258	3.810

Table 2.2 The 2NN sp^3s^* TB parameters for GaAs, InAs, GaP, GaN, and InN compounds obtained by using the fundamental bandgaps in Table 2.1

(eV)	GaAs	InAs	GaP	GaN	InN
$E_{s,a}$	−8.4399	−9.5381	−8.1124	−12.915	−12.860
$E_{p,a}$	0.9252	0.7733	1.0952	3.1697	1.9800
$E_{s,c}$	−2.6569	−2.7219	−2.1976	−1.5844	−0.3994
$E_{p,c}$	3.5523	3.5834	4.0851	9.0302	8.0200
$E_{s^*,a}$	6.6235	7.2730	8.4796	12.2000	10.6300
$E_{s^*,c}$	7.4249	6.6095	7.1563	12.2000	13.0000
$4V_{s,s}$	−6.4210	−5.6052	−7.4909	−8.8996	−4.2285
$4V_{x,x}$	1.9850	1.8398	2.1516	5.3500	3.9800
$4V_{x,y}$	4.9100	4.3977	5.1213	8.6200	7.4100
$4V_{sa,pc}$	4.2390	3.0205	4.2724	6.4000	3.8100
$4V_{pa,sc}$	5.15358	5.3894	6.3075	7.2400	6.1900
$4V_{s^*a,pc}$	3.80624	3.2191	4.6184	7.0600	6.8800
$4V_{pa,s^*c}$	4.7009	3.7234	5.0534	1.8200	3.3600
ε_{sx}	0.2459	0.1441	0.2325	0.9500	0.6150
ε_{xy}	−0.1050	0.0249	−0.22	1.0100	0.7100
λ_a	0.0553	0.1385	0.0578	0.0035	0.0035
λ_c	0.1338	0.1290	0.0222	0.0410	0.1100

The inclusion of spin–orbit coupling in the sp^3s^* TB model increases the size of the 10×10 Hamiltonian matrix to 20×20 matrix, which is diagonalized for each **k** vector to obtain the semiconductor band structure. The spin–orbit effects are included by coupling different spin states of different on-site p orbitals through the spin–orbit interaction. A TB parameterization of the matrix elements for the sp^3s^* 2NN interaction are obtained by fitting the obtained bandgaps given in Table 2.1 to those produced by pseudopotential theory [27], as verified by experimental data [28–30]. The optimized TB parameters are listed in Table 2.2 for GaAs, InAs, GaP, GaN, and InN with cubic crystal structures.

Having reliable diagonal matrix elements allows one to make a realistic TB parametrization of the off-diagonal matrix elements representing the first NN and the 2NN interactions in the calculations of binary and ternary semiconductor electronic band structures. As a first test of the accuracy of the 2NN sp^3s^* TB model, calculated electronic band structures of GaAs and InAs are shown in Fig. 2.4, which exhibit the reproduced conduction and valence band structures, including the

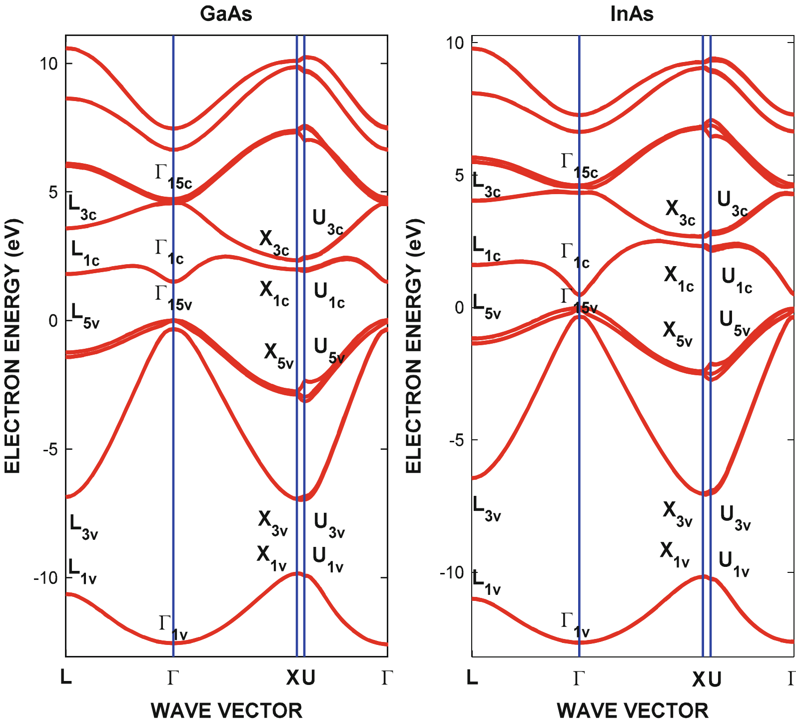

Fig. 2.4 Energy band structures of GaAs and InAs bulk semiconductors along $\Gamma - L$ and $\Gamma - X$ directions, obtained by using the 2NN sp^3s^* TB orbital basis sets

heavy-hole band, light-hole band, and spin–orbit splitting bands, of GaAs and InAs. In obtaining Fig. 2.4, TB interaction parameters $4V_{s*,p}$ and $4V_{p,s*}$ were adjusted to fit the X bands, and the 2NN interaction parameters ε_{sx} and ε_{xy} were chosen to get a good fit to the L bands in reproducing the pseudopotential energy bands [27].

Figure 2.5a, b, and c display the results of the 2NN sp^3s^* TB model for the conduction band and valence band electronic structures of GaP, GaN and InN compounds. As shown in Figs. 2.4 and 2.5 for bulk GaAs, InAs, GaP, GaN, and InN, adding the excited s^* state to the sp^3 basis set on the cation and anion atoms, with the 2NN interactions and spin–orbit coupling of p-states, makes it possible to better simulate the conduction band structure of III–V compounds, reproducing the pseudopotential bands [27] and measured bandgaps [28–30] at high symmetry points of the energy dispersion curve, which cannot be performed with NN or 2NN sp^3 ETB models. We should point out that the accuracy of our 2NN sp^3s^* TB model calculations depends on a good description of the band structures of GaAs, InAs, GaP, GaN, and InN compounds by the pseudopotential theory and/or accuracy of the experimental data.

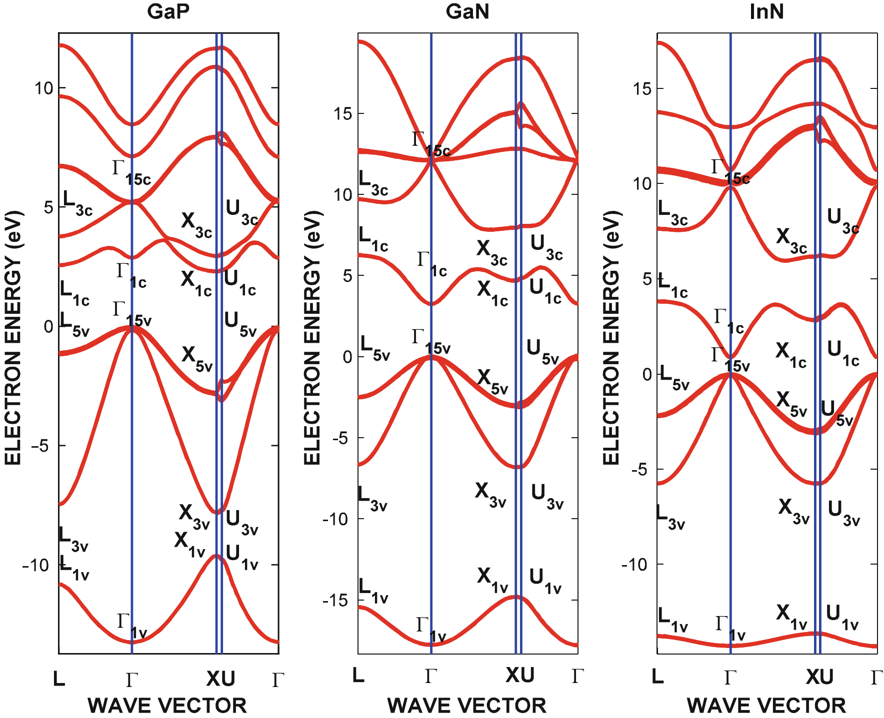

Fig. 2.5 Energy band structure of GaP, GaN, and InN compounds along $\Gamma - \mathrm{L}$ and $\Gamma - \mathrm{X}$ directions, obtained by using the 2NN sp^3s^* TB orbitals basis set listed in Table 2.2

2.4 Band Structure of Ternary Semiconductors

Within the framework of the 2NN sp^3s^* TB model, the effects of alloy composition and interface strain on the electronic band structure of heterostructures are calculated by using the so-called *modified virtual crystal approximation* (MVCA) [12–20]. The MVCA allows us to accurately take into account the disorder-induced nonlinear variation of the lattice constant and TB parameters in calculating electronic band structure properties such as bandgaps, conduction, and valence band offsets at the interface and, in turn, the effective masses of charge carriers. One first formulates the compositional dependence of bond length (or lattice constant) of ternary semiconductors ABC of an ABC/AC heterostructure written as the sum of undistorted bond length, $d_{\mathrm{VCA}} = (1 - x)d^0_{\mathrm{AC}} + x d^0_{\mathrm{BC}}$, obtained by using the virtual crystal approximation (VCA), and the distortion in bond length, $d_{\mathrm{relax}} = x(1 - x)\delta_{\mathrm{c}}(d_{\mathrm{BC}}(x) - d_{\mathrm{AC}}(x))$, due to cation–anion relaxation of binary in ternary [12–20]:

$$d(x) = d_{\mathrm{VCA}} + d_{\mathrm{relax}} = (1-x)d^0_{\mathrm{AC}} + x d^0_{\mathrm{BC}} + x(1-x)\delta_{\mathrm{c}}(d_{\mathrm{BC}}(x) - d_{\mathrm{AC}}(x)), \quad (2.19)$$

where $d_{\mathrm{AC}}(x)$ and $d_{\mathrm{BC}}(x)$ are the bond lengths of AC and BC binaries, respectively, in $\mathrm{A}_{1-x}\mathrm{B}_x\mathrm{C}$ ternary:

$$d_{\mathrm{BC}}(x) = (1-x)d^0_{\mathrm{AC}} + xd^0_{\mathrm{BC}} + (1-x)\xi_{\mathrm{BC:A}}(d^0_{\mathrm{BC}} - d^0_{\mathrm{AC}}), \tag{2.20}$$

$$d_{\mathrm{AC}}(x) = (1-x)d^0_{\mathrm{AC}} + xd^0_{\mathrm{BC}} + x\xi_{\mathrm{AC:B}}(d^0_{\mathrm{AC}} - d^0_{\mathrm{BC}}) \tag{2.21}$$

where d^0_{AC} and d^0_{BC} are the undistorted bond lengths of host materials AC and BC. δ_{c} in (2.19) is the difference between two dimensionless relaxation parameters $\xi_{\mathrm{BC:A}}$ and $\xi_{\mathrm{AC:B}}$ [31].

$$\delta_{\mathrm{c}} = \xi_{\mathrm{AC:B}} - \xi_{\mathrm{BC:A}} = \frac{1}{1 + \frac{\alpha_{\mathrm{AC}}}{6\alpha_{\mathrm{BC}}}\left(1 + 10\frac{\beta_{\mathrm{AC}}}{\alpha_{\mathrm{AC}}}\right)} - \frac{1}{1 + \frac{\alpha_{\mathrm{BC}}}{6\varepsilon_{\mathrm{AC}}}\left(1 + 10\frac{\beta_{\mathrm{BC}}}{\alpha_{\mathrm{BC}}}\right)}. \tag{2.22}$$

The effect of compositional disorder on the 2NN $\mathrm{sp^3s^*}$ TB Hamiltonian matrix elements is then described in terms of the host bond length and the distorted bond length by the substitutional impurity without any adjustable parameter [12–20]. The diagonal elements in the 2NN $\mathrm{sp^3s^*}$ TB Hamiltonian matrix for an $\mathrm{A}_{1-x}\mathrm{B}_x\mathrm{C}$ ternary semiconductor are expressed as a nonlinear function of composition [12–20]:

$$E_{\alpha/\beta}(x) = (1-x)E_{\alpha/\beta}(\mathrm{AC}) + xE_{\alpha/\beta}(\mathrm{BC}) + x(1-x)\delta_c\Delta E_{\alpha/\beta}, \tag{2.23}$$

where $\Delta E_{\alpha/\beta} = E_{\alpha/\beta}(\mathrm{AC}) - E_{\alpha/\beta}(\mathrm{BC})$, with α and β representing the fitted energies of the s, p, and s* states of anion and cation atoms forming the AC and BC bulk semiconductors. The optimized TB parameters given in Table 2.2 are used in the calculations of the electronic structures of bulk GaPN, InAsN, and GaAsN nitride ternaries in k-space for various ternary alloy compositions, displayed in Fig 2.6a, b, and c showing the expected trend in band structures.

Note that there is a considerable lattice mismatch across ternary/binary heterointerfaces. Interface strain due to lattice mismatch causes a shift in the lattice constant of the epilayer: $a = (1+\varepsilon)a_0$, where ε is the symmetric strain tensor. Therefore, the bond lengths and off-site TB matrix elements are modified with strain. Consequently, the electronic properties of heterostructure constituents will be modified with respect to their unstrained values. The off-site TB matrix elements representing the NN interactions, known as the hopping strength, are correspondingly modified with respect to their unstrained values and are often determined by assuming that they obey the Harrison scaling law [26]: $V^s_{ll'm} = V_{ll'm}(a/a_0)^{-\eta_{llm}}$, where $V^s_{ll'm}$ is the strained and $V_{ll'm}$ the unstrained values of interaction potentials for anion and cation atoms. The exponents η_{llm} are determined so as to reproduce the strain variations of the band structure of relevant semiconductors under hydrostatic pressure, namely, the volume deformation potential $a_{gl} = -B(\partial E_{gl}/\partial P)$ for the corresponding bandgap energies at Γ, L, and X high symmetry points, which depend on the experimental values. This suggests that in order to obtain reliable and accurate TB parameters, one must go through a difficult fitting process that depends on the mapping of a large number of orbital coupling parameters on the set of observables

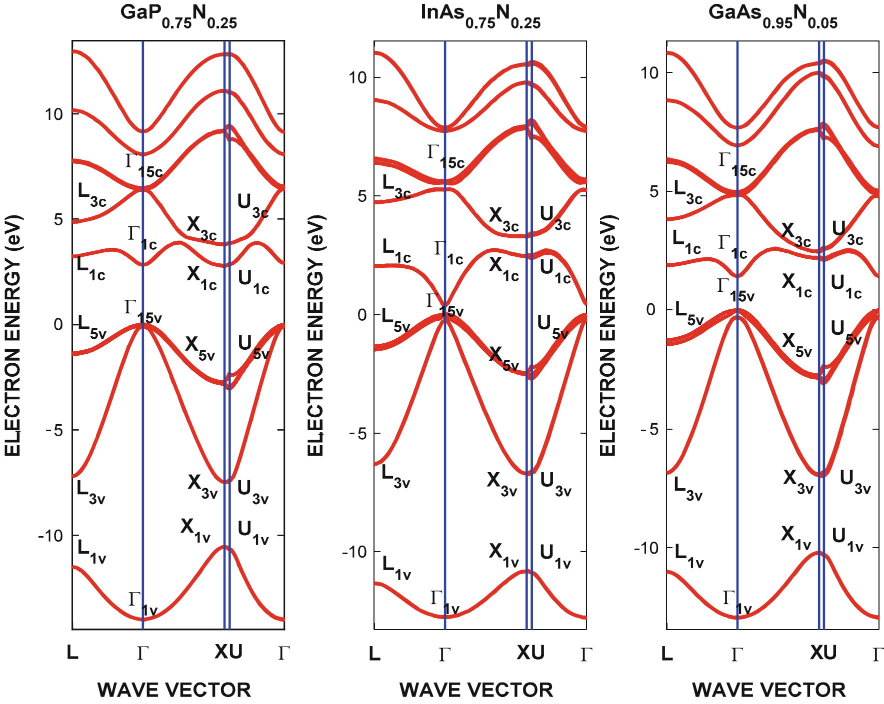

Fig. 2.6 Electronic band structures of GaPN (*left*), InAsN (*middle*), and GaAsN (*right*) bulk nitride semiconductors obtained by using 2NN sp^{3}s* TB orbitals basis sets

and, in many cases, there are not many analytical expressions available. In such a process, an accurate and reliable determination of the strain effects on the energy levels by fitting the off-site TB matrix elements to set of observables is difficult. One can overcome this difficulty by using the statistical thermodynamic model [32] to study the interface strain effects on the electronic structure of heterostructure at symmetry points.

In determining the effects of interface strain on the energy band structures of heterostructures within the so-called statistical thermodynamic model of semiconductors [32], in which the conduction electrons and valence holes are treated as electrically charged chemical particles, one first expresses the shifts in the conduction and valence band edges at the Γ, L and X high symmetry points obtained by using the 2NN sp^{3}s* TB orbitals basis sets as given by (2.7), (2.8) and (2.9). One then writes the shifts in the conduction and valence band energy levels and consequently, the bandgap energies of the heterojunction constituents as a function of temperature and pressure as

$$E_{ci}(T,P) = E_{ci} + C^{0}_{ciP}T(1 - 1nT) - \frac{a_{ci}}{B}\left[P - \frac{P^2}{2B} - \frac{(1+B')P^3}{6B^2}\right], \quad (2.24)$$

$$E_{v}(T,P) = E_{v} + C^{0}_{vP}T(1 - 1nT) - \frac{a_{v}}{B}\left[P - \frac{P^2}{2B} - \frac{(1+B')P^3}{6B^2}\right], \quad (2.25)$$

where E_v is the top of valence band at $k = 0$ (Γ symmetry point) and $a_v = -B(\partial E_v/\partial P)$ is its deformation potential. The index i corresponds to the Γ, L, and X symmetry points in the first Brillouin zone: $E_{c1} = E_{c\Gamma}$, E_{cL}, and E_{cX} are the conduction band minima at the Γ, L, and X symmetry points with deformation potentials $a_{c\Gamma} = -B(\partial E_{c\Gamma}/\partial P)$, $a_{cL} = -B(\partial E_{cL}/\partial P)$, and $a_{cX} = -B(\partial E_{cX}/\partial P).B$ is the bulk modulus and $B' = \partial B/\partial P$ is its pressure derivative. $C^{O}_{cP} = C^{o}_{nP} - C^{O}_{oP} = -C^{o}_{pP} + \Delta\, C^{O}_{P}$ and $C^{o}_{vP} = C^{o}_{pP}$ are the standard state heat capacities of electron in conduction band valley E_{ci} and that of the valence hole at the top of the valence band energy E_v at constant pressure, with $\Delta\, C^{O}_{P} = C^{O}_{cP} + C^{o}_{vP} = C^{o}_{nP} + C^{o}_{pP} - C^{O}_{oP}$ as the change in the standard heat capacity of reaction. $C^{o}_{nP} = C^{o}_{pP} = (5/2)k_B$ for bare electrons and holes, k_B is the Boltzmann's constant.

Figure 2.6a, b, and c displays the lowest bandgap energies at the Γ, L, and X high symmetry points of the GaPN (left), InAsN (middle), and GaAsN (right) nitride-based ternary alloy components of GaAsN/GaAs, InAsN/InN and GaPN/GaP heterostructures. These figures clearly indicate that interface strain effects on the bandgaps points can be quite large when the bandgap deformation potential is large. As one can see from Fig. 2.7a, b, and c, the predicted principal bandgaps of nitride-based ternary alloys at Γ, L, and X high symmetry points, especially at Γ, are in excellent agreement with experimental data [28–30]. The bandgaps of the GaPN, InAsN, and GaAsN nitride-based ternary semiconductors first decrease with alloy composition (for N composition) roughly 25%, showing a negative slope, and increase gradually with alloy composition, having a large positive slope, in close agreement with experiments carried out on these materials. This observation suggests that by using the optimized 2NN sp^3s^* TB parameters for bulk GaAs, GaN, InAs, and GaP binary compounds, given in Table 2.2, the 2NN sp^3s^* TB model allows one to determine the nonlinear composition dependence of principal bandgaps of nitride-based ternary semiconductors without any empirical fitting and/or any adjustable parameters. This conclusion suggests that the 2NN sp^3s^* TB model can be a useful design tool for electronic and optoelectronic devices.

A comparison of predictions with experimental bandgap data for nitride ternaries, shown in Figs. 2.6, indicates that the proposed form of the 2NN sp^3s^* TB model predicts that the fundamental bandgaps of ternary semiconductors vary with alloy composition as

$$E_{gl}(x) = (1-x)E_{gl\mathrm{AC}} + xE_{gl\mathrm{BC}} - \Delta E(x),$$
$$\Delta E(x) = x(1-x)[E_{gl}(AC) - E_{gl}(BC)_l], \quad (2.26)$$

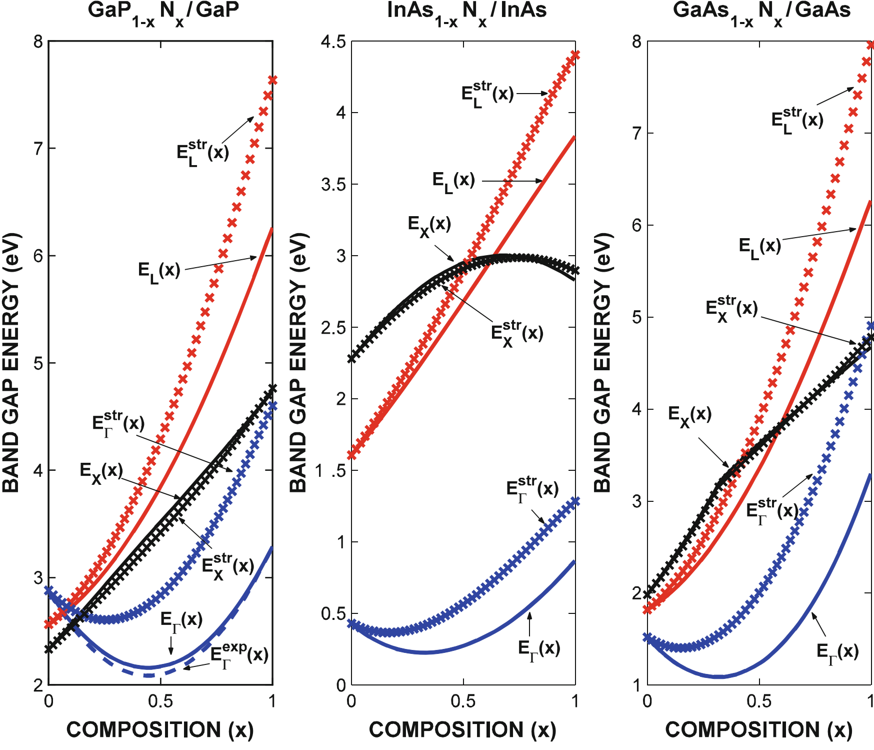

Fig. 2.7 Fundamental bandgaps of ternaries in GaPN/GaP (*left*), InAsN/InAs (*middle*), and GaAsN/GaAs (*right*) heterostructures calculated using the 2NN sp^3s^* TB orbitals basis set

where $\Delta E(x)$ represents the nonlinear effects of alloy composition on the fundamental bandgap energies of ternary semiconductors. Bandgap energies of GaPN, InAsN, and GaAsN appear to have positive bowing over the entire alloy composition range ($0 \leq x \leq 1$).

2.5 Band Offsets in Ternary/Binary Structures

The key feature involved in understanding the impact of nitride-based ternary/binary low-dimensional semiconductor structures on the performance of electronic and optical devices is the effect of alloy composition and strain variation on their energy band structure across the interface. Conduction and valence band offsets across the interface, shown in Fig. 2.8, control the electronic properties of heterostructure devices. In the context of the 2NN sp^3s^* TB model, the valence band offset across an ABC/AC ternary/binary heterostructure can be obtained by taking the difference between the valence band energies of the constituent bulk semiconductors screened

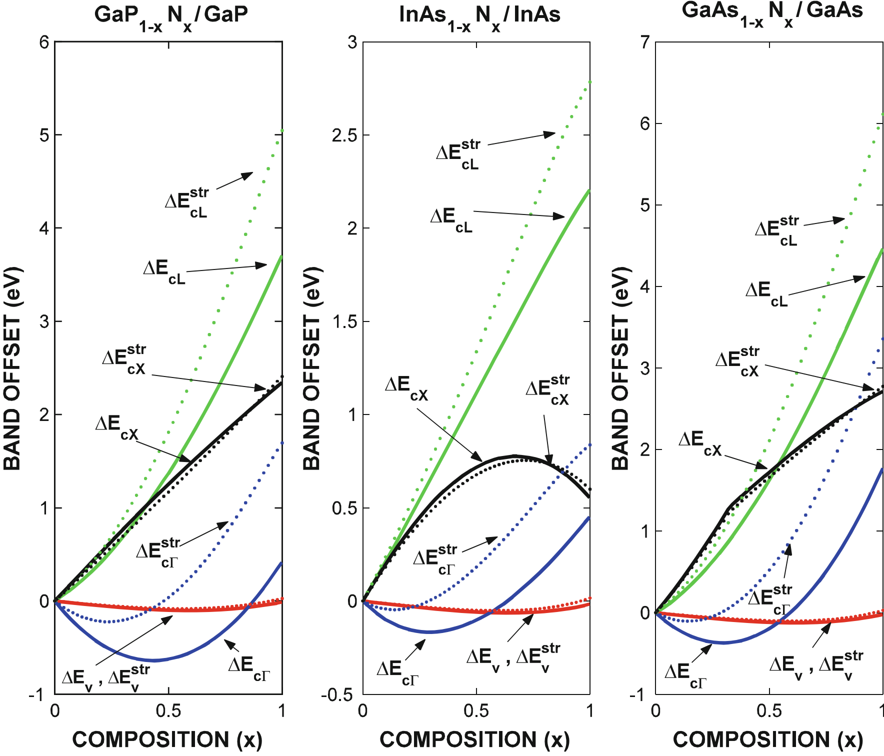

Fig. 2.8 Valence and conduction band offsets of GaPN/GaP (*left*), InAsN/InAs (*middle*), and GaAsN/GaAs (*right*) heterostructures calculated using the 2NN sp^3s^* TB model

with their optical dielectric constant, and then the conduction band offset for a given Γ, L, and X high symmetry point of the Brillouin zone is given as the difference between the bandgap difference, written as [32]:

$$\Delta E_{\mathrm{v}} = \left(\frac{E_{\mathrm{v}}}{\varepsilon_{\infty}}\right)_{\mathrm{BC}} - \left(\frac{E_{\mathrm{v}}}{\varepsilon_{\infty}}\right)_{\mathrm{ABC}},$$
$$\Delta E_{ci} = E_{ci\,\mathrm{ABC}} - E_{ci\,\mathrm{BC}} = \Delta E_{gi} - \Delta E_{\mathrm{v}}, \tag{2.27}$$

where $E_{\mathrm{v}} = E_{\mathrm{v}}(\Gamma_{15})$ is the top of the valence band at the Γ high symmetry point and $E_{ci} = E_{\Gamma_{6c}}, E_{L_{6c}}$, and $E_{X_{6c}}$are the bottom of the conduction bands at the Γ, L, and X high symmetry points, determined with the proposed form of the 2NN sp^3s^* TB model discussed in "TB View of Semiconductor Structures" section using the optimized TB parameters listed in Table 2.2. Here, $\Delta E_{gi} = E_{gi}(\mathrm{ABC}) - E_{gi}(\mathrm{BC})$ is the difference between bandgaps of the bulk ABC ternary and BC binary compound semiconductors with bandgaps $E_{gi}(\mathrm{ABC})$ and $E_{gi}(\mathrm{BC})$, where $E_{gi} = E_{g\Gamma}, E_{g\mathrm{L}}$, and $E_{g\mathrm{X}}$ are the principal bandgaps at the Γ, L, and X

symmetry points. $\varepsilon_\infty(\text{ABC})$ and $\varepsilon_\infty(\text{BC})$ are the optical dielectric constants of bulk ABC ternary and BC binary semiconductors. The band offsets in III–V nitride-based ternary/binary heterostructures are shown in Fig. 2.7 for GaPN/GaP (left), InAsN/InAs (middle), and GaAsN/GaAs (right) as a function of interface strain for the entire composition range ($0 \leq x \leq 1$).

As shown in Fig. 2.8, the interface strain effect on the valence band offsets in the GaPN/GaP, InAsN/InAs, and GaAsN/GaAs nitride-based heterostructures is rather small because of the smaller valence band deformation potentials. However, the interface strain effects on conduction band offsets at Γ, L, and X high symmetry points can be quite large because of the large conduction band deformation potentials. Furthermore, the conduction band offset of the InAsN/InAs structure at the X high symmetry point has a negative slope and is fairly nonlinear with composition. When we analyze the compositional variations of conduction band offsets at the Γ high symmetry point of the first Brillouin zone, we note that they are mostly negative at lower compositions $0.0 < x < 0.50$ and become positive for larger compositions, $0.50 < x < 1$. We can say that GaPN/GaP, InAsN/InAs, and GaAsN/GaAs nitride-based heterointerfaces are type II for smaller alloy compositions ($0.0 < x < 0.50$) and become type I as the alloy composition increases ($0.50 < x < 1.0$).

2.6 Semiempirical sp^{3}d^{5}s* TB Model

From comparison of electronic band structures calculated with pseudopotential theory and sp^3 and sp^{3}s* ETB models, Jancu et al. [21] realized that the excited d-states make a critical contribution to both the valence band maximum at the Γ high symmetry point and to the conduction band dispersion curves at the X and L symmetry points; and he developed an NNsp^{3}d^{5}s* semiempirical TB model with NN interactions to calculate the electronic band structure of group IV and III–V semiconductors. The valence band and conduction band dispersion curves obtained with the NNsp^{3}d^{5}s* model are found to overcome most of the limitations of the earlier TB models. This accurate description of the second conduction band and the transverse effective masses at the X- and L-symmetry points are found to be in good agreement with experimental data, leading to a reliable TB model for the calculation of the optical properties involving high symmetry points at the edge of the first Brillouin zone of tetrahedral semiconductors. Figure 2.9 shows the comparison of the electronic band structure and DOS of GaAs calculated using the 2NN sp^{3}s* and NN sp^{3}d^{5}s* TB methods. Correspondingly, Fig. 2.10 exhibits the band structure and DOS of GaN calculated using the NN sp^{3}d^{5}s* TB method [21] and DFT [22].

In the framework of the NN sp^{3}d^{5}s* TB models, the effects of alloy composition on the electronic band structure of ternary/binary heterostructures are calculated using MVCA [14–16,20]. This MVCA approximation makes it possible to calculate the disorder nonlinear variation of the lattice constant and TB parameters in the determination of the electronic structure properties (such as bandgaps and band

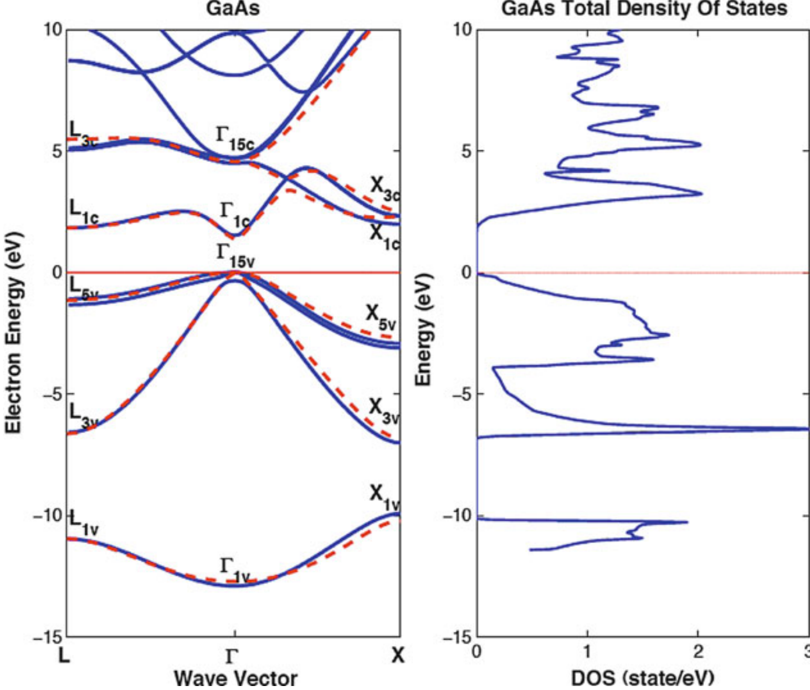

Fig. 2.9 Electronic band structure and DOS of GaAs calculated using the 2NN sp^3s^* (*dashed*) and NN $sp^3d^5s^*$ (*solid*) TB methods

offsets as shown in Fig. 2.11 for AlGaAs/GaAs heterostructures at 300 K) from fundamental bandgap energy and conduction and valence band offsets compared in Fig. 2.11 with results of DFT calculations carried out by our group and experiment.

2.7 Conclusion

The realization of the full potential of low-dimensional semiconductor structures for electronic device technologies requires a reliable and precise predictive process and performance simulation models that are consistent with the fundamental principles of solid-state physics and quantum mechanics. The use of low-dimensional semiconductor structures in device design allows the device engineer to locally modify the energy band structure of the constituents in order to control the motion of charge carriers. When two semiconductors with different physical and chemical properties and thicknesses are grown upon each other, the lattice mismatch and thermal expansion gradient over the growth temperature causes interface strain that modifies the electronic properties of both materials, including the band offsets, and consequently, the energy of the moving charge carriers at the conduction and

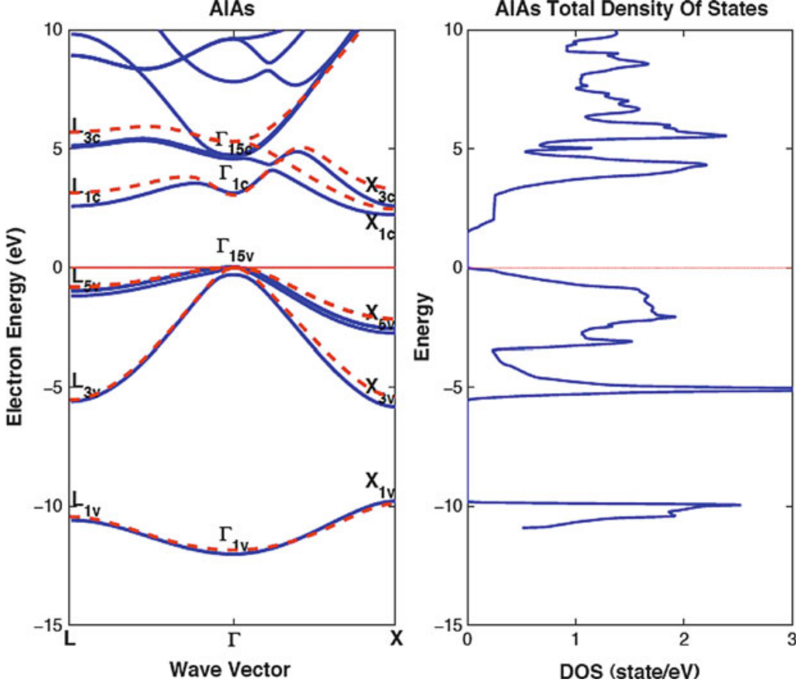

Fig. 2.10 Electronic band structure and DOS of AlAs calculated using the NN $sp^3d^5s^*$ TB method (*solid*) and DFT (*dashed*)

valence band edges must change across the heterointerface, influencing the device performance. Key issues involved are understanding the formation and determining the magnitude of the conduction and valence band offsets at the interfaces of low-dimensional structures, which dominate various device properties and has received considerable attention among the device scientists and engineers over the years.

In this chapter, we presented a general methodology for a qualitatively reliable and quantitatively precise calculation of the electronic band structure of low-dimensional semiconductor heterostructures. The models discussed in this chapter include the semiempirical sp^3 TB theory and DFT of band structure modeling, which can be implemented very easily in current transport modeling for low-dimensional semiconductor structures to insure accurate design and simulation of electronic and optoelectronic devices.

Acknowledgements This work was partially supported by the Scientific and Technical Research Council of Turkey (TÜBİTAK) under Grant No: TBAG-105T463. Two of us, H. H. Gürel and Ö. Akıncı, greatly acknowledge the Ph.D. student fellowships by Turkish State Planning Agency (DPT). The authors would like to greatly acknowledge the computer usage of High Performance Computing Laboratory of Informatics Institute at stanbul Technical University.

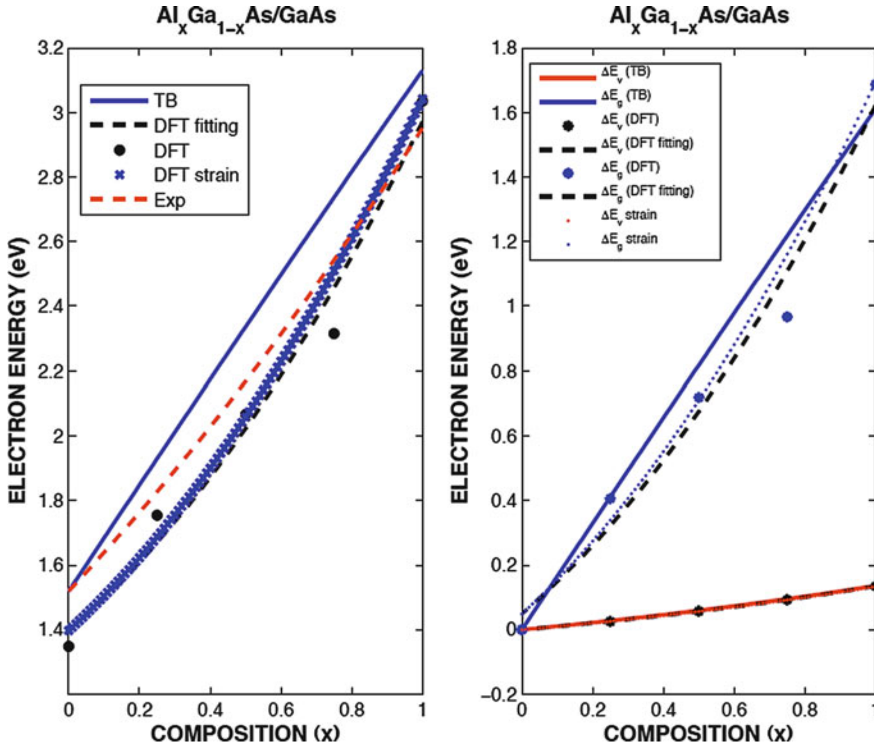

Fig. 2.11 Composition effects on bandgaps and band offsets in an AlGaAs/GaAs heterostructure calculated using the NN $sp^3d^5s^*$ TB method (*solid*) and DFT (*dashed*)

References

1. H. Morkoç, H. Ünlü, G. Ji, *Principles and Technology of MODFETs*, vols. 1, 2 (Wiley, Chichester, 1991)
2. B. Gil (ed.), *Group III Nitride Semiconductors Compounds: Physics and Applilcations* (Oxford Science Publications, Oxford, 1998)
3. H. Ünlü, H. Morkoç, Solid State Technol. **31**, 83 (1988).
4. H. Morkoç, H.Ünlü, in *Semiconductors and Semimetals*, vol. 24, ed. by R. Dingle (1987), p. 135, (Academic Press, 1987)
5. H. Ünlü, H. Morkoç, S. Iyer, in *Gallium Arsenide Technology*, vol. 2, ed. by D.K. Ferry (1990), p. 231, (Howard & Sams, 1990)
6. H. Morkoç, H.Ünlü, H. Zabel, N. Otsuka, Solid State Technol. **31**, 71 (1988)
7. H. Kroemer, Proc. IRE **45**, 1535 (1957)
8. H. Kroemer, Proc. IEEE **70**, 13 (1982)
9. J.-M. Jancu et al., Phys. Rev. B **57**, 6493 (1998)
10. A. Di Carlo, Semicond. Sci. Technol. **18**, R1 (2003)
11. G.L. Bir, G.E. Pikus, *Symmetry and Strain – Induced Effects in Semiconductors* (Wiley, New York, 1974).
12. H. Ünlü, Phys. Status Solidi (B) **216**, 107 (1999)
13. Ö. Akıncı, H.H. Gürel, H. Ünlü, Thin Solid Films **517**, 2431 (2009)

14. H.H. Gürel, Ö. Akıncı, H. Ünlü, Thin Solid Films **516**, 7098 (2008)
15. Ö. Akıncı, H.H. Gürel, H. Ünlü, Phys. Status Solidi (C) **5**(2), 478 (2008)
16. Ö. Akıncı, H.H. Gürel, H. Ünlü, J. Nanosci. Nanotechnol. **8**, 540 (2008)
17. H.H. Gürel, Ö. Akıncı, H. Ünlü, Phys. Status Solidi (C) **4**(2), 316 (2007)
18. H.H. Gürel, Ö. Akıncı, H. Ünlü, Superlattices Microstruct **40**(4–6), 588 (2006)
19. Ö. Akıncı, H.H. Gürel, H. Ünlü, Thin Solid Films **511–512**, 684 (2006)
20. H.H. Gürel, Ö. Akıncı, H. Ünlü, Comput. Mater. Sci. **33**, 269 (2005)
21. P. Vogl, H.P. Hjalmarson, J.D. Dow, J. Chem. Solids **44**, 365 (1983)
22. J.-M. Jancu et al., Phys. Rev. B **57**, 6493 (1998)
23. J.-M. Jancu et al., Appl. Phys. Lett. **81**, 4838 (2002)
24. J.C. Slater, G.F. Koster, Phys. Rev. **94**, 1498 (1954)
25. D.J. Chadi, M.L. Cohen, Phys. Status Solidi **68**, 405 (1975)
26. W.A. Harrison, *Elementary Electronic Structure* (World Scientific, Singapore, 1999)
27. M.L. Cohen, J.R. Chelikowsky, *Electronic Structure and Optical Properties of Semiconductors*, 2nd edn. (Springer, Berlin, 1989)
28. O. Madelung (ed.), *Numerical Data and Functional Relationships in Science and Technology*, vol. 17a (Springer, Berlin, 1982)
29. O. Madelung (ed.), *Numerical Data and Functional Relationships in Science and Technology*, Part a of vol. 17 (Springer, Berlin, 1982) and Part d of Vol. 17 (1984)
30. I. Vurgaftman, J.R. Meyer, L.R. Ram-Mohan, J. Appl. Phys. **89**(11), 5815 (2001)
31. J.L. Martins, A. Zunger, Phys. Rev. B **30**, 6217 (1984)
32. H. Ünlü, Solid State Electron. **35**, 1343 (1992)

Chapter 3
Graphene: Properties and Theory

Norman J. Morgenstern Horing

Abstract This chapter presents information (in slide form) about graphene properties, its massless relativistic spectrum, its Green's function with and without a magnetic field, and its dielectric screening. This chapter also includes graphene energy loss, van der Waals interaction, transport, and a detailed analysis of its kinetic equations for DC and AC conductivity. Device applications are also discussed.

- Outline of the Slide Presentation
  - Introduction
    - Device-Friendly Material Properties for Applications
    - Sample Preparation-Original Experiments
    - Structure-Unusual Properties
    - Massless Relativistic Dirac Spectrum
  - Graphene Hamiltonian and Green's Functions for Null and Finite Magnetic Field
  - Dielectric Screening Properties
  - Graphene Energy Loss; van der Waals Interactions and Other Features
  - Transport-Theory Background; Conductivity Minimum
  - Kinetic Equation: DC and AC
    - Formulation and Solution
    - Conductivity—Results and Discussion
  - Conclusions—Device Applications

N.J.M. Horing (✉)
Department of Physics and Engineering Physics, Stevens Institute of Technology, Hoboken, NJ 07030, USA
e-mail: nhoring@stevens.edu

H. Ünlü and N.J.M. Horing (eds.), *Low Dimensional Semiconductor Structures*, NanoScience and Technology, DOI 10.1007/978-3-642-28424-3_3,
© Springer-Verlag Berlin Heidelberg 2013

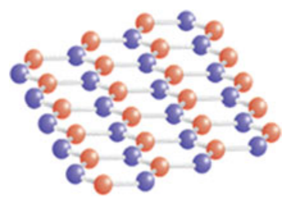

3.1 Graphene

3.1.1 Device-Friendly Material Properties

- High mobility at room temperature
- High electron density: 10^{13} cm^{-2} in single subband
- Long mean free path at room temperature – facilitates *ballistic transport*
- Temperature stability of graphene
- Exhibits quantum hall effect at room temperature

3.1.2 Applications

- Convenience of planar form (*not* tube) for commercial device fabrication
- Sensors-detection of single adsorbed molecule
- Actuator for electromechanical resonator
- Spin valve
- Graphene-based FET

3.1.3 Introduction: Sample Preparation Techniques: Original Experiments

- In 2004, a group of physicists from Manchester University, UK, led by A. Geim and K. Novoselov, obtained graphene starting with 3D graphite and extracting a single sheet using a technique called *micromechanical cleavage* [Science **306**, 666 (2004)].
- Recently, Walt de Heer's group at Georgia Institute of Technology demonstrated a new method to obtain graphene: *exfoliation* of intercalated graphitic compounds and Si *sublimation* from SiC substrates [J. Phys. Chem. B **108**, 19912 (2004)].

3.1.4 Introduction: Structure

- Graphene is composed of a single 2D layer of carbon atoms in a hexagonal honeycomb lattice

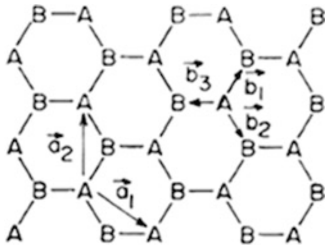

The honeycomb lattice is a superposition of two triangular sublattices. The basic vectors are $\vec{a}_1 = (\sqrt{3}/2, -1/2)a$ and $\vec{a}_2 = (0,\ 1)a$, and the sublattice is connected by $\vec{b}_1 = (1/2\sqrt{3}, 1/2)a$, $\vec{b}_2 = (1/2\ \sqrt{3}, -1/2)a$, and $\vec{b}_3 = (-1/\sqrt{3}, 0)a$.

3.1.5 Introduction: Structure, Massless Dirac Spectrum

- In graphene, low-energy electrons behave as *massless relativistic fermions* due to their linear energy spectrum around two nodal, zero-gap points (K and K') in the Brillouin zone. Electron/hole energies are proportional to $+/-$ momentum.

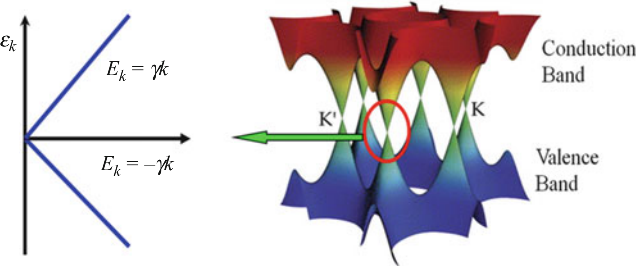

Fig. 3.1 Schematic of graphene band structure

[$\gamma^2 = 3\alpha^2 a^2/4$, α is the hopping parameter in tight-binding approximation and a is the lattice spacing; note that γ also plays the role of a *constant Fermi velocity* (i.e., independent of carrier density).]

3.2 Graphene Hamiltonian I

- Hamiltonian

The graphene Hamiltonian of free electrons/holes with 2D momentum **p** near $s = K$ or $s = K'$ (Dirac points) in pseudospin basis is given by ($\vec{\sigma} = \sigma_1, \sigma_2$ represents the Pauli spin matrices; γ is the Fermi velocity)

$$\breve{h}_0^{(s)} = \gamma \vec{p} \cdot \vec{\sigma} = \gamma \begin{pmatrix} 0 & p_x - \text{sgn}(s) i p_y \\ p_x + \text{sgn}(s) i p_y & 0 \end{pmatrix}$$

$$\text{sgn}(s) = \begin{cases} 1 & s = K \\ -1 & s = K'. \end{cases}$$

3.3 Graphene Hamiltonian II

- In our study, two basis sets are used: the *pseudospin* basis above and the *pseudohelicity* basis.
- The unit cell of graphene contains two nonequivalent carbon atom structures (two triangular sublattices), which can be represented as two different states. In *pseudospin representation*, these two atom structures correspond to the two states in a spin 1/2 system.
- The *pseudohelicity* basis is the basis of Hamiltonian eigenstates (diagonal); helicity is the component of pseudospin in the momentum direction.
- The pseudospin of carriers in graphene near Dirac points is parallel or antiparallel to momentum. Correspondingly, the pseudohelicity of carriers, equal to 1 or −1, is characterized as a left-handed or right-handed state in the pseudohelicity basis. This feature enables us to describe the low-energy electrons in graphene as *massless relativistic fermions*.
- Relativistic phenomenology follows: “zitterbewegung”, Klein tunneling, etc.

3.4 Graphene Hamiltonian III

Introducing a unitary transformation to go from a pseudospin basis to a pseudohelicity basis

$$U_p^{(s)} = \frac{1}{\gamma p} \begin{pmatrix} p_x - \text{sgn}(s) i p_y & p_x + \text{sgn}(s) i p_y \\ \gamma p & \gamma p \end{pmatrix},$$

$\breve{h}_0$ can be diagonalized as $[\varepsilon_\mu = (-1)^{\mu+1} \gamma p]$

$$\hat{h}_0^{(s)} = \left[U_p^{(s)} \right]^+ \breve{h}_0^{(s)} U_p^{(s)} = \text{diag}[\varepsilon_1(p), \varepsilon_2(p)].$$

The carriers experience scattering by impurities. In the pseudohelicity basis, the corresponding potential takes the form:

$$T(\mathbf{p}, \mathbf{k}) = U_p^+ V(|\mathbf{p} - \mathbf{k}|) U_{\mathrm{k}}.$$

3.4.1 Graphene: Green's Functions for Null Field and Finite Magnetic Field

Hamiltonian–Pseudospin Representation

$$\breve{h}_0^s = \gamma \vec{\sigma} \cdot \vec{p}; \hbar \to 1;\ \gamma_v = \gamma \operatorname{sign}(v)$$

Green's Functions

$$(i \overleftrightarrow{I} \partial / \partial t - \breve{h}_0^s) \overleftrightarrow{G} (\vec{p}, t) = \overleftrightarrow{I}\, \delta(t - t').$$

In position–frequency representation, the 2×2 matrix G-equation is $[\vec{R} = \vec{r} - \vec{r}';$ $X = x - x'; Y = y - y'; T = t - t' \to \omega]$,

$$\overleftrightarrow{G}(\vec{R}, \omega) = \begin{bmatrix} G_{11}(\vec{R}, \omega) & G_{12}(\vec{R}, \omega) \\ G_{21}(\vec{R}, \omega) & G_{22}(\vec{R}, \omega) \end{bmatrix} = \int \frac{d^2 \vec{p} e^{i \vec{p} \cdot \vec{R}}}{(2\pi)^2} \overleftrightarrow{G}(\vec{p}, \omega),$$

$$\left[\overleftrightarrow{I} \omega - \gamma \sigma_x \frac{1}{i} \frac{\partial}{\partial X} - \gamma_v \sigma_y \frac{1}{i} \frac{\partial}{\partial Y} \right] \overleftrightarrow{G}(\mathbf{R}, \omega) = \overleftrightarrow{I}\, \delta(X) \delta(Y).$$

A. *Retarded* Green's function (in momentum representation, $\vec{p}$; $\omega \to \omega + i0^+$)

$$G_{11}^R(\vec{p}, \omega) = G_{22}^R(\vec{p}, \omega) = \omega / (\omega^2 - \gamma^2 p^2);$$
$$G_{12}^R(\vec{p}, \omega) = G_{21}^{R*}(\vec{p}, \omega) = \gamma (p_x - i p_y) / (\omega^2 - \gamma^2 p^2);$$

Spectral weight $\overleftrightarrow{A}(\vec{p}, \omega) = -2 \operatorname{Im}[\overleftrightarrow{G}(\vec{p}, \omega)]$.
Spectrum: $\omega = \pm \gamma p$($+$ for electrons; $-$ for holes).
B. *Thermodynamic Green's function*

$$\overleftrightarrow{G}^{\left\{ \begin{smallmatrix} < \\ > \end{smallmatrix} \right\}}(\vec{p}, \omega) = i \begin{Bmatrix} f_0(\omega) \\ -1 + f_0(\omega) \end{Bmatrix} \overleftrightarrow{A}(\vec{p}, \omega).$$

3.4.1.1 Landau-Quantized Graphene Green's Function in Magnetic Field I

$$(\vec{p} \to \vec{p} - \frac{e}{2} \vec{B} \times \vec{r})$$
$$G(\vec{r}, \vec{r}'; t, t') = C(\vec{r}, \vec{r}') G'(\vec{r} - \vec{r}'; t - t'),$$

where $C(\vec{r}, \vec{r}') = \exp\left[\frac{ie}{2\hbar c} \vec{r} \cdot \vec{B} \times \vec{r}' \right]$

and$(\vec{R} = \vec{r} - \vec{r}'; \; X = x - x'; \; Y = y - y')$
$G'(\vec{r} - \vec{r}'; \; t - t')$ is determined by
$[\omega - \gamma\sigma_x \Pi_{XY} - \gamma_\nu \sigma_y \Pi_{YX}] G'(\mathbf{R}, \omega) = I\delta(X)\delta(Y).$

Here, $\hbar \to 1$; $c \to 1$; $\gamma_\nu = \gamma \, \mathrm{sign}(\nu)$ and

$$\Pi_{XY} \equiv \frac{1}{i}\frac{\partial}{\partial X} + \frac{eB}{2}Y \quad \text{and} \quad \Pi_{YX} \equiv \frac{1}{i}\frac{\partial}{\partial Y} - \frac{eB}{2}X,$$

which yields G'_{11} in a magnetic field in frequency representation as

$$G'_{11}(\mathbf{R};\Omega) = \frac{-\mathcal{M}\Omega_c}{4\pi} \int_0^\infty d\tau \frac{e^{i\Omega\tau}}{\sin(\Omega_c\tau/2)} \exp\left\{ \frac{i\mathcal{M}\Omega_c[X^2 + Y^2]}{4\tan(\Omega_c\tau/2)} \right\}.$$

3.4.1.2 Landau-Quantized Graphene Green's Function in Magnetic Field II

The identifications for $\underline{\nu = K}$ are

$$\underline{\nu = K}: \; \Omega = \omega + \frac{\gamma\gamma_\nu}{\omega}eB = \omega + \frac{\gamma^2}{\omega}eB; \mathcal{M} = \frac{\omega}{2\gamma^2}; \; \Omega_c = \frac{2\gamma^2}{\omega}eB.$$

Expanding the τ integrand as a generator of Laguerre polynomials, L_n, we obtain

$$G'_{11}(\vec{R};\omega)_K = G'_{22}(\vec{R};\omega)_K =$$
$$= G'^{*}_{11}(R;\omega)_K = \frac{eB}{2\pi}\omega \exp\left(-\frac{eB}{4}[X^2 + Y^2]\right) \sum_{n=0}^{\infty} \frac{L_n\left(\frac{eB}{2}[X^2 + Y^2]\right)}{\omega^2 - 2n\gamma^2 eB}$$

and $\quad \omega G'_{21} = [\gamma \, \Pi_{XY} + i\gamma_\nu \Pi_{YX}] G'_{11}.$

3.4.1.3 Landau-Quantized Graphene Green's Function in Magnetic Field III

For $\underline{\nu = K'}$, the identifications are

$$\underline{\nu = K'}: \; \Omega = \omega + \frac{\gamma\gamma_\nu}{\omega}eB = \omega - \frac{\gamma^2}{\omega}eB; \mathcal{M} = \frac{\omega}{2\gamma^2}; \; \Omega_c = \frac{2\gamma^2}{\omega}eB,$$

and in this case,

$$G'_{11}(\mathrm{R},\omega)_{K'} = G'_{22}(\mathrm{R},\omega)_{K'} = \frac{eB}{2\pi}\omega \exp\left(-\frac{eB}{4}[X^2+Y^2]\right) \times \sum_{n=0}^{\infty} \frac{L_n\left(\frac{eB}{2}[X^2+Y^2]\right)}{\omega^2 - 2(n+1)\gamma^2 eB}.$$

SPECTRA

- $\nu = K;\ \omega' = \pm\sqrt{2n\gamma^2 eB}$,
- $\nu = K';\ \omega = \pm\sqrt{2(n+1)\gamma^2 eB}$.

3.4.1.4 Landau-Quantized Graphene Green's Function in Magnetic Field IV

Another representation in circular coordinates:
The Bessel wave equation

$$\left[\frac{\partial^2}{\partial R^2} + \frac{1}{R}\frac{\partial}{\partial R} - \frac{\mathcal{M}^2\Omega_c^2 R^2}{4} + 2\mathcal{M}\Omega\right] G'_{11}(R;\Omega) = \frac{\mathcal{M}}{\pi}\frac{\delta(R)}{R}$$

yields $G'_{11}(\mathbf{R};\Omega) = G'_{22}(\mathbf{R};\Omega) = \frac{\mathcal{M}}{2\pi} Z_2(i\mathcal{M}\Omega_c/2, \sqrt{2\mathcal{M}\Omega}, R)$,
where Z_2 is the second Bessel wave function*.

3.4.2 Graphene Quantum Dot in Magnetic Field

Green's Function for Dot Region, G'_{dot}, *in Terms of Full-Sheet Green's Function,* G'
Characterize dot by potential dip, $U(\vec{r}) = \alpha\delta^{(2)}(\vec{r})$
($\alpha < 0$ is the product of Q-well depth times dot area):

$$G'_{dot}(\mathbf{r}_1,\mathbf{r}_2;\omega) = G'(\mathbf{r}_1,\mathbf{r}_2;\omega) + \alpha G'(\mathbf{r}_1,0;\omega)\,[I - \alpha G'(0,0;\omega)]^{-1} G'(0,\mathbf{r}_2;\omega)$$

where $G'(0,0;\omega) \to G'(|\vec{r}_1 - \vec{r}_2| \to a, \omega)$ and "a" is dot width.

Dispersion relation

$$\Delta = [(1-\alpha G'_{11})(1-\alpha G'_{22}) - \alpha^2 G'_{12}G'_{21}] = 0.$$

Approximate energy solutions: ω_K, $\omega_{K'}$, $[L_n(x) = \text{Laguerre poly}]$

*P. Moon, E. Spencer, *Field Theory Handbook*, 2nd edn. (Springer, 1971), pp. 171ff.

$$\omega_K = \frac{\alpha eB}{4\pi} e^{-eBa^2/4} L_n\left(\frac{eBa^2}{2}\right)$$
$$\pm \frac{1}{2}\sqrt{\left(\frac{\alpha eB}{2\pi}\right)^2 e^{-eBa^2/2}\left(L_n\left(\frac{eBa^2}{2}\right)\right)^2 + 8n\gamma^2 eB},$$
$$\omega_{K'} = \frac{\alpha eB}{4\pi} e^{\frac{-eBa^2}{4}} L_n\left(\frac{eBa^2}{2}\right)$$
$$\pm \frac{1}{2}\sqrt{\left(\frac{\alpha eB}{2\pi}\right)^2 e^{\frac{-eBa^2}{4}}\left(L_n\left(\frac{eBa^2}{2}\right)\right)^2 + 8(n+1)\gamma^2 eB}.$$

Exact numerical solutions are provided in Figures 3.2, 3.3, 3.4 below:

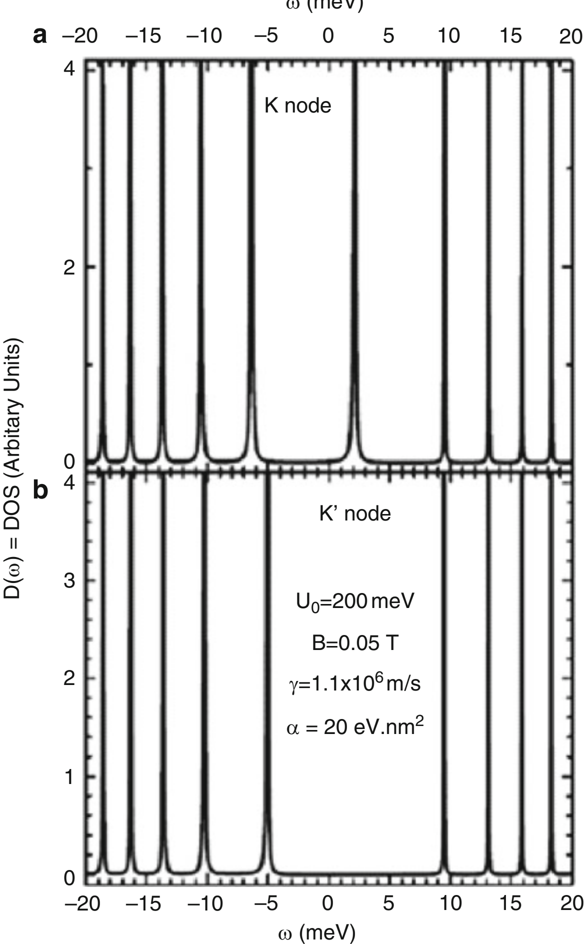

Fig. 3.2 Density of states for $\boldsymbol{K}$, $\boldsymbol{K}'$ nodes as function of energy $\boldsymbol{\omega}$ in meV

Fig. 3.3 Energy levels for K node splintered by Landau quantization as function of $\boldsymbol{B}^{1/2}$

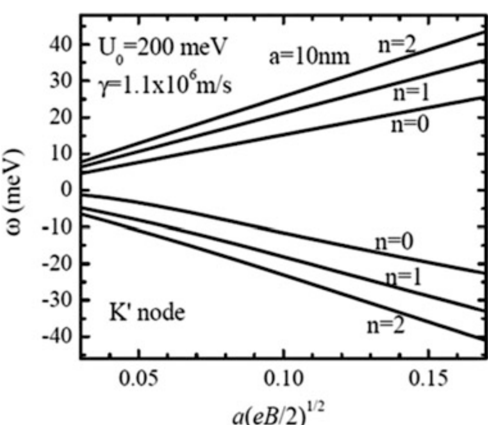

Fig. 3.4 Same as Fig. 3.3, but for $\boldsymbol{K}'$ node (instead of $\boldsymbol{K}$ node)

3.4.3 More about Graphene Quantum Dots

Graphene Q-Dots: *Matulis and Peeters* [*arXiv 0711.446v1 [cond-mat.mes-hall]28 Nov. 2007*] found that Dirac fermions in a cylindrical quantum dot potential are *not* fully confined, but form quasibound states. Their line broadening decreases with orbital momentum. It decreases dramatically for energies close to barrier height due to total internal reflection of electron wave at the dot edge.

3.5 Dielectric Screening Function, K, (on the 2D Graphene Sheet)

$$K(\bar{p}, \omega + i0^+) = \varepsilon^{-1}(\bar{p}, \omega + i0^+) = \left[1 + \alpha(\bar{p}, \omega + i0^+)\right]^{-1},$$

where K is inverse of the dielectric function ε; polarizability α is given by

$\alpha(\bar{p},\omega + i0^+) = -\frac{2\pi e^2}{p} R(\bar{p},\omega + i0^+)$, where $R = \delta\rho/\delta V_{\text{eff}}$ is the density perturbation response function ("ring" diagram): $R(\bar{p},\omega + i0^+) = \Im_< - \Im_>^*$, and

$$\Im_> = \int_0^\infty dt e^{-i(\omega - io^+)t} \int \frac{d^2q}{(2\pi)^2} Tr. \left[\overleftrightarrow{G}_<(\bar{q};-t) \overleftrightarrow{G}_>(\bar{q}-\bar{p};t) \right],$$

$$\Im_< = \int_{-\infty}^0 dt e^{-i(\omega + io^+)t} \int \frac{d^2q}{(2\pi)^2} Tr. \left[\overleftrightarrow{G}_>(\bar{q};-t) \overleftrightarrow{G}_<(\bar{q}-\bar{p};t) \right].$$

["Tr." denotes the trace ("spur") of the matrix.]

3.5.1 Graphene Polarizability: Degenerate Limit (T = 0°K, No Magnetic Field)

Density Perturbation Response Function, "Ring" Diagram R

$$R(x,\nu) = \delta\rho/\delta V_{\text{eff}} = D_0 \tilde{R}(x,\nu); \quad D_0 \equiv \frac{1}{\gamma}\sqrt{\frac{g_s g_\nu n}{\pi}},$$

where $\tilde{R}(x,\nu) = \tilde{R}^+(x,\nu) + \tilde{R}^-(x,\nu)$ and $\tilde{R}^+(x,\nu) = \tilde{R}_1^+(x,\nu)\theta(\nu - x) + \tilde{R}_2^+(x,\nu)\theta(x-\nu)$ (dimensionless variables; $\hbar \to 1$; $\nu = \omega/E_{\text{F}}$; $x = p/k_{\text{F}}$; $g_{s,\nu} = 2$ are pseudospin and valley degeneracies; $\theta(z)$ is the Heaviside unit step function), where the real parts are (notation: $\tilde{R} \equiv -\tilde{\Pi}$),

$$\begin{aligned} \text{Re}\tilde{\Pi}_1^+(x,\nu) = 1 - \frac{1}{8\sqrt{\nu^2 - x^2}} \{ & f_1(x,\nu)\theta(|2+\nu| - x) \\ & + \text{sgn}(\nu - 2 + x) f_1(x,-\nu)\theta(|2-\nu| - x) \\ & + f_2(x,\nu)[\theta(x+2-\nu) + \theta(2-x-\nu)] \}, \\ \text{Re}\tilde{\Pi}_2^+(x,\nu) = 1 - \frac{1}{8\sqrt{x^2 - \nu^2}} \{ & f_3(x,\nu)\theta(x - |\nu+2|) \\ & + f_3(x,-\nu)\theta(x - |\nu-2|) \\ & + \frac{\pi x^2}{2}[\theta(|\nu+2| - x) + \theta(|\nu-2| - x)] \}, \end{aligned}$$

and the imaginary parts are

$$\mathrm{Im}\tilde{\Pi}_1^+(x,\nu) = \frac{-1}{8\sqrt{\nu^2-x^2}}\left\{ f_3(x,-\nu)\theta(x-|\nu-2|) + \frac{\pi x^2}{2}[\theta(x+2-\nu) + \theta(2-x-\nu)]\right\},$$

$$\mathrm{Im}\tilde{\Pi}_2^+(x,\nu) = \frac{\theta(\nu-x+2)}{8\sqrt{x^2-\nu^2}}[f_4(x,\nu) - f_4(x,-\nu)\theta(2-x-\nu)],$$

and $-\tilde{R}^-(x,\nu) = \dfrac{\pi x^2\theta(x-\nu)}{8\sqrt{x^2-\nu^2}} + i\dfrac{\pi x^2\theta(\nu-x)}{8\sqrt{\nu^2-x^2}}$.

Here,

$$f_1(x,\nu) = (2+\nu)\sqrt{(2+\nu)^2-x^2} - x^2\ln\frac{\sqrt{(2+\nu)^2-x^2}+(2+\nu)}{|\sqrt{\nu^2-x^2}+\nu|},$$

$$f_2(x,\nu) = x^2\ln\frac{\nu-\sqrt{\nu^2-x^2}}{x},$$

$$f_3(x,\nu) = (2+\nu)\sqrt{x^2-(2+\nu)^2} + x^2\sin^{-1}\frac{2+\nu}{x},$$

$$f_4(x,\nu) = (2+\nu)\sqrt{(2+\nu)^2-x^2} - x^2\ln\frac{\sqrt{(2+\nu)^2-x^2}+(2+\nu)}{x}.$$

[B. Wunch et al., New J. Phys. **8**, 318 (2006); E.H. Hwang, S. Das Sarma, Phys. Rev. B **75**, 205418 (2007); K.W.-K. Shung, Phys. Rev. B **34**, 979 (1986)]

3.5.2 Graphene Plasmon

Low wave number plasmon

$$\varepsilon(p\to 0;\omega) = 0$$

$$\bullet \Rightarrow \omega = \tilde{\omega}_0 p^{1/2}[1 - q_o p/8p_F^2],$$

where $\tilde{\omega}_0 = (g_s g_\nu e^2 E_\mathrm{F}/2\kappa)^{1/2} \to n^{1/4}$ (not $n^{1/2}$ as in normal 2D plasma)

n = 2D equilibrium carrier density of graphene

κ is background dielectric constant

$q_o = g_s g_\nu e^2 p_\mathrm{F}/\gamma\kappa$ is the *graphene Thomas–Fermi wave number*; with the *graphene Fermi energy* given by $E_\mathrm{F} = -\gamma p_\mathrm{F}$ and $p_\mathrm{F} = [4\pi n/g_s g_\nu]^{1/2}$.

3.5.3 New Graphene Transverse Electric Mode in Terahertz Range

[*Mikhailov & Ziegler, Phys. Rev. Lett.* ***99****, 016803 (2007)*]

- *New Graphene TE Mode*

$1.667 < \hbar\omega/E_F < 2$
15THz $\le f \le$ 18 THz

- *TM Mode: 2D Graphene plasmon–polariton*

$\hbar\omega/E_F < 1.667$

3.5.4 Coupling of Graphene and Surface Plasmons

- Screening function, K, of coupled system

(suppress lateral wave number $\bar{q}$ and frequency ω; z_0 is separation)

$$K(z_1, z_2) = K_{\text{semi}}(z_1, z_2) - \frac{\alpha_{2D} e^{|\bar{q}|z_0} J(z_1) K_{\text{semi}}(z_0, z_2)}{1 + \alpha_{2D} e^{|\bar{q}|z_0} J(z_0)},$$

where α_{2D} is the graphene polarizability above and

$$K_{\text{semi}}(z_1, z_2) = \theta(-z_1) \left\{ \delta(z_1 - z_2) + \delta(z_2) e^{|\bar{q}|z_1} \left(\frac{1 - \varepsilon_0(\omega)}{1 + \varepsilon_0(\omega)} \right) \right\} + \theta(z_1) \left\{ \frac{\delta(z_1 - z_2)}{\varepsilon_0(\omega)} + \delta(z_2) e^{-|\bar{q}|z_1} \frac{1}{\varepsilon_0(\omega)} \left(\frac{\varepsilon_0(\omega) - 1}{\varepsilon_0(\omega) + 1} \right) \right\},$$

with $J(z_0) = \int dz_3 K_{\text{semi}}(z_0, z_3) e^{-|\bar{q}|z_3}$,
and $\varepsilon_0(\omega) = 1 - \omega_p^2/\omega^2$; ω_p is the semi-infinite bulk plasmon frequency.

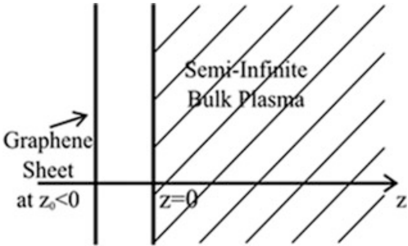

Fig. 3.5 Schematic of a graphene sheet near the surface of a semi-infinite bulk plasma

- Coupled graphene and surface plasmon dispersion relations

($\omega_{2D} \equiv \tilde{\omega}_0 q^{1/2}$ for the graphene 2D plasmon and $\omega_s = \omega_p/\sqrt{2}$ for the surface plasmon of the semi-infinite bulk)

- Two coupled modes

$$\omega_{\pm}^2 = \frac{\left[\omega_{2D}^2 + \omega_s^2(1+\beta\xi)\right]}{2(1+\beta)} \pm \frac{\sqrt{(\omega_{2D}^2 + \omega_s^2[1+\beta\xi])^2 - 4(1+\beta)\omega_{2D}^2\omega_s^2\xi}}{2(1+\beta)}$$

contain the graphene interband correction

$$\beta = (\hbar\omega/2E_F)^2 << 1$$

for acoustic plasmon roots and

$$\xi = 1 - e^{2|\bar{q}|z_0}$$

exhibits z_0 dependence on separation.

3.6 Graphene Energy Loss Spectroscopy and van der Waals Interaction

- *Power loss* = $\vec{f} \cdot \vec{v}$ (K(z$_1$, z$_2$;$\bar{p}$,ω) is the screening function; $\vec{v}$ is the velocity of the energetic passing particle):

$$\vec{f} = -4\pi(Ze)^2\left[\nabla_1 \int dz_2 \int \frac{d^2\bar{p}}{(2\pi)^2} e^{i\bar{p}\cdot\bar{r}_1} \int \frac{dp_z}{2\pi} e^{ip_z z_2} e^{-i(p\cdot\bar{v}+p_z v_z)t_1} e^{-i(\bar{p}\cdot\bar{R}_0+p_z z_0)} \times \frac{K(z_1, z_2, \bar{p}; \omega = \bar{p}\cdot\bar{v} + p_z v_z)}{\bar{p}^2 + p_z^2}\right]_{r_1 = vt_1 + R_0}.$$

- *Parallel: stopping power—high velocity*

Charge *Ze* moves with speed $\vec{v}$ parallel to graphene plane at height above it:

$$[\lambda \equiv (\gamma e^2 \sqrt{n\pi g_s g_v}/\kappa\hbar)^{1/2}]$$

- $$\frac{dW}{dt} = -\frac{Z^2e^2\lambda^4}{2v^3} e^{-(\lambda^2 H/v^2)}\left[K_0\left(\frac{\lambda^2 H}{v^2}\right) + K_1\left(\frac{\lambda^2 H}{v^2}\right)\right]$$

[$K_0(x)$ and $K_1(x)$ are modified Bessel functions].

Perpendicular: total work done by charge passing through graphene sheet

$$\circ \quad |W| = v_z \frac{\pi D_0 p_{\mathrm{F}}}{\gamma} \left(\frac{Ze^2}{\kappa}\right)^2 \left(c'\pi - 4 - \frac{2(c'^{2-2})}{\sqrt{c'^{2-4}}} \cos^{-1(\frac{2}{c'})}\right)$$

($c' = 2\pi e^2 D_0/\kappa p_{\mathrm{F}}$; D_0 defined on slide 18).

3.6.1 Atom/Graphene van der Waals Interaction I

vdW interaction energy to second order in Coulomb potential:

$$E_{\nu dW}^{(2)} = \frac{4}{3\hbar\varepsilon_0} \sum\nolimits_n' \int_0^\infty \frac{\mathrm{d}u}{2\pi} \frac{\omega_{n0} |\vec{D}_{0n}|^2}{u^2 + \omega_{n0}^2} \int_0^\infty \mathrm{d}p p^2 e^{-2p|Z|} \frac{\alpha^{2D}(p, iu)}{\varepsilon_0 + \alpha^{2D}(p, iu)},$$

where $|Z|$ = distance between the atom and the 2D graphene sheet; ω_{n0} is the energy difference of the atomic electron levels; $\omega_{n0} = E_n^{\mathrm{a}} - E_0^{\mathrm{a}}$; $\vec{D}_{0n}$ is the matrix element of the atom's dipole moment operator between atomic electron levels n, 0; and $\alpha^{2\mathrm{D}}(p, \omega)$ is the dynamic, nonlocal polarizability of the graphene sheet. The prime on $\sum'$ denotes omission of the $n = 0$ term; ε_0 is the background dielectric constant.

3.6.2 Atom/Graphene van der Waals Interaction II

$$\text{Undoped}: \alpha^{2\mathrm{D}}(p, iu) = -\left(\frac{g_s g_v \pi e^2}{8\varepsilon_0 \hbar}\right) \frac{p}{\sqrt{u^2 + \gamma^2 p^2}}.$$

Expansion of $E_{\nu dw}$ in inverse powers of $|Z|$ is *not* available since it would involve expanding the p-integrand in powers of p/u, causing divergences in the final u-integration. However, for atomic frequencies (ω_{n0}^{a}), the polarizability is small, $\alpha^{2\mathrm{D}}(p, iu) << 1$, and we have the p-integral as

$$\begin{aligned}\int_0^\infty dp \ldots &\cong -\left(\frac{g_s g_v \pi e^2}{8\varepsilon_0 \hbar}\right) \int_0^\infty \mathrm{d}p e^{-2p|Z|} \frac{p^3}{\sqrt{u^2 + \gamma^2 p^2}} \\ &\cong -\left(\frac{g_s g_v \pi e^2}{8\varepsilon_0 \hbar}\right) \frac{u\pi}{8\gamma^2} \frac{\partial^2}{\partial |Z|^2} \left[\mathbf{H}_1\left(\frac{2|Z|}{\gamma} u\right) - Y_1\left(\frac{2|Z|}{\gamma} u\right)\right],\end{aligned}$$

where $\mathbf{H}_1(x)$ is the Struve function and $Y_1(x)$ is the Bessel function of the second kind.

3.6.3 Graphene Double Layer van der Waals Interaction

$$\frac{E_{\nu dW}^{(2)}}{\text{area}} = \frac{1}{\pi}\int_0^\infty \mathrm{d}u \int \frac{\mathrm{d}^2\bar{q}}{(2\pi)^2} \int \mathrm{d}z_2 \int \mathrm{d}z_3 \overline{\overline{K}}_{\mathrm{A}}(z_2, z_3; \bar{q}, iu)\overline{\overline{K}}_{\mathrm{B}}(z_3, z_2; \bar{q}, iu)$$

with

$$\overline{\overline{K}}_{\mathrm{A,B}}(z_1, z_2, \bar{q}, \omega) = -\delta(z_2 \pm z_0)e^{-|\bar{q}||z_1 \pm z_0|}\alpha_{2\mathrm{D}}(q, iu)[1 + \alpha_{2\mathrm{D}}(q, iu)]^{-1},$$

where $\alpha_{2\mathrm{D}}(q, \omega)$ is the graphene single sheet 2D polarizability. In the plasma-pole approximation, this yields

$$\frac{E_{\nu \mathrm{d}W}^{(2)}}{\text{area}} = \frac{(g_s g_v)^2 e^4}{4096\kappa^2\gamma\hbar|z_0|^3}\left[\frac{\delta}{(\delta^2-1)} - \frac{1}{(\delta^2-1)^{3/2}}\ln\left(\frac{\delta+1+\sqrt{\delta^2-1}}{\delta+1-\sqrt{\delta^2-1}}\right)\right],$$

and $\delta = g_s g_v \pi e^2/8\kappa\gamma\hbar = 1.432$: z_0 is the separation of the two sheets of graphene. (The quantity in square brackets is approximately 0.528.)

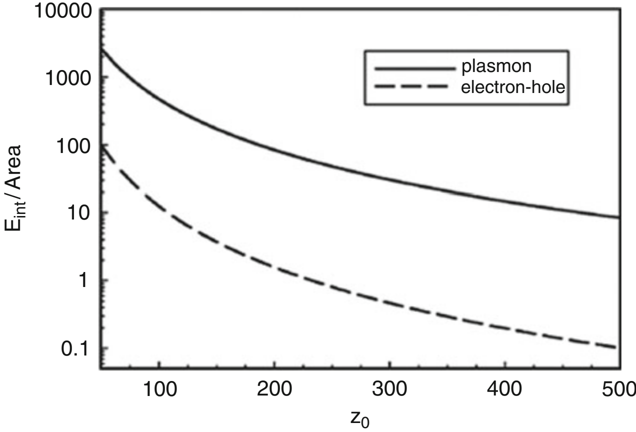

Fig. 3.6 Plasmon (*solid line*) and electron–hole (*dashed line*) contributions to graphene double layer νdW energy as functions of separation, z_0

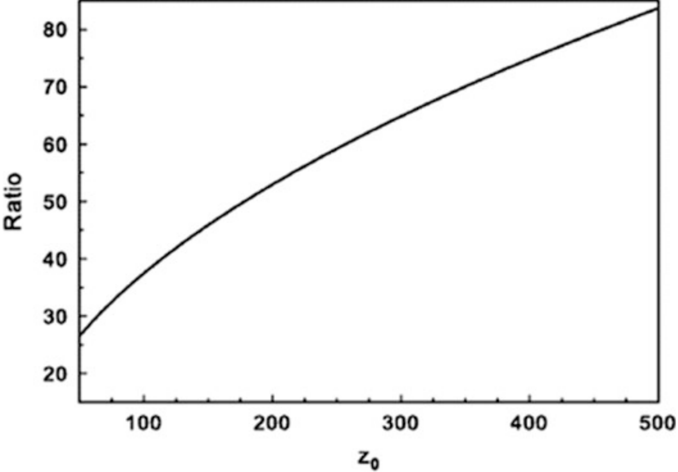

Fig. 3.7 Ratio of plasmon to electron–hole E_{vdw} contributions, as a function of $z_0 \equiv Z$

3.6.4 Graphene Quasiparticle Self-Energy, $\sum$

A. Screened Coulomb self-energy, $\sum_{\text{Coul}}$, due to electron–electron (e–e) Coulomb interaction, U_{Coul}:

$$\sum_{\text{Coul}}(1,2) \Rightarrow -iV_{\text{eff}}(1-2)G(1,2),$$

where the *screened* e–e Coulomb potential is

$$V_{\text{eff}}(1-2) = \int d3K(2-3)U_{\text{Coul}}(3-1).$$

Conclusions:

[*Das Sarma, Hwang & Tse, Phys. Rev.* ***B75***, *121406(R)(2007)*]
Intrinsic graphene is a marginal Fermi liquid (quasiparticle spectral weight vanishes near Dirac point).
Extrinsic graphene is a well-defined Fermi liquid (doping induces Fermi liquid behavior).
B. Phonon-induced self-energy

$$\tilde{V}_{\text{eff}}(1,2) = \Gamma_{\text{ep}}(\vec{x}_1)D^{\circ}(t_1;t_2)\Gamma_{\text{ep}}(\vec{x}_2),$$

$\Gamma_{ep}(\vec{x}_1)$ measures electron–ion interaction strength; $D^\circ(t_1, t_2)$ is the free phonon Green's function, and

$$\sum_{\text{phonon}} (1,2) \Rightarrow -i\,\tilde{V}_{\text{eff}}(1,2)G(1,2).$$

Conclusions:

[*Tse & Das Sarma, Phys. Rev. Lett.**99**, 236802(2007)*]
Phonon-mediated e–e coupling has a large effect on graphene band structure renormalization.

3.6.5 Electronic Superlattices in Corrugated Graphene

Isacsson et al., arXiv:0709.2614v1[cond-mat.mes-hall]17Sep.(2007)

Theory of electron transport in corrugated graphene ribbons, with ribbon curvature inducing an electronic superlattice (SL) having its period set by the corrugation wavelength. Electron current depends on SL band structure, and for ribbon widths with transverse level separation comparable to band edge energy, strong current switching occurs.

3.7 Graphene Transport: Experimental Background

- In experiments involving graphene, many intriguing transport phenomena have been observed. Plot of conductivity as a function of gate voltage (V_g):

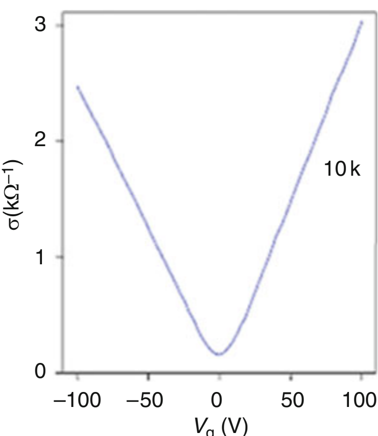

Science **306**, 666 (2004)
Nature **438**, 197 (2005)
Nature **438**, 201 (2005)

- The existence of a "residual" conductivity at zero gate voltage

$$\sigma^{\min} \approx 4e^2/h.$$

- Conductivity varies almost linearly with the electron density, high mobility at room temperature.
- Quantum Hall Effect at *room temperature*

Science, **315**, 1379 (2007).

3.8 Graphene Transport: Theoretical Background-A

- In terms of theoretical calculations, there has been some confusion about the actual value of the minimum "residual" conductivity:

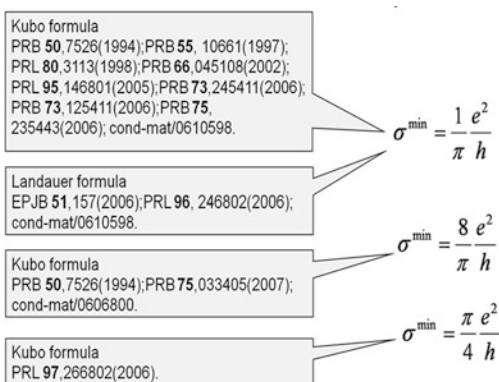

3.9 Graphene Transport: Theoretical Background-B

- Ziegler demonstrated that, within the Kubo formalism, the magnitude of residual conductivity is sensitive to the *order in which the dc (zero frequency) and dissapationless limits* are taken[cond-mat/0701300]
- Adam et al. showed that the minimum "residual" conductivity arises from *nonvanishing electron density* at zero gate voltage which may be induced by impurity potentials. Analyzing random fluctuations of gate voltage, they gave a quantitative explanation of the experimentally observed "residual" conductivity [cond-mat/0705.1540].

3.10 Kinetic Equation for Graphene

- In the present work, we propose a kinetic equation to investigate transport in graphene in the diffusive regime. The effect of *interband polarization* on conductivity is incorporated.
- We find that the conductivity has a *minimum* for the electron density $N_{\mathrm{e}} \approx 0.11\, N_{\mathrm{i}}$ (N_{i} is the impurity density). The value of this minimum is about $4.42e^2/h$ for RPA-screened electron–impurity scattering.
- For $N_{\mathrm{e}} < 0.11\, N_{\mathrm{i}}$, the conductivity is proportional to $(N_{\mathrm{e}})^{-1}$.
- However, the conductivity, σ, varies almost linearly with N_{e} for $N_{\mathrm{e}} > 0.11\, N_{\mathrm{i}}$.

3.10.1 *Kinetic Equation Formulation for Current and Distribution Function*

- The current is expressed in terms of elements of the distribution function, ρ, as ($\mathbf{n}$ is the unit normal vector to the graphene plane)

$$\mathbf{J} = g_s \gamma e \sum_{\mathbf{p},s} \frac{1}{p} \left\{ \mathbf{p} \left\{ [\hat{\rho}_{\mathbf{p}}^{(s)}]_{11}(\mathbf{p}) - [\hat{\rho}_{\mathbf{p}}^{(s)}]_{22}(\mathbf{p}) \right\} + 2\,\mathrm{sgn}\,(s)\mathbf{p} \times \mathbf{n}\,\mathrm{Im} \left\{ [\hat{\rho}_{\mathbf{p}}^{(s)}]_{12}(\mathrm{p}) \right\} \right\}$$

spin degeneracy (points to g_s)

elements of distribution function ρ. (points to $[\hat{\rho}_{\mathbf{p}}^{(s)}]_{11}$, $[\hat{\rho}_{\mathbf{p}}^{(s)}]_{22}$, $[\hat{\rho}_{\mathbf{p}}^{(s)}]_{12}$)

- The kinetic equation for the linear electric field part of the distribution function, $\hat{\rho}_1^{(s)}(\mathrm{p})$, is given by

$$e\mathbf{E} \cdot \nabla_{\mathrm{p}} \left[\hat{\rho}_0^{(s)} \right]_{\mu\mu} (\mathrm{p}) = - \left[\hat{I}_s^{(1)} \right]_{\mu\mu}$$

$$2i\gamma p \left[\hat{\rho}_1^{(s)} \right]_{12} (\mathrm{p}) = - \left[\hat{I}_s^{(1)} \right]_{12}$$

scattering terms. (points to $[\hat{I}_s^{(1)}]_{\mu\mu}$ and $[\hat{I}_s^{(1)}]_{12}$)

3.10.2 *Kinetic Equation: Solution I*

- Solution of the kinetic equation

$$[\boldsymbol{v}_\mu^{(s)}(\mathrm{p}) = \nabla_{\mathrm{p}} \varepsilon_\mu^{(s)}(\mathrm{p}) = (-1)^{\mu+1} \gamma \mathrm{p}/p],$$

$$\left[\hat{\rho}_1^{(s)} \right]_{\mu\mu} (\mathrm{p}) = e\mathbf{E} \cdot \boldsymbol{v}_\mu^{(s)}(\mathrm{p}) \Lambda_\mu^{(s)}(p),$$

$$\left[\hat{\rho}_1^{(s)} \right]_{12} (\mathrm{p}) = \frac{e\gamma}{p} [\mathrm{E} \times \mathrm{p} \cdot \mathrm{n}] \Phi^{(s)}(p).$$

- Diffusive regime of validity (l = diffusion length)— $k_{\mathrm{F}} l > 1$.
- Definitions of $\Lambda_\mu^{(s)}(p)$, $\Phi^{(s)}(p)$ follow.

3.10.3 Kinetic Equation: Solution II

The functions $\Lambda_\mu^{(s)}$ and $\Phi^{(s)}(p)$ can be expressed in terms of microscopically calculated relaxation times as

$$\Lambda_\mu^{(s)}(p) = -\tau_\mu^{(a)}(p) \frac{\partial \left\{ \left[\hat{\rho}_0^{(s)} \right]_{\mu\mu} (\mathrm{p}) \right\}}{\partial \varepsilon_\mu^{(s)}(\mathrm{p})} + \mathrm{sgn}(s) \mathrm{Im}[\Phi^{(s)}(p)],$$

$$Re[\Phi^{(s)}(p)] = -\frac{\mathrm{sgn}(s)}{4\gamma^2 p^2} \sum_\mu \left\{ \gamma p \frac{\partial \{ [\hat{\rho}_0^{(s)}]_{\mu\mu}(p) \}}{\partial \varepsilon_\mu^{(s)}(p)} \right\},$$

$$\mathrm{Im}[\Phi^{(s)}(p)] = -\frac{\mathrm{sgn}(s)}{16\gamma^3 p^3} \left[\frac{1}{\tau_1^{(b)}(\mathrm{p})} + \frac{1}{\tau_2^{(b)}(\mathrm{p})} \right] \times \sum_\mu \left[\gamma p \frac{\partial \{ [\hat{\rho}_0^{(s)}]_{\mu\mu}(\mathrm{p}) \}}{\partial \varepsilon_\mu^{(s)}(\mathrm{p})} \right].$$

3.10.4 Kinetic Equation: Conductivity I

- We finally arrive at the microscopically determined conductivity:

$$\sigma = -\frac{e^2}{2} g_s \gamma^2 \sum_{p,\mu,s} \left\{ \left[\tau_\mu^{(a)}(p) + \frac{1}{4\gamma^2 p^2 \tau^{(b)}(p)} \right] \frac{\partial \left\{ [\hat{\rho}_0^{(s)}]_{\mu\mu}(\mathrm{p}) \right\}}{\partial \varepsilon_\mu^{(s)}(\mathrm{p})} \right\},$$

where

$$[\tau_\mu^{(a,b)}(p)]^{-1} = \pi N_i \sum\nolimits_k |V(p-k)|^2 \delta[\varepsilon_\mu(p) - \varepsilon_\mu(k)] A^{(a,b)}(\phi_k),$$

$$A^{(a)}(\phi) = \sin^2\phi, \quad \text{and} \quad A^{(b)}(\phi) = (1-\cos\phi)^2,$$

$$[\tau^{(b)}(p)]^{-1} \equiv [\tau_1^{(b)}(p)]^{-1} + [\tau_2^{(b)}(p)]^{-1}.$$

Conductivity involves not only a term proportional to $(N_i)^{-1}$, but also a term linear in impurity density.

3.10.5 Static Screening Dielectric Function

- RPA-screened model

$$\varepsilon(q) = 1 + \frac{q_s}{q} \begin{cases} 1 & \text{if } q \le 2k_\mathrm{F} \\ 1 + \frac{\pi q}{8k_\mathrm{F}} - \frac{1}{2}\sqrt{1 - \left(\frac{2k_\mathrm{F}}{q}\right)^2} - \frac{q}{4k_\mathrm{F}} \sin^{-1}\left(\frac{2k_F}{q}\right) & \text{if } q > 2k_\mathrm{F} \end{cases},$$

$q_s = 4e^2 k_\mathrm{F}/(\hbar\tilde{\kappa}\gamma)$ is the Thomas–Fermi screening wave vector ($\tilde{\kappa}$ is the static background dielectric constant)
[Kenneth W.-K. Shung, Phys. Rev. **B34**, 979 (1986); T. Ando, J. Phys. Soc. Jpn. **75**, 074716 (2006); B. Wunsch et al. New J. Phys. 8, 318(2006); E.H. Hwang et al. PRL **98**, 186806 (2007)]

3.10.6 Conductivity Results and Discussion I

- At zero temperature, $k_\mathrm{F} = \sqrt{4\pi N_\mathrm{e}/g_\mathrm{s} g_\mathrm{v}}$,

$$\sigma|_{T=0} = e^2 \pi g_\mathrm{s} g_\mathrm{v} \gamma k_\mathrm{F} \left[\tau_1^{(\mathrm{a})}(k_\mathrm{F}) + \frac{1}{4\gamma^2 k_\mathrm{F}^2 \tau^{(b)}(k_\mathrm{F})}\right],$$

where g_v characterizes the valley degeneracy and g_s the spin degeneracy.
Obviously, there is a minimum in the dependence of conductivity on the impurity density; consequently, there is also a minimum in the charge carrier density indicated here.

3.10.7 Conductivity Results and Discussion II

- For a short-range scattering model [PRL **92**,256602(2006)],

$$V(p-k) \approx \pi\gamma/(2k_\mathrm{F})$$

$$\sigma|_{T=0} = \frac{e^2}{\pi}\left[\frac{16N_\mathrm{e}}{\pi N_\mathrm{i}} + \frac{3\pi N_\mathrm{i}}{32 N_\mathrm{e}}\right].$$

RESULTS:

- Minimum conductivity at zero temperature

$$\sigma|_{T=0} \ge \sigma_{\min} = e^2\sqrt{6}/\pi = 2\sqrt{6}e^2/h \approx 4.9e^2/h.$$

- Carrier density at minimum conductivity

$$\sigma|_{T=0} = \sigma_{\min} \text{ if } N_e = N_e^c = N_i \pi \sqrt{6}/32 \approx 0.24 N_i,$$

when $N_e > N_e^c$, the first term in $\sigma|_{T=0}$ is important, giving rise to a linear dependence of conductivity on electron density.

3.10.8 Conductivity Results and Discussion III

- RPA-screened Coulomb scattering model

$$V(q) = \frac{e^2}{2\varepsilon_0 \kappa \varepsilon(q) q}.$$

- Zero temperature conductivity

$$\sigma|_{T=0}^{\text{RPA}} = \frac{e^2}{\pi}\left[\frac{N_e}{N_i G(2r_s)} + \frac{N_i F(2r_s)}{4N_e}\right],$$
$$(r_s = e^2/(4\pi\varepsilon_0 \kappa \gamma)).$$

- $G(x)$, $F(x)$ are specified below.

3.10.9 Conductivity Results and Discussion IV

Above,

$$G(x) = \frac{x^2}{8}\int_0^{2\pi} d\theta \frac{\sin^2\theta}{(\sin\frac{\theta}{2} + x)^2}$$
$$= x^2 \begin{cases} \frac{\pi}{4} + 3x - \frac{3\pi}{2}x^2 + |x|(3x^2 - 2)\arccos(1/x)[x^2 - 1]^{-1/2} & \text{for} |x| > 1 \\ \frac{\pi}{4} + 3x - \frac{3\pi}{2}x^2 + x(3x^2 - 2)\text{Re}[\text{arctanh}(1/\sqrt{1 - x^2})][1 - x^2]^{-1/2} & \text{for } 0 \leq x \leq 1 \end{cases},$$

and

$$F(x) = \frac{x^2}{8}\int_0^{2\pi} \mathrm{d}\theta \frac{(1 - \cos\theta)^2}{(\sin\frac{\theta}{2} + x)^2}$$
$$= x^2 \begin{cases} \frac{\pi}{2} - 4x + 3x^2\pi - \frac{2x^3}{x^2 - 1} + |x^3|(8 - 6x^2)\arccos(1/x)(x^2 - 1)^{-3/2} & \text{for } |x| > 1 \\ \frac{\pi}{2} - 4x + 3x^2\pi - \frac{2x^3}{x^2 - 1} - x^3(8 - 6x^2)\text{Re}[\text{arctanh}(1/\sqrt{1 - x^2})](1 - x^2)^{-3/2} & \text{for } 0 \leq x \leq 1 \end{cases}$$

3.10.10 Conductivity Results and Discussion V

- Our results are in good agreement with the experimental data: The observed minimum conductivity is about $4e^2/h$, while we obtain $\sigma_{\min} \approx 4.42e^2/h$ for RPA-shielded Coulomb scattering with $N_e \approx 0.11\, N_i$.
- We also find almost linear dependence of the conductivity on carrier density for $N_e > 0.11\, N_i$.

3.10.11 Conductivity Results and Discussion VI

- We find that conductivity increases with decreasing electron density for $N_e < 0.11 N_i$ in the diffusive regime. Actually, random fluctuations of gate voltage may cause an increase of residual carrier density, leading to $N_e > 0.11 N_i$. In this situation, it would be difficult to observe the increase of conductivity with decreasing electron density.

3.10.11.1 Conclusions I

- We have investigated transport in graphene in the diffusive regime using a kinetic equation approach. The contribution from electron–hole interband polarization to conductivity was included (it was ignored in all previous studies).
- We found that the conductivity of electrons in graphene contains two terms: one of which is inversely proportional to impurity density, while the other one varies linearly with the impurity density.

3.10.11.2 Conclusions II

- Our numerical calculation for the RPA-screened Coulomb scattering potential and our analytical results for a short-range scattering potential indicate that the *minimum* (rather than "residual") conductivity in the diffusive regime is in the range 4–$5e^2/h$. We also obtained linear dependence of the conductivity on electron density for higher N_e/N_i values.

3.11 Dynamic AC Conductivity

- We have also developed a kinetic equation to investigate the dynamic AC conductivity of graphene due to impurity scattering in the diffusive regime. The effect of *interband coherence* on conductivity is incorporated.

- We find that, when the frequency of the AC electric field is less than a critical value, ω_0, of order of THz, the conductivity has a *minimum* as a function of electron density.
- For $\omega > \omega_0$, the dynamic AC conductivity varies monotonically with electron density.

3.11.1 AC Kinetic Equation Formulation for Current and Distribution Function → $\hat{\rho}$

- The current is expressed in terms of elements of distribution function $\hat{\rho}$ as (**n** is unit vector normal to graphene sheet)

$$\mathbf{J}(T) = g_s \gamma e \sum_{\mathbf{p},\nu} \frac{1}{p} \left\{ \mathbf{p} \left\{ \left[\hat{\rho}_{\mathbf{p}}^{(\nu)} \right]_{11} (T,\mathbf{p}) - \left[\hat{\rho}_{\mathbf{p}}^{(\nu)} \right]_{22} (T,\mathbf{p}) \right\} + 2\,\mathrm{sgn}(\nu)\, \mathbf{p} \times \mathbf{n}\, \mathrm{Im} \left\{ \left[\hat{\rho}_{\mathbf{p}}^{(\nu)} \right]_{12} (T,\mathbf{p}) \right\} \right\}.$$

spin degeneracy

valley index

elements of distribution function

- In the presence of a dynamic AC electric field, $\mathbf{E}(T) = \mathbf{E}_0 e^{-i\omega T}$, the kinetic equation for the linear electric field part of the distribution function, $\hat{\rho}_1^{(\nu)}(\omega, \mathrm{p})$, in frequency representation, is determined by

$$i\omega \left[\hat{\rho}_1^{(\nu)} \right]_{\mu\mu} (\omega, \mathrm{p}) - e\mathbf{E}_0 \cdot \nabla_p \left[\hat{\rho}_0^{(\nu)} \right]_{\mu\mu} (\mathbf{p}) = - \left[\hat{I}_s^{(1)} \right]_{\mu\mu},$$

$$i\omega \left[\hat{\rho}_1^{(\nu)} \right]_{12} (\omega, \mathrm{p}) + 2i\gamma p \left[\hat{\rho}_1^{(\nu)} \right]_{12} (\omega, \mathrm{p}) = - \left[\hat{I}_s^{(1)} \right]_{12},$$

→ scattering terms.

3.11.1.1 AC Kinetic Equation: Solution I

- Solution of the kinetic equation

$$[\boldsymbol{v}_\mu^{(\nu)}(\mathrm{p}) = \nabla_{\mathrm{p}} \varepsilon_\mu^{(\nu)}(\mathrm{p}) = (-1)^{\mu+1} \gamma \mathrm{p}/p],$$

$$\circ \left[\hat{\rho}_1^{(\nu)} \right]_{\mu\mu} (\omega, \mathrm{p}) = e\mathbf{E}_0 \cdot \boldsymbol{v}_\mu^{(\nu)}(\mathrm{p}) \Lambda_\mu^{(\nu)}(\omega, \mathrm{p}),$$

$$\circ \left[\hat{\rho}_1^{(\nu)} \right]_{12} (\omega, \mathrm{p}) = \frac{e\gamma}{p} [\mathrm{E}_0 \times \mathrm{p} \cdot \mathrm{n}] \Phi^{(\nu)}(\omega, \mathrm{p}).$$

- Diffusive regime of validity, $k_F l >> 1$ (*l is diffusion length).*
- Definitions of $\Lambda_\mu^{(s)}$ and $\Phi^{(s)}(p)$ follow.

3.11.1.2 AC Kinetic Equation: Solution II

The functions $\Lambda_{\mu}^{(s)}$ and $\Phi^{(s)}(p)$ can be expressed in terms of microscopically calculated relaxation times $\tau_{\mu}^{(a,b)}(\mathrm{p})$ as

$$\Lambda_{\mu}^{(v)}(\omega,\mathrm{p}) = -\frac{1}{i\omega\tau_{\mu}^{(a)}(\mathrm{p})-1}\left\{\tau_{\mu}^{(a)}(\mathrm{p})\frac{\partial\left\{\left[\hat{\rho}_0^{(v)}\right]_{\mu\mu}(\mathrm{p})\right]}{\partial\varepsilon_{\mu}^{(v)}(\mathrm{p})}\right.$$
$$\left.+\ \mathrm{sgn}(v)\mathrm{Im}[\Phi^{(v)}(\omega,\mathrm{p})]\right\};$$
$$\mathrm{Re}[\Phi^{(v)}(\omega,\mathrm{p})] = 2\tau^{(b)}(\mathrm{p})(\omega+2\gamma\mathrm{p})\mathrm{Im}[\Phi^{(v)}(\omega,\mathrm{p})],$$
$$\mathrm{Im}[\Phi^{(v)}(\omega,\mathrm{p})] = -\mathrm{sgn}(v)\sum_{\mu}\left[\frac{1}{2(i\omega\tau_{\mu}^{(a)}(\mathrm{p})-1)}\frac{\partial\left\{\left[\hat{\rho}_0^{(v)}\right]_{\mu\mu}(\mathrm{p})\right\}}{\partial\varepsilon_{\mu}^{(v)}(\mathrm{p})}\right]$$
$$\times\left[2\tau^{(b)}(\mathrm{p})(\omega+2\gamma\mathrm{p})^2+\frac{1}{2\tau_{\mu}^{(a)}(\mathrm{p})}\right.$$
$$\left.+\sum_{\mu}\frac{1}{2\tau_{\mu}^{(a)}(\mathrm{p})[i\omega\tau_{\mu}^{(a)}(\mathrm{p})-1]}\right]^{-1}.$$

- Thus, the conductivity is given by

$$\mathbf{J}(\omega) = \frac{e^2}{2}g_s\gamma^2\mathbf{E}_0\sum_{\mathrm{p},v}\{[\Lambda_1^{(v)}(\omega,\mathrm{p})+\Lambda_1^{(v)}(\omega,\mathrm{p})]+2\mathrm{sgn}(v)\mathrm{Im}[\Phi^{(v)}(\omega,\mathrm{p})]\},$$

where

$$[\tau_{\mu}^{(a,b)}(\mathrm{p})]^{-1} = \pi N_i\sum\nolimits_k|V(\mathrm{p}-k)|^2\delta[\varepsilon_{\mu}(\mathrm{p})-\varepsilon_{\mu}(k)]A^{(a,b)}(\phi_k),$$
$$A^{(a)}(\phi) = \sin^2\phi,\ \text{and}\ A^{(b)}(\phi) = (1-\cos\phi)^2,$$
$$[\tau^{(b)}(\mathrm{p})]^{-1} \equiv [\tau_1^{(b)}(\mathrm{p})]^{-1}+[\tau_2^{(b)}(\mathrm{p})]^{-1}.$$

3.11.1.3 AC Results and Discussion I

- At zero temperature, $k_{\mathrm{F}} = \sqrt{4\pi N_{\mathrm{e}}/g_{\mathrm{s}}g_{\mathrm{v}}}$
- For a short-range impurity scattering potential model [PRL **92**,256602(2006)]

$$V^{\mathrm{SR}}(q) = \pi\gamma/(2k_{\mathrm{F}}).$$

- Maximum frequency for occurrence of a minimum: $\omega_0 \sim 5\,\text{THz}$

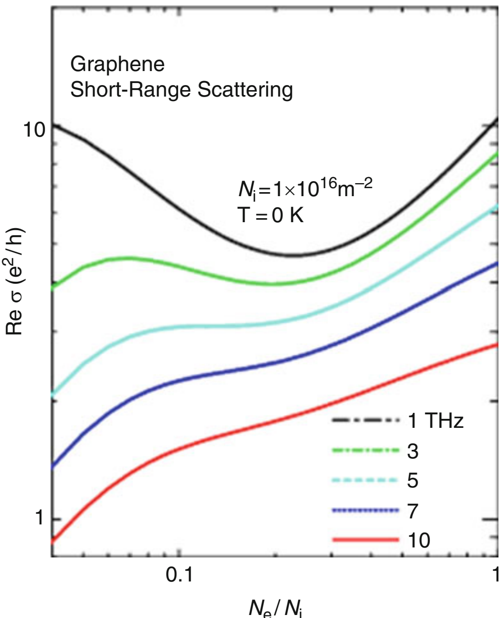

Dynamic AC conductivity as a function of N_e/N_i for several frequencies in the terahertz range (N_e = carrier density, N_i = impurity density).

3.11.1.4 AC Results and Discussion II

- We find that, for $\omega < \omega_0 = 5$ THz, there is a minimum in the electron-density dependence of real part of conductivity in the case of a short-range scattering potential.
- For $\omega > \omega_0$, the real part of conductivity monotonically decreases with decreasing electron density.

3.11.2 Dynamic AC Conductivity

- Sum rules for the optical conductivity have been analyzed by Gusynin et al. [Phys. Rev. B **75**, 165407 (2007)].
- Mishchenko has examined the effect of electron–electron interactions on optical conductivity [Phys. Rev. Lett. **98**, 216801 (2007)].

3.11.2.1 AC Results and Discussion III

- For a RPA-screened model, $V(q) = \frac{e^2}{2\varepsilon_0 \tilde{\kappa}\, \varepsilon(q) q}$,

where

$$\varepsilon(q) = 1 + \frac{q_s}{q} \begin{cases} 1 & if\ q \le 2k_F \\ 1 + \frac{\pi q}{8k_F} - \frac{1}{2}\sqrt{1 - \left(\frac{2k_F}{q}\right)^2} - \frac{q}{4k_F}\sin^{-1}\left(\frac{2k_F}{q}\right) & if\ q > 2k_F \end{cases}.$$

Here, $q_s = 4e^2 k_F/(\hbar\tilde{\kappa}\gamma)$ is the Thomas–Fermi screening wave vector ($\tilde{\kappa}$ is the static background dielectric constant).
[K.W.-K. Shung, Phys. Rev. **B34**, 979 (1986); T. Ando, J. Phys. Soc. Jpn. **75**, 074716 (2006); B. Wunsch et al., New J. Phys. **8**, 318 (2006); E.H. Hwang et al., PRL **98**, 186806 (2007)]

3.11.2.2 AC Results and Discussion IV

- For long-range RPA-screened impurity scattering potential, $\omega_0 \approx 3$ THz.

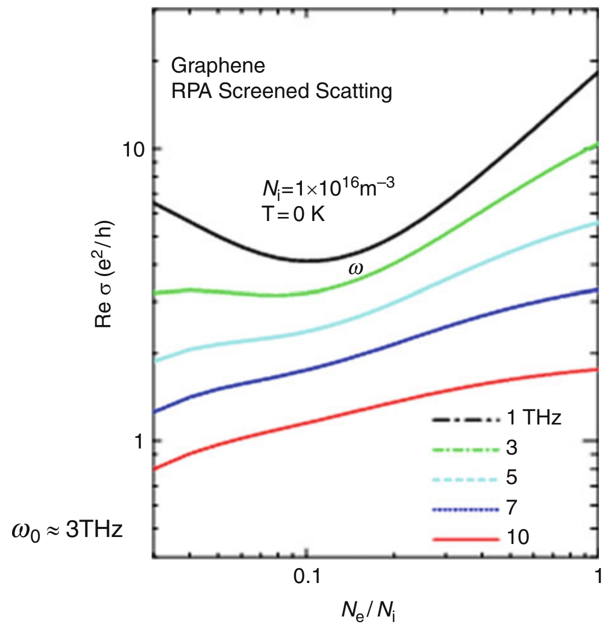

Dynamic AC conductivity as a function of N_e/N_i for several frequencies in the terahertz range, calculated with RPA-screened scattering.

- Maximum frequency for occurrence of a minimum: $\omega_0 \sim 3$ THz.

3.11.3 AC Conclusions

- We have analyzed the dynamic AC conductivity of graphene in the diffusive regime using a kinetic equation approach. Both short-range and long-range RPA-screened electron–impurity scatterings have been considered. The role of electron–hole interband coherence in conductivity has been taken into account.
- When the frequency of the AC electric field is less than a critical value, $\omega < \omega_0$, of order of several THz, the conductivity has a *minimum* as function of electron density. For $\omega > \omega_0$, the dynamic AC conductivity monotonically decreases with decreasing electron density.

3.12 Device-Friendly Features of Graphene I

- Because carbon nanotubes conduct electricity with very low resistance, they have attracted strong interest for use in transistors and other devices.
- But serious obstacles remain for volume production of nanotubes:
  - Inability to produce nanotubes of consistent sizes and consistent electronic properties
  - Difficulty of integrating nanotubes into electronic devices
  - High electrical resistance that produces heating and energy loss at junctions between nanotubes and the metal wires connecting them

3.12.1 Device-Friendly Features of Graphene II

- In graphene, the carrier mobilities *at room temperature* can reach 3,000–27,000 $\mathrm{cm}^2/\mathrm{Vs}$ [Science **306**, 666 (2004); **312**, 1191 (2006)], making graphene an extremely promising material for future nanoelectronic devices. Graphene mobilities up to 200,000 cm^2/Vs have been reached. [P.R.L. **100**, 016602 (2008) "*Electron-Phonon scattering is so weak that, if extrinsic disorder is eliminated, room temperature mobilities* $\sim$200,000 cm^2 */Vs are expected over a technologically relevant range of carrier concentration.*"]
- Since the mean free path for carriers in graphene can reach $L = 400$ nm at room temperature, graphene-based *ballistic* devices seem feasible, even at relaxed feature sizes compared to state-of-the-art CMOS technology.
- Stable to high temperatures $\sim$3,000 K; great strength
- Graphene's *flatness* makes it likely to be amenable to commercial fabrication techniques in the style of the highly developed top-down CMOS compatible process flows, a substantial advantage over carbon nanotubes.

3.12.2 Device-Friendly Features of Graphene III

- Schedin et al. reported that graphene-based chemical *sensors* are capable of detecting minute concentrations (1 part per billion) of various active gases and allow us to discern *individual* events when a molecule attaches to the sensor's surface [cond-mat/0610809].
  - High 2D surface/volume ratio maximizes role of adsorbed molecules as donors/acceptors.
  - High conductivity.
  - Low noise.
  - High sensitivity, detects *single* molecule.

3.12.3 Device-Friendly Features of Graphene IV

- A simple *spin valve* structure has already been fabricated using graphene to provide the spin transport medium between ferromagnetic electrodes [cond-mat/0704.3165].

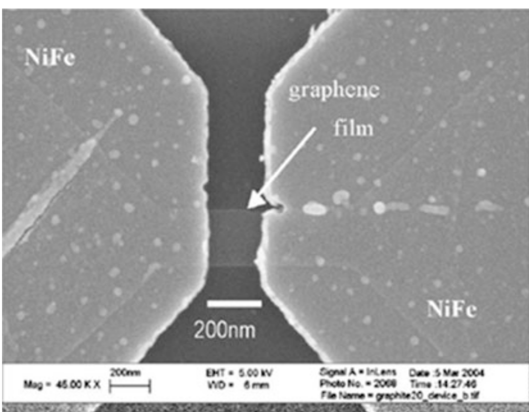

  - Long spin lifetime, low spin/orbit coupling, high conductivity
  - Inject majority spin carriers, increase chemical potential of majority spins
  - Resistivity changes, signal varies with gate voltage [Hill, Geim, Novoselov and Cho, Chen, Fuhrer].

3.12.4 Device-Friendly Features of Graphene V

- J. Scott Bunch et al. demonstrated that graphene in contact with a gold electrode can be used to electrostatically actuate an *electromechanical resonator* [Science 315, 490 (2007)].

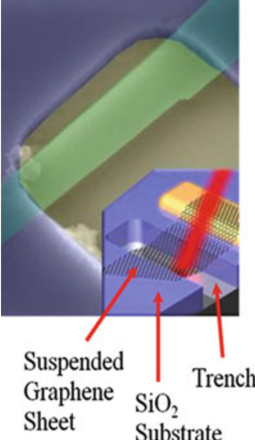

  - 2D graphene sheet suspended over trench in SiO_2 substrate
  - Motion activated by rf gate voltage superposed on dc-V_g (dc gate voltage), applied to graphene sheet
  - Electrostatic force between graphene and substrate results in oscillation of graphene sheet
  - Also, optical actuation by laser focused on sheet, causing periodic contraction/expansion of graphene layer

3.12.5 Device-Friendly Features of Graphene VI

- Using graphene, "proof-of-principle" *FET transistors*, loop devices, and circuitry have already been produced by Walt de Heer's group [http://gtresearchnews.gatech.edu/newsrelease/graphene.htm] [Also, Lemme et al.].
- Quantum interference device using ring-shaped graphene structure was built to manipulate electron wave interference effects.

Acknowledgements It is a pleasure to acknowledge the important contributions of my collaborators:

Prof. S. Y. Liu, Shanghai Jiao Tong University, China and Prof. V. Fessatidis, Fordham University, Bronx, NY.

NJMH gratefully acknowledges partial support of this work by DARPA under grant #HR0011-09-1-0008.

Chapter 4
Functionalization of Graphene Nanoribbons

Haldun Sevinçli, Mehmet Topsakal, and Salim Ciraci

Abstract With the synthesis of a single atomic plane of graphite, namely, graphene honeycomb structure, a new perspective for carbon-based electronics is opened. The one-dimensional graphene nanoribbons (GNRs) have different band-gap values depending on their edge shape and width. In this contribution, we report our results showing that repeated heterostructures of GNRs of different widths form multiple quantum-well structures. The widths of the constituent parts as well as the bandgap, and also the magnetic ground state of the superlattices are modulated in direct space. We provide detailed analysis of these structures and show that superlattices with armchair edge shapes can be used as resonant tunneling devices and those with zigzag edge shape have unique features for spintronic applications. We also discuss another route of functionalizing 2D graphene, 1D GNR, and superlattices with 3d-transition metal (TM) atom adsorption.

4.1 Introduction

Carbon plays a unique role in nature by forming a number of very different structures. It is not only because it is capable of forming complex networks, which are fundamental to organic chemistry, but also due to the seldom properties of its zero-, one-, two-, and three-dimensional allotropes, which are subjects of solid state physics. Its 3D structures (diamond and graphite) have been known since ancient times, whereas the zero (fullerenes) and 1D (carbon nanotubes and linear atomic

S. Ciraci (✉)
Department of Physics, Bilkent University, 06800 Ankara, Turkey

UNAM, Institute of Materials Science and Nanotechnology, Bilkent University, 06800 Ankara, Turkey
e-mail: ciraci@fen.bilkent.edu.tr

H. Ünlü and N.J.M. Horing (eds.), *Low Dimensional Semiconductor Structures*, NanoScience and Technology, DOI 10.1007/978-3-642-28424-3_4,
© Springer-Verlag Berlin Heidelberg 2013

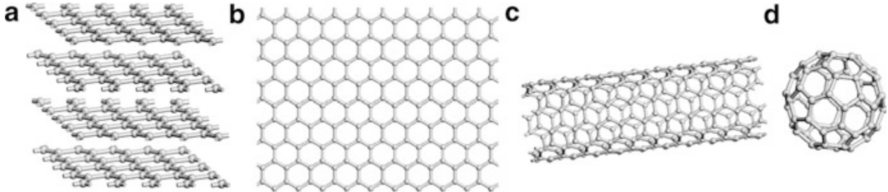

Fig. 4.1 Graphitic carbon allotropes of three, two, one, and zero dimensions (**a**–**d**), respectively

chains) were discovered within the last 10–20 years. The experimental observation of 2D carbon (graphene) has been accomplished only recently [1].

Observation of truly 2D graphene made it necessary to reconsider the existing theories on low-dimensional crystals [2–4]. Despite earlier theories against the existence of perfect 2D crystals, a detailed analysis of the problem beyond the harmonic approximation has led to the conclusion that the interaction between bending and stretching long-wavelength phonons could, in principle, stabilize atomically thin membranes through their deformation in the third dimension. Analysis of the phonon dispersions within the quasi-harmonic approximation shows that 2D and 1D honeycomb structures of Si, Ge, and BN are also stable [5, 6].

The 2D honeycomb structure of graphene plays a crucial role for understanding other graphitic forms (Fig. 4.1), and the electronic properties of graphene are governed by the binding characters of its orbitals. A σ bond is formed between neighboring carbon atoms by sp^2 hybridization between one s-orbital and two p-orbitals. The remaining p-orbitals are perpendicular to the graphene plane and they form covalent bonds leading to a π-band.

Graphene is a zero bandgap semiconductor with linear dispersion of bands near the Fermi level. This particular dispersion gives rise to the lower energy excitations to behave as massless Dirac fermions with an effective speed of light v_F–10^6 m/s. Hence, at low energies, unusual properties of quantum electrodynamics are expected to be observed on graphene lattice. One of the interesting features of Dirac fermions is the deterministic (unit probability) transmission through tunneling barriers of arbitrary width and height when incident normally. This counterintuitive property of ultra-relativistic particles, known as Klein paradox, was previously attributed only to exotic phenomena such as black hole evaporation; now graphene serves as a basis to verify these [7].

Besides its unusual properties, graphene is a candidate for a large number of applications and has the potential to offer new concepts in materials research and fundamental science [8, 9]. A variety of methods have been proposed or demonstrated in order to functionalize graphene-based materials for new device applications [10–20] such as hydrogen storage media [10, 11], gas sensors [12], spin-valve devices [13–17], transistors [18, 19], and resonant tunneling devices [20].

In this chapter, we present our work on functionalization of graphene nanoribbons (GNRs). The methods used are the empirical tight binding method and density functional theory (DFT) [29] (see Appendix A for details of DFT calculations).

Below, we first present a review of fundamental electronic and magnetic properties of graphene and GNRs, which will form a basis for the following sections, where we analyze the superlattice structures of armchair and zigzag GNRs. We also discuss the effects of adsorbed Ti atoms on the electronic and magnetic properties. We conclude this chapter with our findings.

4.2 Electronic and Magnetic Properties of 2D and 1D Graphene

4.2.1 Electrons in Honeycomb Lattice

The hexagonal lattice of graphene and its reciprocal lattice are shown in Fig. 4.2a and b. The lattice vectors are $a_1 = a(\sqrt{3}/2, 3/2)$ and $a_2 = a(-\sqrt{3}/2, 3/2)$ with $a = 1.42$ Å being the nearest neighbor distance. Correspondingly, the reciprocal lattice vectors are $b_1 = 2\pi/3a(\sqrt{3}, 1)$ and $b_2 = 2\pi/3a(-\sqrt{3}, 1)$. The corners of the first Brillouin zone, $K = 2\pi/3a(1/\sqrt{3}, 1)$ and $K' = 2\pi/3a(-1/\sqrt{3}, 1)$ are of particular importance for the physics of graphene. These points are called the Dirac points close to which the energy dispersion becomes linear as it will be discussed below.

The tight-binding Hamiltonian has the simple form

$$H_{\mathrm{TB}} = -t \sum_{<i,j>\alpha\sigma} (c^{+}_{i\,\alpha\,\sigma} c_{j\,\alpha'\,\sigma} + H.c.),$$

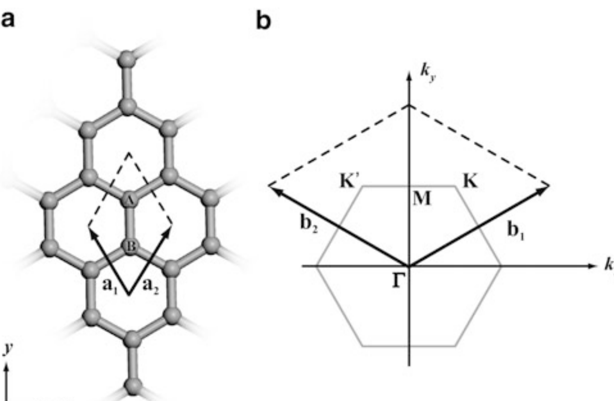

Fig. 4.2 (**a**) The lattice structure and the unit cell vectors of graphene. A and B atoms belong to different sublattices. (**b**) The corresponding Brillouin zone and the special k-points **r**, **M**, **K**, and **K′**

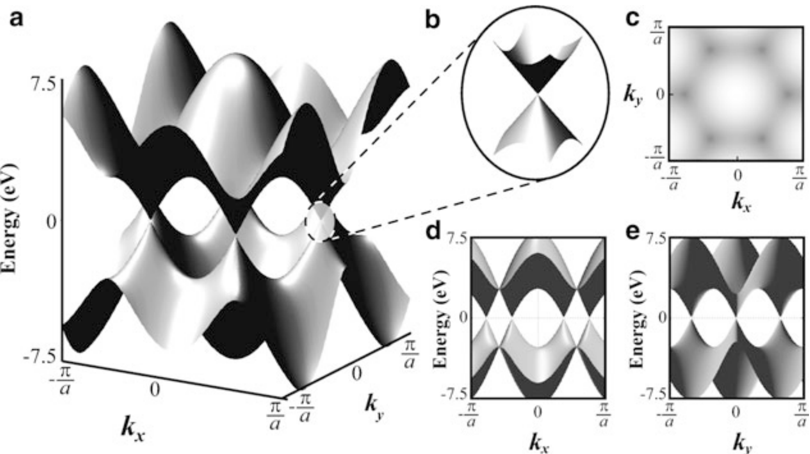

Fig. 4.3 The full band structure of graphene for $-\pi/a < kx, ky < \pi/a$ (**a**), and a zoom in of the band structure close to one of the Dirac points (**b**). (**c**) Two dimensional map of the conduction band. *Darker* regions indicate lower energy. (**d–e**) The full band structure from special view points corresponding to the band structures along the k_x- and k_y-directions. The k_x-direction can be named as the zigzag direction, and the k_y-direction as the armchair direction, and the *ky*-direction as the armchair direction in accordance with Fig. 4.2a (See also Figs. 4.5 and 4.6)

where $c^{+}_{i\,\alpha\,\sigma}(c_{i\,\alpha\,\sigma})$ creates (annihilates) an electron on site R_i with spin σ on the α sublattice, with α = A or B. The nearest neighbor ($\langle i, j\rangle$) hopping energy is $t \simeq 2.7$ eV [21]. The energy bands obtained from this Hamiltonian have the form

$$E_{\pm}k = \pm t\sqrt{3 + f(k)}$$

with

$$f(k) = 2\cos(\sqrt{3}k_x a) + 4\cos\left(\frac{\sqrt{3}}{2}k_x a\right)\cos\left(\frac{3}{2}k_y a\right),$$

where the plus sign applies to π−, and the minus sign to the π*-bands. Evidently, the above bands satisfy electron-hole symmetry by being symmetric around the zero of the energy. The full band structure of graphene obtained from the tight-binding Hamiltonian is shown in Fig. 4.3a. In Fig. 4.3b a zoom-in of the band structure to one of the Dirac points is shown. Figure 4.3d and e shows the band structure from two special view points.

The energy dispersions can be expanded around K (or K') as $E_{\pm} \sim \pm h v_{\mathrm{F}}|q|$ [22, 23]. Here, the Fermi velocity is $v_{\mathrm{F}} = 3ta/2\hbar$ and $k = K + q$ with $|q| << |K|$, which enables us to write $f(k) = -3 + 9a^2(q_x^2 + q_y^2)/4$. In contrast to the usual case where $v = \sqrt{2E/m}$, the Fermi velocity of low-energy electrons of graphene does not depend on energy or momentum, which is the source of unusual effects.

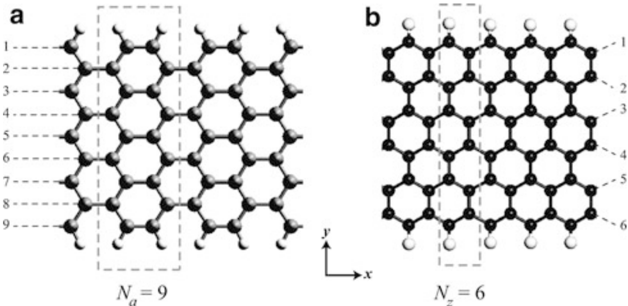

Fig. 4.4 Lattice structures of (**a**) AGNR(9) and (**b**) ZGNR(6). Unit cells of the structures are delineated, x-axis points the growth direction. The number $N_a = 9$ stands for the number of dimer lines while $N_z = 6$ stands for the number of zigzag chains along the x-direction

4.2.2 Electronic and Magnetic Properties of GNRs

The electronic structure and magnetic properties of GNRs are primarily determined by their edge shapes and their widths [24–28]. Their electronic structures also depend on whether the dangling bonds of the edge atoms are passivated or not. In this section, all the GNRs considered are those passivated with hydrogen. In Fig. 4.4a and b, the lattice structures and the unit cells of GNRs with armchair and zigzag edge shapes, respectively, are shown. Following the current literature, we denote GNRs having armchair edge shape with N_a dimer lines in the unit cell as AGNR(N_a), and those having zigzag edge shape with N_z zigzag chains in the unit cell as ZGNR(N_z).

DFT calculations show that AGNRs are direct bandgap semiconductors and their band gaps follow three curves depending on their width, namely, N_a [17]. For a given nonnegative integer n, $N_a = 3n + 1$ yields the highest bandgap whereas $N_a = 3n - 1$ yields the lowest, $N_a = 3n$ lying in between as shown in Fig. 4.5. As n increases, all three curves approach zero without crossing each other.

Although tight-binding calculations predict a zero bandgap for all ZGNRs [24] [e.g., Fig. 4.6a], DFT calculations show that all ZGNR are semiconductors and their bandgaps decrease monotonically with N_z, for $N_z > 4$ [45]. For all N_z values the highest valence band and the lowest conduction band give rise to a high density of states near the Fermi energy. These states are localized at the edges of the ZGNR and this give rise to an antiferromagnetic (AFM) ground state. Eventually, it is possible to express this magnetic transition by adding an on-site Hubbard term to the tight-binding Hamiltonian as

$$H_{\mathrm{TB}} = -t \sum_{<i,j>\alpha\sigma} (c^{+}_{i\alpha\sigma} c_{j\alpha'\sigma} + H.c.) + U \sum_{i,\alpha} c^{+}_{i\alpha\sigma} c_{i\alpha\sigma} c^{+}_{i\alpha\sigma'} c_{i\alpha\sigma'}$$

where is the on-site repulsion energy (26).

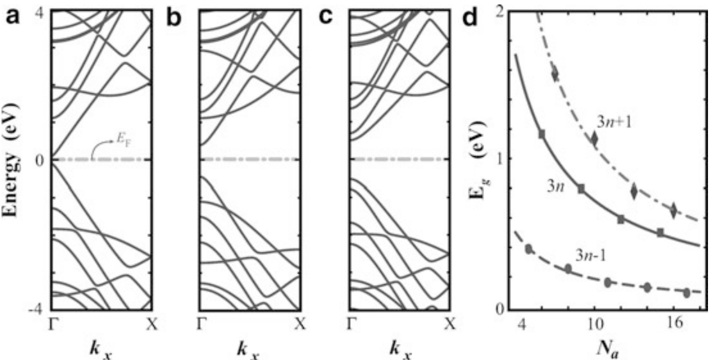

Fig. 4.5 Band structures of AGNRs belonging to different families: (**a**) $N_\mathrm{a} = 3n - 1 = 8$, (**b**) $N_\mathrm{a} = 3n = 9$, and (c) $N_\mathrm{a} = 3n + 1 = 10$. (**d**) Bandgaps of the families as a function of N_a. Band structures are obtained using plane-wave DFT calculations, zero of the energy is set to E_F (Reproduced from Ref. [20])

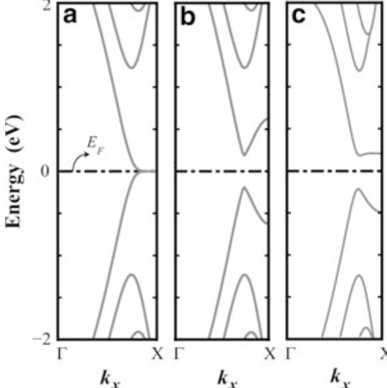

Fig. 4.6 Band structures of ZGNR(8) calculated by using three different methods: (**a**) tight-binding bands, (**b**) tight-binding bands including Hubbard correction within mean field approximation, where $U = 1.3\,\mathrm{eV}$, and (**c**) bands obtained from plane-wave DFT calculations. Zero of the energy axis is set to E_F

This Hamiltonian can be solved in the mean field approximation numerically. While the tight binding solution of the ZGNR Hamiltonian in the absence of Hubbard term yields a zero band gap semiconductor, upon inclusion of the Hubbard term ZGNR is found to be a direct band gap semiconductor (Fig. 4.6b) with edge states localized at the opposite edges having opposite spins. Such a magnetic solution of the Hubbard Hamiltonian for bipartite lattices was previously proved by Lieb [30], and these results are also verified by DFT calculations as shown in Fig. 4.6c.

4.3 Functionalization Through Superlattice Formation

The remarkable properties of GNRs discussed above, especially their bandgaps varying with their widths, suggest that the heterostructures formed by the segments of GNRs with different widths may have interesting electronic and magnetic properties. Here, the crucial issues to be addressed are how the electronic structure will be affected from the discontinuity of crystal potential at the junction; what the character of the band discontinuity and the resulting band alignment will be; and whether these discontinuities will result in confined states. In this section, we address these questions for both armchair and zigzag GNR superlattices (AGSL and ZGSL, respectively), and investigate the new functions which graphene-based materials can acquire upon size modulation.

4.3.1 Superlattices of Armchair Graphene Nanoribbons

Relative to the longitudinal axis in the armchair direction, one can distinguish three possible angles to make junctions with armchair or zigzag edge shapes as shown in Fig. 4.7a. A 60° angle gives rise to the armchair edge at the interface, whereas 30° and 90° angles result in zigzag edges. Some of the possible superlattice shapes are given in Fig. 4.7b–d.

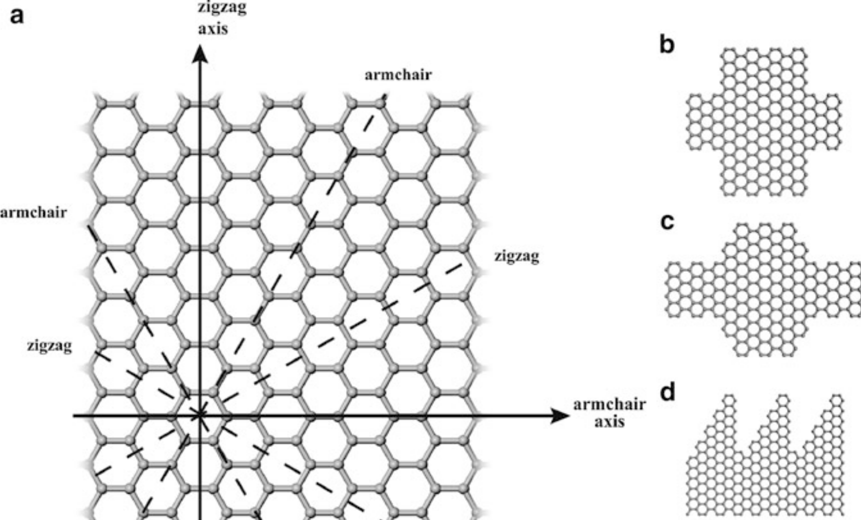

Fig. 4.7 (**a**) Crystallographic directions giving rise to armchair and zigzag edge shapes. Possible junction angles leading to armchair or zigzag edge shapes are indicated. 60° angle with the horizontal (armchair) axis results in armchair edge at the interface, whereas 30° and 90° give zigzag edges. Some of the possible superlattice shapes are shown, namely, (**b**) sharp rectangular, (**c**) smooth, (**d**) and sawtooth-like

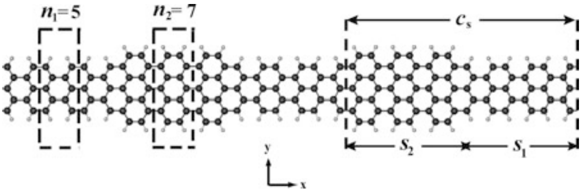

Fig. 4.8 Atomic structure of AGSL ($n_1 = 5$, $n_2 = 7$; $s_1 = 3$, $s_2 = 3$). The superlattice unit cell and primitive unit cell of each segment are delineated (Reproduced from Ref. [20])

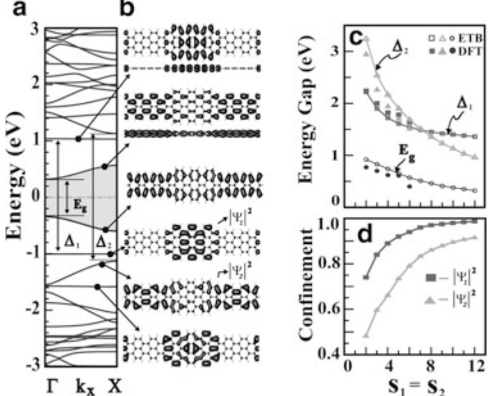

Fig. 4.9 Electronic structure of AGSL(5,7,3,3). (**a**) Band structure with flat bands corresponding to confined states. (**b**) Isosurface charge density of propagating and confined states. (**c**) Variation of various superlattice gaps with $s_1 = s_2$. (**d**) Confinement of states versus $s_1 = s_2$ calculated by ETB. All data except those in (**d**) are calculated by using first-principles method within DFT (Reproduced from Ref. [20])

In order to avoid mixed edge shapes, we focus on the junctions with smooth interfaces making 60° angle with the armchair axis. We first consider a superlattice AGSL(n_1,n_2;s_1,s_2) made by the segments of AGNR(n_1) and AGNR(n_2). Here, s_1 and s_2 specify the lengths (in terms of the number of GNR unit cells) of the segments having different widths. Figure 4.8 shows the superlattice AGSL(5,7;3,3). AGNR(5) and AGNR(7) are direct bandgap materials with bandgaps of 0.39 and 1.57 eV, respectively. The combined heterostructure with a symmetric junction has a bandgap of 0.65 eV. The band structure of segments and the supercell is shown in Fig. 4.9. Junction formation by these constituents gives rise to dramatic changes in the band structure of the superlattice. While the highest valance and the lowest conduction bands are dispersive, the bands below and above the dispersive ones are simply flat. The isosurface charge density plots distinguish the different characters of these bands. For example, as highest valence band states propagate across the superlattice, the states of the second (flat) band are confined to the wider part of AGSL(5,7;3,3) consisting of AGNR(7) segment. These flat band states are identified as *confined states*.

The confined states have been treated earlier in commensurate or pseudomorphic junctions of two different semiconductors, which form a periodically repeating superlattice structure. These superlattices have grown layer by layer and they form a sharp lattice matched interface [31–33]. Owing to the band discontinuities at the interface, they behave as a multiple quantum-well structure, obeying the effective mass theory. Generally, a particular state, which is propagating in one region (or segment), is confined if it cannot find a matching state in the adjacent region having the same energy. For a superlattice of small n_1 or n_2, spacings between energy levels are significant and, hence, localization of states in one of the regions is more frequent. This argument, which is relevant for superlattices of long constituent segments, may not be valid for short segments (i.e., small s_2 and s_2).

2D conduction band electrons (valence band holes), confined to the well, display a number of electronic and optical properties. In the present case, both the bandgap and the size (width) of the graphene ribbon are periodically modulated in direct space and the carriers are 1D. On the other hand, the atomic arrangement and lattice constants at both sides of the junction are identical; the heterocharacter concerns only the width of the ribbons at different sides. Electronic and transport properties of graphene multiple quantum-well structures can be controlled by a number of structural parameters. In addition to n_1, n_2, s_1, s_2, symmetry of the junction, $\Delta n = n_2 - n_1$, even–odd disparity of $n_1/2$ and $n_2/2$, type of the interface between two different ribbons and the shape of the superlattice (namely sharp rectangular or smooth wavy) influence the properties. As shown in Fig. 4.10, superlattice bandgaps decrease as s_1 increases from 3 to 8. This is a clear evidence for quantum size effect. In terms of the weight of the states in the segment s_2, i.e., $\int_{s_2} |\Psi(r)|^2 \mathrm{d}r$, we see that the confinement of states increases with increasing s_1; but it disappears for $s_1 = s_2 = 1$. Confinement increases with increasing $s_1 = s_2$, and hence with increasing barrier width, since the penetration of states into the barrier decreases). For example, AGSL(5,7;s_1,s_2) has $E_\mathrm{g} = 0.66, 0.48, 0.38, 0.32, 0.27$ eV for $s_2 = 3$ and $s_1 = 3, 4, 5, 6, 7$, respectively. Conversely, $E_\mathrm{g} = 0.72$, 079, 0.83, 0.84 eV for $s_1 = 3$ and $s_2 = 4, 5, 6, 7$, respectively. On the other hand, the energy of the flat-band states confined to s_2 and their weight are practically independent of s_1.

We also investigate the effects of changing n_1 from 7 to 9. Two nanoribbons containing 10 and 18 carbon atoms in their unit cell are merged. Variation of $\Delta n = n_1 - n_2$ results in a wide variety of electronic structures. For example, in contrast to AGSL(5,7;3,3), the highest valence and lowest conduction bands of AGSL(5,9;3,3) are flat bands with $E_\mathrm{g} = 0.70$ eV; dispersive bands occur as second valence and conduction band, having a gap of 1.18 eV between them. Since the first valence and conduction bands are confined in a wider region of the structure, this ribbon can act as a resonant tunneling double barrier (RTDB) device. The narrow regions act as a barrier and wider region as a quantum well. We have complete confinement of charges for some of states in the wider region. On the other hand, the states that are mostly confined in narrower region can penetrate to the wider regions. The variation of s_1 for AGSL(5,9;s_1,s_2) family has similar consequences to the AGSL(5,7;s_1,s_2). Again, we see that the confinement of states increase with increasing s_1. As shown in Fig. 4.11a–c superlattice bandgaps decrease as s_1

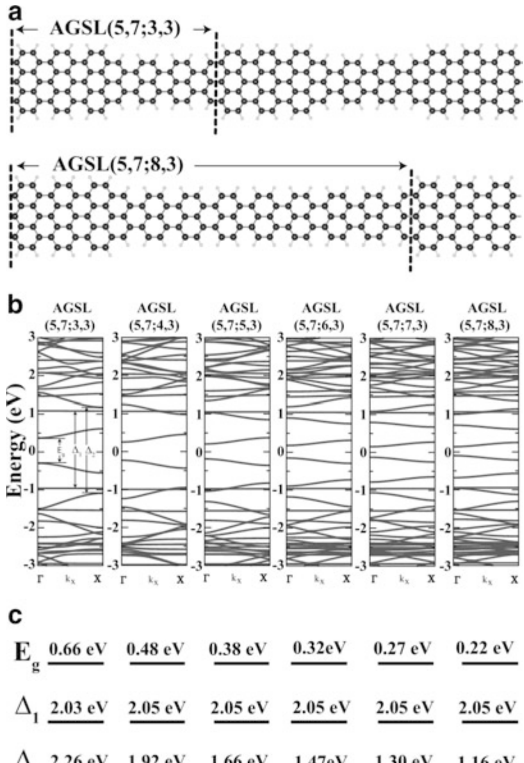

Fig. 4.10 The effect of the variation of length of the narrower region s_1 of AGSL (5,7; s1,3) from $s_1 = 3$–8. Note that the narrower region is acting like a barrier for the confined state. (**a**) Atomic structure and superlattice unit cell. (**b**) The variation of band structures. (**c**) The numerical values for energy gaps E_g, Δ_1, and Δ_2. E_g is the actual bandgap of the structure, which comes from a dispersive state. Δ_1 is the bandgap of highest localized state while Δ_2 is the bandgap for the next dispersive state. The energy of the flat-band states related to Δ_1 is confined to s_2 and their weights are practically independent of s_1. Calculations are carried out by using first-principles plane-wave methods within DFT (see Appendix A) (Reproduced from Ref. [20])

increase from 3 to 7. On the other hand, the energy of the flat-band states confined to s_2 and their weight are practically independent of s_1. As shown in Fig. 4.11d–f, the band gaps of localized conductance and valence states decrease with the increase in s_2. These findings reveal that charge confinement in size-modulated GNRs is closely related with the structural parameters of heterostructure.

In Fig. 4.12, we demonstrate that the confined states can occur not only in narrow (small n_1 and n_2) but also in wide superlattices having significant modulation of the width. The above trends corresponding to small n_1 and n_2 become even more interesting when n_1 and n_2 increase. The electronic band structure of AGSL(n_1,n_2;s_1,s_2) with $n_1 = 21$ or 41, but $n_2 > n_1$ and $s_1 = s_2 > 3$ calculated using ETB method shows that for small Δn, confinement is weak and bands are dispersive, but confinement increases as Δn increases. Interestingly, E_g of AGSL($n_1 = 21, n_2; 3, 3$) is, respectively, 0.46, 0.12, 0.49, and 0.04 eV for $n_2 = 23$, 25, 27, and 29. In ETB method used here, the Bloch states having band index 1 and wave vector k are expressed in terms of the linear combination of the orthonormalized Bloch sums $\chi_i(k,r)$ constructed for each atomic orbital p_z localized at different carbon atoms, i, with the proper phase of k, namely, $\Psi_l(k,r) = \sum_i a_{i,l}(k)\chi_i(k,r)$. Accordingly, the contribution of the orbital at site

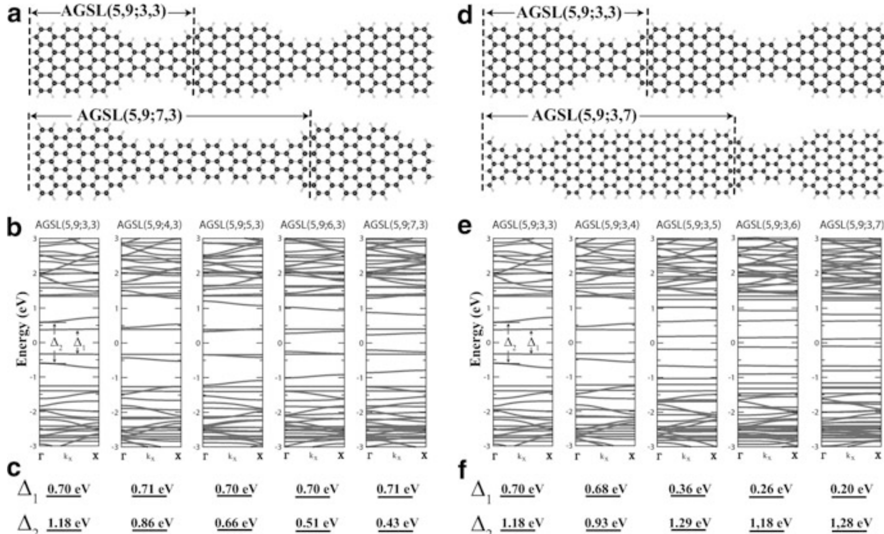

Fig. 4.11 Variation of energy band structure with superlattice parameters for AGSL(5,9,s_1,s_2) is investigated. $s_2 = 3$ is kept fixed while s_1 is varied from 3 to 7 (**a**–**c**), and then $s_1 = 3$ is kept fixed while s_2 is varied from 3 to 7 (**d**–**f**). Highest valence and lowest conduction bands of AGSL(5,9;3,3) are confined at the wider region. So their energies are practically insensitive to the length s_2 of the narrow region (**b**). But the spatial extend of the wave functions of these states influence their energies so that the band gap closes as s_2 is increased (**e**). Calculations have been performed using DFT method (see Appendix A).

i to the normalized charge density of $\Psi_l(k, r)$ is given by $\rho_i = \left|\sum_l a_{i,l}(k)\right|^2$. In Fig. 4.12, ρ_i is scaled with the radius of circles located at atomic site i.

The electronic properties are also strongly dependent on whether the geometry of the superlattice is symmetric (having a reflection symmetry with respect to the superlattice axis along the x-direction) or saddle (one side is straight, other side is periodically carved), all having the same Δn. While the saddle structure of AGSL(5,9;3,3) has the largest direct gap between dispersive conduction and valence bands, its symmetric structure has the smallest gap, but with the largest number of confined states. Horn-like smooth connection between wide and narrow segments (where the ribbon is carved from both sides smoothly and symmetrically) may give rise to adiabatic electron transport and focused electron emission [34].

4.3.1.1 Resonant Tunneling Double Barrier Device

In this section, we focus on a finite segment (flake) of GNR and calculate its transport properties. In accordance with the results of the previous section, we investigate the effect of confinement on transport properties upon modulation of the

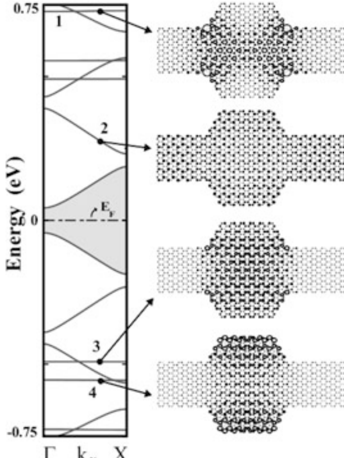

Fig. 4.12 Energy band structure of the AGSL(17,35;11,9) superlattice and the charge densities of selected bands. As seen clearly, states associated with flat bands 1, 3, and 4 are confined but the state with dispersive band indicated by 2 is propagating. Calculations have been performed using ETB method (Reproduced from Ref. [20])

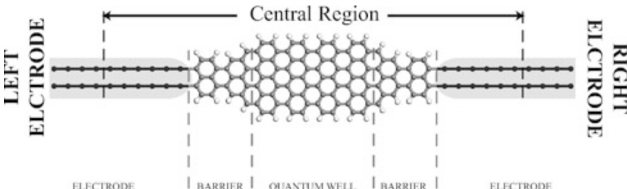

Fig. 4.13 Resonant tunneling double barrier device consisting of AGNR(5) and AGNR(9) segments. Parts of electrodes are included at both sides of AGNR segment as parts of the central device (Reproduced from Ref. [20])

ribbon width. We consider a finite armchair graphene nanoribbon with AGNR(5) and AGNR(9) as constituent parts having a total length of 8 unit cells, as shown in Fig. 4.13. Such a device is relevant for applications and uses the highest occupied molecular orbitals (HOMO) and lowest unoccupied molecular orbitals (LUMO) confined in the wide region.

Recently, patterning of GNRs [35], and also GNRs with varying widths [36, 37] are achieved, and it is shown experimentally that transport through GNRs is primarily influenced by the boundary shape [35]. These experiments reveal the importance of charge confinement effects on the conductance. Moreover, a suppression of conductance of GNRs by Coulomb blockade due to formation of multiple quantum dots in series, which are likely to form during the etching process, is also reported [37]. These facts support our idea that construction of a double

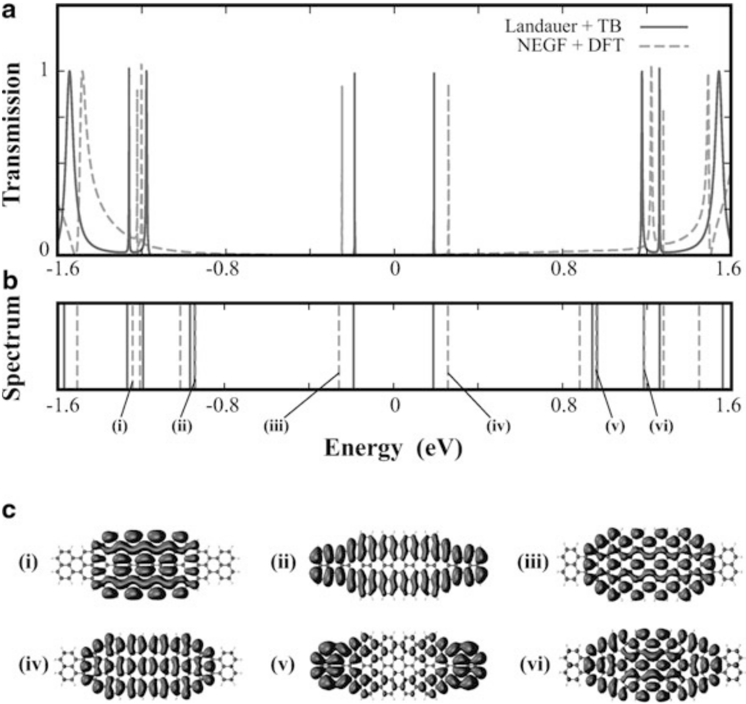

Fig. 4.14 (**a**) Transmission coefficient versus energy calculated under zero bias. Zero of the energy axis is set to the Fermi level. *Solid* curve stands for the DFT-based calculation whereas the *dashed* curve represents the ETB-based result within Landauer approach. (**b**) The energy spectrum of the uncoupled AGNR segment. (**c**) Charge densities of selected energy levels of the uncoupled AGNR segment indicating confined versus extended states (Reproduced from Ref. [20])

barrier device by modulating the width of a nanoribbon is realizable experimentally. For our quantum transport calculations, we consider generic metallic electrodes of two widely separated (weakly coupled) monatomic carbon chains. Carbon chains are known to have high cohesive energy and axial strength, and exhibit stability even at high temperatures [42]. Because of their flexibility and reactivity, carbon chains are suitable for structural and chemical functionalizations, and they are good metals with two quantum conductance channels, which make 4 units of quantum conductance at the Fermi level for the electrodes that we consider. Six principal layers of electrodes are included at both sides of resonant tunneling double barrier (RTDB) as parts of the central device. Metallic electrodes make perfect contacts with the central RTDB device. The transmission coefficient T reflects the combined electronic structure of central RTDB device, electrodes, and their contacts as shown in Fig. 4.14a.

The HOMO, LUMO and other confined states are identified through the energy level diagram [see Fig. 4.14b] and the isosurface charge density plots, obtained from plane wave *ab initio* calculations [see Fig. 4.14c]. The confined states give

rise to sharp peaks originating from resonant tunneling effect. States extending to the whole RTDB are coupled with the states of electrodes, and they are shifted and contributed broader structures in the transmission curve.

The resonant tunneling effect is not affected by the width of the barrier regions [namely, narrow AGNR(5) segments in Fig. 4.13a], considerably. The confined LUMO and HOMO states are weakly sensitive to the length of the barriers. This feature of confined states can also be observed from the energies of confined states (flat bands) of Fig. 4.11; for tunneling transport, wider barriers mean exponentially lower coupling between the quantum well region and the electrodes, which result in even sharper peaks at approximately the same energies.

4.3.2 Superlattices of Zigzag Graphene Nanoribbons

In this section, first-principles plane wave calculations [50] within DFT [29] using projector augmented wave (PAW) potentials [47] are performed (see Appendix A) to show that periodically repeated junctions of segments of zigzag ribbons with different widths can form stable superlattice structures. The energy bandgap and magnetic state of the superlattice are modulated in the real space. Edge states with spin polarization can be confined in alternating quantum wells occurring in different segments of ribbons. Even more remarkable is that the AFM ground state can be changed to ferrimagnetic (FRM) one in asymmetric junctions.

Zigzag graphene ribbons, i.e., ZGNR(N_z) with N_z zigzag chains in its unit cell, are characterized by the states at both edges of ribbon with opposite spin polarization [24]. These edge states attribute an AFM character (see Sect. 4.2). Under applied electric field the ribbon can become half-metallic [16].

We consider segments of two zigzag ribbons of different widths and different lengths, namely ZGNR(N_{z1}) and ZGNR(N_{z2}), which can make superlattice structures [32] with atomically perfect and periodically repeating junctions. Normally, the superlattice geometry can be generated by periodically carving small pieces from one or both edges of the nanoribbons [43]. Typical superlattices and their structural parameters are schematically described in Fig. 4.15. ZGNR(N_{z1})/ZGNR(N_{z2}) superlattices can be viewed as if a thin slab with periodically modulated width in the xy-plane. The electronic potential in this slab is lower ($V < 0$) than outside vacuum ($V = 0$). Normally, states in this thin potential slab propagate along the x-axis; but the propagation of specific states in ZGNR(N_{z2}) is hindered by the potential barrier above and below the narrow segment, ZGNR(N_{z1}). Eventually, these states are confined to the wide segments, and in certain cases also to the narrow segments. Here, the confinement of the states has occurred due to the geometry of the system. Defining the confinement in a segment i as $\int_i |\Psi(r)|^2 \mathrm{d}r$, the sharper the interface between ZGNR(N_{z1}) and ZGNR(N_{z2}) the stronger becomes the confinement.

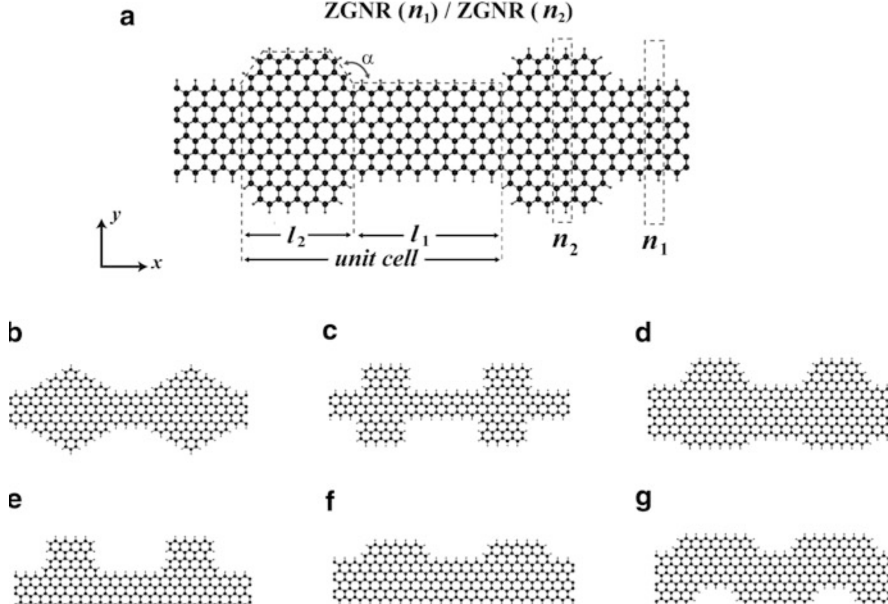

Fig. 4.15 Typical superlattice structures of zigzag graphene ribbons, ZGNR(N_{z1})/ZGNR(N_{z2}). N_{z1} and N_{z2} are the number of zigzag chains in the longitudinal direction; l_1 and l_2 are lengths of alternating ZGNR segments in numbers of hexagons along the superlattice axis. a is the angle between the x-axis and the edge of the intermediate region joining ZGNR(N_{z1}) to ZGNR(N_{z2}). $a = 120°$ or $90°$ for (**b**–**g**). *Dark-large balls* and *small-light balls* indicate carbon and hydrogen atoms, respectively (Reproduced from Ref. [14])

We show a symmetric superlattice ZGNR(4)/ZGNR(8) in Fig. 4.16. Spin-up and spin-down edge states at the top of the valence band of AFM superlattice are confined to the opposite edges of the narrow segments of the superlattice. Normal flat band states near -1.2 eV are confined to the wide segments of ZGNR(8). The energy band structure of the superlattice is dramatically different from those of the constituent nanoribbons. If the lengths of the segments are sufficiently large, these segments display the bandgap of the corresponding infinite nanoribbon in real space. The total magnetic moment of spin-up and spin-down edge states is zero in each segment, but the magnetic moment due to each edge state is different in adjacent segments. As a result, the superlattice remains to be an AFM semiconductor, but the magnitudes of the magnetic moments of the edge states are modulated along the x-axis. The coupling between the magnetic moments localized in the neighboring segments is calculated to be 15 meV per unit cell. The modulation of magnetic moments can be controlled by the geometry of the superlattice. For example, as shown in Fig. 4.16d, the magnetic moments of the atoms in the wide segment are practically zero and, hence, the superlattice is composed of AFM and nonmagnetic (NM) segments. However, as $l_2 \to 10$ the magnetic moments of the edge atoms at the wide segment become significant.

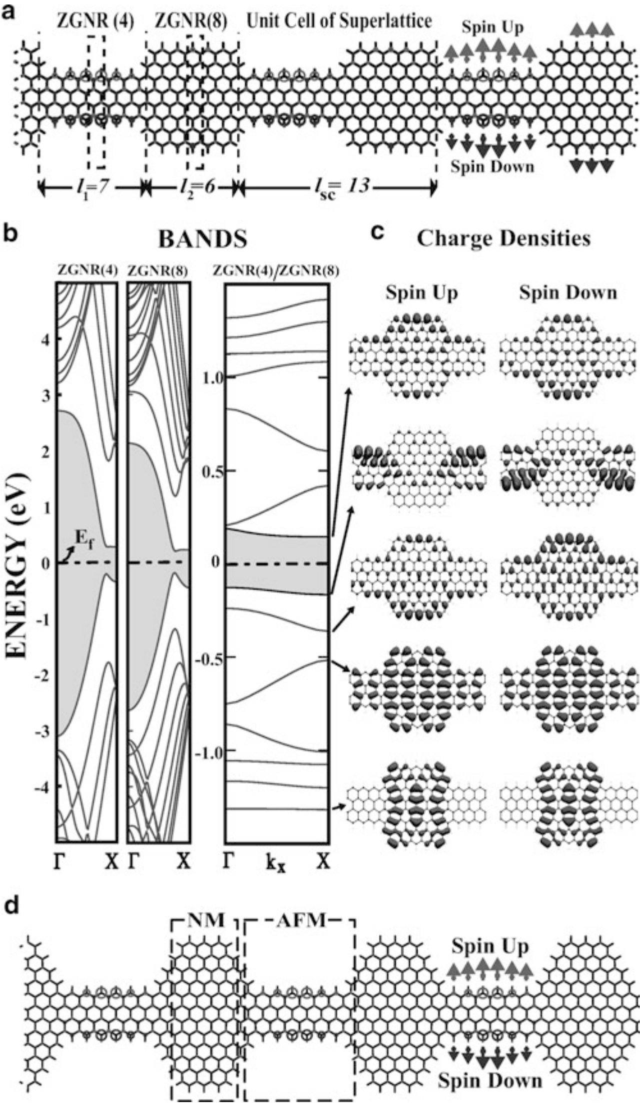

Fig. 4.16 (**a**) A schematic description of the symmetric ZGNR(4)/ZGNR(8) superlattice with relevant structural parameters. Magnetic moments on the atoms are shown in the *left* cell by *dark* and *light circles* and *arrows* for positive and negative values. l_{sc} is the length of the superlattice unit cells in terms of number of hexagons along the x-axis. (**b**) Energy band structures of antiferromagnetic (AFM) ZGNR(4), ZGNR(8) ribbons and AFM ZGNR(4)/ZGNR(8) superlattice. (**c**) Charge density isosurfaces of specific superlattice states. Zero of the energy is set to Fermi level, E_F. The gap between conduction and valence bands are shaded. (**d**) A specific form of superlattice ZGNR(4)/ZGNR(12) with alternating AFM and nonmagnetic (NM) segments in real space. Calculations have been performed using DFT method (see Appendix A) (Reproduced from Ref. [14])

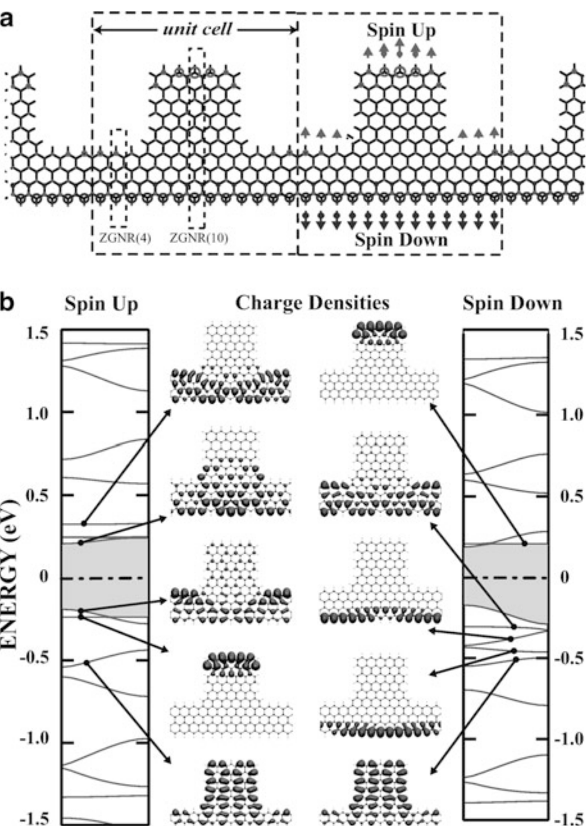

Fig. 4.17 (**a**) A schematic description of an asymmetric ZGNR(4)/ZGNR(10) superlattice. Total majority and minority spins shown by *light* and *dark circles* (for spin-up and spin-down, respectively) attribute a ferrimagnetic (FRM) behavior. (**b**) Energy band structure of the FRM semiconductor and charge density isosurfaces of specific propagating and confined states of different spin polarization. Calculations have been performed using DFT method (see Appendix A) (Reproduced from Ref. [14])

Asymmetric superlattice structure shown in Fig. 4.17 is even more interesting. While the spin-down states remain propagating at the flat edge of the superlattice, spin-up states are confined predominantly at the opposite edge of the wide segments. Confinement of states and absence of reflection symmetry breaks the symmetry between spin-up and spin-down edge states. Hence, the superlattice formation ends up with a FRM semiconductor having different bandgaps for different spin states. In agreement with Lieb's theorem [30, 44], the net magnetic moment calculated to be 2 is equal to the difference of the number of atoms belonging to different sublattices. Flat bands at the edges of spin-up valence band and spin-down conduction band are of particular interest. The spin states of these bands are confined to the discontinuous

edges of the wide segment, which behave as a quantum well. Since a device consisting of a finite size superlattice connected to two electrodes from both ends has high conductance for one spin direction, but low conductance for the opposite one, it operates as a spin valve. Moreover, spin-down electrons injected to this device are trapped in one of the quantum wells generated in a wide segment. As a final remark, we note that the DFT method underestimates the bandgaps found in this work [45]. However, this situation does not affect our conclusions in any essential manner.

4.4 Functionalization Through TM-Atom Doping

Another route in functionalization of graphene-based materials is adsorbing TM atoms on them. In this section, we present results of *ab initio* total energy DFT calculations concerning the equilibrium geometries, electronic and magnetic properties of 3d TM atom adsorbed graphene, AGNR, and AGSL.

We first investigate the binding energies and minimum energy geometries of either (2×2) or (4×4) unit cell of graphene when a Ti, Co, Fe, Cr, or Mn atom adsorbed. Three different sites are considered for adsorption to a (2×2) unit cell which are the hollow site (H) above the center of a hexagon, the bridge site (B) over a carbon–carbon bond, and the top site (T) over a carbon atom. H-site is the minimum energy site for Ti, Co, Fe, and Mn, whereas Cr prefers the B-site. We check the magnetic state of the structure by doubling the previous geometry in both lattice vector directions and setting the initial magnetic state as AFM. The minimum energy geometries, magnetic states, binding energies, and total magnetic moments of adsorption to (2×2) graphene cell are given in Table 4.1. Comparison of binding energies of adsorption on (2×2) cell with that of (4×4) cells indicates that bindings to the smaller one are weaker. This is because TM–TM coupling is more significant in (2×2) case and this coupling energy is subtracted from the binding energy (see Appendix A).

We calculate the charge accumulation for majority ($\uparrow$) and minority ($\downarrow$) spins for Ti adsorption on (4×4) cell as $\Delta\rho_{\uparrow(\downarrow)} = \rho_{\uparrow(\downarrow)}$ [graphene + Ti] $-\rho_{\uparrow(\downarrow)}$[graphene] $-$

Table 4.1 Minimum energy adsorption sites and magnetic states (either ferromagnetic (FM) or antiferromagnetic(AFM)) for single-sided adsorption of one TM atom adsorbed per (2×2) cell

	Ti	Co	Fe	Cr	Mn
	H AFM	H FM	H FM	B AFM	H AFM
E_b(eV)	1.58 (1.95)	1.20 (1.27)	0.66 (1.02)	0.18 (0.20)	0.10 (0.17)
μ_{tot}(μB)	0.0	1.31	3.02	0.0	0.00
d (Å)	2.32	2.12	2.21	2.39	2.47

The binding energies (E_b), the total magnetic moments μ_{tot}, and the distances to the nearest C atom (d) are also listed. The binding energy of a single TM atom adsorbed on a (4×4) cell is given in parentheses for the sake of comparison

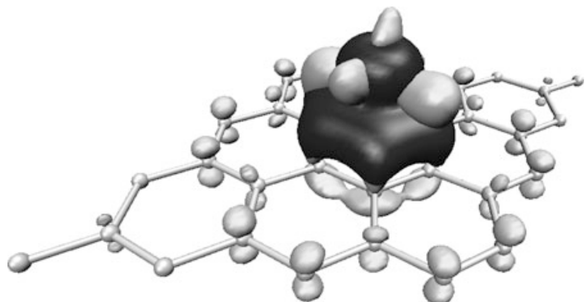

Fig. 4.18 Spin resolved charge accumulation (i.e. $\Delta\rho_{\uparrow(\downarrow)} > 0$) obtained from the charge density difference calculation for one Ti atom adsorbed to each (4×4) cell of graphene (see the text). *Dark* and *light* regions indicate the isosurfaces of majority and minority spin states, respectively. Calculations have been performed using DFT method (see Appendix A) (Reproduced from Ref. [46])

$\rho_{\uparrow(\downarrow)}$ [Ti]. Here $\rho_{\uparrow(\downarrow)}$ [graphene+Ti] is the total charge of the majority and minority spin states of one Ti atom adsorbed to each (4×4) cell of graphene. $\rho_{\uparrow(\downarrow)}$ [graphene] and $\rho_{\uparrow(\downarrow)}$ [Ti] are the charge densities of noninteracting bare graphene and Ti atom having the same positions as in the case of graphene and adsorbed Ti. The accumulation of spin-dependent charge densities due to adsorption are shown with the isosurface plot in Fig. 4.18. An increase in the majority spin density between graphene and Ti is accompanied with a net increase in minority spin density on Ti. The difference in majority and minority spin densities demonstrate the induced magnetization on $2p_z$ orbitals of the carbon atoms.

We also examine the variation of electronic and magnetic properties of TM-adsorbed AGNR's with different widths. We define the TM atom coverage θ as the number of TM atoms per unit cell and study the cases with $\theta = 1$ and 2. In the $\theta = 1$ case, we examine all the hollow sites for adsorption for AGNR's with $N_a = 4, 5, 6, 7, 8$, and 9. For all TM species and all N_a edge, hollow site is found to have the minimum energy. Transition state analysis for the species with the strongest binding is given in Fig. 4.19. The energy barrier for a Ti atom to hop from the middle hexagon of a AGNR(7) unit cell to the edge hexagon is 0.48 eV, whereas the barrier height is 0.97 eV in the reverse direction [see Fig. 4.19c] These results suggest that the diffusion of Ti atoms to form clusters is hindered by a significant energy barrier. We further examine the TM-adsorbed AGNRs by considering $\theta = 2$ case. We keep the first TM atom at the hollow of the edge hexagon and check all the possible adsorption sites for the second TM atom. We calculate three cases with $N_a = 4, 5$, and 6 to sample the three families of AGNR band structures. The energy is lowered by TM–TM interaction, so the second TM atom prefers the hexagon, which is closest to both the first TM atom and the ribbon edge [see Fig. 4.20a]. Consequently, a zigzag chain of TM atoms is formed at the edge of the AGNR. Such a chain formation either metallizes the system or it gives to half-metallicity. For example, zigzag chain of Fe on AGNR(5) is half-metallic with an energy gap

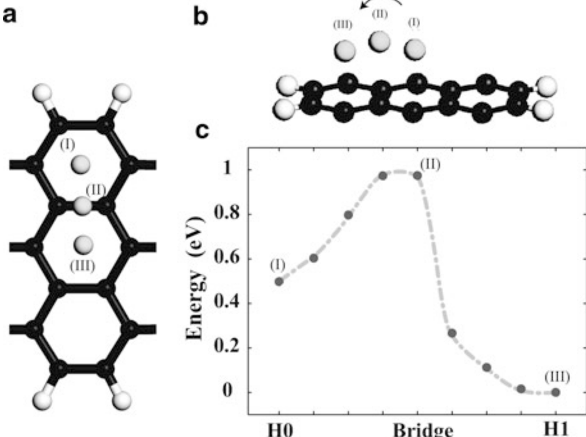

Fig. 4.19 Transition state analysis of Ti adsorbed on AGNR(7) between H0 and H1 sites above the bridge site. (**a**) *Top view* of three adsorption sites of Ti on AGNR(7) from H0 to H1, i.e., H0 bridge and H1 sites are shown. (**b**) *Side view* for these three adsorption sites. Adsorption to the C–C bridge gives the farthest position to the AGNR plane. (**c**) Total energy per unit cell for Ti adsorption on the path from H0 to H1 as explained in the text. Calculations have been performed using DFT method (see Appendix A) (Reproduced from Ref. [46])

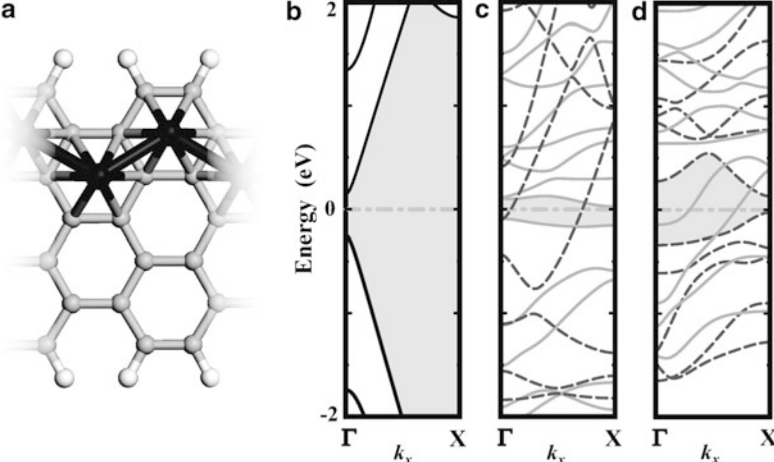

Fig. 4.20 Zigzag chains are formed at the AGNR edge for $\theta = 2$ coverage (**a**). Band structures of (**b**) bare AGNR(5) and $\theta = 2$ coverage of AGNR(5) (**c**) with Fe, and (**d**) with Ti. Fermi Energy is set to zero. In (**c**) and (**d**), *dark-dashed curves* are the bands with majority spin, and *light-solid curves* are the bands of the minority spin. Fe adsorption opens a gap of 0.10 eV for the minority spin while the majority spin is metallic. Adsorption of Ti makes the minority spin metallic while the majority spin has an energy gap of 0.16 eV at the Fermi energy (Reproduced from Ref. [46])

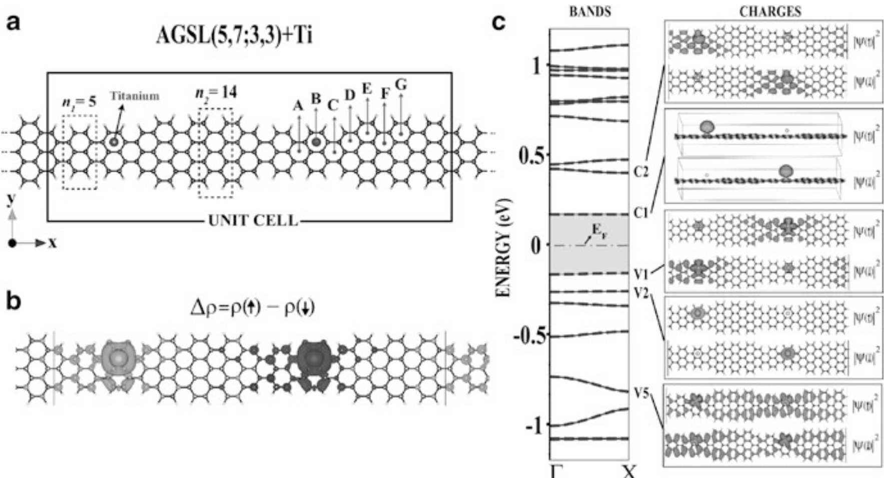

Fig. 4.21 (**a**) Atomic configuration of Ti-adsorbed AGSL(5,7;3,3). The primitive unit cells are delineated by *dashed lines*. The possible adsorption sites are labeled by letters A–G. (**b**) Isosurface of difference charge density of spin-up and spin-down states, $\Delta\rho = \rho(\uparrow) - \rho(\downarrow)$. *Light* regions correspond to positive and *dark* regions correspond to negative difference. (**c**) Energy band structure and isosurface charge density of selected spin states. $\Psi(\uparrow)$ is for spin-up component and $\Psi(\downarrow)$ is for spin-down component

of 0.10 eV for minority spin electrons [Fig. 4.20c]. Similarly, Ti zigzag chains at the edges of AGNR(4) and AgNR(5) are half-metallic with energy gaps of 0.05 and 0.16 eV for the majority spin electrons [Fig. 4.20d].

These results show that the ribbon width and the interaction of the TM atom with ribbon edge play important roles in the electronic properties of GNRs. We furthermore investigated Ti atom adsorption on armchair graphene superlattice structures that are studied in Section 4.3. For Ti adsorption, we have chosen AGSL(5,7;3,3) superlattice whose atomic configuration is presented in Fig. 4.8. All the hexagons from (A)–(G) in Fig. 4.21a has been checked and we found that (B) site corresponds to the minimum energy configuration. Ti atoms prefer to stay in narrower parts of the superlattice. This result is predictable when our previous results about adsorption on AGNR are analyzed. Binding energy is higher for adsorption on AGNR(5) compared to adsorption on AGNR(7) [46]. The magnetic configuration of two Ti atoms was investigated and we found that antiferromagnetic arrangement of the spins of two Ti atoms is 8 meV, energetically more favorable than ferromagnetic arrangement. The exchange energy is calculated from the difference of E_{AFM} (antiferromagnetic state) and E_{FM} (ferromagnetic state) and is related to J in the Heisenberg Hamiltonian. The relatively small exchange energy shows that indirect exchange coupling between Ti atoms is small when mediated through superlattice structures of graphene ribbons. Isosurface plots of difference in charge density between up-spin and down-spin states, $\Delta\rho = \rho(\uparrow) - \rho(\downarrow)$ in Fig. 4.21b clearly reveals the antiferromagnetism in the system.

The electronic structure of AGSL(5,7;3,3) in Fig. 4.9a is dramatically affected upon Ti adsorption. Figure 4.21c shows the electronic band structure and band-decomposed charge density analysis of the new structure in Fig. 4.21a. Each band consists of one spin-up and one spin-down state, which are located on different regions of the superlattice. The flat bands around Fermi level corresponds to confined states. The first valence band (V1) and second conduction band (C2) have their charge densities mostly confined in narrow regions of the superlattice. First conduction (C1) and second valence (V2) bands are d-states of titanium. The fifth valence band states (V5) propagate throughout the superlattice.

4.5 Conclusions

We reviewed two routes for functionalization of GNRs, which are superlattice formation through width modulation and adding modifying magnetic properties through TM atom doping. Various types of quantum structures made by size modulation of graphene-based nanoribbons are examined. The confinement of spin-unpolarized and spin-polarized electron and hole states can lead to interesting effects such as resonant tunneling and spin confinement. Variation of the bandgaps, confined state energies, and the strength of confinement with the width and length and composition of the constituent nanoribbons are the key features for future applications. Also, the variations in electronic and magnetic properties upon TM atom adsorption are analyzed depending on the adsorbate concentration, adsorption site, and the species of the adsorbent. We show that it is possible to obtain half-metallic GNRs through TM atom adsorption.

Appendix A: Details of density functional theory calculations

In calculating the electronic and magnetic properties using density functional theory [29], projector augmented wave (PAW) [47] approach within a PW91 [48]-GGA [49] approximation for the exchange and correlation functional is used as currently implemented in the VASP [50] software. Geometry optimizations are performed by allowing all atomic positions to vary; for bulk structures all cell parameters are optimized as well. The atomic positions are optimized by the conjugate gradient method, and the system is considered to be at equilibrium when Hellman–Feynman forces are below 10 me V/A. Monkhorst–Pack meshes with sufficient number of k-points are used to converge the energies. For 1D and 2D structures, the minimum size of the implemented k-point meshes are (21,1,1) and (11,11,1), respectively. Periodic boundary conditions are implemented in all directions, where sufficiently large vacuum (minimum of 10 Å) is inserted in directions without crystal symmetry to prevent artificial interactions. The kinetic energy cutoff for the plane wave basis set is chosen as $\hbar^2|k+G|^2/2m = 500$ eV when using PAW potentials and 350 eV

when using ultrasoft pseudopotentials. The convergence criterion for electronic relaxations has been set to 10^{-5} eV for all cases. The binding energies of TM atoms are calculated as $E_b = E[\text{graphene}] + E[\text{TM}] - E[(\text{graphene} + \text{TM})]$ in terms of the total energies of the host cell, $E[\text{graphene}]$, the free TM atom in its ground state $E[\text{TM}]$, and one TM atom adsorbed on a host cell, $E[\text{graphene}] + E[\text{TM}]$. Total energies are calculated in the same supercells keeping other parameters of the calculations fixed.

References

1. K.S. Novoselov, A.K. Geim, S.V. Morozov, D. Yiang, Y. Zhang, S.V. Dubonos, I.V. Grigorieva, A.A. Firsov, Science **306**, 666 (2004)
2. L.D. Landau, E.M. Lifshitz, *Statistical Physics,* 3rd edn. (Pergamon, Oxford, 1980)
3. R.E. Peirls, Helv. Phys. Acta **7**, 81 (1934)
4. N.D. Mermin, Phys. Rev. **176**, 250 (1968)
5. S. Cahangirov, M. Topsakal, E. Akturk, H. Sahin, Salim Ciraci, unpublished (arXiv:0811.4412)
6. M. Topsakal, E. Akturk, S. Ciraci, Phys. Rev. B **79**, 115442 (2009)
7. M.I. Katsnelson, K.S. Novoselov, A.K. Geim, Nat. Phys. **2**, 620 (2006)
8. A.K. Geim, K.S. Novoselov, Nat. Mater. **6**, 183 (2007)
9. K.S. Novoselov, A.K. Geim, S.V. Morozov, D. Jiang, M.I. Katsnelson, I.V. Grigorieva, S.V. Dubonos, A.A. Firsov, Nature **438**, 197 (2005); Y. Zhang, Y.-W. Tan, H.L. Stormer, P. Kim, Nature **438**, 201 (2005)
10. C. Ataca, E. Aktiirk, S. Ciraci, H. Ustunel, Appl. Phys. Lett. **93**, 043123 (2008)
11. C. Ataca, E. Akturk, S. Ciraci, Phys. Rev. B **79**, 041406 (2009)
12. F. Schedin, A.K. Geim, S.V. Morozov, E.W. Hill, P. Blake, M.I. Katsnelson, K.S. Novoselov, Nat. Mater. **6**, 652 (2007)
13. T.B. Martins, R.H. Miwa, A.J.R. da Silva, A. Fazzio, Phys. Rev. Lett. **98**, 196803 (2007)
14. M. Topsakal, H. Sevincli, S. Ciraci, Appl. Phys. Lett. **92**, 173118 (2008)
15. H. Sahin, R.T. Senger, Phys. Rev. B **78**, 205423 (2008)
16. Y.-W. Son, M. L. Cohen, S.G. Louie, Nature **444**, 347 (2006) (see also erratum: Nature **446**, 342 (2007))
17. Y.-W. Son, M.L. Cohen, S.G. Louie, Phys. Rev. Lett. **97**, 216803 (2006) (see also erratum: Phys. Rev. Lett. **98**, 089901(E) (2007))
18. J. Nilsson, A.H. Castro Neto, F. Guinea, N.M.R. Peres, Phys. Rev. B **76**, 165416 (2007)
19. X. Wang, Y. Ouyang, H. Wang, J. Guo, H. Dai, Phys. Rev. Lett. **100**, 206803 (2008)
20. H. Sevincli, M. Topsakal, S. Ciraci, Phys. Rev. B **78**, 245402 (2008)
21. C.H. Xu et al., J. Phys.: Condens. Matter **4**, 6047 (1992)
22. P.R. Wallace, Phys. Rev. **71**, 622 (1947)
23. G.W. Semenoff, Phys. Rev. Lett. **53**, 2449 (1984)
24. M. Fujita, K. Wakabayashi, K. Nakada, K. Kusakabe, J. Phys. Soc. Jpn. **65**, 1920 (1996)
25. L. Pisani, J.A. Chan, B. Montanari, N.M. Harrison, Phys. Rev. B **75**, 064418 (2007)
26. K. Nakada, M. Fujita, G. Dresselhaus, M.S. Dresselhaus, Phys. Rev. B **54**, 17954 (1996)
27. Y. Miyamoto, K. Nakada, M. Fujita, Phys. Rev. B **59**, 9858 (1999)
28. M. Ezawa, Phys. Rev. B **73**, 045432 (2006)
29. W. Kohn, L.J. Sham, Phys. Rev. **140**, A1133 (1965); P. Hohenberg, W. Kohn, Phys. Rev. B **76**, 6062 (1964)
30. E.H. Lieb, Phys. Rev. Lett. **62**, 1201 (1989)
31. L. Esaki, R. Tsu, IBM J. Res. Dev. **14**, 61 (1970)
32. L. Esaki, L.L. Chang, Phys. Rev. Lett. **33**, 495 (1974)

33. L. Esaki, *Highlights in Condensed Matter Physics and Future Prospects, NATO Advanced Studies Institute, Series B: Physics* (Plenum, New York, 1991), p. 285, several relevant references can be found in this proceedings; L.L. Chang, L. Esaki, R. Tsu, Appl. Phys. Lett. **24**, 593 (1974)
34. E. Tekman, S. Ciraci, Phys. Rev. B **40**, 8559 (1989); S. Ciraci, I. P. Batra, Phys. Rev. B **36**, 6194 (1987)
35. Claire Berger, Zhimin Song, Xuebin Li, Xiaosong Wu, Nate Brown, Cecile Naud, Didier Mayou, Tianbo Li, Joanna Hass, Alexei N. Marchenkov, Edward H. Conrad, Phillip N. First, Walt A. de Heer, Science **312**, 1191 (2006)
36. M.-Y. Han, B. Ozyilmaz, Y. Zhang, P. Kim, Phys. Rev. Lett. **98**, 206805 (2007)
37. B. (Ozyilmaz, P.J. -Herrero, D. Efetov, P. Kim, Appl. Phys. Lett. **91**, 192107 (2007)
38. R. Landauer, Philos. Mag. **21**, 863 (1970)
39. S. Datta, *Electronic Transport in Mesoscopic Systems* (Cambridge University Press, Cambridge, 1995)
40. M. Brandbyge, J.-L. Mozos, P. Ordejn, J. Taylor, K. Stokbro, Phys. Rev. B **65**, 165401, (2002)
41. D. Fisher, P. Lee, Phys. Rev. B **23**, 6851 (1981)
42. S. Tongay, R.T. Senger, S. Dag, S. Ciraci, Phys. Rev. Lett. **93**, 136404 (2004)
43. X. Li, X. Wang, L. Zhang, S. Lee, H. Dai, Science **319**, 1229 (2008)
44. J.F.-Rossier, J.J. Palacios, Phys. Rev. Lett. **99**, 177204 (2007)
45. L. Yang, C.-H. Park, Y.-W. Son, M.L. Cohen, S.G. Louie, Phys. Rev. Lett. **99**, 186801 (2007)
46. H. Sevincli, M. Topsakal, E. Durgun, S. Ciraci, Phys. Rev. B **77**, 195434 (2008)
47. P.E. Blochl, Phys. Rev. B **50**, 17953 (1994)
48. J.P. Perdew, J.A. Chevary, S.H. Vosko, K.A. Jackson, M.R. Pederson, D.J. Singh, C. Fiolhais, Phys. Rev. B **46**, 6671 (1992)
49. J.P. Perdew, K. Burke, M. Ernzerhof, Phys. Rev. Lett. **77**, 3865 (1996)
50. G. Kresse, J. Hafner, Phys. Rev. B **47**, 558 (1993); G. Kresse, J. Furthmuller, Phys. Rev. B **54**, 11169 (1996)

Chapter 5
Atom/Molecule van der Waals Interaction with Graphene

Norman J. Morgenstern Horing, Vassilios Fessatidis, and Jay D. Mancini

Abstract We examine the van der Waals interaction between Graphene and an atom/molecule to the second order in the Coulomb interaction between the electrons of the two systems involved. Our analysis extends to dipole–dipole terms of the mutually polarized systems, including plasma nonlocality of the Graphene.

5.1 Introduction: Atom–Graphene van der Waals Interaction and the Plasma Image

The van der Waals interaction between an electrically neutral atom/molecule and a 2D-Graphene sheet is based on mutual polarization of the two systems by the Coulomb interaction between the atomic electrons and the mobile electrons on the sheet, excluding the possibility of sharing or exchanging electrons by penetration of the atomic electron wave functions into the sheet and vice versa. Moreover, the theory of van der Waals attraction assumes that the atom and its electrons are far enough from the mobile electrons of the sheet so that exchange effects are negligibly small. These qualitative statements apply to all van der Waals ($v\mathrm{d}W$) interactions, including atom–atom as well as atom–surface.

To second order in the Coulomb interaction between the adatom electrons and the mobile electrons of the Graphene sheet, the van der Waals interaction energy may be expressed as [1]:

$$E_{v\mathrm{d}W} \cong -\int d^3\mathbf{x}' \int d^3\mathbf{x}'' \int dt''\,\mathbf{V}_{\mathrm{image}}(\mathbf{x}',\mathbf{x}'',t'-t'')\,G_2^{\mathrm{a}}(\mathbf{x}''t'',\mathbf{x}'t';\mathbf{x}''t''^{+},\mathbf{x}'t'^{+}). \tag{5.1}$$

N.J.M. Horing (✉)
Department of Physics and Engineering Physics, Stevens Institute of Technology, Hoboken, NJ 07030, USA
e-mail: nhoring@stevens.edu

H. Ünlü and N.J.M. Horing (eds.), *Low Dimensional Semiconductor Structures*, NanoScience and Technology, DOI 10.1007/978-3-642-28424-3_5,
© Springer-Verlag Berlin Heidelberg 2013

Here, G_2^{a} is the two-particle Green's function of the atomic electrons, including the full complement of intra-atom electron–electron interactions averaged in the ground state of the atom $|\Phi_0^{\mathrm{a}}\rangle$, but with no effects from the Graphene electrons. The image potential, $\mathbf{V}_{\mathrm{image}}$, due to the polarization of the Graphene electron plasma by the Coulomb field of a point charge outside may be written in terms of the G_2^{m} two-particle Green's function of the plasma of mobile Graphene electrons using the inverse dielectric (screening) function, K^{m}, of the Graphene plasma. Discarding G_1^{m} terms and δ-terms, which are not pertinent to this discussion, we have:

$$K^{\mathrm{m}}(1,2) \to i\int d^4 3\mathbf{V}(1-3)G_2^{\mathrm{m}}(3,2;3^+,2^+) = i\int d^3\mathbf{x}^{iv}\mathbf{V}(\mathbf{x}'-\mathbf{x}^{iv}) \times G_2^{\mathrm{m}}(\mathbf{x}^{iv}t',\mathbf{x}''t'';\mathbf{x}^{iv}t'^+,\mathbf{x}''t''^+). \tag{5.2}$$

Here, G_2^{m} includes the effects of mobile electron–electron interactions within the Graphene sheet, and $\mathbf{V}$ is the unscreened Coulomb potential. The corresponding image potential given by, $\mathbf{V}_{\mathrm{image}}(1) = \mathbf{V}_{\mathrm{eff}}(1) - \mathbf{V}(1)$, is:

$$\begin{aligned}\mathbf{V}_{\mathrm{image}}(\mathbf{x}',\mathbf{x}'',t'-t'') = & \int d^3\mathbf{x}''' \left[K^{\mathrm{m}}(\mathbf{x}',\mathbf{x}''';t'-t'')\mathbf{V}(\mathrm{x}'''-\mathbf{x}'')\right] - \mathbf{V}(\mathbf{x}'-\mathbf{x}'') \\ = & \; i\int d^3\mathbf{x}''' \int d^3\mathbf{x}^{iv}\mathbf{V}(\mathbf{x}'-\mathbf{x}^{iv}) \\ & \times G_2^{\mathrm{m}}(\mathbf{x}^{iv}t',\mathbf{x}'''t''';\mathbf{x}^{iv}t'^+,\mathbf{x}''t''')\mathbf{V}(\mathbf{x}'''-\mathbf{x}'') \\ & -\mathbf{V}(\mathbf{x}'-\mathbf{x}''),\end{aligned} \tag{5.3}$$

which yields $E_{v\mathrm{d}W}$ in an alternative form as:

$$\begin{aligned}E_{v\mathrm{d}W} = & -i\int d^3\mathbf{x}' \int d^3\mathbf{x}'' \int d^3\mathbf{x}''' \int d^3\mathbf{x}^{iv} \int dt''\mathbf{V}(\mathbf{x}'-\mathbf{x}^{iv}) \\ & \times G_2^{m}(\mathbf{x}^{iv}t',\mathbf{x}'''t''';\mathbf{x}^{iv}t'^+,\mathbf{x}''t'''^+)\mathbf{V}(\mathbf{x}'''-\mathbf{x}'') \\ & \times G_2^{\mathrm{a}}(\mathbf{x}''t'',\mathbf{x}'t';\mathbf{x}''t''^+,\mathbf{x}'t'^+) \\ & -[\text{direct non-image counterpart}].\end{aligned} \tag{5.4}$$

This result can be obtained [1] using a straightforward perturbation theory to the second order in the Coulomb interaction between the electrons of the adatom and those of the Graphene plasma. As in perturbation theory, G_2^{m} and G_2^{a} (alternatively, K^{m} and G_2^{a}) are to be determined in the absence of atom–surface coupling. It is convenient to write the result in the form of (5.1), which suggests interpreting $E_{v\mathrm{d}W}$ in terms of a self-energy of the atomic electrons due to screening of their Coulomb interaction by the Graphene electrons. Here, we can fruitfully employ the determination of $\mathbf{V}_{\mathrm{image}}$ in the presence of dynamic, nonlocal screening by the Graphene electrons as discussed below.

The effective potential $\mathbf{V}_{\text{eff}}(1)$ at a space–time point $1 = (\mathbf{r}_1, t_1)$, generated by the Coulomb potential $\mathbf{V}(2)$ impressed at $2 = (\mathbf{r}_2, t_2)$ by an atomic electron, is associated with polarization of the 2D mobile Graphene electrons as:

$$\mathbf{V}_{\text{eff}}(1) = \int d^4 2 K^{\text{m}}(1,2)\mathbf{V}(2), \tag{5.5}$$

where $K^{\text{m}}(1,2)$ is the 3D screening function of the 2D plasma, inverse to its direct dielectric function $\varepsilon(3,2)$ in a 3D space–time matrix sense:

$$\int d^4 3 K^{\text{m}}(1,3)\varepsilon(3,2) = \delta^4(1,2). \tag{5.6}$$

Here, $\varepsilon(3,2)$ is the direct dielectric function of the 2D plasma in 3D real space–time representation. One must also recognize that there is a density perturbation involved in the Graphene response dynamics, such that

$$\begin{aligned}\rho(1) &= \int d^4 3 R(1,3)\, \mathbf{V}_{\text{eff}}(3)\\ &= \int d^4 3 \int d^4 4\; R(1,3)K^{\text{m}}(3,4)\mathbf{V}(4),\end{aligned} \tag{5.7}$$

with $R(1,3) = \delta\rho(1)/\delta\mathbf{V}_{\text{eff}}(3)$ as the density-perturbation response function. Writing $\varepsilon(3,2)$ in terms of the polarizability $\alpha(3,2)$, (5.6) becomes an RPA-type integral equation:

$$K^{\text{m}}(1,2) = \delta^4(1-2) - \int d^4 3\; \alpha(1,3)K^{\text{m}}(3,2). \tag{5.8}$$

The polarizability $\alpha(1,3)$ can be expressed in a form that describes both the free-electron Graphene response and an additive static background contribution ($\mathbf{V}$ is the interelectron Coulomb interaction of the 2D Graphene sheet, and $\alpha_0 = \varepsilon_0 - 1$ is the additive background polarizability):

$$\alpha(1,3) = -\int d^4 4\mathbf{V}(1-4)R(4,3) + \alpha_0\delta^4(1-3). \tag{5.9}$$

This yields

$$\begin{aligned}K^{\text{m}}(1,2) &= \frac{1}{\varepsilon_0}\delta^4(1-2)\\ &\quad + \frac{1}{\varepsilon_0}\int d^4 3 \int d^4 4\mathbf{V}(1-4)R(4,3)K^{\text{m}}(3,2).\end{aligned} \tag{5.10}$$

In the RPA, $R(4,3)$ is the lowest ring diagram and the integral (5.10) is just the sum of ring diagrams. Considering translational invariance in the $\overline{r} = (x, y)$ plane

of the planar 2D-graphene sheet and in time (but not for z), we obtain the Fourier transform:

$$K^{\mathrm{m}}(1,2) = K^{\mathrm{m}}(\overline{r}_1 - \overline{r}_2, z_1, z_2; t_1 - t_2) \rightarrow K^{\mathrm{m}}(\overline{p}, z_1, z_2; \omega), \tag{5.11}$$

with respect to space $\overline{r}_1 - \overline{r}_2 \rightarrow \overline{p}$ and time $t_1 - t_2 \rightarrow \omega$.

To determine the 3D screening function $K^{\mathrm{m}}(\overline{p}, z_1, z_2; \omega)$ that is the inverse of the 2D plasma dielectric function $\varepsilon(\overline{p}, z_1, z_2; \omega)$ in 3D space, we employ the inversion condition of (5.6) in the form:

$$\int dz_2 K(\overline{p}, z_1, z_2; \omega)\, \varepsilon(\overline{p}, z_2, z_3; \omega) = \delta(z_1 - z_3), \tag{5.12}$$

which may be applied by writing $\varepsilon(\overline{p}, z_1, z_2; \omega)$ as:

$$\varepsilon(\overline{p}, z_1, z_2; \omega) = \delta(z_1 - z_2) + \alpha(\overline{p}, z_1, z_2; \omega), \tag{5.13}$$

in terms of the Graphene sheet polarizability $\alpha(\overline{p}, z_1, z_2; \omega)$. For electron motion confined to a single 2D-plane sheet, the density-perturbation response function has its z arguments localized to the sheet by positional δ-functions of the form:

$$R(\overline{p}, z_1, z_2; \omega) = \delta(z_1)\delta(z_2) R^{2\mathrm{D}}(\overline{p}, \omega). \tag{5.14}$$

Here, $R^{2\mathrm{D}}(\overline{p}, \omega)$ describes the response properties of the electron density perturbation *on* the 2D Graphene sheet, such that the 2D electron polarizability on the sheet is given by $\alpha^{2\mathrm{D}}(\overline{p}, \omega) = -R^{2\mathrm{D}}(\overline{p}, \omega)/p$ (where, in (5.9), we introduced the 2D Fourier transform in the Coulomb potential). With this in view, we have:

$$\varepsilon(\overline{p}, z_1, z_2; \omega) = \varepsilon_0 \delta(z_1 - z_2) + \delta(z_2)\alpha^{2\mathrm{D}}(\overline{p}, \omega) e^{-p|z_1|}, \tag{5.15}$$

where $p = |\overline{p}|$ and $\varepsilon_0 = 1 + \alpha_0$ for the background. We attempt inversion in the form:

$$\begin{aligned} K^{\mathrm{m}}(\overline{p}, z_1, z_2; \omega) = {} & \frac{1}{\varepsilon_0}\delta(z_1 - z_2) \\ & + \frac{1}{\varepsilon_0}\delta(z_2) e^{-p|z_1|}[\widetilde{K}^{2\mathrm{D}}(\overline{p}, \omega) - 1]. \end{aligned} \tag{5.16}$$

The determination of $\widetilde{K}^{2\mathrm{D}}(\overline{p}, \omega)$ is carried out by requiring satisfaction of the inversion condition in the form of (5.12). Equating coefficients of like positional delta functions, we obtain:

$$\widetilde{K}^{2\mathrm{D}}(\overline{p}, \omega) = \left(1 + \frac{\alpha^{2\mathrm{D}}(\overline{p}, \omega)}{\varepsilon_0}\right)^{-1} \equiv \left[\widetilde{\varepsilon}^{\,2\mathrm{D}}(\overline{p}, \omega)\right]^{-1}. \tag{5.17}$$

5.2 Nonlocal Dipolar van der Waals Interaction of an Atom/Molecule and Graphene

The atomic electron $G_2^{\rm a}$-function involved in E_{vdW} has the form:

$$G_2^{\rm a} \to \left\langle \Phi_0^{\rm a} \left| \rho_a(\mathbf{x}'', t'')\rho_a(\mathbf{x}', t')\right| \Phi_0^{\rm a} \right\rangle, \tag{5.18}$$

where $\rho_{\rm a}(\mathbf{x}, t)$ is the density operator for the atomic electrons. Recognizing that the atom has a fixed number of electrons and is electrically neutral (in the absence of ionization), we denote the energy eigenstates of the atomic electrons by $|\Phi_n^{\rm a}\rangle$, with ground state $|\Phi_0^{\rm a}\rangle$. These states of the atomic electrons bear the full complement of correlations due to electron–electron interactions of the electrons within the atom. Their completeness is expressed by:

$$1 = \sum_n |\Phi_n^{\rm a}\rangle\langle\Phi_n^{\rm a}|, \tag{5.19}$$

so that

$$G_2^{\rm a}(\mathbf{x}''t'', \mathbf{x}'t'; \mathbf{x}''t''^+, \mathbf{x}'t'^+) = \sum_n \langle\Phi_0^{\rm a}|\rho_a(\mathbf{x}'', t'')|\Phi_n^{\rm a}\rangle\langle\Phi_n^{\rm a}|\rho_a(\mathbf{x}', t')|\Phi_0^{\rm a}\rangle. \tag{5.20}$$

Employing an atomic electron time-translation operator $e^{-iH_{\rm a}(t'-t'')}$ to bring the times of the two density operators into coincidence, we have:

$$G_2^{\rm a}(\mathbf{x}''t'', \mathbf{x}'t'; \mathbf{x}''t''^+, \mathbf{x}'t'^+) = \sum_n \langle\Phi_0^{\rm a}|\rho_{\rm a}(\mathbf{x}'', t'')|\Phi_n^{\rm a}\rangle\langle\Phi_n^{\rm a}|e^{iH_{\rm a}(t'-t'')} \times\rho_{\rm a}(\mathbf{x}', t'')e^{-iH_{\rm a}(t'-t'')}|\Phi_0^{\rm a}\rangle \tag{5.21}$$

and, since the energies of the atomic electron eigenstates are denoted by:

$$H_{\rm a}|\Phi_n^{\rm a}\rangle = E_n^{\rm a}|\Phi_n^{\rm a}\rangle, \tag{5.22}$$

we have

$$G_2^{\rm a}(\mathbf{x}''t''; \mathbf{x}'t'; \mathbf{x}''t''^+; \mathbf{x}'t'^+) = \sum_n \left\langle\Phi_0^{\rm a}|\rho_{\rm a}(\mathbf{x}'', t'')|\Phi_n^{\rm a}\right\rangle \times\left\langle\Phi_n^{\rm a}|\rho_{\rm a}(\mathbf{x}', t'')|\Phi_0^{\rm a}\right\rangle e^{i(E_n^{\rm a}-E_0^{\rm a})(t'-t'')}. \tag{5.23}$$

Understanding that both the density operators and the energy eigenstates are now evaluated at the same time such that the matrix elements are independent of time, we write:

$$\langle\Phi_0^{\rm a}|\rho_{\rm a}(\mathbf{x}'', t'')|\Phi_n^{\rm a}\rangle = \langle\rho_{\rm a}(\mathbf{x}'')\rangle_{0n}$$

and with

$$\omega^{\mathrm{a}}_{n0} = E^{\mathrm{a}}_n - E^{\mathrm{a}}_0,$$

we have

$$G^{\mathrm{a}}_2(\mathbf{x}''t''; \mathbf{x}'t'; \mathbf{x}''t''^{+}; \mathbf{x}'t'^{+}) = \sum_n{}' \langle \rho_{\mathrm{a}}(\mathbf{x}'')\rangle_{0n} \langle \rho_{\mathrm{a}}(\mathbf{x}')\rangle_{n0} e^{i\omega^{\mathrm{a}}_{n0}(t'-t'')}. \tag{5.24}$$

(The prime on the $\Sigma \to \Sigma'$ indicates that the $n = 0$ term is excluded, since it has no time dependence and yields a constant, static contribution, which is irrelevant to the van der Waals interaction.) Substitution of this into (5.1) yields E_{vdW} in terms of the Fourier time transform of $\mathbf{V}_{\mathrm{image}}(t' - t'') \to \mathbf{V}_{\mathrm{image}}(\omega)$ as:

$$E_{vdW} = \int d^3\mathbf{x}' \int d^3\mathbf{x}'' \int_{-\infty}^{\infty} \frac{\mathrm{d}\omega}{2\pi i} \mathbf{V}_{\mathrm{image}}(\mathbf{x}', \mathbf{x}''; \omega) \sum_n{}' \left(\frac{\langle \rho_{\mathrm{a}}(\mathbf{x}'')\rangle_{0n} \langle \rho_{\mathrm{a}}(\mathbf{x}')\rangle_{n0}}{\omega - \omega^{\mathrm{a}}_{n0}} \right), \tag{5.25}$$

where we have taken account of nonlocality in time in performing the time integration. Considering spatial-translational invariance in the lateral plane $\bar{\mathbf{x}} = (x, y) \to \bar{\mathbf{p}}$ and using $\mathbf{V}_{\mathrm{image}}(z', z''; \bar{p}, \omega)$ obtained from (5.16) and (5.17), we obtain the result for E_{vdW} using a multipole expansion, mandated by the spatially confined distribution of the atomic electrons. To dipole–dipole terms, it is given by:

$$E_{vdW} = \frac{4}{3\hbar\varepsilon_0} \sum_n{}' \int_0^{\infty} \frac{du}{2\pi} \frac{\omega^{\mathrm{a}}_{n0} |\mathbf{D}_{0n}|^2}{u^2 + (\omega^{a}_{n0})^2} \int_0^{\infty} dp p^2 e^{-2p|Z|} \frac{\alpha^{2\mathrm{D}}(p, iu)/\varepsilon_0}{1 + \alpha^{2\mathrm{D}}(p, iu)/\varepsilon_0}, \tag{5.26}$$

where $|Z|$ is the distance of the atom from the 2D-planar quantum well ($\mathbf{D}_{0n}$ is the matrix element of the atom's dipole moment operator between its electronic eigenstates $0, n$).

Equation (5.26) is a useful point of departure to determine both local and nonlocal structures of the van der Waals interaction. $\alpha^{2\mathrm{D}}(\overline{p}, \omega)$ was determined for Graphene [2–6] for null magnetic field (division by ε_0 corresponds to putting $\mathbf{V} \to \widetilde{\mathbf{V}} = \mathbf{V}/\varepsilon_0$ or $e^2 \to \tilde{e}^2 = e^2/\varepsilon_0$). For the undoped case, $\alpha^{2\mathrm{D}}(p, iu)$ is presented in Ref. [6] (5.10) as:

$$\alpha^{2\mathrm{D}}(p, iu) = -\left(\frac{g_{\mathrm{s}} g_{\mathrm{v}} \pi e^2}{8\varepsilon_0 \hbar} \right) \frac{p}{\sqrt{u^2 + \gamma^2 p^2}}, \tag{5.27}$$

where γ is the Graphene Fermi velocity and $g_{\mathrm{s}}, g_{\mathrm{v}}$ are its spin and valley degeneracies. It should be noted that an expansion of E_{vdw} in inverse powers of $|Z|$ is *not* available since it would involve expansion of the p-integrand of (5.26) in powers of p/u, which would cause divergences in the final u-integration. However, for atomic frequencies $(\omega^{\mathrm{a}}_{n0})$, the polarizability is small, $\alpha^{2\mathrm{D}}(p, iu) \ll 1$, and we have the p-integral of (5.26) as:

$$\int_0^\infty dp \ldots \cong -\left(\frac{g_s g_v \pi e^2}{8\varepsilon_0 \hbar}\right) \int_0^\infty dp e^{-2p|Z|} \frac{p}{\sqrt{u^2+\gamma^2 p^2}}. \tag{5.28}$$

This integral may be rewritten using [7]:

$$\int_0^\infty \frac{x e^{-\mu x}}{\sqrt{x^2+\beta^2}} dx = \frac{\beta\pi}{2}[\mathbf{H}_1(\beta\mu) - Y_1(\beta\mu)] - \beta, \tag{5.29}$$

where $\mathbf{H}_1(x)$ is the Struve function and $Y_1(x)$ is the Bessel function of the second kind, with the result:

$$\int_0^\infty dp \ldots \cong -\left(\frac{g_s g_v \pi e^2}{8\varepsilon_0 \hbar}\right) \frac{u\pi}{8\gamma^2} \frac{\partial^2}{\partial |Z|^2} \left[\mathbf{H}_1\left(\frac{2|Z|}{\gamma}u\right) - Y_1\left(\frac{2|Z|}{\gamma}u\right)\right]. \tag{5.30}$$

References

1. N.J.M. Horing, L.Y. Chen, Magnetoimage effects in the van der Waals interaction of an atom and a bounded, dynamic, nonlocal plasmalike medium. Phys. Rev. A **66**, 042905-1–042905-15 (2002)
2. K.W.-K. Shung, Dielectric function and plasmon structure of stage-1 intercalated graphite. Phys. Rev. B **34**, 979–993 (1986)
3. K.W.-K. Shung, Lifetime effects in low-stage intercalated graphite systems. Phys. Rev. B **34**, 1264–1272 (1986)
4. T. Ando, Screening effect and impurity scattering in monolayer graphene. J. Phys. Soc. Jpn. **75**, 074716-1–074716-7 (2006)
5. E.H. Hwang, S. Das Sarma, Dielectric function, screening, and plasmons in two-dimensional graphene. Phys. Rev. B **75**, 205418-1–205418-6 (2007)
6. B. Wunsch, T. Stauber, F. Sols, F. Guinea, Dynamical polarization of graphene at finite doping. New J. Phys. **8**, 318-1–318-15 (2006)
7. I.S. Gradshteyn, I.M. Ryzhik, *Table of Integrals, Series, and Products*, 7th edn. (Academic Press, New York, 2007), p. 345, Eq. (3.366.3)

Chapter 6
Optical Studies of Semiconductor Quantum Dots

H. Yükselici, Ç. Allahverdi, A. Aşıkoğlu, H. Ünlü, A. Baysal, M. Çulha, R. İnce, A. İnce, M. Feeney, and H. Athalin

Abstract Optical absorption (ABS), steady-state photoluminescence (PL), resonant Raman, and photoabsorption (PA) spectroscopies are employed to study quantum-size effects in II–VI semiconductor quantum dots (QDs) grown in glass samples. We observe a size-dependent shift in the energetic position of the first exciton peak and have examined the photoinduced evolution of the differential absorption spectra. The Raman shifts of the phonon modes are employed to monitor stoichiometric changes in the composition of the QDs during growth. Two sets of glass samples were prepared from color filters doped with CdS_xSe_{1-x} and $Zn_xCd_{1-x}Te$. We analyze the optical properties of QDs through the ABS, PL, resonant Raman, and PA spectroscopies. The glass samples were prepared from commercially available semiconductor doped filters by a two-step thermal treatment. The average size of QDs is estimated from the energetic position of the first exciton peak in the ABS spectrum. A calculation based on a quantized-state effective mass model in the strong confinement regime predicts that the average radius of QDs in the glass samples ranges from 2.9 to 4.9 nm for CdTe and from 2.2 to 9.3 nm for $CdS_{0.08}Se_{0.92}$. We have also studied the nonlinear optical properties of QDs by reviewing the results of size-dependent photoinduced modulations in the first exciton band of CdTe QDs studied by PA spectroscopy.

6.1 Introduction

The first observation of quantum size effects in zero-dimensional entities was made by Ekimov and Onushchenko in 1981 [1], who reported a blueshift in the optical absorption (ABS) edge of nanometer-sized CuCl semiconductors. This marked

H. Yükselici (✉)
Department of Physics, Yıldız Technical University, 34210 Davutpaşa, Istanbul, Turkey
e-mail: mhyukselici@gmail.com

H. Ünlü and N.J.M. Horing (eds.), *Low Dimensional Semiconductor Structures*, NanoScience and Technology, DOI 10.1007/978-3-642-28424-3_6,
© Springer-Verlag Berlin Heidelberg 2013

the beginning of an era of new physics called nanophysics or nanotechnology. Semiconductor nanocrystals, often called *quantum dots* (QDs) have been studied extensively for a quarter century due to their potential applications as nonlinear optical devices in optoelectronics, fluorescent labels in bioengineering, and window materials in solar cells [2–5]. Nanometer-sized crystals have distinctive optical properties due to the confinement of charged particles in all three space dimensions. The bandgap can be modified to optimize the optical properties of the nanostructure by controlling its size. The most commonly used method for growing QDs is thermally or chemically controlled precipitation in solid or liquid matrices. CdS_xSe_{1-x} QDs in glass have been most widely studied in a model system for quantum-confinement effects through linear/nonlinear optical methods and structural characterizations such as TEM and SAXS [2, 3, 6–8]. CdTe, another member of group II–VI QDs, is especially important because its bandgap is close to the optimum wavelength for the conversion of solar radiation into electricity. Studies show that it is possible to grow CdTe QDs in glass with high-quality optical properties comparable to those of CdS_xSe_{1-x} QDs.

It has recently been demonstrated through pump-probe spectroscopy that CdTe nanocrystals in glass can be employed as a nonlinear optical switch with a response time less than 1 ps when the pump beam is chopped at a frequency of 3.1 kHz [9]. Optical studies on group II–VI QDs mostly model the first exciton peak in ABS spectra to estimate the size and dispersion of nanocrystals [1,10,11], while a steady-state photoluminescence (PL) spectroscopy has been reserved for investigating trap states [12–15]. Raman scattering measurements are used to obtain direct information about the local composition of the QDs and to eliminate competing crystal stoichiometry effects from the confinement-induced shift of optical spectra. We have studied variously sized samples of CdS_xSe_{1-x} and CdTe QDs in glass, precipitated by solid-phase precipitation. We report the results of our ABS, steady-state PL, and resonant Raman spectroscopies in the study of the growth kinetics of QDs.

There are three size regimes depending on the bulk exciton Bohr radius, as depicted in Fig. 6.1. In the strong confinement regime, all the potentials can be neglected with respect to the kinetic energy and the confinement potential. The electron and hole motions are decoupled and they reduce to those of free particles of effective masses m_e* and m_h*, respectively. In the weak confinement regime, the bulk properties of the semiconductor dominate to a large extent. The Coulomb interaction should not be neglected when the radius R approaches the exciton Bohr radius a_B.

6.2 Solid-Phase Precipitation in Glass

The starting material for growing the nanoparticles was a commercially available color filter glass. The glass as received was first melted at about 1,000°C for 15 min to dissolve the particles and quench the melt rapidly to room temperature. Then

STRONG CONFINEMENT	$R << a_B$
INTERMEDIATE CONFINEMENT	$R \approx a_B$
WEAK CONFINEMENT	$R >> a_B$

II – VI	a_B(nm)
CdS	2.8
CdSe	5.6
CdTe	7.5

$$a_B = a_e + a_h$$

$$a_h = \frac{\in \hbar^2}{m_h^* e^2}$$

$$a_e = \frac{\in \hbar^2}{m_e^* e^2}$$

Fig. 6.1 Various size regimes for semiconductor quantum dots depending on the radius R. Exciton Bohr radii are given for typical II–VI semiconductors; $a_{h(e)}$ is exciton Bohr radius for a hole (electron), $m^*_{h(e)}$ the effective mass for a hole (electron), and $\in$ is dielectric constant of the semiconductor

the glass samples were heat-treated at a temperature below the glass transition temperature to initiate nucleation. Finally, the glass samples were heat-treated at a temperature higher than the glass transition temperature to grow the nanoparticles.

There are three stages identified for the growth of nanocrystals; nucleation takes place by random fluctuations in the local concentration of reactants, followed by diffusion-limited growth in which the radius of the average nanocrystal increases with the square root of heat-treatment time ($R_{ave} \propto t^{1/2}$). Finally, after the available concentration of reactants has dropped below a critical level, Ostwald ripening or coarsening sets in: larger particles grow at the expense of smaller particles with the radius of the average nanocrystal proportional to the cubic root of heat-treatment time ($R_{ave} \propto t^{1/3}$) [10, 16–19]. It is possible to separate the nucleation and growth stages by a two-step heat-treatment procedure. In general, it may be said that the longer the heat-treatment time or the higher the temperature, the larger the nanocrystals grow. The driving force for fluctuation in the concentration of the local reactant is the difference in Gibbs free energy of the initial and final states. If any fluctuation is able to lower the free energy, then the initial condition is unstable. Thus, the only barrier to such fluctuation is the limiting atomic movement. Heat treatment at the glass transition temperature overcomes this barrier and the final stable state is reached [20–22].

After quenching the melt to room temperature, the samples appear colorless. Primary heat treatment below the glass transition temperature does not produce color. The secondary heat treatment above the glass transition temperature produces color. The color progresses to yellow then light orange, brown, and finally red, as the heat treatment time and/or temperature increases. The color is a sign of the production of nanocrystals or QDs. When the samples turn from transparent to a dark-reddish color, it indicates that QDs have formed. In Fig. 6.2, ABS spectra are presented for as-received color filter glass doped with CdSe. This was then melted at $\sim$ 1000°C for 15 min to dissolve the particles, heat-treated at 450°C for 5 h, and then

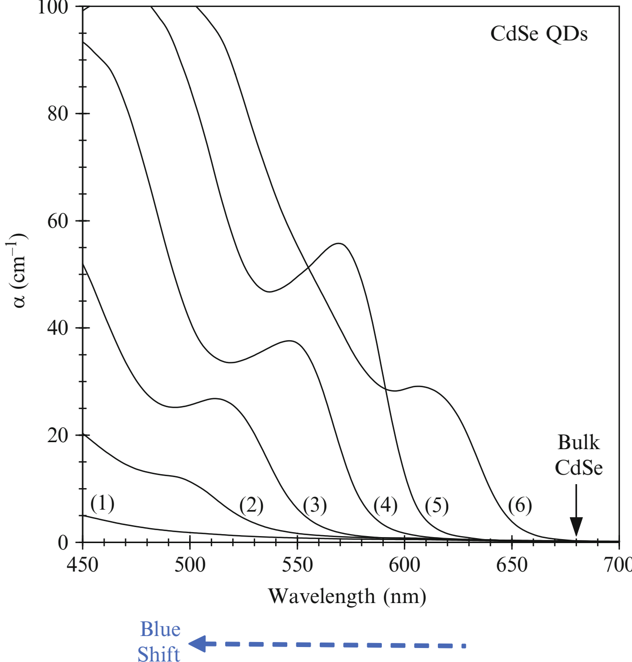

Fig. 6.2 Optical absorption spectra for $CdS_{0.08}Se_{0.92}$ QDs heat-treated at 450°C for 5 h (primary annealing) and then at different temperatures for different periods of time. Details for the samples are given in Table 6.1 below

heat-treated at different temperatures for various periods of time (secondary heat treatment). Details of the samples are given in Table 6.1. As the color progresses or as the QDs grow, an absorption peak appears. The peak is due to the absorption of light by nanocrystals. Its height is proportional to the volume fraction; its shift is proportional to the size of the QDs; and its sharpness is proportional to the size dispersion. The lowest transition energy for the bulk crystal is blueshifted when the size is reduced, indicating a quantum confinement effect.

6.3 Particle-in-a-Box Model to Determine the Average Nanocrystal Radius and Size Distribution

The quantum theory of charged particles whose motions are confined to all three space dimensions within a semiconductor QD embedded in a host matrix has been extensively studied [23–28] and a detailed model presented. Here, a simplified

Table 6.1 Experimental details for CdS_xSe_{1-x} QDs in glass samples

Sample	Color	Radius (nm)	FWHM (nm)	Secondary Annealing
1		–	–	600°C ½ h
2		2.2	–	625°C 1 h
3		2.4	0.33	625°C 2 h
4		2.8	0.38	625°C 4 h
5		3.1	0.39	625°C 8 h
6		4.5	–	650°C 8 h

Average radii were determined from the energetic position of the first transition energy. The particle size distribution was determined by simulating the first exciton peak with a Gaussian absorption band

version of this model is presented to determine the quantized energy levels. The Hamiltonian for charged particles in the nanocrystal is as shown below:

$$H = \frac{\hbar^2}{2m^*_{\mathrm{e(h)}}}\nabla^2 + V_{\mathrm{e(h)}}(\vec{r}_{\mathrm{e(h)}}) - \frac{e^2}{\varepsilon\left|\vec{r}_{\mathrm{e}} - \vec{r}_{\mathrm{h}}\right|} + \cdots$$

The first term is the combined kinetic energy of an electron and a hole, the second term represents confinement potential energies, and the third term is the Coulomb interaction energy between the hole and an electron. There are other terms called surface polarization energy; they represent the self-energy of an electron and hole due to their image charges and the mutual interaction energy between an electron and hole via image charges such as exchange interaction energy and interaction energy between the charge in the nanocrystal and its image charge in the dielectric host (polarization energy). Assuming strong confinement or infinite potential well height, all the interaction terms are negligible except the first two terms in the Hamiltonian, thus the Schrödinger equation for a particle in a spherical box enables quantized energy levels to be found as

$$H\Psi = E\Psi$$

$$E_{(n_{\mathrm{e}},l_{\mathrm{e}}),(n_{\mathrm{h}},l_{\mathrm{h}})} = E_{\mathrm{g}} + \frac{\hbar^2}{2R^2}\left[\frac{x^2_{n_{\mathrm{e}},l_{\mathrm{e}}}}{m^*_{\mathrm{e}}} + \frac{x^2_{n_{\mathrm{h}},l_{\mathrm{h}}}}{m^*_{\mathrm{h}}}\right]$$

The particle in a spherical box model (or quantized-state effective mass model for charged particles in a spherical potential well) predicts a linear relation between $1/R^2$ and E_{1s1s}. If $x_{n;l}$ is the root of the first-order Bessel function $j_1(x_{n;l}) = 0$, the first exciton peak position is given by the relation [29]:

$$E_{\mathrm{1s,1s}}(\mathrm{eV}) = E_{\mathrm{g}}(\mathrm{eV}) + \frac{0.376}{\mu[R(\mathrm{nm})]^2}, \tag{6.1}$$

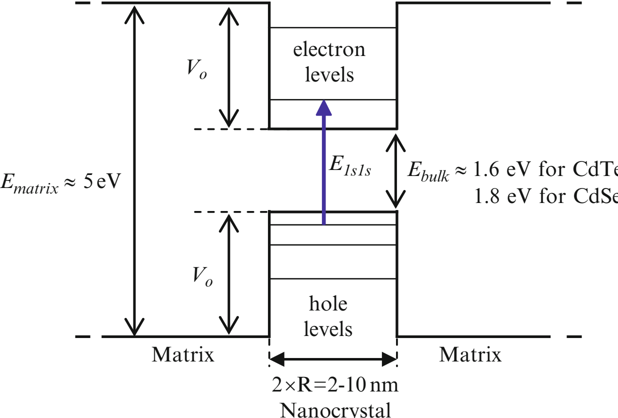

Fig. 6.3 A schematic representation of the energy band diagram for semiconductor quantum dots in glass matrix. The lowest transition energy between a hole and an electron level is denoted by E_{1s1s}. V_o is the finite potential well height

where E_g is the bulk bandgap energy of the semiconductor, μ the reduced mass of an electron–hole pair in units of electron rest mass m_o(kg), and R the average radius of the nanoparticles. The expression for the dielectric confinement energy of an exciton depends on the quantum dot shape. Glass is the dielectric material within which nanoparticles are embedded. The bandgap is approximately 5 eV for glass, 1.6 eV for bulk CdTe, and 1.8 eV for bulk CdSe. A schematic of the energy band diagram is shown in Fig. 6.3. The height of the potential well confining the charged particles (electrons and holes) is finite and may vary depending on the dielectric host.

Employing Mie scattering and effective-medium theory to calculate the ABS coefficient at an energy of $h\upsilon = E$ for the composite (QDs/glass), the ABS coefficient can be expressed as:

$$\alpha_{\mathrm{obs}}(h\nu) = \sum_{R_{\mathrm{min}}}^{R_{\mathrm{max}}} \frac{(2l+1)}{\sigma\sqrt{\pi}} N(R) \exp\left\{-\frac{[E-E(R)]^2}{2\sigma^2}\right\},$$

where $N(R)$ is a Gaussian weighting function for the particle size distribution, $(2l + 1)$ is the oscillator strength of the transition, and σ the standard deviation of the homogeneous broadening.

Each absorption spectrum was analyzed separately and the best fit parameters for average radius and size dispersion were determined. In Fig. 6.4, the average radius is plotted against the heat-treatment time for $n = 1/2$ and 1/3, and in Fig. 6.5, the size dispersion against average radius for CdTe QDs in glass is plotted [30].

The straight line in Fig. 6.4 is the linear fit for the heat treatment times up to 16 h. This is consistent with the diffusion-limited growth, which predicts a linear relation between the average radius and the square root of heat-treatment time. In the second

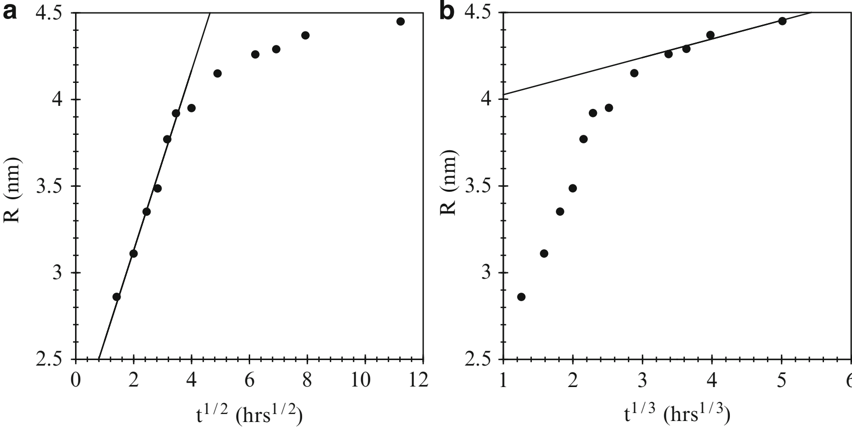

Fig. 6.4 Average nanocrystal radius is plotted against the square root of heat-treatment time in (**a**) and the cubic root of heat-treatment time in (**b**) for CdTe quantum dots in glass. The straight line in (**a**) is the linear fit for heat-treatment times up to 15 h and in (**b**) the linear fit for heat-treatment times greater than 40 h

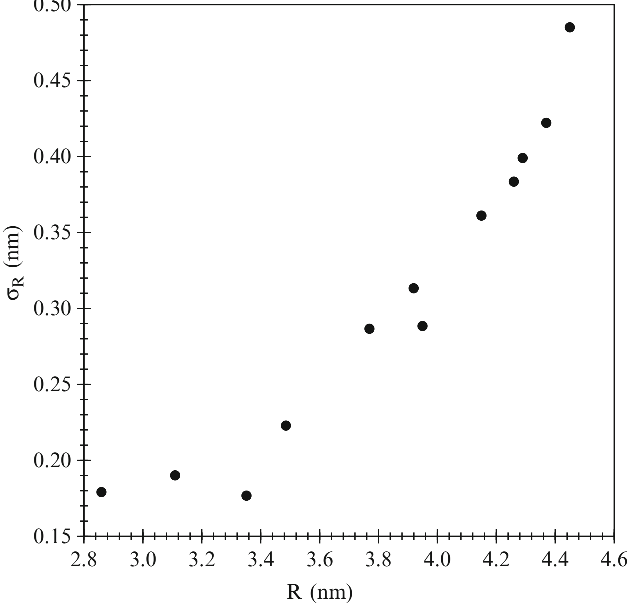

Fig. 6.5 Size dispersion (σ_R) as a function of average nanocrystal radius (R).

graph on the right, the average nanocrystal radius is plotted against the cubic root of heat-treatment time. The straight line is the linear fit for heat-treatment times greater than 40 h, consistent with Ostwald ripening which predicts a linear relation between the radius and the cubic root of the heat-treatment time. The slope of the straight line is proportional to the growth rate. The growth rate decreases slowly as one goes from 15 to 40 h of heat-treatment time. At that intermediate stage, nanocrystals appear to undergo diffusion-limited growth and ripening simultaneously.

As shown in the figure, the size dispersion increases almost linearly with radius above the average nanocrystal radius of around 3.5 nm indicating, perhaps, that growing nucleation centers may be influenced by nearest neighbor QDs so that they spread out dynamically

6.4 Raman and Photoluminescence Spectroscopies

Resonant Raman measurements can determine phonon energy for specific lattice vibrations. Raman scattering measurements were used to directly obtain information about the local composition of the QDs, enabling competing crystal stoichiometry effects to be eliminated from the confinement-induced shift of optical spectra [31]. Resonant Raman spectra excited by an Ar^{+} laser at 514.5 nm are shown in Fig. 6.6 [32]. Heat-treatment times and/or temperature increase are displayed from top to bottom. The ternary compound of CdSSe crystal displays a two-mode behavior in the Raman spectra. The peak near 200 and 300 cm^{-1} wave numbers are due to zone-center longitudinal optical (LO) phonons of CdSe- and CdS-like modes in nanocrystals, respectively. The peak at 206 cm^{-1} in Fig. 6.6 is due to a zone-center LO phonon made of CdSe and the peak position does not shift with time or/and temperature. Therefore, we conclude that the composition does not change with the growth of QDs for CdSe in glass.

In Fig. 6.7, Raman spectra for CdTe QDs in glass are shown. The Raman spectra for doubly heat-treated samples possess a two-peak structure: a lower intensity peak between 157–160 cm^{-1} and a higher intensity peak between 190 and 195 cm^{-1} [33]. Raman peak positions, determined by fitting the experimental data to Gaussian line shapes and linear backgrounds, against heat-treatment time show that the higher intensity peak is blueshifted from $\sim$190 to $\sim$195 cm^{-1} during the first 16 h of secondary heat-treatment time and then redshifted slowly back to its initial value of $\sim$190 cm^{-1}. Previous studies show that Raman peaks shift due to three mechanisms: phonon confinement, lattice contraction, and/or zinc incorporation into nanocrystals [34–40]. Phonon confinement leads to a redshift and lattice contraction to a blueshift in the Raman peak position. Therefore, neither phonon confinement nor lattice contraction alone can explain both the blueshift during the first 16 h and the redshift afterward, observed in Fig. 6.7 for the higher intensity Raman peak during the secondary heat-treatment process. However, zinc incorporation (ejection) into (out of) the nanocrystal during precipitation can alter significantly the LO phonon vibrational frequency.

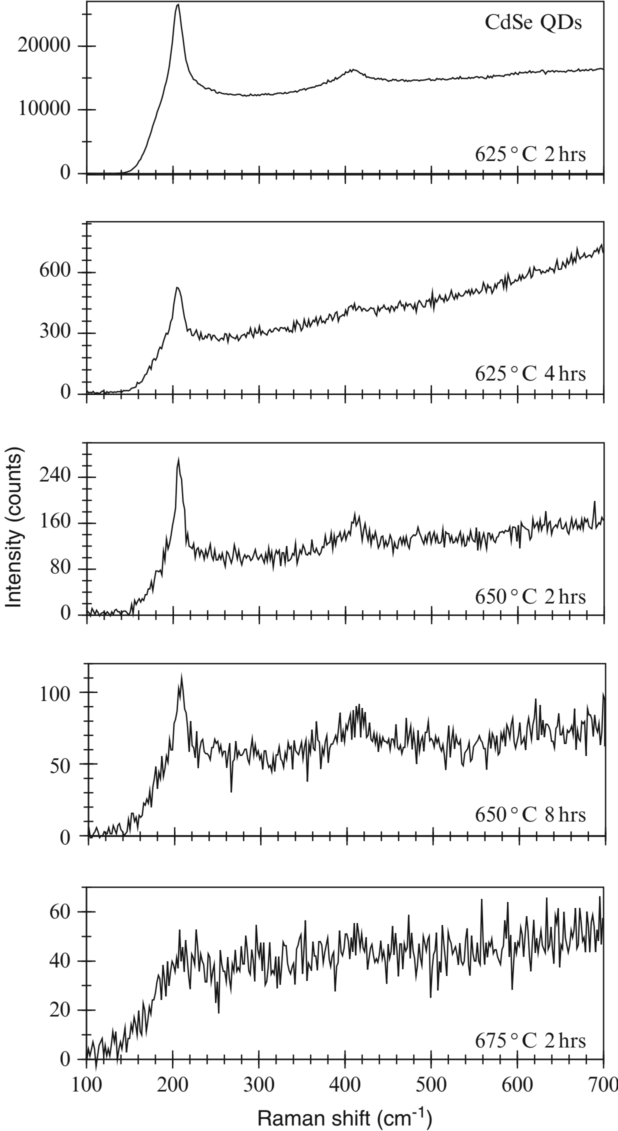

Fig. 6.6 Resonant Raman spectra excited at 514.5 nm for CdSe QDs in glass

Nanocrystals can also be obtained in liquid solutions by the so-called interrupted precipitation method, but the average size cannot be varied easily due to the flexibility of the surrounding medium. Following a previously reported method [41], CdSe QDs in liquid have also been synthesized from a crude/precursor solution containing cadmium acetate, oleic acid, phenyl ether, and triocthylphosphine selenide heated at 170°C for 1 min, under stirring and nitrogen flow. Steady-state PL and absorption

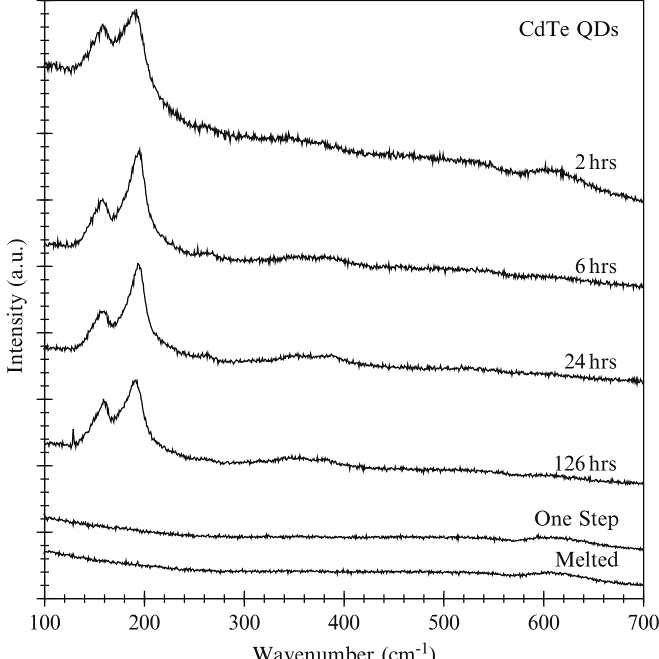

Fig. 6.7 Raman spectra for as-received color filter glass samples doped with CdTe melted at 1,000°C for 15 min (marked 'melted'), heat-treated at 550°C for 16 h, and then at 590°C from 2 to 126 h

spectra for CdTe QDs in glass and CdSe QDs in liquid are presented in Fig. 6.8. On the left graph, we present steady-state PL and absorption spectra for CdTe QDs in glass. The samples marked "Melted" and "One-step" have no PL peaks because QDs are not yet present. On the right graph, steady-state PL spectra for CdSe QDs are presented. The PL spectra display a two-peak structure. PL measurements provide information on trap states [42], which may elucidate the microscopic structure formed in the glass and aqueous solution samples. The PL spectrum has a two-peak structure: the peak close to the asymptotic absorption edge is presumed to be due to surface-assisted electron–hole recombination because it is redshifted by ~100 meV from the absorption edge and the other low-energy peak is due to deep trap levels.

An average radius of ~3.7 nm for CdSe QDs is estimated from the energetic position of the asymptotic absorption edge. The CdTe QDs display a one-peak structure in the PL spectra close to the asymptotic absorption edge of absorption spectrum. The PL structure observed in Fig. 6.8 is identified in terms of surface-assisted electron-hole recombination band because (1) it is slightly redshifted from the first exciton band and (2) the size of the redshift decreases with the dot radius from 166 meV for $R_{\mathrm{ave}} = 3.40$ nm to 92 meV for $R_{\mathrm{ave}} = 4.65$ nm [30].

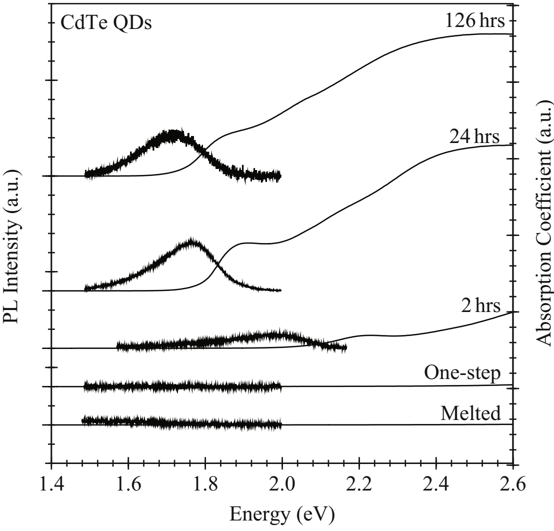

Fig. 6.8 Photoluminescence (PL) spectra of two different size CdTe nanocrystals on the *left-hand side* of the graph. The optical absorption spectra also are included on the *right-hand side* to better interpret the PL spectra

6.5 Photoabsorption spectra

A schematic view of the pump-and-probe experimental setup is presented in Fig. 6.9. A particular spot of the sample is excited with an Ar-ion pump beam at 488 nm and a tungsten-probe beam. The intensities of transmitted probe light with the pump beam, both on and off, were measured and the differential ABS coefficient was calculated according to

$$\Delta\alpha = -\frac{In(I_{\text{with pump}}/I_{\text{without pump}})}{d}$$

where I is the intensity of probe light and d the thickness of the sample.

In Fig. 6.10, the negative of the differential absorption coefficient versus light energy is represented for three different size samples. The main feature observed here is the three-lobed structure. The positive peak is due to the bleaching of the absorption.

There are three possible explanations for the three-lobed structure observed in Fig. 6.10: (1) the thermal effects, which might be induced by the use of a continuous laser source as the pump in the experiments, (2) absorption saturation by state filling, and (3) static electric field (Stark effect). Most notably the modulation of the 1s1s absorption band observed disappears immediately after the pump beam is turned off.

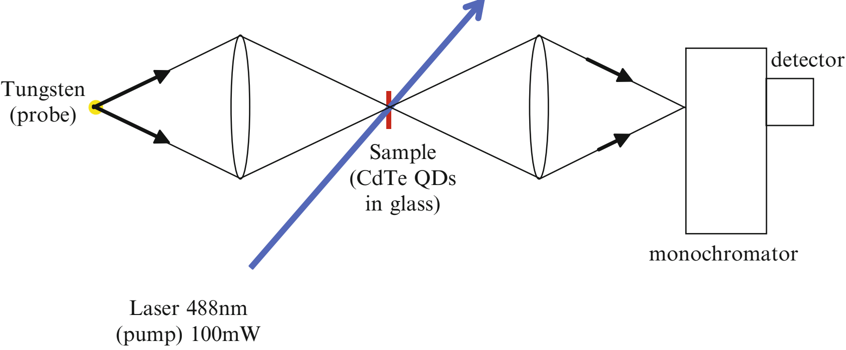

Fig. 6.9 A schematic view of pump-and-probe experimental setup

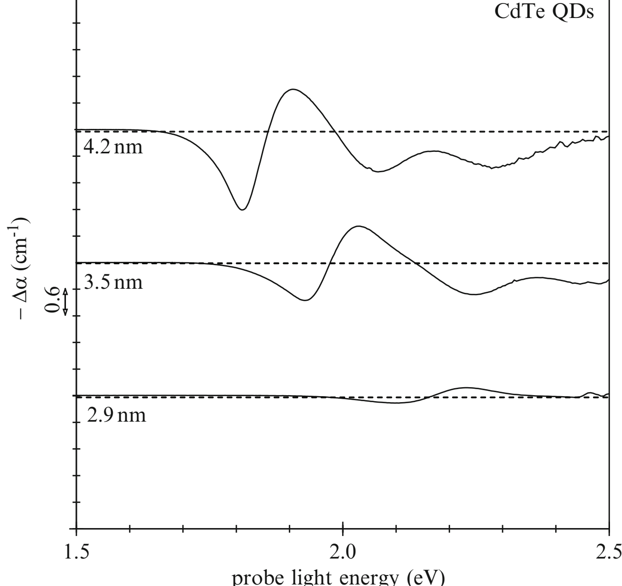

Fig. 6.10 Differential optical absorption (photomodulation) spectra obtained by taking the difference between the optical absorption spectra with laser pump beam (at intensity 100 mW at 488 nm) on and off for three different radii of CdTe QDs in glass [30]

The effect is transient. Therefore, the explanation may be excluded, since thermal effects have long relaxation times [43].

State filling contributes to the redshift to some extent, as discussed in the previous section. It is proposed that the dominant mechanism for the redshift observed here is induced by the electric field of the trap charges at surface states. As observed in Fig. 6.8, the difference between 1s1s and PL bands, and its decrease with size,

support this proposal. As reported in previous studies [44, 45], nanocrystals with large surface-to-volume ratio have surface states to trap charge carriers. The nanocrystal within the electric field of the trapped charges will have a redshifted Gaussian absorption band, as in the electroabsorption spectra of CdS_xSe_{1-x} nanoparticles in glass reported in the literature [46–48].

6.6 Quantum Dots in Solution Phase

The QDs can also be synthesized in solution phase. Due to the fact that the emission and absorption properties of QDs can be tuned by changing their size or core size and shell thickness in a core-shell structure, the customized QDs can be prepared for a specific application. They are excellent fluorescing structures that can be used for imaging and detection applications. Since they are semiconducting materials, they resist photodecomposition upon their exposure to laser light for a longer period of time compared to that of molecules used in fluorescence-based detection schemes and imaging applications. Besides, their quantum yield is much higher than that of molecules, making fluorescence much brighter. With these properties, they are excellent candidates for biomedical, cellular imaging, and many other fluorescence applications. However, their toxicity and low water solubility is their major limitation, especially for biomedical and cellular applications. Therefore, there is an effort to eliminate these limitations by coating the QD surface using several different approaches. The first water-soluble QDs were synthesized in 1998 [49, 50]. In later years, polymer-coated [52], protein- [51, 53], peptide- [54], oligonuclotide- [55], carbohydrate- [56, 57] attached QDs were synthesized. In recent literature, there are reports of a number of ways to overcome the toxicity and water-solubility problems [53, 58, 59].

Since the synthesis temperature for the QD synthesis is very high, the solvents such as -*n*-octylphosphine oxide (TOPO) and hexadecylamine with high boiling points are used. These solvents also help to stabilize and prevent the uncontrolled growth of the QDs, as they are synthesized by their adsorption onto the QDs.

In our laboratories, the synthesis and surface modifications of CdSe/ZnS core-shell QDs are in progress. First, the CdSe QDs are synthesized in TOPO by using $Cd(CH_3COO)_2$ and Se as precursors. The influence of temperature and reaction time on QD size has been investigated. Figure 6.11 shows the evolution of fluorescence emission of QDs formed at different time intervals at 130°C (A), and the size distribution (B) of the CdSe QDs synthesized at three different temperatures: 130°C, 140°C, and 160°C. The size measurements were formed using dynamic light scattering (DLS) (Zeta Sizer Nano SZ, Malvern Instruments Ltd, UK). Figure 6.12 shows the atomic force microscopy (AFM) image of a single CdSe QD. The next step shows coating of the CdSe core with a ZnS shell, which facilitates chemical attachment of biological molecules through the ZnS-S-bond.

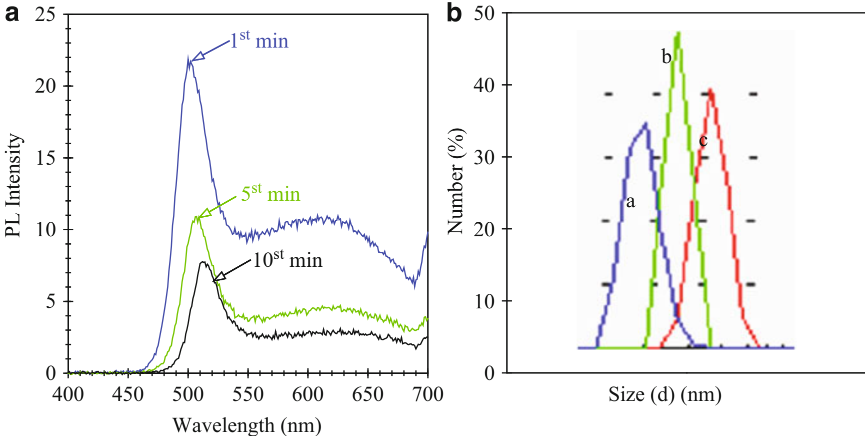

Fig. 6.11 The emission profiles (**a**) of CdSe QDs at different time intervals as they are synthesized at 130°C. The size distribution (**b**) of CdSe QDs at three different temperatures: 130°C (∼2 nm) (**a**), 140°C (∼2.7 nm) (**b**), and 160°C (∼3.6 nm) (**c**)

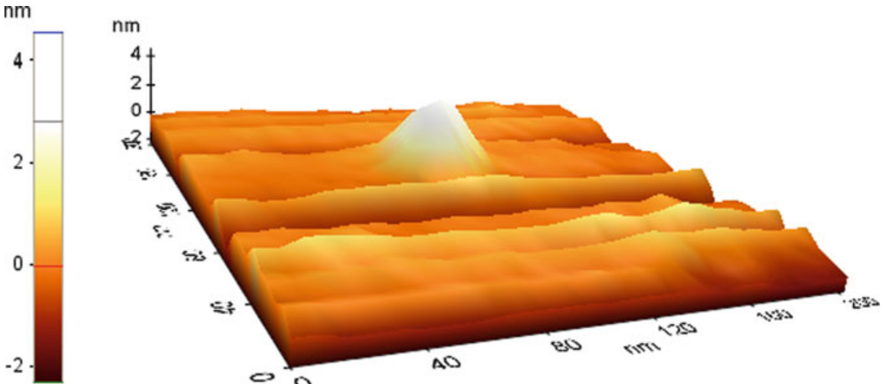

Fig. 6.12 AFM image of the QDs synthesized at 160°C

6.7 Interferometric Analysis of QD Samples

Using a homemade interferometric system, which determines the refractive indexes to within an uncertainty of 10^{-3} [1], the QDs grown in glass samples were analyzed. The UV-VIS spectra of the QD samples determined the approximate size of the QDs. Three such samples of similar QD density were analyzed along with an undoped glass sample to determine a relationship between quantum dot size and refractive index.

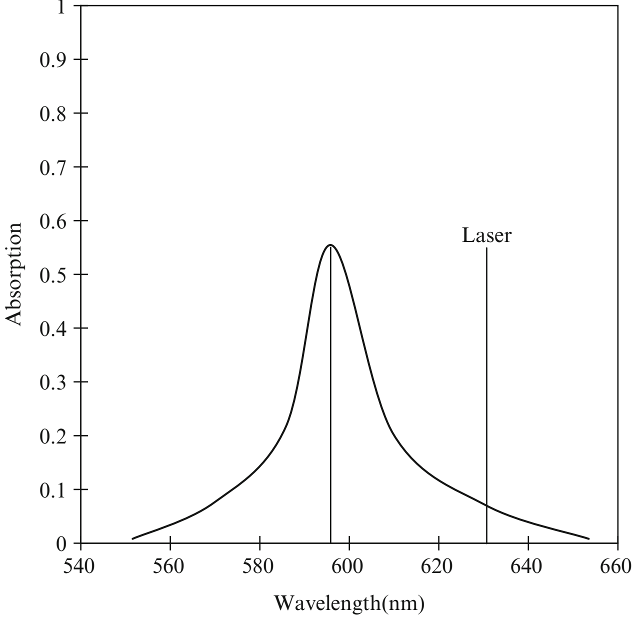

Fig. 6.13 QD absorption profiles showing tail absorption of QD at radius of approximately 2.1 nm

Two of the samples had significantly reduced the refractive indexes compared to the undoped material. Their radii were such that their active absorption range was well away from the laser wavelength. In this case, the QDs act as opaque defects within the sample and depress the refractive index of the glass, depending on the overall density and size of the QDs. Since they operate in the normal dispersion regime, their refractive indexes vary very slowly with the absorption wavelength and, thus, the size (radius).

The other sample, however, was near enough to the laser resonance (632.8 nm) to undergo tail absorption (Fig. 6.13).

Anomalous dispersion (absorption) occurred here causing uncertainty in the refractive index to increase to tenfold compared to that of the previous two samples, and a significant absorption of laser intensity occurred. Absorption wavelengths of the samples are shown schematically in Fig. 6.13 compared to that of the laser resonance.

In Fig. 6.14, the refractive indexes of the samples are shown, compared to their radii, which appears to show a slight decrease in the refractive index with increasing radius; however, more work is required to accurately determine whether this is an accurate description [60].

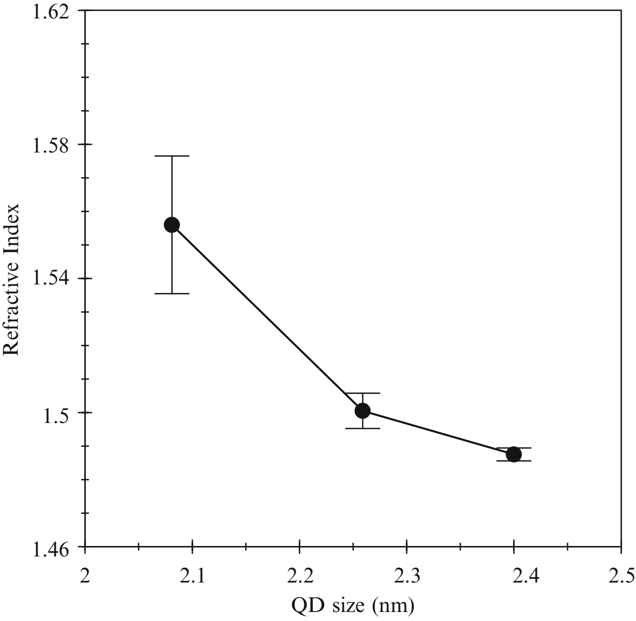

Fig. 6.14 Measured refractive index versus calculated QD radii

References

1. A.I. Ekimov, A.A. Onushchenko, JETP Lett. **34**, 345 (1981)
2. C. Flytzanis, F. Harbe, M.C. Klein, D. Ricard, in *Optics in Complex Systems* (SPIE, Bellingham, 1990)
3. R. Jain, R.C. Lin, J. Opt. Soc. Am. **73**, 647 (1983)
4. A.J. Nozik, Phys. E **14**, 115 (2002)
5. W.C.W. Chan, D.J. Maxwell, X. Gao, R.E. Bailey, M. Han, S. Nie, Curr. Opin. Microbiol. **13**, 40 (2002)
6. N.F. Borelli, D.W. Hall, H.J. Holland, D.W. Smith, J. Appl. Phys. **61**, 5399 (1987)
7. G. Banfi, V. Degiorgio, D. Ricard, Adv. Phys. **47**, 447 (1998)
8. T.M. Hayes, L.B. Lurio, P.D. Persans, J. Phys. Condens. Matter **13**, 425 (2001)
9. L.A. Padilha, A.A.R. Neves, E. Rodriguez, C.L. Cesar, L.C. Barbosa, C.H. Brito Cruz, Appl. Phys. Lett. **86**, 161111 (2005)
10. Y. Fuyu, J.M. Parker, Mater. Lett. **6**, 233 (1988)
11. M.H. Yukselici, J. Phys. Condens. Matter **14**, 1153 (2002)
12. G. Mei, S. Carpenter, P.D. Persans, Solid State Commun. **80**, 557 (1991)
13. K.L. Stokes, P.D. Persans, Mater. Res. Soc. Symp. Proc. **358**, 241 (1995)
14. G. Mei, J. Phys. Condens. Matter **4**, 7521 (1992)
15. D.R.M. Junior, F. Qu, A.M. Alcalde, N.O. Dantas, Microelectronics J. **34**, 643 (2003)
16. J.A. Williams, G.E. Rindone, H.A. McKinstry, J. Am. Ceramic Soc. **64**, 702 (1981)
17. S.A. Gurevich, A.I. Ekimov, A.I. Kudryavtsev, O.G. Lyubliskaya, A.V. Osinskii, A.S. Usikov, N.N. Faleev, Semiconductors **28**, 486 (1994)
18. R.J. Borg, G.J. Dienes, *An Introduction to Solid State Diffusion* (Academic Press, London, 1988)
19. I.M. Lifshitz, V.V. Slyozov, J. Phys. Chem. Solids **19**, 35 (1961)

20. D. Turnbull, in *Solid State Physics*, ed. by F. Seitz, D. Turnbull (Academic, New York, 1956)
21. E.M. Lifshitz, L.P. Pitaevskii, *Physical Kinetics*, vol. 10 (Pergamon, Oxford**,** 1981)
22. R. Kampmann, R. Wagner, *Decomposition of Alloys: The Early Stages* (Pergamon, Oxford, 1984)
23. L. Brus, Appl. Phys. **53**, 465 (1991)
24. V.L. Colvin, K.L. Cunningham, A.P. Alivisatos, J. Chem. Phys. **101**, 7122 (1994)
25. C. Flytzanis, D. Ricard, M.C. SchanneKlein, J. Lumin. **70**, 212 (1996)
26. A.L. Efros, M. Rosen, Annu. Rev. Mater. Sci. **30**, 475 (2000)
27. A.D. Yoffe, Adv. Phys. **50**, 1 (2001)
28. A.V. Rodina, A.L. Efros, A.Y. Alekseev, Phys. Rev. B **67**, 155312 (2003)
29. F. Henneberger, J. Puls, Ch. Spiegelberg, A. Schülzgen, H. Rossman, V. Jungnickel, A.I. Ekimov, Semicond. Sci. Technol. **16**, A41 (1991)
30. M.H. Yukselici, C. Allahverdi, J. Lumin. **128**, 537 (2008)
31. A. Tu, P.D. Persans, Appl. Phys. Lett. **58**, 1506 (1991)
32. B. Can Ömür, A. Aşıkoğlu, Ç. Allahverdi, M.H. Yükselici, J. Mater Sci. 45, 112 (2010)
33. M.H. Yükselici, Ç. Allahverdi, H. Athalin, Mater. Chem. Phys. 119, 218 (2010)
34. Y.N. Hwang, S. Shin, H.L. Park, S.H. Park, U. Kim, H.S. Jeong, E. Shin, D. Kim, Phys. Rev.B **54**, 15129 (1996)
35. H. Yükselici, P.D. Persans, T.M. Hayes, Phys. Rev. B **52**, 11763 (1995)
36. X.S. Zhao, J. Schroeder, P.D. Persans, T.G. Bilodeau, Phys. Rev.B **43**, 12580 (1991)
37. J. Schroeder, M. Silvestri, X.S. Zhao, P. Persans, L.W. Hwang, Mater. Res. Soc. Symp. Proc. **272**, 251 (1992)
38. A. Tu, Ph.D. thesis, Rensselaer Polytechnic Institute (1991)
39. H. Richter, Z.P. Wang, L. Ley, Solid State Commun. **39**, 625 (1981)
40. P.M. Fauchet, I.H. Camphell, Crit. Rev. Solid State Mater. Sci. **14**, 579 (1988)
41. Rong He, Hongchen Gu, Colloids Surf. A: Physicochem. Eng. Aspects **272**, 111 (2006)
42. F. Hache, M.C. Klein, D. Ricard, C. Flytzanis, J. Opt. Soc. Am. B **8**, 1802 (1991)
43. N. Peyghambarian, S.W. Koch, A. Mysyrowicz, *Introduction to Semiconductor Optics* (Prentice-Hall, Enlewood Cliffs, 1993), pp. 333–335
44. V. Esch, B. Fluegel, G. Khitrova, H.M. Gibbs, Xu Jiajin, K. Kang, S.W. Koch, L.C. Liu, S.H. Risbud, N. Peyghambarian, Phys. Rev. B **42**, 7450 (1990)
45. L.A. Padilha, A.A.R. Neves, C.L. Cesar, L.C. Barbosa, C.H.B. Cruz, Appl. Phys. Lett. **85**, 3256 (2004)
46. , S. Nomura, T. Kobayashi, Solid State Commun. **73**, 425 (1990)
47. K.L. Stokes, H. Yukselici, P.D. Persans, Solid State Commun. **92**, 195 (1994)
48. K.L. Stokes, P.D. Persans, Phys. Rev. B **54**, 1892 (1996)
49. WC. Chan, S. Nie, Science **281**, 2016–2018 (1998)
50. M. Bruchez Jr., M. Moronne, P. Gin, S. Weiss, A.P. Alivisatos, Science **281**, 2013–2016 (1998)
51. T. Pellegrino, L. Manna, S. Kudera, T. Liedl, D. Koktysh, AL. Rogach, S. Keller, J. Radler, G. Natile, W.J. Parak, Nano Lett. **4**, 703–707 (2004)
52. K. Hanaki, A. Momo, T. Oku, A. Komoto, S. Maenosono, Y. Yamaguchi, K. Yamamoto, Biochem. Biophys. Res. Commun. **302**, 496–501 (2003)
53. E.R. Goldman, E.D. Balighian, H. Mattoussi, M.K. Kuno, J.M. Mauro, P.T. Tran, G.P. Anderson, J. Am. Chem. Soc. **124**, 6378–6382 (2002)
54. M.E. Akerman, W.C. Chan, P. Laakkonen, S.N. Bhatia, E. Ruoslahti, Proc. Natl. Acad. Sci. USA **99**, 12617–12621 (2002)
55. R. Mahtab, J.P. Rogers, C.J. Murphy, J. Am. Chem. Soc. **117**, 9099–9100 (1995)
56. F. Osaki, F. Kanamori, S. Sando, T. Sera, Y. Aoyama, J. Am. Chem. Soc. **126**, 6520–6521 (2004)
57. Y.F. Chen, T.H. Ji, Z. Rosenzweig, Nano Lett. **3**, 581–584 (2003)
58. R. Savic, L.B. Luo, A. Eisenberg, D. Maysinger, Science **300**, 615–618 (2003)
59. P.L. Soo, L.B. Luo, D. Maysinger, A. Eisenberg, Langmuir **18**, 9996–10004 (2002)
60. R. Ince, E. Sınır, M. Feeney, M.H. Yükselici, A.T. Ince, Opt. Commun. **281**, 3831–3836 (2008)

Chapter 7
Friedel Sum Rule in One- and Quasi-One-Dimensional Wires

Vassilios Vargiamidis, Vassilios Fessatidis, and Norman J. Morgenstern Horing

Abstract We consider the Friedel sum rule (FSR) in the context of scattering in one- and quasi-one-dimensional ballistic wires with a double δ potential. In particular, we analyze the relation between the density of states (DOS) obtained from the energy derivative of the Friedel phase (or the scattering matrix) and that obtained from the Green's function. We show that the local FSR is valid when a correction term is included. Various properties of the one-dimensional local DOS are also discussed.

7.1 Introduction

Densities of states (DOS) are of great relevance and importance in calculations of various physical properties. For example, the thermodynamic properties and electron conduction phenomena depend on the DOS of the system under consideration. The concept of the DOS and its decomposition into partial DOS (PDOS) proved to be useful in studies of electron transport through phase-coherent mesoscopic systems [1–7]. Noise properties, pump current, and heat flow of an adiabatic quantum pump can also be expressed in terms of PDOS [8].

In one-dimensional (1D) or quasi-one-dimensional (Q1D) problems, the local PDOS can be obtained via functional derivatives of the scattering matrix [3–5], the elements of which are calculated from the Fisher-Lee relation [9]. The total local DOS at a given energy can either be obtained by the summation of the local PDOS or by the imaginary part of the diagonal elements of the Green's function. The global DOS, associated with an entire segment of the system, can then be calculated by spatial integration of the local quantity.

N.J.M. Horing (✉)
Department of Physics and Engineering Physics, Stevens Institute of Technology, Hoboken, NJ 07030, USA
e-mail: nhoring@stevens.edu

H. Ünlü and N.J.M. Horing (eds.), *Low Dimensional Semiconductor Structures*, NanoScience and Technology, DOI 10.1007/978-3-642-28424-3_7,

© Springer-Verlag Berlin Heidelberg 2013

However, the global DOS is also related to the elements of the scattering matrix via the Friedel sum rule (FSR) [10, 11]. Although it is approximately valid in certain regimes [3, 6, 12, 13], the FSR can lead to the exact DOS when a correction term is included. The deviation between the DOS and the energy derivative of the Friedel phase was discussed previously for several model systems [3, 12, 13].

The aim of this chapter is to investigate the range of validity of the FSR in 1D and Q1D scattering, using the simple model of a double δ-function potential. The DOS is first calculated directly from the Green's function and then from the derivative of the Friedel phase with respect to particle energy. It is shown that the FSR is perfectly valid in both 1D and Q1D wires when a correction term is included. In addition, it is shown that the peaks of the DOS coincide with the peaks of the transmission probability. Some important properties of the local DOS are also analyzed in the 1D case. Although the 1D scattering is a simple textbook problem; it, nevertheless, serves the purpose of illustrating important aspects of the local DOS, which are in direct connection with present-day modeling of experimental data of mesoscopic samples [14]. It also serves the purpose of testing the validity of the FSR in a simple model potential.

The chapter is organized as follows. In Sect. 7.2, the local and integrated local DOS are examined in a 1D ballistic wire with two δ-function scatterers and the FSR is analyzed. In Sect. 7.3, we investigate the validity of the FSR in a Q1D wire. Section 7.4 summarizes the relevant results.

7.2 Local Density of States and Friedel Sum Rule for the One-Dimensional Wire

We consider a ballistic 1D conducting channel with two δ barriers of equal strength, which are placed symmetrically with respect to the origin. The scattering matrix S in the particle energy E is represented as a 2×2 symmetric matrix with elements $S_{\alpha\beta}$. The indices α and β label the outgoing and incoming scattering channels, respectively. They take the values 1 and 2 to designate the left and right asymptotic regions. Specifically, $S_{11}(S_{22})$ is the reflection amplitude back into the left (right) region for carriers incident from the left (right) asymptotic region. Also, $S_{21}(S_{12})$ is the transmission amplitude from the left (right) lead to the right (left) lead. Due to symmetry, $S_{11} = S_{22}$ and $S_{21} = S_{12}$. The reflection and transmission probabilities are determined as $R = |S_{11}|^2$ and $T = |S_{21}|^2$, respectively.

The elements of the scattering matrix can be obtained from the Fisher-Lee relation [9] as:

$$S_{\alpha\beta}(E) = -\delta_{\alpha\beta} + i\hbar\sqrt{v_\alpha v_\beta}\, G(x_\alpha, x_\beta; E) \tag{7.1}$$

where $v_\alpha = \hbar k_\alpha / m$ is the particle velocity in lead α and v_β is the velocity in lead β, while $G(x_\alpha, x_\beta; E)$ is the retarded single-particle Green's function. Since the potential is uniform (except for the two δ-barriers), the wave numbers are equal,

$|k_\alpha| = |k_\beta| = |k|$, and related to the energy by $E = \hbar k^2/2m$. The local PDOS, $\nu_{\alpha\beta}(x, E)$, are calculated in terms of the scattering-matrix elements and the Green's function [3] as:

$$\nu_{\alpha\beta}(x, E) = -\frac{\hbar\sqrt{v_\alpha v_\beta}}{4\pi}\left[S^*_{\alpha\beta}(E)G(x_\alpha, x; E)G(x, x_\beta; E) + H.c.\right], \tag{7.2}$$

Together with (7.1), the last equation expresses the local PDOS fully in terms of the Green's function. Having obtained the local PDOS, we can calculate the total local DOS, $\nu(x, E)$, by adding the local PDOS over all scattering channels of the system:

$$\nu(x, E) = \sum_{\alpha\beta} \nu_{\alpha\beta}(x, E) \tag{7.3}$$

However, the total local DOS can also be calculated from the imaginary part of the diagonal elements of the Green's function:

$$\nu(x, E) = -\frac{1}{\pi}\mathrm{Im}\left\{G(x, x; E)\right\}, \tag{7.4}$$

The DOS, $\rho(E)$, can then be obtained by spatially integrating over the region confined by the two δ-barriers:

$$\rho(E) = \int_{-a}^{a} \mathrm{d}x\, \nu(x, E) = -\frac{1}{\pi}\int_{-a}^{a} \mathrm{d}x\, \mathrm{Im}\{G(x, X, ; E)\}. \tag{7.5}$$

On the other hand, the DOS is related to the scattering matrix via the FSR as:

$$\rho(E) = \frac{1}{\pi}\frac{\partial\theta_f(E)}{\partial E} + \mathrm{Im}\left\{\frac{S_{11}(E) + S_{22}(E)}{4\pi E}\right\} \tag{7.6}$$

where $\theta_\mathrm{f}(E)$ is the Friedel phase defined by:

$$\theta_\mathrm{f}(E) = \frac{1}{2i}\ln \mathrm{Det}\{S(E)\} \tag{7.7}$$

In the following, we will denote the right-hand side of (7.6) by $\rho_\mathrm{f}(E)$, i.e., $(1/\pi)(\partial\theta_\mathrm{f}/\partial E) + \mathrm{Im}\{(S_{11} + S_{22})/4\pi E\} = \rho_\mathrm{f}(E)$.

Note that in the usual formulation of the FSR [15–17] only the first term appears on the right-hand side of (7.6). This is due to the fact that the FSR measures the variation of the DOS of the whole space due to the presence of a scattering potential in a finite interval of space. However, here we consider the local DOS integrated in the scattering region, $[-a, a]$.

Before presenting an analysis of the FSR, we first discuss the local DOS as derived from the Green's function.

7.2.1 Local Density of States

The scattering problem defined above is associated with the Hamiltonian

$$H = -\frac{\hbar^2}{2m}\frac{\mathrm{d}^2}{\mathrm{d}x^2} + U(x), \tag{7.8}$$

where $U(x)$ is the scattering potential given by:

$$U(x) = V\delta(x+a) + V\delta(x-a), \tag{7.9}$$

with $V \geq 0$, and $\delta(x)$ is the Dirac δ-function. For the above Hamiltonian, the retarded Green's operator, $G = (E - H + i0^+)^{-1}$, can be expressed in position representation [18] as a linear integral equation:

$$G(x,x';E) = G^{(0)}(x,x';E) + \int dx'' G^{(0)}(x,x'';E)U(x'')G(x'',x';E). \tag{7.10}$$

The Green's function can be interpreted as the quantum mechanical probability amplitude for the propagation of the particle from x' to x. Since we are interested only in scattering states, we focus on the continuous part of the spectrum of H. The free particle Green's function is given by $G^{(0)}(x,x';E) = (-i/\hbar v)\mathrm{e}^{ik|x-x'|}$ with the particle velocity $v = \hbar k/m$. The solution of (7.10) proceeds in a straightforward manner and the resulting expression is:

$$G(x,x';E) = \left(\frac{1}{i\hbar v}\right)\mathrm{e}^{ik|x-x'|} - \left(\frac{1}{i\hbar v}\right)\mathrm{e}^{ik|x+a|}\frac{w(i-w)\mathrm{e}^{ik|a+x'|} + w^2\mathrm{e}^{2ika}\mathrm{e}^{ik|a-x'|}}{(1+iw)^2 + w^2\mathrm{e}^{4ika}}$$
$$-\left(\frac{1}{i\hbar v}\right)e^{ik|x-a|}\frac{w^2e^{2ika}e^{ik|a+x'|} + w(i-w)e^{ik|a-x'|}}{(1+iw)^2 + w^2e^{4ika}}, \tag{7.11}$$

where we introduced the dimensionless quantity $w = V/\hbar v$. With the help of the Green's function, we can easily obtain the transmission and reflection amplitudes from the Fisher-Lee relation (7.1) as:

$$t(E) = S_{21}(E) = \frac{\mathrm{e}^{2ika}}{(1+iw)^2 + w^2\mathrm{e}^{4ika}}, \tag{7.12}$$

and

$$r(E) = S_{11}(E) = \frac{w(w-i) - w(w+i)\mathrm{e}^{4ika}}{(1+iw)^2 + w^2\mathrm{e}^{4ika}} \tag{7.13}$$

With the help of (7.11), (7.12), and (7.13) the diagonal elements of the Green's function in the three regions can be expressed as:

$$G(x,x;E) = \left(\frac{1}{i\hbar v}\right)\times\begin{cases} 1 + r(E)e^{-2ik(x+a)}, & (x \leq -a) \\ 1 - t(E)[2w(i-w)\cos(2kx)+2w^2e^{2ika}], & (-a < x < a) \\ 1 + r(E)e^{2ik(x-a)}, & (x \geq a). \end{cases} \tag{7.14}$$

It is interesting to mention here that from the knowledge of the Green's function, one can not only calculate the local DOS from (7.4) and the scattering amplitudes from (7.1), but also other quantities, such as the characteristic times (i.e., traversal, reflection, and dwell times) for the motion of a particle in the presence of a scattering potential.

The local DOS can be obtained from (7.4) but the resulting expression is lengthy. However, in the region between the two δ-barriers, it simplifies considerably and is given by:

$$v(x,E) = \frac{2}{hv}T(1+2w^2) - \frac{4w}{hv}T[w\cos(2ka) - \sin(2ka)]\cos(2kx), \tag{7.15}$$

where $h = 2\pi\hbar$ is Planck's constant and $T = |t|^2$ is the transmission probability.

In the numerical calculations, we set $\hbar = 1$ and $m = 1/2$, yielding [19] an energy unit $\varepsilon_0 = 17.7$ meV and a length unit $l_0 = 5.7$ nm.

In Fig. 7.1a, we show the transmission probability plotted versus the incident electron energy for $V = 2.5\varepsilon_0 l_0$ and $a = 2.5l_0$. Note that the energies of the transmission peaks can be found by solving, numerically, the transcendental equation:

$$\cot z = -\frac{z_0}{z}, \tag{7.16}$$

where $z = kL$, $z_0 = VL/2$, and we have set $L = 2a$ for the distance between the δ-barriers.

In Fig. 7.1b, we show the local PDOS and total local DOS [$v_{\alpha\beta}$ and v, in units of $(\varepsilon_0 l_0)^{-1}$] plotted versus x/λ. In this calculation, we set $E = 0.2823\varepsilon_0$ for which $T = 0.5$, while the rest of the parameters are the same as in (a). For this energy value, the particle wavelength is $\lambda = 2.36L$. The two vertical arrows, located at $x = \pm L/2$, are schematic representations of the two δ potentials. The behavior of the local PDOS and total local DOS between the two barriers is different from their behavior in the region outside the barriers. On the left (right) of the barriers, the shape of $v_{\alpha\beta}$ and v is determined only by left (right)-injected states, which give rise to Friedel-like oscillations. In fact, on the left (right) of the barriers, the right (left)-injected states contribute as a constant to $v_{\alpha\beta}$ and v. We remark here that the diagonal PDOS, $v_{\alpha\alpha}$, which are associated with reflection, can be negative. But the off-diagonal elements, $v_{\alpha\beta}$ ($\alpha \neq \beta$), which are associated with transmission, are positive. Note that due to symmetry, $v_{\alpha\beta} = v_{\beta\alpha}$.

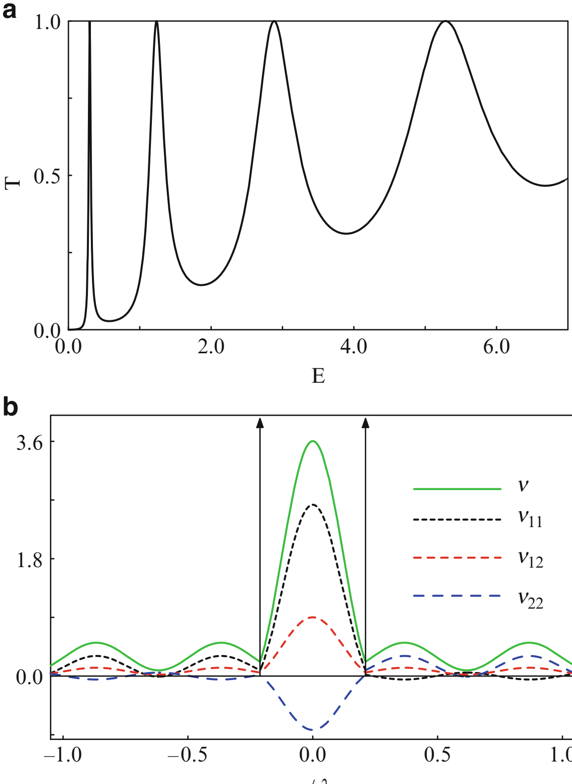

Fig. 7.1 (**a**) Transmission probability T through a double δ-barrier system vs incident electron energy (E, in units of ε_0). The δ-barriers (shown schematically by the vertical arrows) are placed symmetrically at $a = \pm 2.5 l_0$, having equal strengths $V = 2.5\varepsilon_0 l_0$. (**b**) Local partial densities of states $\nu_{\alpha\beta}$ ($\alpha = 1, 2$ and $\beta = 1, 2$), and total local DOS ν [in units of $(\varepsilon_0 l_0)^{-1}$] vs. the dimensionless parameter x/λ, where λ is the wave length. We have used the energy value $E = 0.2823\varepsilon_0$ for which $T = 0.5$

In the region between the barriers, there is a contribution both from left- and right-injected states, which may produce oscillatory behavior due to interference effects. This is illustrated in Fig. 7.2, in which the total local DOS [ν, in units of $(\varepsilon_0 l_0)^{-1}$] is plotted versus the dimensionless parameter x/L for several values of energy. The rest of the parameters are the same as in Fig. 7.1. The solid (green) line corresponds to the energy of the first transmission peak in Fig. 7.1a ($E = 0.2981\varepsilon_0$) for which the wavelength is $\lambda = 2.3L$. The long-dashed (red) line, which exhibits oscillatory behavior between the barriers, corresponds to the second transmission peak ($E = 1.23\varepsilon_0$) for which $\lambda = 1.12L$. In fact, the number of these oscillations increases by one at every consecutive transmission peak. When a perfect transmission occurs, we note that the Friedel-like oscillations, which are associated with reflection, vanish. On the other hand, the short-dashed (blue) line corresponds to the first transmission minimum [$T = 0.1$ in Fig. 7.1a], which occurs at $E = 0.49\varepsilon_0$. As expected, the total local DOS between the δ-barriers is greatly suppressed at the transmission minimum. However, outside the barriers, it exhibits oscillations due to large reflection.

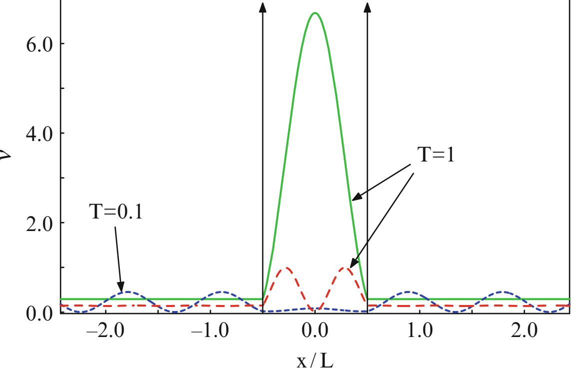

Fig. 7.2 Total local density of states [ν, in units of $(\varepsilon_0 l_0)^{-1}$] vs. the dimensionless parameter x/L, where $L = 2a$ is the distance between the two δ-barriers. The δ-barriers are shown schematically by the *vertical arrows*. The values of V and L are those used in Fig. 7.1. The *solid* (*green*) *line* corresponds to the energy of the first transmission peak, while the long-dashed (*red*) *line* corresponds to the energy of the second transmission peak in Fig. 7.1a. The *short-dashed* (*blue*) line corresponds to the energy of the first transmission minimum

7.2.2 Friedel Sum Rule

As mentioned above, one way to obtain the DOS is via the Green's function of the system, i.e., (7.5). Since we are interested in the DOS between the two barriers, a simple integration of the expression given in (7.15) yields

$$\rho(E) = \frac{2L}{h\nu} T(1 + 2w^2) - \frac{wT}{\pi E} \sin(2ka)[w\cos(2ka) - \sin(2ka)]. \tag{7.17}$$

On the other hand, the DOS is related to the energy derivative of the Friedel phase via the FSR, i.e., (7.6). The essence of the FSR is to count the number of states in the scattering region by counting the resonant peaks of the phase derivative [10–12, 20]. Although the validity of the FSR has been demonstrated for several 1D model systems [12] in the WKB limit, there are cases in which it fails to count the states correctly; for example, in the case of certain graphs [20], the FSR fails due to the degeneracies in the spectrum.

We compare now the exact expression for the DOS as derived from the Green's function (i.e., 7.17) with the DOS obtained from the FSR. We demonstrate below that, if the correction (second) term is retained in (7.6), the FSR is perfectly valid. If the correction term is omitted, the FSR still holds, except for a small deviation at the low-energy transmission minima.

In order to be more precise, we first write the scattering matrix as:

$$S(E) = \begin{pmatrix} r(E) & t'(E) \\ t(E) & r'(E) \end{pmatrix}. \tag{7.18}$$

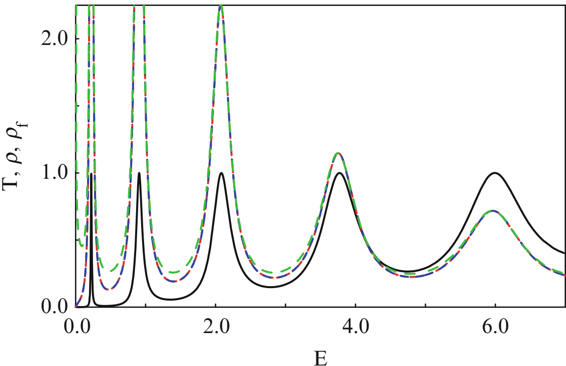

Fig. 7.3 Transmission probability T [*solid* (*black*) *line*], density of states ρ [*dotted* (*red*) *line*], ρ_{f} [*short-dashed* (*blue*) *line*], and ρ_{f} without the correction term [*long-dashed* (*green*) *line*] in units of ε_0^{-1} vs incident electron energy (E, in units of ε_0) for the double δ-barrier model. Note that the Friedel sum rule is valid. If the correction term is omitted, there is a small deviation between ρ and ρ_{f} at the low-energy transmission minima, which, as the energy increases, becomes negligible. Here, $V = 3\varepsilon_0 l_0$ and $a = 3l_0$

Since time-reversal and inversion symmetries hold, one has additionally $t(E) = t'(E)$ and $r(E) = r'(E)$. It can then easily be shown that the Friedel phase can be expressed in terms of the transmission amplitude as:

$$\theta_{\mathrm{f}}(E) = \frac{1}{2i} \ln\left[-\frac{t(E)}{t^*(E)}\right]. \tag{7.19}$$

With the help of (7.19), one can write the right-hand side of (7.6) as:

$$\rho_{\mathrm{f}}(E) = \frac{t^*(E)}{2\pi i t(E)} \frac{\partial}{\partial E}\left[\frac{t(E)}{t^*(E)}\right] + \mathrm{Im}\left\{\frac{r(E)}{2\pi E}\right\}. \tag{7.20}$$

In Fig. 7.3 we show the exact DOS, $\rho(E)$, given by (7.17) [dotted (red) line], $\rho_{\mathrm{f}}(E)$, given by (7.20) [short-dashed (blue) line], and $\rho_{\mathrm{f}}(E)$ with the correction term omitted [long-dashed (green) line] as functions of energy. The solid (black) line shows the transmission probability plotted versus energy. The parameter values are $V = 3\varepsilon_0$ and $a = 3l_0$. We notice that the FSR is valid over the whole energy range. Note also the generally good agreement between the exact DOS, $\rho(E)$, and the DOS, $\rho_{\mathrm{f}}(E)$, calculated from the FSR with the correction term omitted. The only deviation occurs at the low-energy transmission minima. However, as the energy increases the deviation becomes gradually negligible. In addition, the energy values of the transmission peaks coincide with the energies of the peaks in the DOS. We also remark that, from the DOS, one can also obtain the dwell time, $\tau_{\mathrm{D}}(E)$, in the scattering region as $\tau_{\mathrm{D}}(E) = \pi\hbar\rho(E)$. Thus, a peak in the DOS essentially implies a peak in the dwell time.

7.3 Friedel Sum Rule in a Quasi-One-Dimensional Wire

We consider now a ballistic uniform quantum wire in which electrons are confined along the y direction (transverse direction) but are free to propagate along the x direction. The Hamiltonian can be written as:

$$H = -\frac{\hbar^2}{2m}\left(\frac{\partial^2}{\partial x^2} + \frac{\partial^2}{\partial y^2}\right) + V_c(y) + U(x, y), \tag{7.21}$$

where $V_c(y)$ is the confining potential taken to be an infinite square well (i.e., $V_c(y) = 0$ for $0 \leq y \leq W$ and infinite otherwise). The scattering potential is that of two δ-function scatterers with equal strengths γ, which are located at $x = \pm a$,

$$U(x, y) = \gamma\delta(y - y_i)[\delta(x + a) + \delta(x - a)], \tag{7.22}$$

where y_i is the lateral position of the scatterers.

The energy eigenvalues of the unperturbed Hamiltonian $H_0 = H - U$ are given by $E = E_n + (\hbar^2 k_n^2/2m)$, where n is the subband index, and $E_n = n^2 E_1$ are the subband energies with $E_1 = \hbar^2\pi^2/2mW^2$ and $n = 1, 2, 3, \ldots$.

For the above Hamiltonian, the retarded Green's operator, $G = (E - H + i0^+)^{-1}$, can be expressed as an integral equation:

$$\begin{aligned} G(x, y; x', y'; E) = {} & G^{(0)}(x, y; x', y'; E) \\ & + \int \mathrm{d}x'' \int \mathrm{d}y'' G^{(0)}(x, y; x'', y''; E) U(x'', y'') \\ & G(x'', y''; x', y'; E), \end{aligned} \tag{7.23}$$

where $G^{(0)}(x, y; x', y'; E)$ is the Green's function of the unperturbed Hamiltonian. The solution of (7.23) proceeds similarly to the 1D case. The resulting expression takes the form:

$$\begin{aligned} G(x, y; x', y'; E) = {} & G^{(0)}(x, y; x', y'; E) \\ & + \gamma G^{(0)}(x, y; -a, y_i; E) \frac{(1 - \Xi_1) G^{(0)}(-a, y_i; x', y'; E) + \Xi_2 G^{(0)}(a, y_i; x', y'; E)}{(1 - \Xi_1)^2 - \Xi_2^2} \\ & + \gamma G^{(0)}(x, y; a, y_i; E) \frac{\Xi_2 G^{(0)}(-a, y_i; x', y'; E) + (1 - \Xi_1) G^{(0)}(a, y_i; x', y'; E)}{(1 - \Xi_1)^2 - \Xi_2^2} \end{aligned} \tag{7.24}$$

where we introduced the quantities Ξ_1 and Ξ_2 defined by:

$$\Xi_1 = -i \sum_{n=1}^{\infty} |\Phi_n(y_i)|^2 w_n, \tag{7.25}$$

and

$$\Xi_2 = -i \sum_{n=1}^{\infty} |\Phi_n(y_i)|^2 w_n \mathrm{e}^{2ik_n a}, \tag{7.26}$$

which depend on the number of channel modes $\Phi_n(y)$ included in the calculation. Also, $w_n = \gamma/\hbar v_n$ is a dimensionless quantity with v_n the particle velocity in channel mode n.

We will be interested in the single-subband regime $E_1 < E < E_2$, in which only the first mode propagates along the wire while the higher (evanescent) modes may contribute via tunneling. This contribution becomes especially important when the electron energy E approaches the bottom of the second subband E_2. In this single-channel transport regime, the transmission amplitude is found to be:

$$t_{11}(E) = \mathrm{e}^{2ika}\left[1 + \frac{2m\gamma}{ik_1\hbar^2}|\Phi_1(y_i)|^2 \frac{1 - \Xi_1 + \Xi_2\cos(2k_1 a)}{(1-\Xi_1)^2 - \Xi_2^2}\right] \tag{7.27}$$

The lowest four modes have been kept in the numerical calculation. However, one can either explicitly include higher evanescent modes in Ξ_1 and Ξ_2, or incorporate their effect into a renormalized value of the scattering strength [21]. We found that the validity of the FSR is independent of the number of evanescent modes.

In the following, the width of the wire is taken to be $W = 3l_0$ and, for convenience, we express all energies in units of E_1.

The DOS between the two δ-function scatterers is now given by:

$$\rho(E) = -\frac{1}{\pi}\int_{-a}^{a}\mathrm{d}x \int_0^W \mathrm{d}y \mathrm{Im}\{G(x,y;x,y;E)\}, \tag{7.28}$$

which is a generalization of (7.5). On the other hand, the scattering matrix is still a 2×2 symmetric matrix, i.e., it is identical to that given in (7.18) with the replacement $r \to r_{11}$ and $t \to t_{11}$. The Friedel phase can then be written as in (7.19) with $t \to t_{11}$.

In Fig. 7.4 we show the exact DOS, $\rho(E)$, obtained from (7.28) [dotted (red) line], $\rho_\mathrm{f}(E)$ [short-dashed (blue) line], and $\rho_\mathrm{f}(E)$ with the correction term omitted [long-dashed (green) line] as functions of the incident electron energy. The solid (black) line shows the transmission probability of the Q1D wire plotted versus the electron energy over the first subband. Here, we chose $\gamma = 9\varepsilon_0 l_0^2$, $a = 5.3l_0$, and $y_i = (5/12)W$. We notice that, as in the 1D case, the FSR is valid in the Q1D wire. However, when the electron energy approaches the second subband minimum (i.e., $E \to E_2$) both ρ and ρ_f grow rapidly. This is due to the fact that the scattering properties of a quantum wire are determined primarily by the shape of the lowest evanescent mode around the scattering centers [21]. In fact, in the limit $E \to E_2$, the decay length $1/k_2$ of the evanescent mode (where $k_2 = [2m(E_2 - E)]^{1/2}/\hbar$ is the evanescent wave vector) and the evanescent DOS both become infinite due to the rapid population of the second subband. This is a general characteristic of Q1D scattering and has also been found in the particular case of one δ-function scatterer

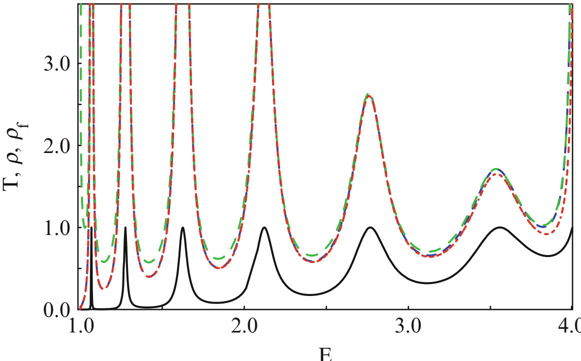

Fig. 7.4 Transmission probability T [*solid* (*black*) *line*], density of states ρ [*dotted* (*red*) *line*], ρ_{f} [*short-dashed* (*blue*) *line*], and ρ_{f} without the correction term [*long-dashed* (*green*) *line*] in units of E_1^{-1} vs incident electron energy (E, in units of E_1) for two repulsive δ-function scatterers in a ballistic quantum wire. The width of the wire is $W = 3l_0$, while the δ-function scatterers are placed symmetrically at $a = \pm 5.3l_0$, having equal strengths, $\gamma = 9\varepsilon_0 l_0^2$, and equal transversal positions $y_i = (5/12)W$. Similarly to the 1D case, the FSR is valid while, if the correction term is omitted, there is a small deviation at the low-energy transmission minima

in a ballistic Q1D wire [21]. We also note that, even if the correction term is omitted, $\rho_{\mathrm{f}}(E)$ is still in good agreement with $\rho(E)$ except at the low-energy transmission minima. In addition, the energies at which the transmission probability has peaks coincide with the energies of the peaks in the DOS.

The above-mentioned behavior of the DOS is in fact the main difference from the 1D case; namely, if the electron energy is away from the second subband threshold in a Q1D wire with two repulsive scatterers, the behavior of the DOS is similar to that in the 1D case.

7.4 Summary

We have investigated various features of the local FSR in 1D and Q1D ballistic wires with a double δ-potential. In both cases, the exact DOS was compared with the energy derivative of the Friedel phase. The 1D local DOS was also discussed.

In both 1D and Q1D wires with repulsive scatterers, our analysis revealed that: (1) the FSR is valid when the correction term is included and (2) the energy values that determine the peaks in the transmission probability coincide with the energies of the peaks in the DOS. We remark that, in the absence of the correction term, the FSR is still valid except for small deviations at the low-energy transmission minima.

The 1D local DOS and its partial contributions were also examined. The vanishing of the Friedel-like oscillations was demonstrated for energies at which the transmission probability becomes unity. To this end, we emphasize that the FSR

plays an important role in mesoscopic physics because it allows us to express, for instance, the charge distribution in terms of the scattering properties. In this context, local electronic properties (probed by scanning tunneling microscopy) can be used to relate the conductance correction due to the charged scanning tip with the local DOS in mesoscopic structures [14].

References

1. M. Büttiker, J. Phys. Condens. Matter **5**, 9361 (1993)
2. M. Büttiker, H. Thomas, A. Prêtre, Z. Phys. B **94**, 133 (1994)
3. V. Gasparian, T. Christen, M. Büttiker, Phys. Rev. A **54**, 4022 (1996)
4. M. Brandbyge, M. Tsukada, Phys. Rev. B **57**, R15088 (1998)
5. S. Souma, A. Suzuki, Phys. Rev. B **65**, 115307 (2002)
6. S. Bandopadhyay, P.S. Deo, Phys. Rev. B **68**, 113301 (2003)
7. M.L. Ladrón de Guevara, P.A. Orellana, Phys. Rev. B **73**, 205303 (2006)
8. M. Moskalets and M. Büttiker, Phys. Rev. B **66**, 035306 (2002).
9. D.S. Fisher, P.A. Lee, Phys. Rev. B **23**, 6851 (1981)
10. R. Dashen, S.-K. Ma, H.J. Bernstein, Phys. Rev. **187**, 345 (1969)
11. Y. Avishai, Y.B. Band, Phys. Rev. B **32**, 2674 (1985)
12. T. Taniguchi, M. Büttiker, Phys. Rev. B **60**, 13814 (1999)
13. A. Levy Yeyati, M. Büttiker, Phys. Rev. B **62**, 7307 (2000)
14. M.G. Pala, B. Hackens, F. Martins, H. Sellier, V. Bayot, S. Huant, T. Ouisse, Phys. Rev. B **77**, 125310 (2008)
15. J. Friedel, Philos. Mag. **43**, 153 (1952)
16. M.G. Krein, Mat. Sb. **33**, 597 (1953)
17. K. Huang, *Statistical Mechanics* (Wiley, New York, 1963)
18. E.N. Economou, *Green's Functions in Quantum Physics* (Springer-Verlag, Berlin, 1983)
19. For GaAs the value of $\hbar^2/2m$ is 570 meV nm^2. In the numerical calculations of this paper we take $\hbar^2/2m$ equal to unity. We can then choose the energy unit to be $\varepsilon_0 = 17.7$ meV which yields a length unit of $l_0 = 5.7$ nm
20. C. Texier, M. Büttiker, Phys. Rev. B **67**, 245410 (2003)
21. D. Boese, M. Lischka, L.E. Reichl, Phys. Rev. B **62**, 16933 (2000)
22. V. Vargiamidis, H.M. Polatoglou, Phys. Rev. B **71**, 075301 (2005)

Chapter 8
Effects of Temperature on the Scattering Phases and Density of States in Quantum Wires

Vassilios Vargiamidis, Vassilios Fessatidis, and Norman J. Morgenstern Horing

Abstract We investigate the effects of temperature on the scattering phases in a quantum wire with an attractive scatterer. We consider two bound states, belonging to different subbands, which couple to a scattering channel and give rise to two Fano resonances. In this context, we first demonstrate the deviation of the transmission phase from the Friedel phase at the zeros of the transmission. It is then shown that temperature effects tend to smear sharp features of the transmission phase; namely, the phase drops become less than π and acquire finite widths, which increase linearly in the low-temperature regime. The influence of temperature on the Friedel phase and density of states is also examined.

8.1 Introduction

In electron transport through mesoscopic systems, the phase plays an important role. Interest in the behavior of the wave function phase in quantum transport devices started with experiments addressing the phase shift of an electron transmitted through a quantum dot [1–4]. These important experiments demonstrated the presence of a coherent component in the current while, at the same time, a strange behavior of the transmission phase was revealed; namely, the transmission phase drops suddenly by π in the conductance valleys.

In relation to these experiments, the behavior of the various phases that appear in the scattering matrix were investigated theoretically [5–9] and the existence of two important phases with different behavior was emphasized [5, 6]; namely, the phase of the transmission amplitude and the phase that appears in the Friedel sum rule [10]. The Friedel sum rule relates the density of states to the charge of the

N.J.M. Horing (✉)
Department of Physics and Engineering Physics, Stevens Institute of Technology, Hoboken, NJ 07030, USA
e-mail: nhoring@stevens.edu

H. Ünlü and N.J.M. Horing (eds.), *Low Dimensional Semiconductor Structures*, NanoScience and Technology, DOI 10.1007/978-3-642-28424-3_8,
© Springer-Verlag Berlin Heidelberg 2013

system via the phase of the eigenvalues of the scattering matrix [11, 12]. Being related to the charge of the system, the Friedel phase is a continuous function of energy, and cannot exhibit an abrupt behavior.

On the other hand, it was shown [5, 6] that the phase of the transmission amplitude may deviate from the Friedel phase and exhibit sharp drops of π at energies where the transmission probability becomes zero. The co-occurrence of a transmission zero and a sharp phase drop were interpreted in terms of the properties of a Fano resonance, i.e., the destructive interference between a resonant and a nonresonant transmission channels leads to a transmission zero and an associated abrupt jump of the transmission phase. The Fano resonance-based theory offers a simple explanation of the experimental results and was further examined in Refs. [8, 9].

The above-mentioned behavior of the transmission phase may also appear in a quantum wire with some type of coupling potential; for example, coupling due to an attractive scatterer (or embedded quantum dot) [13–17] and local spin–orbit coupling [18], to name a few. In the presence of coupling potential, a bound state in one subband (imaginary wave number in the wire leads) can coexist with an unbound state in another subband. A Fano resonance, in this case, arises when the closed and the open channels are coupled, the channels being the propagating and cutoff subbands. The behavior of the wave function phase in a quantum wire has been briefly treated [17, 19]. However, the relation of the transmission phase to the Friedel phase was not discussed, while temperature effects were not taken into account. One important issue, therefore, is how the scattering phases in a quantum wire are influenced by temperature.

In this chapter, we extend our previous work [17, 19] and investigate the temperature dependence of scattering phases in a quantum wire with an attractive scatterer. We consider the case of one open and two closed channels, the latter two being dominated by their bound states. First, we perform a general analysis without making specific assumptions concerning the shape of the scattering and confining potentials. Such an analysis is able to capture the main physical features, which are independent of the details of the potentials and reveal the relation between the scattering phases. We then employ a specific model scatterer of the short-range type in a parabolically confined quantum wire and examine the effects of temperature on the scattering phases and density of states. It is shown that temperature effects tend to smear sharp features of the phase of the transmission amplitude; namely, the phase drops become less than π, and they are no longer abrupt but acquire finite widths. Furthermore, for a narrow Fano resonance, the Friedel phase and density of states react more sensitively with increasing temperature than for a broad Fano resonance.

The chapter is organized as follows. In Sect. 8.2, we first outline briefly the coupled-channel model and then, by employing the scattering matrix, we discuss the relation of the Friedel phase to the phase of the transmission amplitude. In Sect. 8.3, we examine the effects of temperature on the scattering phases, and a summary of our results is presented in Sect. 8.4.

8.2 Formulation

8.2.1 Local Density of States

We consider a ballistic uniform quantum wire in which electrons are confined along the y direction (transverse direction) but are free to propagate along the x direction, as shown in Fig. 8.1.

In the presence of a scattering potential, the Schrödinger equation describing the electron motion in the wire can be written as:

$$\left[-\frac{\hbar^2}{2m}\nabla^2 + V_{\mathrm{c}}(y) + V(x, y)\right]\Psi(x, y) = E\Psi(x, y), \tag{8.1}$$

where $V_{\mathrm{c}}(y)$ is the confining potential and $V(x, y)$ is the scattering potential. The confining potential gives rise to channel modes $\phi_n(y)$,

$$\left[-\frac{\hbar^2}{2m}\frac{\mathrm{d}^2}{\mathrm{d}y^2} + V_{\mathrm{c}}(y)\right]\phi_n(y) = E_n\phi_n(y) \tag{8.2}$$

where E_n is the threshold energy for mode n. Expanding $\Psi(x, y)$ in terms of the channel-mode wave functions

$$\Psi(x, y) = \sum_{n=0}^{\infty}\psi_n(x)\phi_n(y), \tag{8.3}$$

we obtain from (8.1) coupled-channel equations for $\psi_n(x)$,

$$(E - E_n - \widehat{K})\psi_n(x) = \sum_{l=0}^{\infty} V_{nl}(x)\psi_l(x), \tag{8.4}$$

where $\widehat{K} = -(\hbar^2/2m)\mathrm{d}^2/\mathrm{d}x^2$ and $V_{nl}(x) = \int dy\phi_n^*(y)V(x, y)\phi_l(y)$ are the coupling matrix elements, which form effective potentials for the longitudinal electron motion. These coupling potentials also provide the interaction between channels.

In order to solve (8.4), we first consider the decoupling limit (i.e., $V_{nl} = 0$) and assume that only the first channel mode (i.e., the mode with $n = 0$) can be found in some scattering state. From (8.4), these scattering states can be obtained as solutions of $[\widehat{K} + V_{00}(x) + E_0]\chi_k^{\pm}(x) = E\chi_k^{\pm}(x)$, where $\chi_k^{+}(x)$ and $\chi_k^{-}(x)$ represent the states for which the incident wave comes from $-\infty$ and $+\infty$, respectively. These states describe the background (nonresonant) scattering, which is the scattering

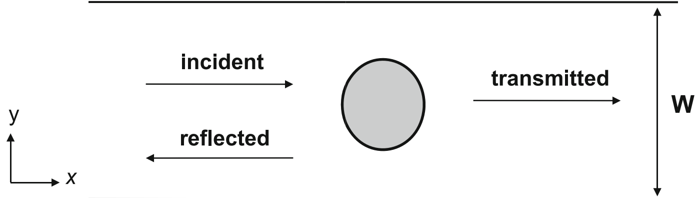

Fig. 8.1 Schematic illustration of a uniform quantum wire with a scatterer. We assume infinite leads and W denotes the effective width of the wire. The incident wave is partly transmitted and partly reflected by the scattering potential $V(x, y)$

in a hypothetical system in which the channel interaction is switched off [20]. In particular, their asymptotic form is given as:

$$\chi_k^{\pm}(x) = \begin{cases} t^{\text{bg}} e^{\pm ikx} & (x \to \pm\infty) \\ e^{\pm ikx} + r_{\pm}^{\text{bg}} e^{\mp ikx} & (x \to \mp\infty) \end{cases} \tag{8.5}$$

where the upper signs correspond to an incident wave from the left. In (8.5) t^{bg} and $r_{\pm}^{\text{bg}}$ denote the background transmission and reflection amplitudes in the wire, while k is the wave vector for the propagating mode given as $k = [2m(E - E_0)]^{1/2}/\hbar$.

In addition to the open channel $n = 0$, we consider two closed ones $n = 1$ and 2, which are dominated by their bound states $\Phi_{01}(x)$ and $\Phi_{02}(x)$, respectively. The equations for the bound states are obtained from (8.4) by setting $V_{nl} = 0$ (for $n \neq l$),

$$(\tilde{E}_j - E_j - \widehat{K})\Phi_{0j}(x) = V_{jj}(x)\Phi_{0j}(x) \quad (j = 1, 2) \tag{8.6}$$

where $\tilde{E}_j$ are the bound state energies.

We now make the approximation of truncating the sum in (8.4) at $n = 2$. The resulting system of three equations is solved in Ref. [17]. The transmission amplitude can, finally, be extracted from the asymptotic form of $\psi_0(x) = t\mathrm{e}^{ikx}$ as:

$$t(E) = t^{\text{bg}} \frac{(E - \tilde{E}_1)(E - \tilde{E}_2) - \bar{\varepsilon}}{\left(E - E_R^{(1)} + i\Gamma_1\right)\left(E - E_R^{(2)} + i\Gamma_2\right) - W_{12}^2}, \tag{8.7}$$

where $\bar{\varepsilon}$ is real and proportional to the coupling potential $|V_{12}|$, $E_R^{(j)} = \tilde{E}_j + \delta_j$ are the shifted quasibound-state (resonant) energies, and Γ_j are the widths of the two resonances. Also, W_{12} is a matrix element, which represents the indirect coupling of the bound states via the open channel. Note that (8.7) yields two Fano line shapes in the transmission probability, $|t|^2$, one in the first and one in the second subband.

We now discuss the relation between the phase of the transmission amplitude and the Friedel phase.

8.2.2 Scattering Phases

For a single transport channel the scattering matrix is represented as a 2×2 unitary matrix at an energy E:

$$S(E) = \begin{pmatrix} r(E) & t'(E) \\ t(E) & r'(E) \end{pmatrix} \tag{8.8}$$

We assume that both time-reversal and inversion symmetries hold and, in this case, one has additionally $t = t'$ and $r = r'$. In terms of the scattering matrix, the Friedel phase is defined by:

$$\theta_{\mathrm{f}}(E) = \frac{1}{2i} \ln \mathrm{Det}\{S(E)\}, \tag{8.9}$$

where, for a time-reversal symmetric system, $\mathrm{Det}\{S(E)\} = -t(E)/t^*(E)$. The derivative of the Friedel phase with respect to the energy of the incident electron is related to the density of states via [5, 6]:

$$\rho(E) = \frac{1}{4\pi i} \mathrm{Tr}\left[S^+(E) \frac{\mathrm{d}S(E)}{\mathrm{d}E} - \frac{\mathrm{d}S^+(E)}{\mathrm{d}E} S(E) \right] = \frac{1}{\pi} \frac{\mathrm{d}\theta_{\mathrm{f}}(E)}{\mathrm{d}E}. \tag{8.10}$$

Integrating (8.10) over the energy interval $[E', E'']$ yields the generalized Friedel sum rule $\pi N(E'', E') = \theta_{\mathrm{f}}(E'') - \theta_{\mathrm{f}}(E')$, which states that the number of electrons N multiplied by π, in the system, equals the difference of the Friedel phase at E' and E''.

With the help of (8.7), (8.8), and (8.9), we can express the Friedel phase as:

$$\theta_{\mathrm{f}}(E) = \theta_{\mathrm{f}}^{\mathrm{bg}}(E) + \theta_{\mathrm{f}}^{\mathrm{r}}(E) \tag{8.11}$$

where

$$\theta_{\mathrm{f}}^{\mathrm{bg}}(E) = \frac{1}{2i} \ln \left[\frac{t^{\mathrm{bg}}}{(t^{\mathrm{bg}})^*} \right], \tag{8.12}$$

and

$$\theta_{\mathrm{f}}^{\mathrm{r}}(E) = \frac{1}{2i} \ln \left(- \prod_{j=1}^{2} \frac{E - E_R^{(j)} - i\Gamma_j}{E - E_R^{(j)} + i\Gamma_j} \right) \tag{8.13}$$

$\theta_{\mathrm{f}}^{\mathrm{bg}}(E)$ originates from the background contribution and varies slowly with energy across a resonance. For simplicity, we assumed the weak coupling regime [15, 17, 19], in which the interaction between the bound states is small and W_{12} can be neglected. The Friedel phase can, finally, be determined as:

$$\theta_{\mathrm{f}}(E) = \theta_{\mathrm{f}}^{\mathrm{bg}}(E) + \sum_{j=1}^{2} \arctan \left(\frac{E - E_R^{(j)}}{\Gamma_j} \right) - \frac{\pi}{2} \tag{8.14}$$

Using (8.14), we obtain the density of states as:

$$\rho(E) = \frac{1}{\pi}\sum\nolimits_{j=1}^{2} \frac{\Gamma_j}{\left(E - E_R^{(j)}\right)^2 + \Gamma_j^2} \tag{8.15}$$

which is a superposition of two Lorentzians with peak positions at the resonant energies. It is worth mentioning here that, in a Fano resonance, the relation between the peak positions of the conductance and the density of states may provide important information about the characteristics of the transmission phase through a quantum dot [21].

On the other hand, the phase of the transmission amplitude can be obtained by expressing (8.7) as $t = |t|e^{i\theta_t(E)}$ where

$$\theta_t(E) = \theta_t^{\mathrm{bg}}(E) + \theta_t^r(E). \tag{8.16}$$

It can be verified that $\theta_t^{\mathrm{bg}} = \theta_{\mathrm{f}}^{\mathrm{bg}}$, which will henceforth be denoted as θ^{bg}. However, the particular form of θ^{bg} depends on the specific type of scattering potential. Concerning $\theta_t^r(E)$, the result of a lengthy but straightforward algebra gives:

$$\tan\theta_t^r(E) = \frac{\Gamma_2(E - E_R^{(1)}) + \Gamma_1(E - E_R^{(2)})}{\Gamma_1\Gamma_2 - (E - E_R^{(1)})(E - E_R^{(2)})} \tag{8.17}$$

With the help of (8.14) and (8.17) one can obtain the relation between the Friedel phase and the phase of the transmission amplitude as:

$$\theta_t(E) = \theta_{\mathrm{f}}(E) - \frac{\pi}{2} + \pi\Theta(x(E)) \tag{8.18}$$

where $x(E) = \tan\theta_t(E)$ and $\Theta(x)$ are the unit step functions. It is seen from (8.18) that $\theta_t(E)$ changes abruptly by π every time $x(E)$ changes the sign. In fact, it can be shown that the energies for which $x(E)$ is discontinuous and changes sign are determined as the solutions of

$$1 - \tan\theta^{\mathrm{bg}}(E)\tan\theta_t^r(E) = 0 \tag{8.19}$$

At these energies the transmission probability vanishes (see below) and the transmission phase deviates from the Friedel phase.

8.2.3 Simple Model Scatterer

The behavior of the scattering phases is illustrated now by employing a scattering potential described by:

$$V(x, y) = -\frac{\hbar^2 \beta}{2m} \delta(x) \exp\left[-\frac{(y - y_i)^2}{\alpha^2}\right], \tag{8.20}$$

which is a δ-function along the propagation direction and having a Gaussian shape in the transverse direction with decay length α and center at $y = y_i$. The lateral extent of the scatterer, quantified by α, may provide an extra parameter for fitting experimental data. The magnitude of β determines the strength of the scattering potential ($\beta > 0$). This type of potential can be used to model, for example, the negative electrostatic influence of a scanning probe microscope (SPM) tip in experiments studying the imaging of coherent electron flow through a narrow constriction in a two-dimensional (2D) electron gas [22, 23]. For such a potential, the coupling matrix elements are given by:

$$V_{nl}(x) = -\left(\frac{\hbar^2 \beta}{2m}\right) \delta(x) v_{nl},$$

where

$$v_{nl} = \int \phi_n^*(y) \exp\left[-\frac{(y - y_i)^2}{\alpha^2}\right] \phi_l(y) \mathrm{d}y \tag{8.21}$$

The confining potential is chosen to be parabolic, $V_c(y) = (1/2) m w_0^2 y^2$ and, therefore, the mode eigenfunctions $\phi_n(y)$ are the well-known harmonic-oscillator wave functions with eigenenergies $E_n = \hbar\omega_0(n + 1/2)$, $n = 1, 2, \ldots$.

In the following numerical calculations, we set $(\hbar^2/2m) = 1$ and take the energy unit as $\varepsilon_0 = 17.7\,\text{meV}$. The length unit is then $L_0 = 5.7\,\text{nm}$. The magnitude of β has dimension of inverse length, so that $(\hbar^2\beta)/2m$ is expressed in meV.

In Fig. 8.2a, we show the transmission probability, $|t|^2$, and the density of states, ρ, plotted versus the incident electron energy. Note that the transmission probability exhibits two Fano resonances, one in the first and one in the second subband, both of which have positive asymmetry parameters (i.e., the resonance energies occur after the energies of the transmission zeros). Note also that the peak positions of the density of states are different from the peak positions of the transmission probability. The values of the parameters in this calculation are $\beta = 4L_0^{-1}$, $\alpha = 0.68L_0$, and $y_i = 0.28L_0$.

In Fig. 8.2b, we show the Friedel phase and phase of the transmission amplitude plotted versus the incident electron energy. The values of the parameters are the same as those used in (a). As expected, the Friedel phase shows a steplike behavior, i.e., it is nearly constant as a function of energy and increases by π continuously as the energy crosses a Fano resonance. The transmission phase also evolves continuously with increasing energy, except at the transmission zeros where sharp phase drops of π occur. This type of phase behavior is similar to that found in other mesoscopic systems [5, 6, 8, 9]. The physical origin of this behavior lies in the existence of quasibound states in the attractive scatterer, which interact with the continuum of states in the quantum channel, resulting in Fano-type resonant interference.

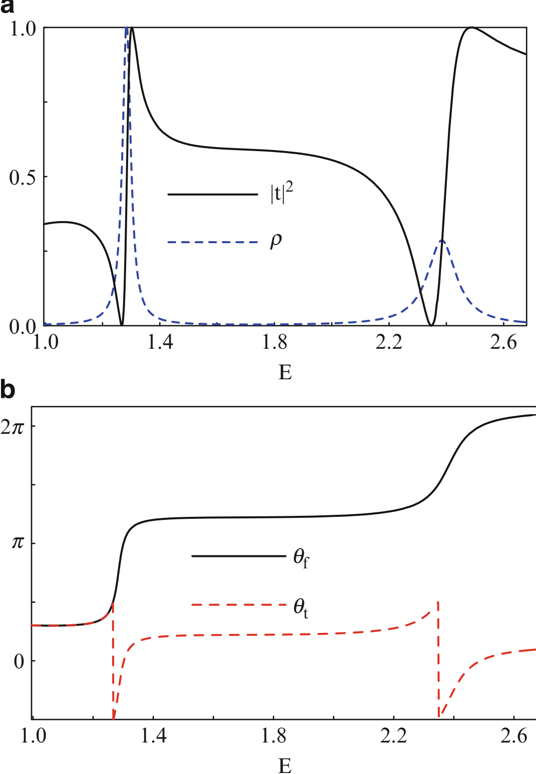

Fig. 8.2 (**a**) Transmission probability, $|t|^2$, and density of states, ρ, plotted vs. the incident electron energy (E, in units of ε_0). (**b**) Friedel phase θ_{f} and phase of the transmission amplitude θ_{t} vs. incident electron energy (E, in units of ε_0). Note the sharp phase drops by π at the zeros of the Fano resonances

8.3 Finite Temperature Effects

To consider thermal effects, we have to convolute the transmission probability and transmission amplitude with the derivative of the Fermi function. The transmission probability is given as:

$$|t(\mu, T)|^2 = -\int \mathrm{d}E f'(E)\, |t(E)|^2 \,, \tag{8.22}$$

where $t(E)$ is the zero-temperature transmission amplitude, and $f(E)$ is the Fermi distribution function given as $f(E) = [\exp((E-\mu)/k_B T) + 1]^{-1}$,

where μ is the chemical potential. Also, the transmission phase is calculated as:

$$\theta_t(\mu, T) = \arctan\left(\frac{\mathrm{Im}\left\{-\int \mathrm{d}E f'(E) t(E)\right\}}{\mathrm{Re}\left\{-\int \mathrm{d}E f'(E) t(E)\right\}}\right). \tag{8.23}$$

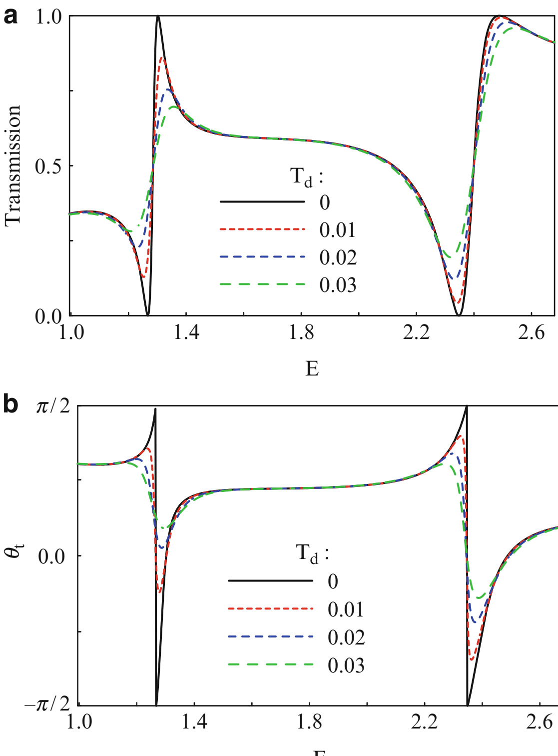

Fig. 8.3 (**a**) Transmission probability $|t|^2$ through the wire vs incident electron energy (chemical potential), plotted for various values of the dimensionless temperature T_d, where $T_\mathrm{d} = k_\mathrm{B}T/\varepsilon_0$. (**b**) Phase of the transmission amplitude θ_t vs. incident electron energy. Note that the abrupt phase jumps of π acquire finite widths and become less than π at finite temperature

We define a dimensionless parameter $T_\mathrm{d} = k_\mathrm{B}T/\varepsilon_0$, which is a measure of temperature. Then $T_\mathrm{d} = 0.01$ corresponds to $T = 2.06\,\mathrm{K}$. The type of integrals involved in (8.22) and (8.23) can be performed analytically with the help of partial fraction expansion, presentation of the Fermi function in terms of the digamma function, and a contour integration. However, the analytical calculation will not be presented in this chapter.

In Fig. 8.3a we show the transmission probability plotted versus the incident electron energy (chemical potential) for increasing values of the parameter T_d. Here, the scatterer parameters are $\beta = 4L_0^{-1}$, $y_i = 0.28L_0$, and $\alpha = 0.68L_0$. Note that by increasing the temperature, it causes rapid smearing of the resonance structure. The physical origin of such a behavior lies in the thermal broadening, via the smooth peak in $f'(E)$, which obscures the resonance as $k_\mathrm{B}T$ becomes comparable to the resonance width. Note also that the effect of temperature on the first (narrower) resonance is stronger. In fact, the amplitude of the first resonance reduces drastically with increasing temperature compared to that of the second resonance.

In Fig. 8.3b, we show the phase of the transmission amplitude plotted versus the incident electron energy (chemical potential) for the same parameter values as in (a). It can be seen that, at finite temperature, the phase discontinuities are lifted as a consequence of the fact that no transmission zeros occur. Specifically, one can

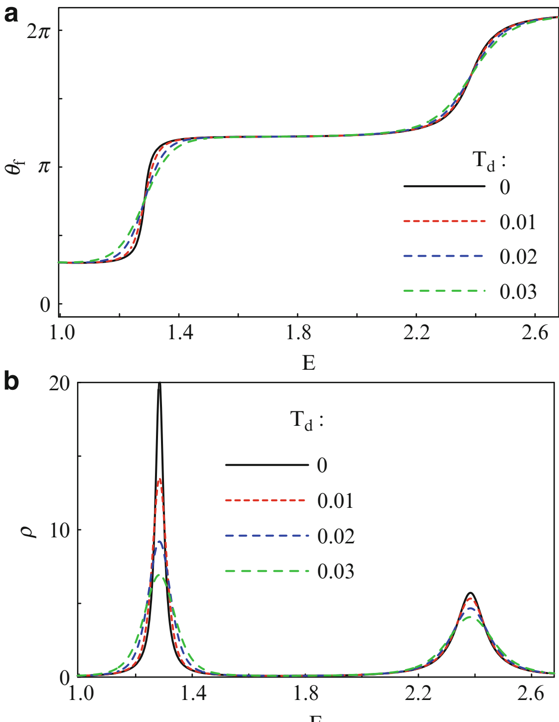

Fig. 8.4 (**a**) Friedel phase θ_{f} vs. incident electron energy (chemical potential), plotted for various values of the dimensionless temperature T_{d}, where $T_{\mathrm{d}} = k_{\mathrm{B}}T/\varepsilon_0$. (**b**) Density of states (ρ, in units of ε_0^{-1}) vs. incident electron energy plotted for various values of T_{d}. The values of the scatterer parameters are the same as in (**a**). Note that the effect of temperature is much stronger on the first (sharper) peak

observe that smearing due to finite temperature tends to average out sharp features of the transmission phase, i.e., the phase drops become less than π, and they are no longer sharp but have finite widths.

The effects of temperature on the Friedel phase and density of states plotted versus the incident electron energy (chemical potential) are shown in Fig. 8.4a and b, respectively, for the same parameter values as those in Fig. 8.3. They are calculated as:

$$\theta_{\mathrm{f}}(\mu, T) = -\int \mathrm{d}E f'(E)\theta_{\mathrm{f}}(E), \tag{8.24}$$

and

$$\rho(\mu, T) = -\int \mathrm{d}E f'(E)\rho(E), \tag{8.25}$$

where $\theta_{\mathrm{f}}(E)$ and $\rho(E)$ are given in (8.14) and (8.15), respectively. Note that the steplike structure of the Friedel phase is smeared out with increasing temperature, while the peaks in the density of states become broader but the peak positions remain unaffected. Note also that, for the narrow Fano resonance, the Friedel phase and density of states exhibit enhanced sensitivity with increasing temperature.

To this end, we remark that the resonance width, which is a measure of the strength of the coupling between the quasibound level and the continuum, can be

varied by means of shifting the position of the scatterer with respect to the 'walls' of the wire. However, since the coupling strengths, V_{01} and V_{02}, to the two quasibound levels strongly depend on the scatterer's position, by displacing the scatterer across the channel, one can produce a very narrow Fano resonance in one subband and a very broad one in the second subband. This will lead to gradually sharper features of the scattering phases near the first resonance, and smoother phase evolution near the second resonance. As a consequence, the temperature dependence will be much stronger in the first resonance than that in the second resonance. The displacement of the scatterer can be achieved by, for example, applying different gate voltage to the two parts of a split gate, which can be thought of as an applied electric field in the transverse direction of the quantum channel. In other words, the electric field causes shifting of the confining potential, which is equivalent to a 'shift' of the scatterer in the opposite direction. This tunability of the scattering phases may prove experimentally useful in electronic transport through narrow channels.

8.4 Summary

In this chapter, we analyzed the behavior of scattering phases and density of states in a quantum wire with an attractive scatterer, focusing on finite temperature effects. In this context, we first showed that the transmission phase deviates from the Friedel phase and exhibits sharp drops of π at the zeros of the Fano resonances. At finite temperature, the sharp drops become less than π and acquire finite widths, which increase linearly in the low-temperature regime. The important role played by the resonance widths was pointed out. The behavior of the Friedel phase and density of states with increasing temperature was also illustrated.

To this end, we point out that our analysis was restricted to a single transport channel. This is an assumption that has been used implicitly in most theoretical studies of similar systems and is also experimentally relevant [2–4]. Besides, it provides a good approximation for modeling a narrow quantum channel. It is also worth noting that the present analysis can also be useful for investigating transport properties and phase behavior through a mesoscopic open ring connected to current leads with an embedded scattering center in one of its arms. In this case, the arm with the scatterer can be treated using the present analysis while the junctions between the leads and the ring can easily be described via a scattering matrix with a coupling parameter.

References

1. A. Yacoby, M. Heiblum, D. Mahalu D, H. Shtrikman, Phys. Rev. Lett. **74**, 4047 (1995)
2. R. Schuster, E. Bucks, M. Heiblum, D. Mahalu, V. Umansky, H. Shtrikman, Nature (London) **385**, 417 (1997)

3. S. Katsumoto, K. Kobayashi, H. Aikawa, A. Sano, Y. Iye, Superlattices Microstruct. **24**, 151 (2003)
4. M. Sigrist, A. Fuhrer, T. Ihn, K. Ensslin, S. E. Ulloa, W. Wegscheider, M. Bichler, Phys. Rev. Lett. **93**, 066802 (2004)
5. T. Taniguchi, M. Büttiker, Phys. Rev. B **60**, 13814 (1999)
6. A.L. Yeyati, M. Büttiker, Phys. Rev. B **62**, 7307 (2000)
7. A. Silva, Y. Oreg, Y. Gefen, Phys. Rev. B **66**, 195316 (2002)
8. T. Nakanishi, K. Terakura, T. Ando, Phys. Rev. B **69**, 115307 (2004)
9. Y.S. Joe, E.R. Hedin, A.M. Satanin, Phys. Rev. B **76**, 085419 (2007)
10. E.R. Hedin, Y.S. Joe, A.M. Satanin, J. Phys.: Condens. Matter. **21**, 015303 (2009)
11. J. Friedel, Philos. Mag. **43**, 153 (1952)
12. R. Dashen, S.K. Ma, H.J. Bernstein, Phys. Rev. **187**, 345 (1969)
13. S.A. Gurvitz, Y.B. Levinson, Phys. Rev. B **47**, 10578 (1993)
14. A.A. Clerk, X. Waintal, P.W. Brouwer, Phys. Rev. Lett. **86**, 4636 (2001)
15. A.M. Satanin, Y.S. Joe, Phys. Rev. B **71**, 205417 (2005)
16. V. Vargiamidis, H.M. Polatoglou, Phys. Rev. B **71**, 075301 (2005)
17. V. Vargiamidis, V. Fessatidis, Phys. Rev. B **79**, 205309 (2009)
18. D. Sánchez, L. Serra, Phys. Rev. B **74**, 153313 (2006)
19. V. Vargiamidis, V. Fessatidis, N.J.M. Horing, J. Appl. Phys. **106**, 043710 (2009)
20. H. Friedrich, *Theoretical Atomic Physics* (Springer, Berlin, 1990), p. 138
21. K. Kobayashi, H. Aikawa, S. Katsumoto, Y. Iye, Phys. Rev. Lett. **88**, 256806 (2002)
22. M.A. Topinka, B.J. LeRoy, S.E.J. Shaw, E.J. Heller, R.M. Westervelt, K.D. Maranowski, A.C. Gosard, Science **289**, 2323 (2000)
23. M.A. Topinka, B.J. LeRoy, R.M. Westervelt, S.E.J. Shaw, R. Fleischmann, E.J. Heller, K.D. Maranowski, A.C. Gosard, Nature **410**, 183 (2001)

Chapter 9
Fabrication of Low Dimensional Nanowire-Based Devices using Dieletrophoresis

Ramazan Kizil

Abstract Bottom-up assembly of nanostructured materials, such as metallic nanowires and carbon nanotubes, has proven to be a facile way of building electronic devices or sensing platforms with unparallel ease of device dimension control. Electric field assisted manipulation of roughly 320 nm diameter 6 μm long nanowires with composition of Au–Ag–Au under ac bias across the lithographically defined parallel electrodes forms the basis of bottom-up assembly approach followed in this study. Nanowires were first aligned electrofluidically under ac bias of 10 V_{pp} and 1 kHz across 5 and 6 μm separated electrodes. Chemical etching of the Ag segment in the nanowires aligned across the predefined electrodes resulted in reduction of the dimension of the electrode separation from 5 μm to 50–100 nm. The alignment yield of 6 μm Au–Ag–Au striped nanowires across gold electrodes was as high as 70%. The nanowires-based device was employed to the capture and electrical characterization of preferably a single 100 nm Au nanosphere in the nanogap.

9.1 Introduction

The famous Austrian physicist Erwin Schrödinger stated in 1952 that mankind would never experiment with just one electron, atom, or molecule. However, eight years later, Feynman envisioned that there are no limitations to arranging atoms as we wish. This dream was realized with the introduction of the proximal probe method in early 1980s. Engineering operations on single molecules became accessible with the advent of scanning probe microscopes that sets the ultimate limit

R. Kizil (✉)
Chemical Engineering Department, Istanbul Technical University, Maslak 34469, Istanbul
e-mail: kizilr@itu.edu.tr

H. Ünlü and N.J.M. Horing (eds.), *Low Dimensional Semiconductor Structures*, NanoScience and Technology, DOI 10.1007/978-3-642-28424-3_9,
© Springer-Verlag Berlin Heidelberg 2013

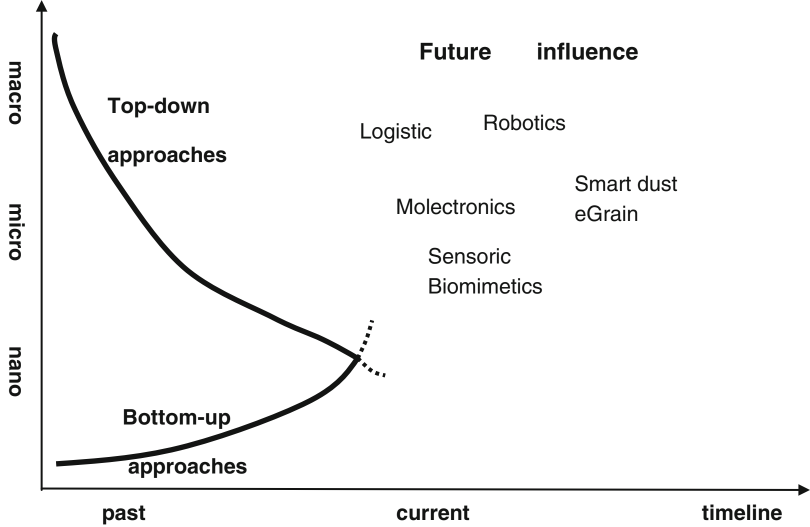

Fig. 9.1 Trends in the methods of miniaturization of material systems and devices in science and technology

of current nanofabrication technology [13]. One of the most facile way of studying electronic behavior of a single metalic or semiconducting particle, (bio)molecules is to create nanometer scale separated electrodes that enables electrical I-V readout. The central feature of such single molecule studies by electronic measurements involves the fabrication of nanometer scale electrodes in which molecules can be accommodated.

Nanotechnology, for many scientists and technologists, is regarded as a process of ultra-miniaturization, by means of which the behavior of matter and transport phenomena at the nanoscale can be investigated. Miniaturization of microsystems through nanotechnology offers new applications, involving challenges along with innovation at each step. Miniaturization, as a critical thrust of nanotechnology, can be accomplished by two different approaches: top-down or bottom-up assembly. The top-down approach is almost at the limits in terms of resolution, while the bottom-up strategies offer the convenience of integrating more layers, molecules, or nanoparticles into a unit with less expense and enabling enhanced precision and resolution. The trends and progressions in system miniaturization are summarized in Fig. 9.1.

The bottom-up assembly approaches of these nanomaterials provide a new dimension to miniaturization of microsytems. Bottom-up strategies incorporating various functionalized nanostructured interface materials contribute significantly to the ever increasing endeavor of shrinking the macroworld to create devices with improved performance and minimize the positional mismatches in existing top-down technologies. Moreover, the integration of one-dimensional (1D) nanostructured

objects, such as carbon nanotubes, metallic or hybrid nanowires, quantum dots and nanoparticles, with microelectrodes provides such systems with unique physical effects due to quantum confinement, a common feature in existing technology.

One of the mainstream applications of the bottom-up approach is to create nanometer scale separated gaps on integrated microsystems to prepare molecular junctions that can be employed for nanosensing molecules or molecular electronics. Nanogap electrodes facilitate the study of electronic transport phenomena in organics and biomolecules, as well as the tailoring of electronic behavior of molecules by means of organic chemistry. However, there are still major challenges and obstacles facing such nanoscale integration of molecules with microcomponents into nanometer scale separated gaps across a pair of electrodes. Most of the current test beds for molecular electronics are not suitable for mass production, and the reliability of these platforms is generally poor. In addition, assembling molecular scale devices on silicon chips at high yield is still a technological challenge. Incorporation of nanosized materials, in general 1D nanostructures, into microelectrodes, that integrate the whole system to the macroscopic world at the wafer scale is still one of the challenges in nanotechnology.

9.2 NanoGap Electrodes

Recent interest in nanotechnology has enabled scientists to fabricate microdevices that can be used for probing single molecules [40]. The main motivation for developing devices wherein a single particle is incorporated arises from the need of fabricating electronic devices with a core part of just one or a few molecules. The other motivation that led scientists to design such microdevices is to investigate electron transport phenomenon in single molecules.

Notwithstanding the keen interest in probing the electrical properties of single molecules, only a few studies have been performed regarding electrical transport in an individual single molecule [1, 40]. This is mainly because the intrinsically small size of a single molecule offers a major challenge when attempting its electrical integration with the external macroscopic world. For this reason, the fabrication of electrodes with nanometer scale gaps is essential for probing single particles electronically.

However, such fabrication of electrodes separated by nanometer size gaps in a controlled manner has proven to be a very challenging task [26]. It first requires nanoscale resolution for definition of the gap locations. Integration of the gap to the macroscopic circuit is another important concern. As summarized in Table 9.1, a variety of techniques to fabricate nanogap electrodes have been addressed by scientists.

Table 9.1 Bottom-up and top-down approaches to fabricate nanometer-scale gap electrodes

Fabrication techniques for creating nm scale separated electrodes	References
Electromigration	[40, 41]; [27]; [51]
Breaking thin wires	[48]
Electron beam lithography	[31, 33]
Tip of a STM	[45]
Metal oxidation on electron beam defined structures	[4, 45]; [28]
Electrochemical narrowing	[23, 31]
Selective etching of molecular beam epitaxy layer	[30]
Use of conducting DNA-based network	[6]

9.3 Nanotechnology Applied to Bio/Molecular Detection and Nanogap Electrodes

Since nanoelectrode sensors having ultra-small width and thickness expressing low dimensions are expected to exhibit high sensitivity and short response time, there is an emerging endeavor to fabricate these kind of sensors for the detection of chemical and biological targets. One of the main challenges in nanobiotechnology is the analysis of biomolecular interactions using microdevices in order to develop a comprehensive understanding about basic mechanisms of life at the gene level. Currently, biomolecular interaction is usually studied using optical markers as used in fluorescence observation [59] and surface plasmon resonance [20]. These optical techniques require excitation and detection sources for the light which are not easily compatible with interdigitated circuits. However, electrical detection of receptor-analyte interactions may facilitate the analysis of biomolecular interactions. Although the electrical detection of biomolecular interactions seems attractive, only a few microsensors, such as an ion-sensitive field-effect transistor (FET) [7], and micrometer-sized gaps in the range of 5–20 μm [42] have been proposed. Cui et al. [7] used a silicon nanowire solid-state FET to fabricate a real-time detection biosensor. The conductance of the nanowire FET was gated by the protonation or deprotonation of the nanowire surface. The surface was modified to facilitate ligand–receptor interactions. The conductance changes due to biotin–streptavidin or biotin–antibiotin interactions were detected using their FET-based sensor. Micrometer-sized gap sensors use receptor labeled gold nanoparticles to bind the ligand on the microdevices. The drawback of the micrometer-sized gaps was that, due to the large gap, the current was not detectable unless a silver enhancer solution was employed to produce a significant conductance change [42, 55]. Recently, Haguet et al. [15] used a 100 nm gap sensor prepared by lithographic techniques to electrically detect biotin–streptavidin interactions on APTMS grafted electrodes sweeping the applied voltage from -0.1 to $+0.1$ V.

Even though gaps were successfully created in all of the works listed in Table 9.1, most of the research was devoted to investigate electron transport of model molecules, such as organic molecules exhibiting room temperature negative differential resistance [1]. Hartzel et al. (2003) and Porath et al. [46] used their nanoelectrodes for measuring electrical transport in DNA molecules. However, the research showed that the conductivity of DNA was affected by many factors, such as humidity of the measurement environment, sequence of DNA, surface of the substrate, the nature of the electrical contact, counterions, and the secondary structure of DNA molecules (Hartzel et al. 2003). Still the electrical behavior of DNA remains controversial. In this matter, one of the useful approaches to the study of electronic behavior of DNA is the rapid hybridization of DNA on electrically activated electrodes ([14]; Heller et al. 2002). Reversal of the electric field (negative bias) at the test site can cause rapid removal of unhybridized DNA, so electrical response after DNA hybridization can be characterized.

9.4 Dielectrophoresis

Dielectrophoresis (DEP) is defined as the translational motion of a neutral matter triggered by polarization effects in a nonuniform electric field [44]. The force tending to produce this kind of response is simply called as the dielectrophoretic force. The word dielectrophoresis refers to both the *distortional* response/strain resulting from an externally imposed electrical stress and the Greek word *phoresis* meaning movement.

When a dielectric particle is suspended in a liquid medium under an electrical field, a dipole moment is induced in the particle as a result of electrical interfacial polarizations. Here, polarization refers to the blocked or restricted motion of the charges. The magnitude and the direction of the induced dipole moment depend upon the frequency and extent of the imposed electric field [25]. The magnitude of the dielectrophoretic force, F_{DEP} (in Newton), for a spherical particle of radius R in an imposed AC electric field E (V/m) of angular velocity ω is expressed as follows [25]:

$$F_{\text{DEP}} = 2\pi\varepsilon R^3 \text{Re}(K^*)\Delta E^2_{(\text{rms})}$$

where complex quantities are indicated with asterisks, and K^* refers to the complex Clausius-Mossotti factor, given by the expression

$$K = \left(\varepsilon_p^* - \varepsilon_m^*\right) / \left(\varepsilon_p^* + 2\varepsilon_m^*\right)$$

with $\varepsilon* = \sigma + i\omega\varepsilon$ (σ represents the conductivity, and ε the absolute permittivity).

The Clausius-Mossotti factor defines the strength of the effective polarization of a spherical particle as a function of particle and medium permittivity. The subscripts p and m refer to the particle and the medium, respectively. Re denotes the real

part of the Clausius-Mossotti factor. The term $\Delta E^2_{(\mathrm{rms})}$ represents the average local nonuniform field strength and gradient. Either positive or negative, the sign real part of the Clausius-Mossotti factor, $\mathrm{Re}(K^*)$, determines the direction of the dielectrophoretic force exerted on the particle. For metallic nanoparticles in aqueous suspensions the value of $\mathrm{Re}(K^*)$ is near unity ($\mathrm{Re}(K^*) \approx 1$) [5]. If the real part of the Clausius-Mossotti factor is positive, the particle experiences a translational force directed toward the regions of high electric field strength, such as the electrode edge. On the other hand, the particle is pushed toward weak field regions, when the sign of the Clausius-Mossotti factor takes negative values.

9.5 Applications of DEP

DEP has been successfully employed in biology, such as microorganism and cell manipulation and discrimination [11, 23, 34, 35, 43], DNA positioning and trapping on microfabricated structures [2, 9, 12, 19, 57, 58], and even in the separation of simulants of biological warfare [22]. Hughes [23] investigated the frequency-dependent polarization of a yeast cell suspended in an aqueous solution (conductivity is 100 mS/cm) and showed that cells experience positive dielectrophoretic forces between 10^4 and 10^8 Hz. Using DEP and flow channels he was able to separate yeast cells but the process was slow. In addition, the process was not suitable for highly concentrated samples, because particle–particle interactions can take place.

Since a strong dipole can be induced in DNA due to the surrounding counterion clouds, DNA has been one of the attractive biomolecules for dielectrophoretic manipulations [2]. If an alternating electric field is imposed on a DNA solution, both the DNA backbone and the counterion cloud become distorted, leading to a charge separation. DNA in a nonuniform electric field is supposed to undergo a dielectrophoretic force and an orientational torque as a result of interaction between the induced polarity in DNA and the electric field [58]. Most of the dielectrophoretic trapping of DNA has been developed for free DNA in an aqueous solution [12].

Nanowires and other 1D nanostructures can also be electrically addressed employing dielectrophoretic force. Smith et al. [50] investigated AC field assisted manipulation of metallic nanowires across interdigitated electrodes. Following this pioneering work, metallic or semiconducting nanoparticles, carbon nanotubes, and nanowires have precisely aligned into predefined electrically activated regions on chips.

9.6 Nanowire Synthesis and Characterization

The most popular technique to synthesize metallic nanowires is electrodeposition of metals from electrolyte solutions into uniform pores of alumina membranes under either constant current (galvonastatically) or constant potential (potenstiostatically).

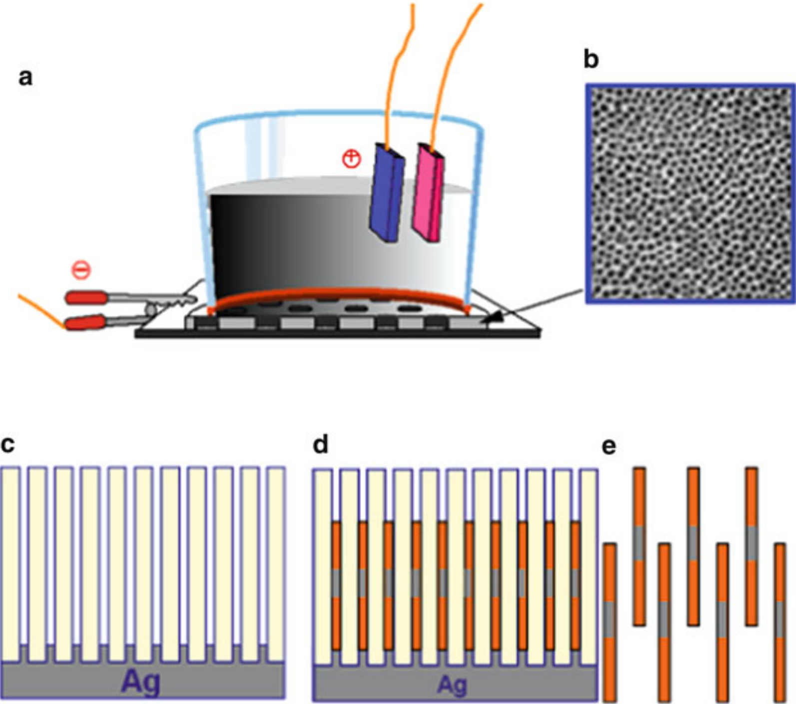

Fig. 9.2 Synthesis stages of template grown Au–Ag–Au nanowires: (**a**) Electrochemical cell for metal deposition into the pores of the alumina membrane, the cathode is silver backed alumina, the anode is platinum mesh. (**b**) Alumina membrane with nanometer scaled uniform cylindrical holes. (**c**) Backside Ag-coated (sputter coating or thermal evaporator) alumina membranes. (**d**) Sequential electrodeposition of metals; the first segment is Au (3 μm), the mid section is Ag (50–100 nm), and the last strip is Au (3 μm). (**e**) Dissolution of alumina membrane in 3 M NaOH and release of nanowires

The alumina membrane is used as the hard template and metals are grown in the holes in cylindrical shape. The size of the electrodeposited nanowires is determined by the pore radius and the current passed through the cathode (length). Keating and coworkers have exhibited sequential metallic segment-grown nanowires for the first time and characterize the stripped nanowires under an optical microscope in the reflection mode with various one-wavelength pass filters [38, 49]. The synthesis route is illustrated in Fig. 9.2.

Nanowires of 6–7 μm length and 220 or 320 nm diameter were synthesized by sequential galvanic deposition of Au for the first strip, then a short Ag (50–100 nm long) segment in the middle, and Au as the third strip attached to the Ag segment as depicted in Fig. 9.2.

It has been shown that due to the intrinsic light reflection behavior of Au, Ag, and other metals (Ni, Pt, Co, etc.), each metallic segment of the nanowires can be selectively identified at a proper wavelength. The size of template-grown nanowires is sufficient enough to make a connection of the nanosystems with macroscopic

measurement devices. For this reason, there is a growing interest in developing a nanowire-based nanodevice or nanosensor that can provide multiplexed and high throughput operation.

9.7 Integration of Nanowires with a Microsystem

1D nanostructures such as nanowires and carbon nanotubes hold great promise for a variety of device applications, including biological and chemical sensors [7, 17, 29, 32], field effect transistors [8, 54], light emitting diodes [52], and lasers [60]. The most critical step in developing nanowire-based devices is the post-growth manipulation and positioning of nanowires in a coherent and useful fashion. Integration of nanowires with a microsystem continues to be a challenge that must be overcome by employing high precision, parallel and high yield assembly techniques. Assembly techniques, such as Langmuir-Blodgett films [56], dry transfer printing with layer by layer assembly [24], and fluidic directed assembly [21], can be used to line up nanowires, but do not offer the ability to align nanowires precisely in desired locations. Electrofluidic assembly by means of DEP [37, 47, 50] and magnetic directed assembly [3, 39, 53] are becoming popular techniques for parallel alignment and precise positioning of single conducting and semiconducting nanowires and carbon nanotubes onto electrically or magnetically activated sites at the wafer scale.

Nanowires of Au–Ag–Au having 6 or 7 μm length and 320 nm diameter can be used to interconnect nanosystems to the macroscopic world, providing ease of targeting and characterization biorecognition mechanisms for even single molecules. These nanowires are becoming attractive materials employed to fabrication of nanodevices and sensors.

9.8 Microchip Design

A cross-sectional view of a microchip is illustrated in Fig. 9.3. In its fabrication, the first step is to develop a SiO_2 layer as an electrical insulator using either dry or wet oxidation.

$$\text{Dry oxidation}: \mathrm{Si} + \mathrm{O_2} \longrightarrow \mathrm{SiO_2}$$

$$\text{Wet oxidation}: \mathrm{Si} + 2\mathrm{H_2O(v)} \longrightarrow \mathrm{SiO_2} + 2\mathrm{H_2}$$

A thin titanium (50 nm)/palladium (100 nm) layer sits above the SiO_2 layer to facilitate electrical contact, serving as the busbar of the microchip. A protective dielectric called spin on glass of about 1 μm (SOG, a Si–O polymer with attached methyl groups) coats the overall surface of the silicon substrate. Lastly, a two-part

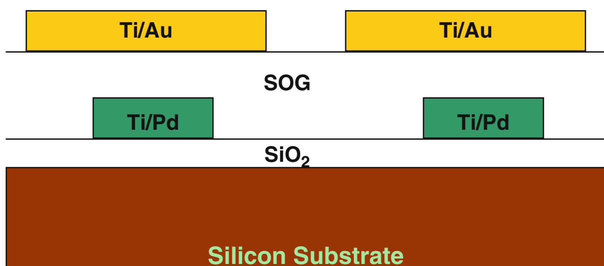

Fig. 9.3 Schematic illustration of a cross-sectional view of a microchip used for nanowire alignment and electrical measurements

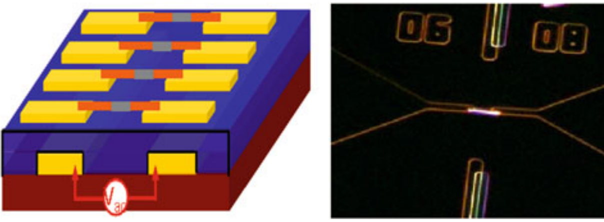

Fig. 9.4 Electric field assisted electrofluidic assembly of nanowires; *left*: a cartoon representation; *right*: optical image of dielectrophoretically aligned nanowire across a pair of electrodes (the 06 × 08'th electrode pair of a 10 × 10 array)

titanium (50 nm)/gold (150 nm) layer stands above the SOG, functioning as the electrodes of the microchip. The microchip used in this study consists of 100 planar micrometer-spaced (3–5 μm) electrodes. The left arms of the palladium busbar connect to a gold pad called top left pad, and the right arms connect to the other pad located at the bottom right corner of the chip in order to establish an electrical bias between the electrodes.

9.9 Nanowire Alignment by DEP

Alignment of the nanowires between the microelectrodes was carried out using a two-point alignment station. An alternating electric field was applied to the electrodes using a signal generator. A nanowire solution (in ethanol) was spread over the microchip, and a 10 V bias with sinusoidal frequency-time dependence was applied to the left and right connection pads of the chip. In order to determine the best alignment condition, the frequency of the ac field was varied between 1 kHz and 1 MHz, as the voltage bias was kept constant at 10 V. The cartoon representation and optical microscope image of nanowire alignment across the planar electrodes are illustrated in Fig. 9.4.

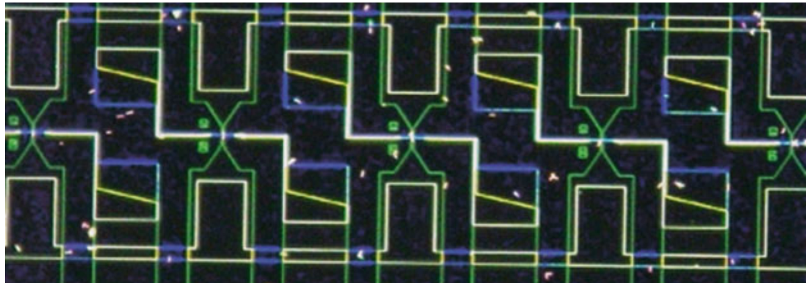

Fig. 9.5 Optical microscope examination of alignment of nanowires on the electrode arrays (10 V AC bias with 1 kHz sinusoidal frequency; the nanowires have diameter 320 nm and length 6 μm)

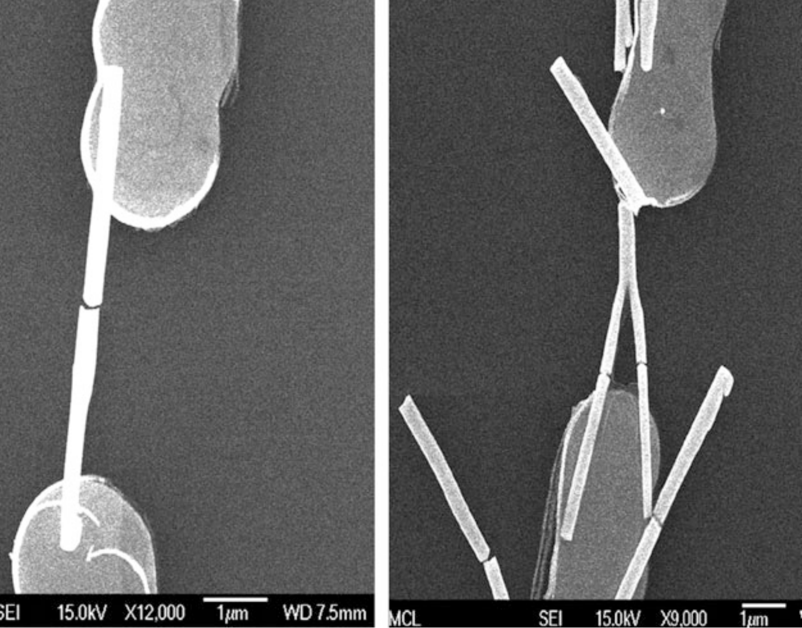

Fig. 9.6 FESEM image of a 50 nm gap between the 320 nm diameter by 6 μm long nanowires formed by chemical etching of the Ag layer in the nanowires. *Left*: Nanogap in a single nanowire. *Right*: Nanogaps from a forked single nanowire (the fork-like structure is due to electrodeposition in the nonregular (forking) pores)

The alignment yield of nanowires on the top electrode-pairs of the chip was tested using optical microscopy. The imposed alternating current at an appropriate frequency induces polarity in the nanowires, and the resultant dielectrophoretic forces push the nanowires toward the high electric field region. Precise alignment of tri-segmented Au–Ag–Au nanowires that are 320 nm diameter by 6 μm long on the chip with yields of 70% is shown in Fig. 9.5.

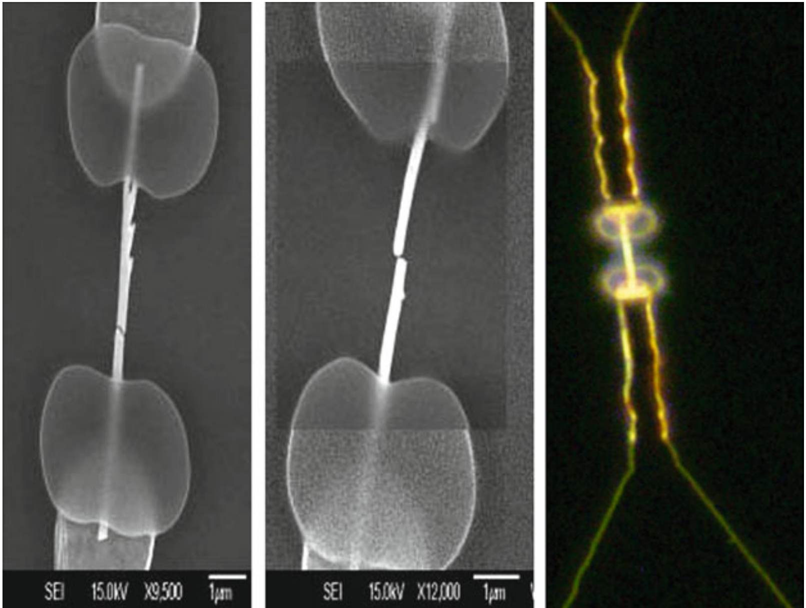

Fig. 9.7 Clamping of etched aligned nanowires using SU8 photoresist (1 μm). *Left* and *middle*: electron microscope images; *right*: optical microscope image

The Ag segment in the Au–Ag–Au nanowires aligned between the microelectrodes was etched using 0.1 M potassium ferricyanide solution. One milliliter of the etchant was poured on the chip and remained for 2 h to remove the Ag segment from the wires. Potassium ferricyanide selectively attacks the Ag, etching it out of the wire aligned between the electrodes. Then, the chip was rinsed with excess deionized (DI) water and dried with compressed air. The removal of Ag segments results in separations of 50–100 nm between the Au edges of the nanowires. This approach facilitates fabrication of nanometer size separated gaps on the lithographically defined 3–5 μm separated electrode pairs. Figure 9.6 illustrates nearly 50 nm sized gap formation by chemical etching of the Ag segment from the Au–Ag–Au nanowire.

However, this chemical treatment for etching Ag in the aligned nanowires leads to movement of the nanowire halves upon drying such that the gaps are no longer nm scale and in some cases the wires had been removed entirely from the electrodes. In order to prevent this effect, we attempted to clamp the nanowires down to the electrode surface either with photoresist coating or metal deposition.

Photoresist clamping prevented aligned nanowires from moving away from the electrodes, but there is still a subtle tilt in the longitudinal axis of the wires (Fig. 9.7) after etching. Fortunately, the gap sizes appear largely unchanged; thus, this effect should not create a major problem in the fabrication of nanowire-based nanogap devices capable of performing electrical characterization.

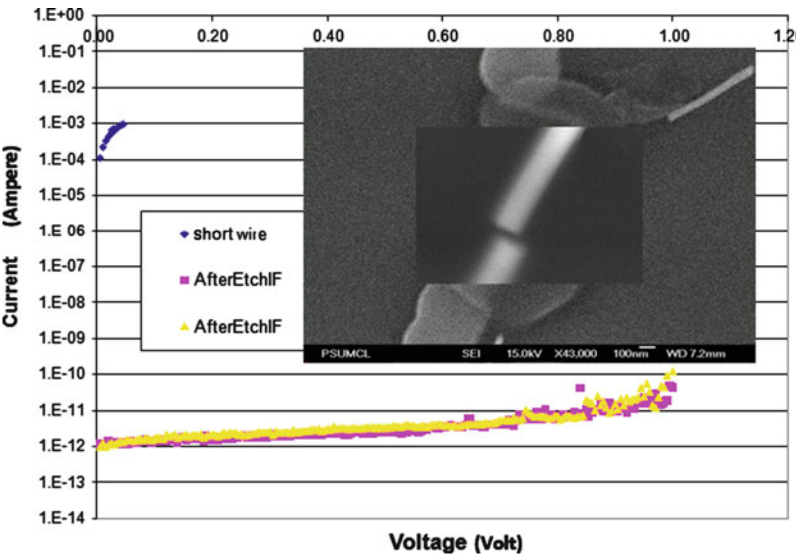

Fig. 9.8 I-V measurements of the Au–Ag–Au nanowires after alignment (short wire), and nanogaps after chemical etching of Ag (after etch response)

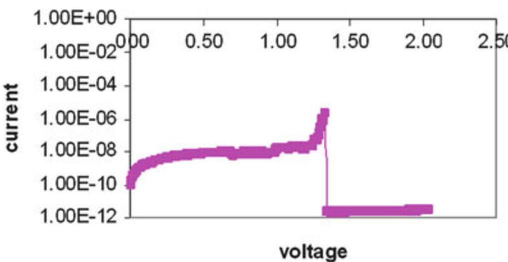

Fig. 9.9 The electromigration effect on Au–Ag–Au nanowires with voltage sweeping from 0 to 2.5 V

In addition to FESEM characterization, nanowires aligned between pairs of gold electrodes at the top of the microchip were characterized by I-V measurements. The resistance of Au–Ag–Au nanowires precisely aligned and clamped onto electrodes was found to be almost similar to that of the bulk resistance of Au. Typical I-V readings from the aligned nanowires showed that the resistance of these nanostructures is between 15 and 50 ohms. The IV results from nanowires were considered to be short measurements (Fig. 9.8). After the removal of the central Ag segment from the wire, sweeping the DC potential between 0 and 1 V the current level changes around the leakage current (in the order of 10^{-13} amp). It appears that nanogap structures formed by Ag removal from the aligned nanowires no longer exhibit conducting behavior. Figure 9.8 shows two different measurements from the same nanogap.

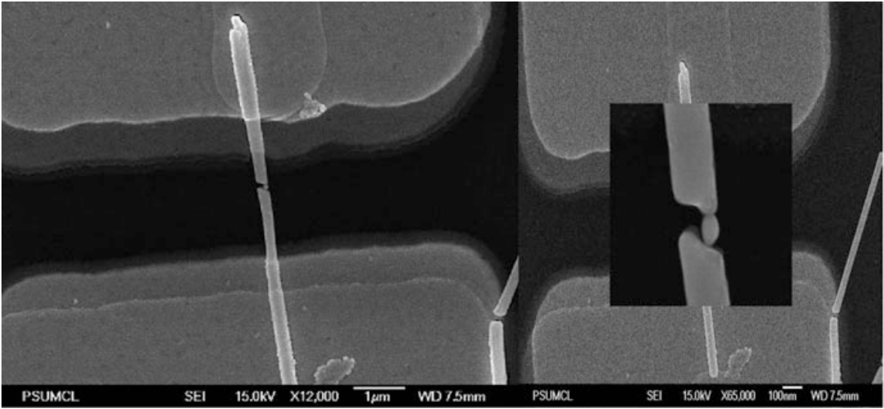

Fig. 9.10 Electron microscopy images of a single 100 nm Au nanoparticle captured in the nanogap device at 12 K and 65 K magnifications

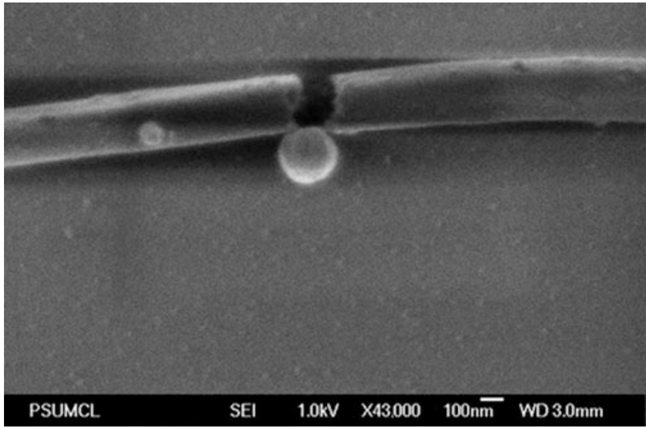

Fig. 9.11 Capture of a 250 nm Au nanoparticle by the nanogap device

It is noteworthy that voltages higher than 1.3 V create currents high enough to melt the nanowire aligned across the electrodes. This phenomenon is known as electromigration. Electromigration is the biased movement of atoms under the influence of an electric field [10], which is responsible for failures in most microelectronic devices. This effect is well characterized in the current-voltage (I-V) readings (the units of ampere and volt) with the current sharply decreased to the leakage current at 1.3 V when sweeping the voltage from 0 to 2.5 V (Fig. 9.9).

Nanogap (50–100 nm in size) based devices fabricated by precise alignment of Au–Ag–Au nanowires on planar electrode pairs were used to capture metallic nanoparticles using dielectrophoretic forces. Au nanoparticles with 100 or 250 nm diameter in ethanol were spread over the microchip and captured in the nanogaps under an AC field.

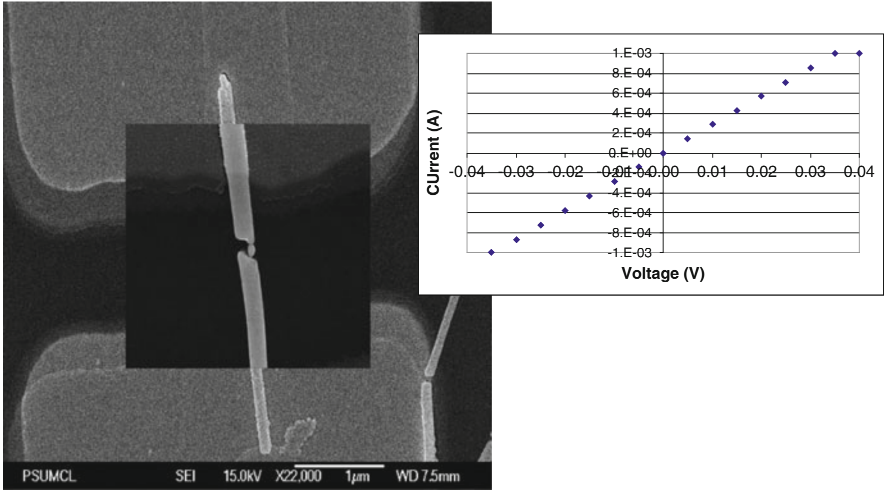

Fig. 9.12 Electron microscope image of a 100 nm Au nanoparticle in the gap and its I-V (units of Ampere (I) and Volts (V)) results, maximum current allowed, the compliance, is 100 mA)

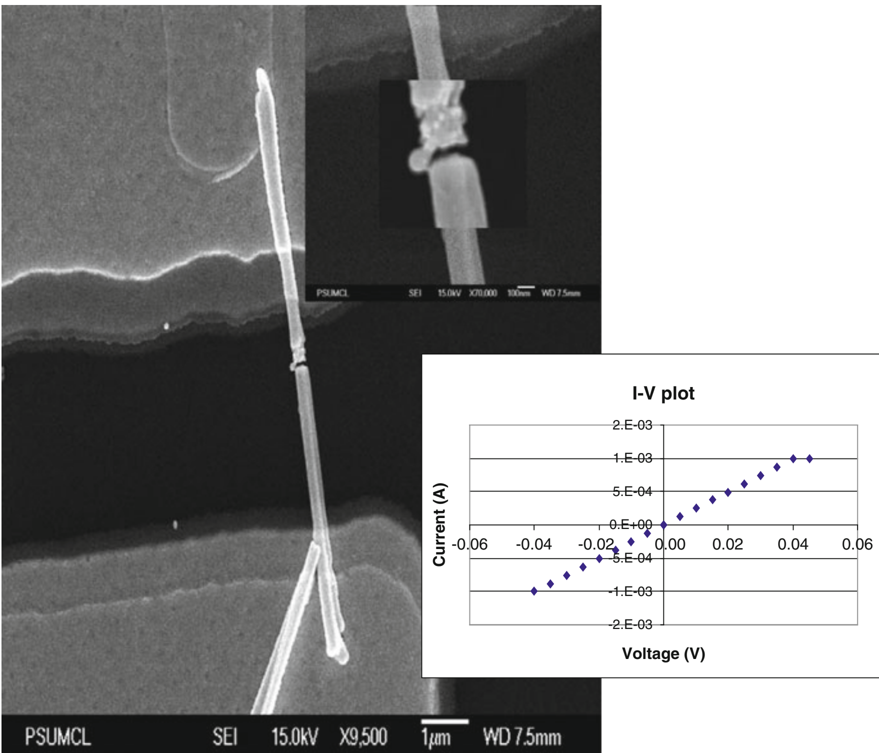

Fig. 9.13 Single nanoparticle capture in the nanogap and I-V characterization of the nanoparticles (compliance, maximum allowed current, is 100 mAmp, scan is cut when current reaches 100 mA)

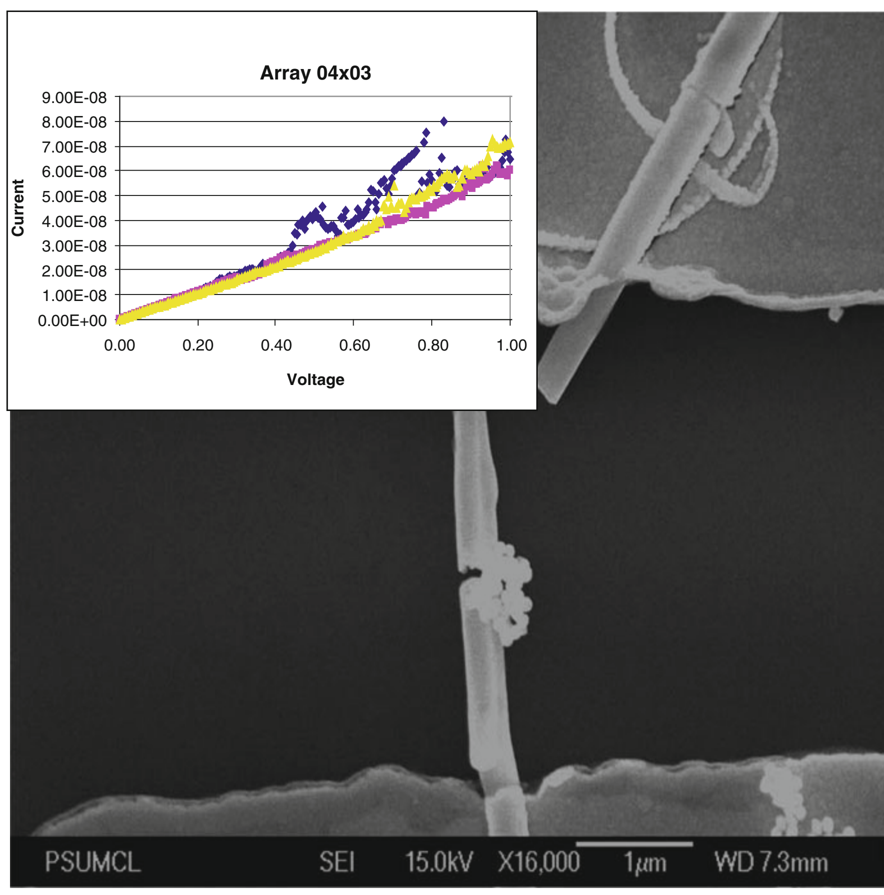

Fig. 9.14 Capture of multiple 100 nm Au nanoparticles in the nanogap and its I-V (units are Ampere and Volts) characterization (3 measurements)

The device having 100 nm gap used to capture Au nanoparticles is illustrated in Fig. 9.10. Applying up to a 2 V AC bias with 1 kHz frequency, a single 100 nm Au nanosphere was captured in the gap. Figure 9.11 illustrates capture of a 250 nm Au nanoparticle in gap.

The capture of spherical Au nanoparticles in the gap is characterized by I-V readings (units are Ampere for current and Volt for voltage). Such electrical responses from captured nanoparticles and the electron microscope images of these captures are illustrated in Figs. 9.12 and 9.13. The I-V results from single nanoparticles capture showed that the electrical conduction is good, resembling bulk electrical resistance. However, it appears that capturing multi-nanoparticles in the gap does not guarantee good electrical contact, resulting in I-V response that differs from that of single nanowire capture.

Figure 9.14 illustrates the multiple capture of 100 nm Au nanoparticles in a 100 nm separated nanogap. The electrical contact is poor, so I-V measurements differ from that of the single nanoparticle response.

In summary, our studies present a simple and powerful approach to facilitate the production of a tunable submicron gap array between electrodes. This research could lead to highly integrated nanosystems using bottom-up assembly technique.

Acknowledgements This chapter was prepared partly from nanowires-based nanoelectronics research at Penn State University, State College, PA. The author acknowledges great help of Dr. Mingwei Lie for microfabrication and invaluable contributions and research idea of professors Christine Keating and Theresa Mayer.

References

1. I. Amlani, A.M. Rawlett, L. Nagahara, K.R. Tsui. An approach to transport measurements of electronic molecules. Appl. Phys. Lett. **80**, 2761–2763 (2002)
2. C.L. Asbury, G. van den Engh. Trapping of DNA in nonuniform oscillating electric fields. Biophys. J. **74**, 1024–1030 (1998)
3. M.A. Banger, C.M. Hangarter, B. Yoo, Y. Rheem, W. Chen, A. Mulchandani, N.V. Myung. Magnetically assembled multisegmented Nanowires and their applications. Electroanalysis. **21**, 61–67 (2009)
4. A. Bezryadin,C. Dekker, G. Schmid. Electrostatic trapping of single conducting nanoparticles between nanoelectrodes. Appl. Phys. Lett. **71**, 1273–1275 (1997)
5. K.H. Bhatt, O.D. Velev. Control and modeling of the dielectrophoretic assembly of on-chip nanoparticle wires. Langmuir. **20**, 467–476 (2004)
6. E. Braun, Y. Eichen, U. Sivan, G. Ben-Yoseph, DNA-templated assembly and electrode attachment of a conducting silver wire. Nature **391**, 775–778 (1998)
7. Y. Cui, Q. Wei, C.M. Lieber, Nanowire nanosensors for highly sensitive and selective detection of biological and chemical species. Science. **293**, 1289–1292 (2001)
8. S.A. Dayeh, C. Soci, P.K.L. Yu, E.T. Yu, D. Wang, Influence of surface states on the extraction of transport parameters from InAs nanowire field effect transistors. Appl. Phys. Lett. **90**, 16212-1–16212-3 (2007)
9. F. Dewarrat, M. Calame, C. Schonenberger, Orientation and Positioning of DNA molecules with an electric field technique. Single Mol. **3**, 189–193 (2002)
10. C. Durkan, M.A. Scheider, M.E. Welland, Analysis of failure mechanisms in electrically stresses Au nanowires. Appl. Phys. Lett. **86**, 1280–1286 (1999)
11. P.R.C. Gascoyne, J. Vykoukal, Particle separation by dielectrophoresis. Electrophoresis **23**, 1973–1983 (2002)
12. W.A. Germishuizen, C. Walti, R. Wirtz, M.B. Johnston, M. Pepper, A.G. Davies, A.P.J. Middleberg, Selective dielectrophoretic manipulation of surface immobilized DNA molecules. Nanotechnology **14**, 896–902 (2003)
13. J.K. Gimzewski, C. Joachim, Nanoscale science of single molecules using local probes. Science **283**, 1683–1688 (2002)
14. C. Gurtner, E. Tu, N. Jamshidi, R.W. Haigis, T.J. Onofrey, C.F. Edman, R. Sosnowski, B. Wallace, M.J. Heller, Microelectronic array devices and techniques for electric field enhanced DNA hybridization in low-conductance buffers. Electrophoresis **23**, 1543–1550 (2002)
15. V. Haguet, D. Martin, L. Marcon, T. Heim, D. Stievand, Combines nanogap nanoparticles nanosensor for electrical detection of biomolecular interactions between polypeptides. Appl. Phys. Lett. **84**, 1312–1215 (2004)

16. B. Hartzell, B. McCord, D. Asare, H. Chen, J.J. Heremans, V. Soghomonian, Comporative current-voltage characteristcs of nicked and repaired DNA. Appl. Phys. Lett. **82**, 4800 (2003)
17. B. He, T.J. Morrow, C.D. Keating, Nanowire sensors for multiplexed detection of biomolecules. Curr. Opin. Chem. Biol. **12**, 522–528 (2008)
18. M.J. Heller, E. Tu, R. Martinsons, R.R. Anderson, C. Gurtner, A. Forster, R. Sosnowski: Active microelectronic array systems for DNA hybridization, genotyping, pharmacogenomics and nanofabrication Applications. In: Dekker, M. (eds.) Integrated Microfabricated Devices, pp. 223–270, Heller and Guttman, Chap. 10 (2002)
19. R. Holzel, N. Gajovic-Eichelmann, F.F. Bier, Oriented and vectorial immobilization of linear M13 dsDNA between interdigitaded electrodes-towards single molecule DNA nanostructures. Biosens. Bioelectron. **18**, 555–564 (2003)
20. J. Homola, S.S. Yee, G. Gauglitz, Surface plasmon resonance sensors: review. Sens. Actuators B **54**, 3 (1998)
21. Y. Huang, X. Duan, Q. Wei, C.M. Lieber, One-dimensional nanostructures into functional Networks. Science **291**, 630–633 (2001)
22. Y. Huang, J. Mo Yang, P.J. Hopkins, S. Kassagne, M. Tirido, A.H. Forster, H. Reese, Separations of simulants of biological warfare agents from blood by a miniaturized dielectrophoresis device. Biomed. Microdevices **5**, 217–225 (2003)
23. M.P. Hughes, Strategies for dielectrophoretic separation in laboratory-on-a-chip systems. Electrophoresis **23**, 2569–2582 (2002)
24. A. Javey, S. Nam, R.S. Friedman, H. Yan, C.M. Lieber, Layer-by-layer assembly of nanowires for three-dimensional, multifunctional electronics. Nano Lett. **7**, 773–777 (2007)
25. T.B. Jones, *Electromechanics of Particles* (Cambridge University Press, Cambridge, 1995)
26. Y.V. Kervennic, H.S.J. van der Zant, A.F. Morpurgo, L. Gurevich, L.P. Kouwenhoven, Nanometer-spaced electrodes with calibrated separation. Appl. Phys. Lett. **80**, 321–323 (2002)
27. S.I. Khondaker, Z. Yao, Fabrication of nanometer spaced electrodes using gold nanoparticles. Appl. Phys. Lett. **81**, 4613 (2002)
28. D.L. Klein, P.L. McEuen, J.E. Bowen Katari, R. Roth, A.P. Alivisatos, An approach to electrical studies of single nanocrystals. Appl. Phys. Lett. **68**, 2574 (1996)
29. J.F. Klemic, E. Stern, M.A. Reed, Hotwiring biosensors. Nat. Biotechnol. **19**, 294–295 (2001)
30. R. Krahne, A. Yacoby, A. Shtrikman, I. Bar-Joseph, T. Dadosh, J. Sperling, Fabrication of nanoscale gaps in integrated circuits. Appl. Phys. Lett. **81**, 730–733 (2002)
31. R. Krahne, T. Dadosh, Y. Gordin, A. Yacoby, A. Shtrikman, D. Mahalu, J. Sperling, I. Bar-Joseph, Nanoparticles and nanogaps: controlled positioning and fabrication. Phys. E **17**, 498–502 (2003)
32. C.Z. Li, H.X. He, A. Bogozi, J.S. Bunch, N.J. Tao, Molecular detection based on conductance quantization of nanowires. Appl. Phys. Lett. **76**, 1333–1335 (2000)
33. K. Liu, P.H. Avouris, J. Bucchignano, R. Martel, S. Sun, J. Michi, Simple fabrication scheme for sub-10nm electrode gaps using electron beam lithography. Appl. Phys. Lett. **80**, 865–867 (2002)
34. R. Mariella, MEMS for bio-assays. Biomed. Microdevices **4**, 77–87 (2002)
35. H. Morgan, M.P. Hughes, N.G. Green, Separation of submicron bioparticles by dielectrophoresis. Biophys. J. **77**, 516–525 (1999)
36. A.F. Morpurgo, C.M. Marcus, D.B. Robinson, Controlled fabrication of metallic electrodes with atomic separation. Appl. Phys. Lett. **74**, 2084–2086 (1999)
37. A. Motayed, M. He, A.V. Davydov, J. Melngailis, S.N. Mohammad, Realization of reliable GaN nanowire transistors utilizing dielectrophoretic alignment technique. J. Appl. Phys. **100**, 114310-9 (2006)
38. S.R. Nicewarner-Pena, R.G. Freeman, B.D. Reiss, L. He, D.J. Pena, I.D. Walton, R. Cromer, C.D. Keating, M.J. Natan, Submicrometer metallic barcodes. Science **294**, 137–141 (2001)
39. S. Niyogi, C. Hangarter, R.M. Thamankar, Y. Chiang, R. Kawakami, N.V. Myung, R.C. Haddon, Magnetically assembled multiwalled carbon nanotubes on ferromagnetic contacts. J. Phys. Chem. B **108**, 19818–19824 (2004)

40. J. Park, A.N. Pasupathy, J.I. Goldsmith, A.V. Soldatov, C. Chang, Y. Yaish, J.P. Sethna, H.D. Abruna, D.C. Ralph, P.L. McEun, Wiring up single molecules. Thin Solid Films **438–439**, 457–461 (2003)
41. H. Park, A.K.L. Lim, A.P. Alivisatos, J. Park, P.L. McEuen, Fabricatiom of metallic electrodes with nanometer separation by electromigration. Appl. Phys. Lett. **75**, 301–303 (1999)
42. S.J. Park, A. Taton, C.A. Mirkin, Array based electrical detection of DNA with nanoparticle probes. Science **295**, 1503 (2002)
43. R. Pethig, V. Bressler, Y. Chen, K.M. Tate, Dielectrophoretic studies of the activation of human T lymphocytes using a newly developed cell profiling system. Electrophoresis **23**, 2057–2063 (2002)
44. H.A. Pohl, *Dielectrophoresis* (Cambridge University Press, Cambridge, 1978)
45. D. Porath, Y. Levi, M. Tarabiah, O. Millo, Tunneling spectroscopy of isolated C60 molecules in the presence of charging effects. Phys. Rev. B **56**, 9829–9833 (1997)
46. D. Porath, A. Bezryadin, S. Vries, C. Dekker, Direct measurements of electrical transport through DNA molecules. Nature **403**, 635–638 (2000)
47. S. Raychaudhuri, S.A. Dayeh, D. Wang, E.T. Yu, Precise semiconductor nanowire placement through dielectrophoresis. Nano Lett. **9**, 2260–2266 (2009)
48. M.A. Reed, C. Zhou, C.J. Muller, T.P. Burgin, J.M. Tour, Conductance of molecular junctions. Science **278**(5336), 252–254 (1997)
49. B.D. Reiss, R. Griffith Freeman, I.D. Walton, S.M. Norton, P.C. Smith, W.G. Stamos, C.D. Keating, M.J. Natan, Electrochemical synthesis and optical readout of striped metal rods with submicron features. J. Electroanalyt. Chem. **522**, 95–103 (2002)
50. P.A. Smith, C.D. Nordquist, T.N. Jackson, T.S. Mayer, B.R. Martin, J. Mbindyo, T.E. Mallouk, Electric-field assisted assembly of metallic nanowires. Appl. Phys. Lett. **77**, 1399–1401 (2000)
51. R. Sordan, M. Burghard, K. Kern, Removable template route to metallic nanowires and nanogaps. Appl. Phys. Lett. **79**, 2073–2075 (2001)
52. C.P.T. Svensson, T. Martensson, J. Tragardh, C. Larsson, M. Rask, D. Hessman, J. Samuelson, J. Ohlsson, Monolithic GaAs/InGaP nanowire light emitting diodes on silicon. Nanotechnology **19**, 305201–305207 (2008)
53. M. Tanase, D.M. Silevitch, A. Hultgreen, L.A. Bauer, P.C. Searson, G.J. Meyer, D.H. Reich, Magnetic trapping and self-assembly of multicomponent nanowires. J. Appl. Phys. **91**, 8549–8551 (2002)
54. C. Thelander, L.E. Fröberg, C. Rehnstedt, L. Samuelson, L.-E. Wernersson, Vertical enhancement-mode InAs nanowires field-effect transistor with 50 nm wrap gate. IEEE Electron Device Lett. **29**, 206–208 (2008).
55. O.D. Velev, E.W. Kaler, In situ assembly of colloidal particles into miniaturized biosensors. Langmuir **15**, 3693–3698 (1999)
56. D. Wang, S. Jin, Y. Wu, C.M. Lieber, Large-scale hierarchical organization of nanowire arrays for integrated nanosystems. Nano Lett. **3**, 1255–1259 (2003)
57. M. Washizu, O. Kurosawa, Electrical manipulation of DNA in microfabricated structures. IEEE Trans. Indust. Appl. **26**, 1165–1172 (1990)
58. M. Washizu, O. Kurosawa, I. Arai, S. Suziki, N. Shimamoto, Application of electrostatic stretch-and positioning of DNA. IEEE Trans. Indust. Appl. **31**, 447–456 (1995)
59. S. Weiss Fluorescence spectroscopy of single biomolecules. Science **283**, 1676–1683 (1999)
60. H. Zhou, M. Wissinger, J. Fallert, R. Hauschild, R. Stelzl, C. Klingshirn, H. Kalt, Ordered, uniform-sized ZnO nanolaser arrays. Appl. Phys. Lett. **91**, 181112-1–181112-3 (2007)

Index

AlAs, 36
AlGaAs, 3, 4, 6, 8, 20, 37
Atomic force microscopy (AFM), 11
Atom/molecule, 93–99

Band gap, 26, 32
Base, 3, 4, 10, 20
Binary, 32
Bottom-up assembly, 144, 158

CdSe, 12–16
Collector, 10
Colloidal, 12, 13
Composition effects, 37
Conduction band, 5, 24, 30, 31, 33, 34
Current gain, 10

Density of states (DOS), 119–141
Dielectrophoretic manipulation, 147–148, 150
Diffusion limited growth, 103, 106, 108
Double well resonant tunneling, 79

Edge magnetism, 73, 74, 83
Emitter, 3, 4, 10, 20
Energy band structure, 19, 22, 30, 32, 35

Fano resonance, 132, 136–138, 140, 141
Fermi level, 9
Friedel phase, 132, 134–138, 140, 141
Friedel sum rule, 119

GaAs, 2–6, 8, 9, 20, 26, 27, 31, 33–35, 37
GaAsN, 29–31, 33, 34
GaN, 26, 28, 31, 34
GaP, 26, 28, 31, 33, 34
Graphene, 39–91, 93–99
Graphene magnetism, 71–74
Graphene nanoribbons, 69–91

Half metals, 82, 87, 89
Heterostructure, 9
Heterostructure bipolar transistors (HBTs), 3, 9, 10, 21

InAs, 4, 26, 27, 31, 33, 34
InGaAs, 4

Landau quantization, 47
Low-dimension electrode systems, 143–158

Massless dirac spectrum, 41
Metal organic chemical vapor deposition (MOCVD), 2
Modulation doped field effect transistors (MODFETs), 3, 8, 19, 36
Molecular beam epitaxy (MBE), 2, 7
Multiple quantum wells, 77

Nanocrystal, 12, 14, 15
Nanoparticle-based devices, 143–158
Nanoscience, 11
Nanotechnology, 11
Nanowires, 143–158
Noise, 21

H. Ünlü and N.J.M. Horing (eds.), *Low Dimensional Semiconductor Structures*,
NanoScience and Technology, DOI 10.1007/978-3-642-28424-3,
© Springer-Verlag Berlin Heidelberg 2013

Optical properties of nanocrystals, 102

Plasma, 93–96
Polarizability, 47, 48, 50, 52, 53

Quantum confinement, 6
Quantum dot, 12
Quantum size effect, 101
Quantum wire, 127–129, 131–141

Recombination, 6

s*, 24, 25, 27, 29
Scanning tunneling microscope (STM), 11
Scattering phases, 131–141
Semiconductor quantum dots, 101–116
Solid phase precipitation, 102–104
Spintronics, 69
Standard state heat capacity, 31
Superlattices, 4, 6, 71, 75–86, 89

Ternary, 32
Transistors, 8, 9
Transmision, 131, 132, 134, 136–141
Transmission electron microscopy (TEM), 12
2D transport, 55–56
Two-dimensional electron gas (2DEG), 8

Valence band, 7, 8, 10, 14, 15, 19–21, 24, 26, 28, 30–36
van der Waals interaction, 93–99